This electronic thesis or dissertation has been downloaded from the King's Research Portal at https://kclpure.kcl.ac.uk/portal/

Magnetic resonance elastography in liver tissue under load

Capilnasiu, Adela

Awarding institution:
King's College London

The copyright of this thesis rests with the author and no quotation from it or information derived from it may be published without proper acknowledgement.

END USER LICENCE AGREEMENT

Unless another licence is stated on the immediately following page this work is licensed

under a Creative Commons Attribution-NonCommercial-NoDerivatives 4.0 International

licence. https://creativecommons.org/licenses/by-nc-nd/4.0/

You are free to copy, distribute and transmit the work

Under the following conditions:

- Attribution: You must attribute the work in the manner specified by the author (but not in any way that suggests that they endorse you or your use of the work).
- Non Commercial: You may not use this work for commercial purposes.
- No Derivative Works - You may not alter, transform, or build upon this work.

Any of these conditions can be waived if you receive permission from the author. Your fair dealings and other rights are in no way affected by the above.

Take down policy

If you believe that this document breaches copyright please contact librarypure@kcl.ac.uk providing details, and we will remove access to the work immediately and investigate your claim.

Download date: 31. Oct. 2023

KING'S College LONDON

Magnetic resonance elastography in liver tissue under load

Doctoral Thesis

Author:

Adela Ioana Căpîlnaşiu

Supervisors:

David Nordsletten, PhD
Ralph Sinkus, PhD

A thesis submitted in fulfillment of the requirements for the degree of Doctor of Philosophy in the

School of Biomedical Engineering & Imaging Sciences
Faculty of Life Sciences & Medicine
King's College London

March, 2020

EPSRC
Engineering and Physical Sciences Research Council

SIEMENS Healthineers

Abstract

Liver disease was recently revealed to be the main cause of death among 35-49 years old people in the UK, with overall mortality rate having quadrupled in the last half century. Causes are related to hepatitis B/C, obesity and alcohol consumption, which can lead to inflammation and fibrosis. One way of assessing liver health is MR-Elastography (MRE), which is a technique that can characterise tissue biomechanical properties by imaging propagating shear waves.

Wave propagation is influenced by local tissue structure, but also by tissue deformation. For example, the liver is deformed during respiratory motion, which leads to changes in the apparent stiffness. Hence it is clinically relevant to investigate the bias induced by large deformation on wave behaviour. A theory was developed in this regard, which links deformation to its effect on wave propagation. The theory has been incorporated into a new MRE reconstruction technique, with the purpose of correcting the bias in apparent stiffness introduced by deformation. To validate this theory, an MRE experiment on poly-vinyl alcohol (PVA) phantoms under a range of large deformations was performed. It was shown that, by combining knowledge of the deformation and material law (here inferred from complementary rheological experiments), the stiffness biasing effects of large deformation on small wave propagation can be undone.

Similar to the phantom work, MRE experiments were performed on deformed *ex vivo* liver samples, which displayed apparent stiffness biases. In order to apply the proposed theory, a viscoelastic liver constitutive law was needed. This was obtained from rheological experiments, where tissue samples were examined under a range of combined large deformations (compression and shear strain) and at multiple frequencies. The complex nature of liver tissue structure posed additional challenges when incorporating the knowledge on deformation and tissue law into the MRE reconstruction. This led to a comprehensive analysis which revealed the importance of accurate assessment of deformation metrics for the recovery of intrinsic tissue properties.

Lastly, healthy volunteers and patients suffering of liver disease were scanned using MRE. Two states were acquired, at end expiration and end inspiration. For both groups, differences in stiffness measurements were observed between the two respiratory states. A comparison of the two groups is discussed, in the context of determining the behaviour of healthy, inflamed and fibrotic liver tissue under deformation.

Acknowledgements

This thesis is a celebration of four years of hard work, persistence and devotion, yet its completion would not have been possible without the continuous support of many academics, colleagues, friends and family.

Foremost, I would like to thank my first supervisor, Dr. David Nordsletten, for the supervision and guidance he offered me throughout this journey. By providing me with constant support in a wide range of topics, but also by challenging me to become more independent, he motivated me to strive to do my best. As this doctoral work had many ups and downs, I am particularly grateful for him not losing faith in me and guiding me back on an ascendant path when I needed it.

I would like to thank my second supervisor, Prof. Ralph Sinkus, for his guidance and support, but also for his patience while teaching me how to handle and interpret MRE data. His feedback and inclination towards clinical applicability helped me keep track of the bigger picture.

I am grateful to Prof. Lynne Bilston for constructive discussions on liver modelling and for inviting me to discover her laboratory in Sydney. I would also like to thank Dr. Lauriane Jugé for performing the *ex vivo* MRE experiments and for her patience in explaining to me the details of the experiment.

I am thankful for my supervisors creating a wonderful working group, as the support and friendship I found there is invaluable. Thus, huge thanks to Dr. Myria Hadjicharalambous for mentoring me in my early doctoral years, as well as for all the support and encouragement during the ups and downs. I would also like to thank Dr. Dan Fovargue for his patience whenever I showed up with random MRE questions. I am extremely grateful for the support of Dr. Marian Troelstra, who added the magic touch of a doctor in improving the liver MRE setup, and for managing the scans of patients and volunteers. I would like to thank Dr. Renee Miller for her help with creating meshes, but also other tools that I needed. An extra shout-out is owed to Dan and Renee for revising parts of this thesis and correcting my awkward English phrases.

I would like to thank the team in charge of MRE hardware and software: Dr. Sila Dokumaci, Dr. Jose de Arcos and Stefan Hoelzl for perfecting the motor code and scanning sequence, and also George Jolly and Omar Darwish for perfecting the MRE hardware.

Many thanks are owed to Sarah Hammoudi and Paola Bello for managing the project (and the group). I would also like to thank Max Balmus, Dr. Marco Fiorito and Dr. Will Zhang for productive discussions and help with various computational tools.

I am also very grateful to Dr. Liya Asner for teaching me how to use $\mathcal{C}$**heart**.

I would like to thank Marlies Hoelzl, Mandy Nio, Pamela Wochner, Anna Wittgenstein and Sandra Hager for productive discussions and support and sweets.

Another shout-out to the great group of people mentioned above (a.k.a. the Elasto-coffee lovers), with whom I enjoyed countless lunches, coffees, pub nights and even wedding celebrations!

I am very grateful for the support of Dr. Radhouene Neji, Sami Jeljeli and James Stirling during scanning, and also for their patience regarding paperwork.

I would like to thank Andreas Hessenthaler for teaching me how to make silicon phantoms, Dr. Ondrej Holub for helping and guiding me in the lab, and Dr. Valery Vishnevskiy for providing me with the registration tool used in this doctoral work.

I would like to thank the members of my TPC committee, Dr. Jack Lee, Dr. Jordy Alastruey and Dr. Oleg Aslanidi for their feedback and guidance during those meetings.

I would like to thank my undergraduate supervisor, Prof. Tobias Preusser, for getting me interested in the world of biomathematics, and to my MSc supervisor, Dr. Nick Jones, for offering me the chance to further explore this area.

I would also like to thank teachers that inspired me along the way - my physics teachers Ion Bararu and the late Claudia Dobrin, my mathematics teachers Mihai Contanu and Andrei Gheorghe, my Romanian teacher Anca Cirligeanu and my English teachers Daniela Craciun and Raluca Nedelcu.

Within the CDT group at KCL, I am thankful to have met my fiends Esther and Giovanna, with whom I enjoyed many dinners and musicals! I would like to thank Emily, Jorge and Sam for the many coffee breaks and also Camila for enabling Christmas gift exchanges between me and my sister in Chile!

Far away from London, I am thankful for friendships that lasted throughout the years. I would like to thank Andra, Daiana, Maria, Radu, Alexandra, Lavinia, Raluca, Babe, Cretu, Victor, Claudiu, Ioana, Oana, Anca, Irina (T), Irina (P), Adina, Raluca and Andrei for the happy (individual) reunions we managed to organise.

I would also like to thank Philip and Sofia, who were a great support for me just before staring my doctoral studies.

I would like to thank Fam. Mosteanu - Elena and Marius - for the emotional support and encouragements they offered me.

A big thanks is owed to the people involved in my dancing life, as this keeps me sane and happy. I would like to thank Tash and Stefano for teaching me two body mechanics in a Waltz, and to Marika for endless support and positivity when teaching me Rumba walks. I would like to thank Sherwin for the best Slow Fox dances and Tianci for

a crazy competitive year. Mostly, I would like to thank Chris for being incredibly understanding of my time limitations during the last stages of this doctoral work and for his dedication during practice.

This work could not have been completed without the greatest continuous support of my family. Thus, I would like to thank Radu and Adriana for all the nice family gatherings. I would also like to thank my grandparents Tuta, Mamica and Tatutu for all their care towards my well-being. I would like to thank my sister Anda, along with James, André and Nicole, for providing me with energy and optimism and for many calls of encouragement and comfort.

A very special mention is owed to Philipp, who also helped me review parts of this thesis. But mostly, I am grateful for all his love, everyday support, and for making me happy.

Finally, none of this would have been possible without the unconditional love and support of my parents, Adriana and Dorin. They encouraged me to aim high and provided me with comfort when I needed it. Thank you for everything you have done for me, as my achievements are because of you!

Publications

Adela Capilnasiu, Myrianthi Hadjicharalambous, Daniel Fovargue, Dharmesh Patel, Ondrej Holub, Lynne Bilston, Hazel Screen, Ralph Sinkus, David Nordsletten. "Magnetic resonance elastography in nonlinear viscoelastic materials under load". *Biomechanics and modeling in mechanobiology* 18, no. 1 (2019): 111-135.

Adela Capilnasiu, Lynne Bilston, Ralph Sinkus, David Nordsletten. "Nonlinear viscoelastic constitutive model for bovine liver tissue". *Biomechanics and modeling in mechanobiology* (2020)

Will Zhang, Adela Capilnasiu, Gerhard Sommer, Gerhard A. Holzapfel, David A. Nordsletten. "An efficient and Accurate Method for Modeling Nonlinear Fractional Viscoelastic Biomaterials". *Computer Methods in Applied Mechanics and Engineering* 362, 112834 (2020)

Daniel Fovargue, Marco Fiorito, Adela Capilnasiu, David Nordsletten, Jack Lee, and Ralph Sinkus. "Towards noninvasive estimation of tumour pressure by utilizing MR elastography and nonlinear biomechanical models". *Scientific Reports* 10, 5588 (2020)

Contents

1 Introduction **1**

1.1 Liver architecture . . . 3
1.2 Liver disease . . . 3
1.2.1 Common causes of liver disease . . . 3
1.2.2 Inflammatory and fibrogenic processes . . . 5
1.2.3 Liver fibrosis staging and inflammation grading . . . 6
1.3 Liver disease assessment methods . . . 7
1.3.1 Liver biopsy . . . 7
1.3.2 Serum markers . . . 7
1.3.3 Imaging modalities . . . 8
1.4 Elastography as an assessment method . . . 10
1.5 Biomechanics of liver . . . 12
1.5.1 Previous work in liver constitutive modelling . . . 13
1.6 Thesis outline . . . 16

2 Theory of continuum mechanics **19**

2.1 Kinematics . . . 19
2.1.1 Deformation gradient . . . 21
2.1.2 Invariants . . . 22
2.1.3 Isochoric kinematic quantities and invariants . . . 22
2.2 Stress tensors . . . 23
2.3 Conservation laws . . . 23
2.3.1 Conservation of mass . . . 24
2.3.2 Conservation of linear momentum . . . 24
2.3.3 Conservation of angular momentum . . . 26
2.4 Perturbed balance equations . . . 27
2.4.1 Linearisation of the perturbed equations of motion . . . 28
2.4.2 Harmonic wave perturbations . . . 30
2.4.3 Periodic nonlinear wave equations in the physical domain . . . 31
2.5 Constitutive equations . . . 32
2.5.1 Hyperelastic solids . . . 32

2.5.2 Viscoelastic solids . . . 32
2.5.3 Liver hyperelastic constitutive equations in literature . . . 33
2.5.4 Liver viscoelastic constitutive equations in literature . . . 38
2.6 Linear viscoelasticity in MRE . . . 41

3 An Efficient and Accurate Method for Modeling Nonlinear Fractional Viscoelastic Materials 42
3.1 Introduction . . . 43
3.2 Fractional Derivatives and their Approximations . . . 45
3.2.1 Caputo fractional derivative . . . 45
3.2.2 Current methods for numerical approximation of the Caputo derivative . . . 46
3.2.3 Prony approximation of the Caputo derivative . . . 48
3.2.4 Discrete Prony approximation of the Caputo derivative . . . 50
3.2.5 Optimizing the Numerical approximation $\hat{D}_t^\alpha$ . . . 54
3.2.6 Numerical implementation . . . 55
3.3 Large Deformation Viscoelastic Solid Mechanics . . . 55
3.3.1 Review of kinematics and kinetics . . . 55
3.3.2 Extension of hyperelastic to viscoelastic models . . . 56
3.3.3 Conservation of mass and momentum . . . 58
3.4 Finite Element Approximation for Viscoelastic Solid Models . . . 58
3.4.1 Continuous and Discrete Weakform System . . . 58
3.4.2 Stress Discretization and Integration with the Prony Approximation . . . 59
3.4.3 Solution procedure . . . 60
3.4.4 Stability of the Discrete Weak form System . . . 61
3.5 Approximation of Polynomial Functions . . . 62
3.6 FE approximation of fractional differential equations . . . 66
3.7 Fractional Approximation applied to Biomechanics in the Liver . . . 70
3.7.1 Finite element model for the mechanical testing of livers . . . 70
3.7.2 Accuracy and convergence . . . 72
3.7.3 Computational cost . . . 73
3.8 Discussion . . . 75
3.8.1 Computational cost . . . 75
3.8.2 Accuracy and convergence . . . 75
3.8.3 Other methods . . . 75
3.8.4 Other applications . . . 76
3.8.5 Practical guidance . . . 77
3.9 Conclusion . . . 77
Supplementary materials . . . 78
3.A Stability Analysis for Linear Fractional Viscoelastic Materials . . . 78

3.B Optimal Prony Series Parameters for Approximating the Caputo Fractional Derivative . . . 82

4 MRE in nonlinear viscoelastic materials under load 84
4.1 Introduction . . . 85
4.2 Materials and Methods . . . 87
4.2.1 Harmonic Wave Motion in Deformed Nonlinear Viscoelastic Materials . . . 87
4.2.1.1 Kinematics, Harmonic Wave Motion and Notation . . . 87
4.2.1.2 Perturbation of Cauchy's Equations of Motion . . . 89
4.2.1.3 Loading Bias of Planar Shear Waves in Pure Compression . . . 92
4.2.2 Nonlinear Viscoelastic Characterisation of PVA . . . 95
4.2.2.1 PVA Phantom preparation . . . 95
4.2.2.2 Rheological testing of PVA phantoms . . . 96
4.2.2.3 Constitutive Modelling of PVA . . . 98
4.2.2.4 Rheology Data Analysis and Model Fitting . . . 99
4.2.3 Harmonic Wave Motion in Deformed PVA . . . 101
4.2.3.1 MRE Experimental setup . . . 102
4.2.3.2 MRE data analysis . . . 103
4.3 Results and Discussion . . . 106
4.3.1 Nonlinear Viscoelastic Model for PVA . . . 106
4.3.2 Loading Bias in Harmonic Wave Motion Under Pure Compression 110
4.3.3 Intrinsic Stiffness Estimation . . . 112
4.3.4 Extension and Impact in Tissue . . . 115
4.3.5 Study Limitations . . . 116
4.4 Conclusions . . . 117
Supplementary materials . . . 118
4.A Simplification to Linearised Elastic Wave Equations . . . 118
4.B Viscoelastic Moduli estimates for PVA material . . . 122
4.C Supplement . . . 125
4.C.1 Silicone phantom . . . 125
4.C.2 PVA phantom . . . 126

5 Nonlinear viscoelastic constitutive model for bovine liver tissue 127
5.1 Introduction . . . 128
5.2 Materials and Methods . . . 130
5.2.1 Kinematics background . . . 130
5.2.2 Nonlinear viscoelastic characterisation of liver tissue . . . 131
5.2.2.1 Sample preparation . . . 132
5.2.2.2 Rheological experimental design . . . 132
5.2.2.3 Modelling the experiment . . . 133

5.2.3 Constitutive modelling of liver tissue . . . 134
5.2.3.1 Viscoelastic modified Mooney-Rivlin model . . . 134
5.2.3.2 Viscoelastic Ogden based model . . . 135
5.2.3.3 Viscoelastic Exponential model . . . 136
5.2.4 Data analysis and model fitting . . . 136
5.2.4.1 Minimisation problem . . . 136
5.2.4.2 L_2 norm . . . 138
5.2.4.3 Point-wise norm . . . 138
5.2.4.4 Parameter-scaling norm . . . 138
5.3 Results . . . 139
5.3.1 Viscoelastic models tailored with the L_2 norm . . . 140
5.3.2 Viscoelastic models tailored with the point-wise norm . . . 141
5.3.3 Viscoelastic models tailored with the parameter-scaling norm . . . 143
5.4 Discussion . . . 146
5.4.1 Overview . . . 148
5.4.2 Extension and impact in-vivo and in-silico . . . 149
5.4.3 Study limitations . . . 150
5.5 Conclusions . . . 150
Supplementary materials . . . 152
5.A Extended models . . . 152
5.A.1 Results employing the extended models . . . 152
5.B Supplement . . . 153

6 Ex vivo MRE liver characterisation **156**
6.1 Materials and methods . . . 157
6.1.1 Harmonic wave motion in loaded liver samples . . . 157
6.1.1.1 Liver sample preparation . . . 158
6.1.1.2 MRE experimental setup . . . 158
6.1.1.3 MRE data analysis . . . 160
6.1.2 Finite element model for the loading of liver samples . . . 163
6.1.2.1 Mesh construction . . . 163
6.1.2.2 Problem specification . . . 164
6.1.3 Registration of deformed liver samples . . . 165
6.2 Results and discussion . . . 166
6.2.1 Harmonic wave motion in undeformed liver samples . . . 166
6.2.2 Loading bias in harmonic wave motion under compression . . . 167
6.2.3 Intrinsic stiffness estimation . . . 169
6.2.4 Deformation estimate from image registration . . . 173
6.3 Conclusions . . . 178
Supplementary materials . . . 180
6.A Nonlinear viscoelasticity in MRE . . . 180

6.A.1 Linearised elastic wave equations for viscoelastic materials 180
6.A.2 Viscoelastic moduli estimates for the *vEXP* model 183
6.B Registration validation 185

7 In vivo MRE liver characterisation **189**
7.1 Scanning protocol 189
7.2 MRE data analysis 190
7.3 Results and discussion 192
7.4 Conclusions 198

8 Conclusions and future directions **199**
8.1 Future directions 201
8.1.1 Deformation metrics 201
8.1.2 Liver constitutive modelling beyond MRE 202
8.1.3 MRE beyond liver tissue investigation 202

List of Figures

1.1.1 Architecture of the liver 4
1.2.1 Inflammation and fibrosis in the liver 5
1.2.2 Stages of liver fibrosis 6

2.1.1 Motion of a deformed body 20
2.5.1 Liver compression-elongation behaviour schematic 36
2.5.2 Liver rheological testing configurations 36
2.5.3 Liver compression-elongation behaviour 37
2.5.4 Rheological schemes of increasing complexity 39

3.3.1 Illustration of spring, dashpot and spring-pot elements 57
3.4.1 Illustration of element level discretization for fractional viscoelasticity . 60
3.5.1 Examples of approximating the fractional derivative 64
3.5.2 The convergence of the approximation of the fractional derivative . . . 66
3.5.3 Examination of the $L^2(I)$ norm error of the truncation error 66
3.6.1 The solution of the Prony series approximation 67
3.6.2 The absolute value of the residuals from the Prony series approximation 68
3.6.3 Convergence of the solution of the fractional diffusion equation 70
3.7.1 Comparison of the model and experimental data from Tan *et al.*[246] . . 71
3.7.2 Illustration of the FEM solution of the liver model under deformation and shear 73

4.2.1 Planar waves through a loaded phantom 94
4.2.2 Illustration of experimental setup, protocol and data in rheological tests 97
4.2.3 Illustration of the MRE test setup 102
4.2.4 Images corresponding to the uncompressed and compressed phantoms . 104
4.3.1 The minimum error obtained by fitting the model to the rheological data for each phantom. 106
4.3.2 Illustration of the model fit considering the 5-parameter model or 3-parameter model. 107
4.3.3 Contribution of each parameter to the model, compared to the data . . 108
4.3.4 Stiffness maps G' and corrected maps M corresponding to the uncompressed and compressed phantoms 111

4.3.5 Average of stiffness maps G' and corrected maps M over all pixels in a phantom, in all deformation states . . . 112
4.C.1 Images corresponding to the silicone phantom . . . 125

5.2.1 Illustration of the experimental setup . . . 132
5.3.1 Maximum torque amplitude across shear strain . . . 140
5.3.2 The minimum error for the L_2 norm . . . 141
5.3.3 Example of the three models fit to the data . . . 141
5.3.4 Lissajous curve exemplifying the *vEXP* model fit to the data . . . 142
5.3.5 The minimum error for the point-wise scaling norm . . . 142
5.3.6 Example of the three models fit to the data . . . 143
5.3.7 Lissajous curve exemplifying the *vEXP* model fit to the data . . . 143
5.3.8 The minimum model error (*vMR**, *vOG* and *vEXP*) for the parameter scaling norm . . . 144
5.3.9 The three models fit to the data acquired at 1Hz, using the parameter scaling norm . . . 144
5.3.10 The three models fit to the data acquired at CS 10% . . . 145
5.3.11 Lissajous curve exemplifying the *vEXP* model fit to the data . . . 145
5.3.12 Absolute linear parameters for the models . . . 146
5.A.1 The minimum model error (vMR^*_{ext}, vOG_{ext} and $vEXP_{ext}$) for the parameter scaling norm . . . 153
5.B.1 Simulations of liver sample compression . . . 153
5.B.2 Simulations of ideal and non-ideal compression . . . 154

6.1.1 Illustration of the liver MRE test setup . . . 159
6.1.2 Images corresponding to the uncompressed and compressed liver samples 160
6.1.3 Liver sample mesh . . . 164
6.1.4 Example tagged images . . . 166
6.2.1 Stiffness maps G' and corrected maps M corresponding to the uncompressed and compressed liver samples . . . 168
6.2.2 Average of stiffness maps G' and corrected maps M corresponding to the uncompressed and compressed liver samples . . . 169
6.2.3 Average of stiffness maps G'' and corrected maps N corresponding to the uncompressed and compressed liver samples . . . 169
6.2.4 Error trend liver MRE . . . 170
6.2.5 Liver sample deformation gradient . . . 172
6.2.6 Sequence of tagged liver samples . . . 173
6.2.7 Anatomical images of a liver sample . . . 174
6.2.8 Deformation gradient for ≈10, 20 and 30% compression . . . 175
6.2.9 Corrected maps M corresponding to ≈10, 20 and 30% compression . . . 176
6.2.10 Effect of deformation gradient on intrinsic stiffness estimation . . . 176
6.2.11 Large vessels in the liver . . . 177

6.B.1 Test images for registration 186
6.B.2 Deformation gradient computed from the registration displacements . . 187
6.B.3 Elastography simulated data, reconstructed using UR and CR 188

7.2.1 *In vivo* liver images in expiration and inspiration 191
7.3.1 Changes in G' and G'' between expiration and inspiration 192
7.3.2 Comparison of average liver stiffness and viscosity between healthy volunteers and patients grouped by fibrosis stage 193
7.3.3 Comparison of average liver stiffness and viscosity between healthy volunteers and patients grouped by inflammation grade 194
7.3.4 Effect of inflammation within each fibrosis stage 195
7.3.5 Effect of fibrosis within each inflammation grade 196
7.3.6 Comparison of the fractional order α parameter between healthy volunteers and patients 197

List of Tables

3.1 Computational cost of approximating the fractional derivative 63
3.2 Comparing the approximation error for the fractional derivative 65
3.3 Reproducing Table 1 from Gao *et al.*[69] 69
3.4 Reproducing Table 2 from Gao *et al.*[69] 69
3.5 Accuracy and convergence of the Prony approximation 72
3.6 Comparison of solving speed for the Grünwald-Letnikov (GL) and Prony approximation methods 74
3.7 Comparison of compute times for a hyperelastic and fractional viscoelastic solutions 74

4.3.1 Best fit parameters for each PVA phantom 107
4.3.2 Best fit parameter for each PVA phantom, while considering remaining parameters to be 0 109
4.3.3 Best fit parameters for each phantom, restricting $C_1, \delta_2 = 0$ Pa 110
4.3.4 MRE minimisation parameters fixing $\alpha = 0.03$ 113

5.2.1 Testing protocol across frequencies, compression and shear deformations. 133

6.2.1 MRE liver tissue parameters 167

7.2.1 Patients' information 191
7.3.1 Average stiffness and viscosity values for healthy volunteers and patients 194

1 Introduction

Liver disease is the primary cause of mortality among 35-49 years old people in the UK[24]. While the mortality rate of cancer, heart disease, diabetes and other major conditions has decreased, for hepatic disease the mortality rate has quadrupled in the last half century. Although liver disease requires a long, chronic onset (even decades), 75% of the cases are detected in the late stages. This worsens the healing prospects, as treatments are less effective and lifestyle changes are difficult to implement. Researchers and clinicians are working towards improving diagnostic methods, such that liver disease can be reliably assessed early on.

Inflammation and fibrosis are two important processes in liver disease, which lead to morphological tissue changes. Inflammation is a wound healing mechanism, which gets activated when an injurious signal is present, and stops when the signal disappears. However, under chronic conditions, inflammation can lead to fibrosis, which can eventually advance into cirrhosis. The most well known injurious causes that are associated with inflammation, fibrogenesis and potentially cirrhosis are hepatitis viruses B and C and alcoholic and non-alcoholic steatohepatitis (fatty liver disease)[65,288]. While inflammation can be easily reversed, fibrosis regression is not well controlled. In animals, some studies have suggested fibrosis reversal, however, in humans the results focus on very specific cases and groups of patients[5,211]. In late stage cirrhosis, liver transplantation becomes the only treatment option. Due to the limited number of organs available and compatibility issues, not all patients can benefit from transplantation. Furthermore, even if a transplantation procedure is undergone, there is the risk that the disease can reappear and progress rapidly[256].

Liver biopsy is the established method used for assessing hepatic disease. It enables microscopic quantification of a small tissue sample, which helps to determine the disease and its severity based on the cellular structure. However, it is an invasive procedure that can lead to complications[210]. Moreover, it provides a localised overview, depending on the sample, and as fibrosis and inflammation are heterogeneously distributed[49], this might lead to erroneous results. Hence, there is a need for alternative diagnosis methods, which can encompass the global state of the liver.

Advancements in medical imaging have led to the development of alternative meth-

ods for liver diagnosis. Among these, Magnetic Resonance Elastography (MRE) is a technique that quantifies tissue mechanical properties (e.g. stiffness, elasticity, viscosity) using steady state mechanical waves propagating through a body. As these properties are impacted by the morphological changes occurring in inflammation and fibrosis[8,277,278], MRE has the potential to identify and stage liver disease, and promising results have been published[114–116,128]. However, one challenge yet to be addressed is the impact of macroscale deformations on wave propagation behaviour. As the liver is deformed during the respiratory motion[179,191], results may be biased, as large deformations trigger a nonlinear tissue response[70,146]. Hence, an apparent stiffness might be observed, where patient-specific kinematics and intrinsic tissue properties are non-trivially combined.

Although liver motion might introduce deformation bias, this could be beneficial from a different perspective. In *ex vivo* experiments, it was shown that the difference between healthy and diseased liver tissue becomes more apparent under large strains[277]. Thus, measuring stiffness in strained tissue could increase diagnostic accuracy. However, a good understanding of the effects of deformation on wave behaviour is required in order to correctly interpret MRE results and accurately quantify disease severity. Challenges include rectifying the linear wave equations assumed to model MRE vibrations[77] with the inherent nonlinear biomechanical behaviour of tissue (as shown in rheological tests[70,146]). Additionally, as MRE operates at frequencies which exhibit the viscoelastic characteristics of tissues ($\approx$50 Hz), viscoelasticity should be accounted for. This leads to convoluted models which are usually difficult to employ for MRE purposes.

The main aim of this thesis is to address the complications arising from large deformations in MRE measurements. As a starting point, a theory linking large deformations and harmonic wave propagation was developed. For validation purposes, a poly-vinyl alcohol (PVA) phantom study was designed, comprising MRE testing at multiple deformation levels. The identification of a suitable material law was achieved from rheological tests. In order to proceed to liver tissue, a nonlinear viscoelastic model was developed, using comprehensive rheological data acquired at a range of compression preloads, oscillatory shear strains and frequencies. Both liver and PVA models rely on nonlinear fractional viscoelasticity, which ensures a simplified form compared to classical viscoelastic models, making them suitable to be integrated in the estimation of MRE stiffness moduli. Hence, these steps constitute a foundation for interpreting MRE *ex vivo* and *in vivo* measurements of deformed liver tissue.

With these considerations in mind, the rest of the section presents the liver architecture, disease mechanism, assessment methods and current state of the art in liver biomechanical modelling. Section 1.1 presents a short overview of liver structure, focusing on the elements relevant in triggering inflammation and fibrosis. Subsequently, section 1.3 reviews the methods used in diagnosing and staging liver disease, further focusing on

MRE in section 1.4. Previous work in biomechanical characterisation of the liver is presented in section 1.5. Finally, the thesis' structure is outlined in section 1.6.

1.1 Liver architecture

The liver is the largest internal organ, situated in the upper right abdominal cavity[1]. Anatomically, two parts can be easily distinguished: the right and left lobes, separated by the falciform ligament (Fig. 1.1.1). Additionally, two smaller lobes can be identified from the inferior side, namely the caudate and quadrate lobes. Functionally, Couinaud classified the liver into eight segments[45,241], based on the first ramification level of the portal vein. At microscopic level, the liver comprises lobules, which are hexagonal functional units (1-2 mm). In the corners of these hexagons, a portal triad is identified, consisting of small branches of the hepatic artery, hepatic portal vein and bile duct. Hence, the liver is a highly vascularised organ.

The liver carries a number of vital functions, having a central role in the metabolic processes[215]. Carbohydrates, fats and proteins are transported from the digestive apparatus to the liver through the portal vein circulation. Additional oxygenated blood is provided through the hepatic artery. The blood mixes in the lobules' sinusoids, where nutrients are absorbed in order to provide energy, while the toxic elements are cleared. The deoxygenated blood is drained via the hepatic veins further into the inferior vena cava.

Aside the blood transportation system, some cellular structures are now introduced, in order to further address the mechanisms of inflammation and fibrosis. Kupffer cells are immune macrophage cells that can be found on the interior endothelium of the sinusoids. The space outside the vessels is mainly occupied by hepatocytes, which constitute most of the liver's mass ($\approx$80%)[215]. They are the main cells that are in charge of the metabolic reactions. The space between hepatocytes and sinusoids is known as the space of Disse, and it contains the blood plasma and facilitates exchange between hepatocytes and blood[161]. It also contains hepatic stellate cells (HSC), which are quiescent under normal conditions. Lastly, the structural shape of the above mentioned elements is provided by the extra-cellular matrix (ECM), that accounts for less than 3% of the area of a healthy section[144].

1.2 Liver disease

1.2.1 Common causes of liver disease

Liver disease is usually related to viral causes (hepatitis B and C), alcohol consumption or build-up of fat in the liver. More rarely, it is related to genetic causes (e.g. hemochromatosis - iron overload) or the autoimmune system (e.g. autoimmune hepatitis (AIH), primary biliary cholangitis).

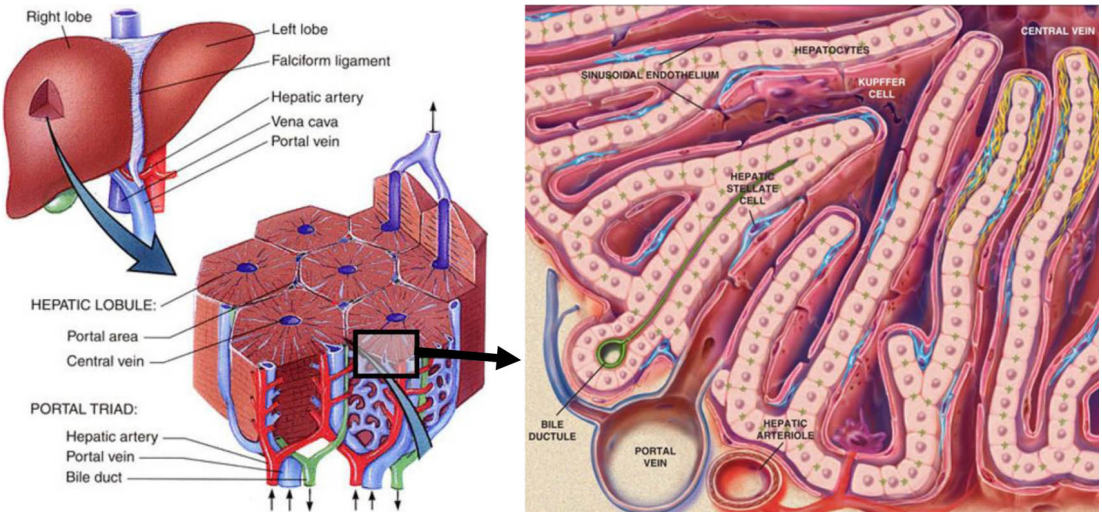

Figure 1.1.1 *Architecture of the liver (figure modified from Yale Medical Cell Biology[275] and Friedman et al.[225], with permission)*

Hepatitis B and C (HBV and HCV) are widespread viral infections. HBV infection often happens at an early age, being transmitted through blood from mother to child or between children. It has a high occurrence mostly in the underdeveloped world. Efforts to control it focus on a vaccination programme in young children[269]. HCV infection occurs mostly due to poor healthcare practices and has a high prevalence worldwide, both in the developed and underdeveloped regions. The most effective treatment is based upon direct-acting antivirals. These viral infections lead to the acute inflammation of the liver. Although they are treatable, they often go undetected, until they cause chronic injury, leading to fibrosis or even cirrhosis.

A different category of liver disease is related to alcohol consumption. Approximately 20% of the people in the UK drink alcohol above the recommended guidelines, which can cause liver injury[25]. A sustained inflammatory stimulus can lead to alcoholic hepatitis (AH) and further on to cirrhosis. In the early stages, alcohol related liver injury is reversible through behavioural changes. In the later stages, medicated treatment is necessary under a complex patient specific scheme[190].

Non-alcoholic fatty liver disease (NAFLD) is another common cause of liver inflammation. Among people suffering of NAFLD, some have simple steatosis, while approximately 30% have non-alcoholic steatohepatitis (NASH)[268]. The latter can further evolve into fibrosis and cirrhosis. NASH is highly correlated with obesity[263], thus being an issue of current importance in the western world. Despite the high incidence, there is no agreed treatment for NASH, and specialists recommend lifestyle changes[26].

The factors presented above are the most common causes of liver inflammation. Despite being, in a sense, easily preventable or treatable in the early stages, these factors produce liver changes that usually go unnoticed for long periods of time. Hence, diagnosis

of liver disease often happens once fibrosis is present. To gain a general understanding of the inflammatory and fibrogenic processes, the next section reviews the changes they trigger in the morphology of the liver.

1.2.2 Inflammatory and fibrogenic processes

Inflammation of the liver is wound healing process that happens in three phases[160], enabling repair of acute damage to liver tissue. In the first phase, HSC engage leukocytes at the place of damage. There, the leukocytes engulf apoptotic cells and further release reactive oxygen species (ROS)[194]. Kupffer cells also generate ROS[65], and this initiation leads to the next phase, which is the activation of the HSC. In this stage, HSC proliferate and transdifferentiate into myofibroblast-cells[90,273], which reinforce the ECM through production of collagen I and III[64]. In the last state, the ECM is low-density and is adapted to act as a scaffolding for the other cells, helping them maintain their role[225].

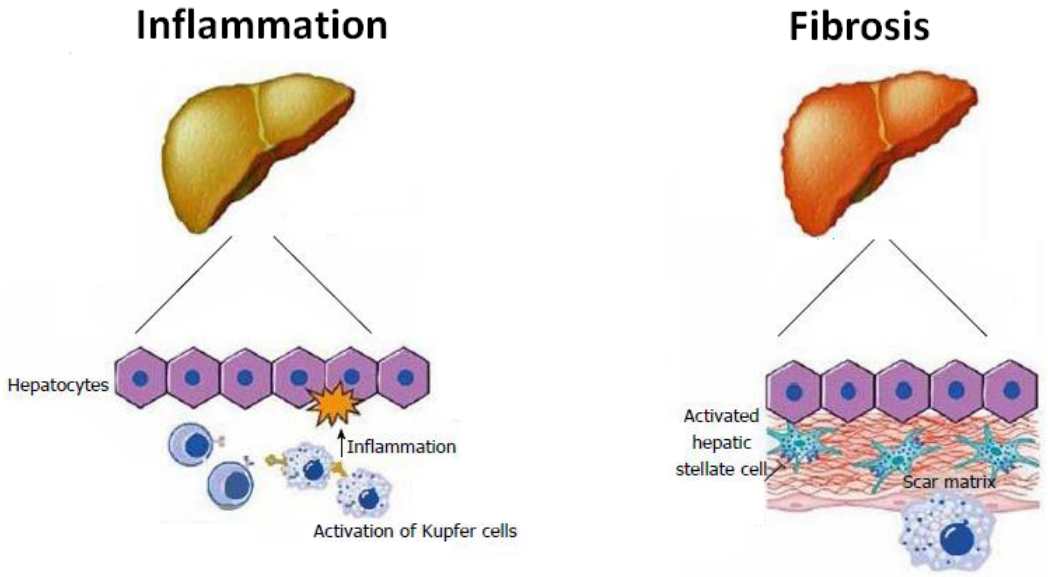

Figure 1.2.1 *Inflammation and fibrosis in the liver (figure modified from Saberi et al.[218])*

In acute injury, this inflammatory process is self-limiting through a negative feedback loop. Kupffer cells produce nitric oxide (NO), which inhibits the HSC[65]. Hence, when the injury disappears, production of HSC is regulated and the ECM degrades, reaching a normal density. However, if the injury becomes chronic, HSC apoptosis is impeded by matrix elements[118] and fibroblasts keep producing collagen, leading to high-density matrix deposition, seen in Fig. 1.2.1, and restriction of NO production. Thus, under chronic conditions, inflammation leads to scarring or incipient fibrosis[160]. Eventually, the deposited ECM can increase even by a factor of 10, changing from low-density to high-density and being deposited in the interstitial space[224]. This impedes the normal

functioning of hepatocytes, HSC and other liver cells.

Inflammation is an active process, defined by increased cellular signalling and cell accumulation at the place of injury. Fibrosis instead is defined by collagen build-up. While inflammation is the precursor of fibrosis, they are not mutually exclusive. Fibrogenic signals are present from the first signs of injury through the secretion of ROS, which increase HSC proliferation. In normal conditions this would be self-regulating, but in chronic inflammation the increased fibrogenic production of HSC cells becomes uncontrollable[224]. However, only a long lasting stimulus can lead to chronic inflammation and further on to scarring and damaged tissue function[59]. Hence, inflammation can evolve into fibrosis, meaning that the two processes are often co-existing. From inflammation and incipient fibrosis to advanced liver fibrosis, there are intermediate stages of increasing severity. An accurate identification of these stages has clinical relevance in the evaluation of patients and administration of suitable treatments.

1.2.3 Liver fibrosis staging and inflammation grading

Currently, liver fibrosis staging is done by histopathological examination of a hepatic sample. Two established scoring systems are in use: METAVIR[11] and Ishak[117]. METAVIR has five categories, while Ishak has seven. Although having more categories means that fine changes in fibrosis can be quantified, it also exhibits less inter-observer reproducibility. Here, let us present the five stages of fibrosis according to the METAVIR score, illustrated in Fig. 1.2.2. Thus, F0 signifies no fibrosis. The F1 stage shows fibrosis around the portal areas, while the F2 stage shows extended fibrosis around the portal areas. F3 shows a further expansion of the fibrosis, which starts forming bridges between portal areas. Lastly, F4 shows thick fibrosis bridges, with the rest of the tissue appearing nodular[151]. This is defined as cirrhosis.

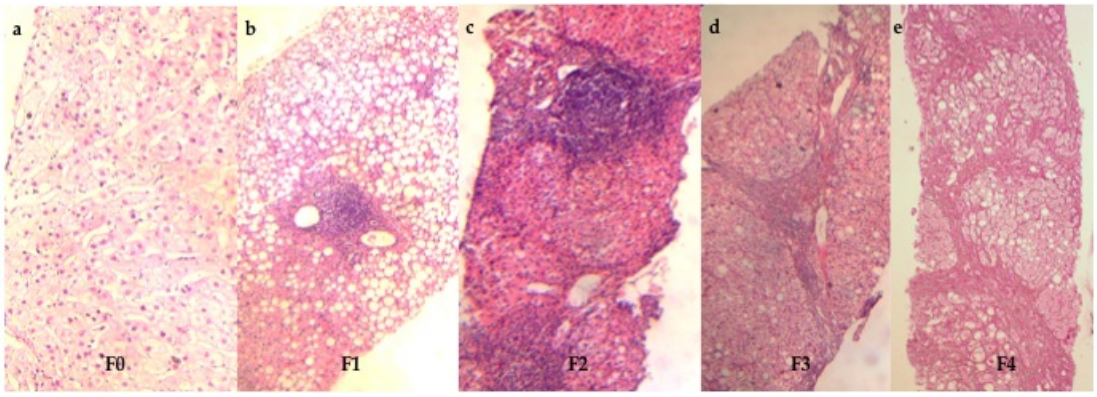

Figure 1.2.2 *Stages of liver fibrosis (figure reproduced from Macarini et al.[151]); (a) F0 - no fibrosis; (b) F1 - incipient portal fibrosis; (c) F2 - extended portal fibrosis; (d) F3 - bridging portal fibrosis; (e) F4 - thick bridging portal fibrosis (cirrhosis)*

The inflammatory activity can also be graded using multiple systems[82]. For consistency,

here we present the METAVIR categories: A0 is the absence of histological activity, A1 marks a mild activity, A2 defines a moderate activity, and finally A3 defines severe inflammatory activity[11]. The METAVIR categorisation system showed good intra- and inter-observer agreement, particularly in fibrosis staging[12]. In chapter 7 of this thesis, the fibrosis and inflammation scores of the patient data is staged using the METAVIR system.

1.3 Liver disease assessment methods

1.3.1 Liver biopsy

The gold standard in assessing the type and degree of liver disease, including inflammation and fibrosis, is biopsy[32]. This procedure involves the excision of a small sample that is analysed as described in section 1.2.3, offering structural and functional information about the tissue. Biopsy is particularly useful in clarifying an uncertain diagnosis due to either co-existing conditions or atypical symptoms. For example, the underlying cause in an obese patient with metabolic abnormalities might be either autoimmune hepatitis or NAFLD. A histopathological classification would help not only to diagnose the cause, but also to assess disease prognosis and further on to plan treatment schemes[210].

The invasiveness of liver biopsy poses risks, although modern standard procedures helped in reducing the occurrence of most adversities. Usually, discomfort due to moderate pain can be expected. The most serious complication is postoperative haemorrhaging. In severe cases, this can be life threatening. Other risks associated are related to infections and puncturing of other organs[210]. These occurrences can successfully be managed if they are swiftly identified.

Liver biopsy poses some limitations. Most importantly, the sampling offers only a local overview of the liver condition[65]. Due to the heterogeneity of fibrosis, this means that a sample may not accurately depict the state of the diseased liver. Additionally, it is observer dependent, which leads to inter-observer variability. Finally, due to the associated invasiveness and risks, repeatability of the procedure is not desirable, thus limiting reproducibility and longitudinal assessments of the disease. Research of other diagnostic methods is ongoing in a number of different directions, and some are reviewed below.

1.3.2 Serum markers

Serum markers are blood tests meant to identify matrix related changes (direct markers) or biochemical changes due to abnormal hepatic function (indirect markers). Their most important advantages are cost effectiveness and convenience of the procedure. However, their main disadvantage is lack of organ specificity, as markers might indicate

inflammatory signals related to other organs.

Among the direct markers, some are associated to matrix deposition, and are investigated for high presence. For example, collagen I, III, IV related serums were investigated and linked, independently, to disease cause. Some correlated with fibrosis severity as well[91]. In the group of non-collagenous related serums, hyaluronic acid has a high predictive value in excluding the presence of significant fibrosis or cirrhosis. However, it only has a moderate correlation with fibrosis stages[169]. Serums related to matrix degradation are investigated for low levels, in order to identify when ECM regulation is impeded. However, abnormalities in serums levels were mostly identified in late fibrosis stages[91].

Indirect markers are also subject of research. They appear to have survival prognosis value and to identify severe fibrosis/cirrhosis[76]. Nonetheless, they lack specificity and sensitivity for identifying intermediate fibrosis stages[91]. One successful combination of indirect markers was achieved in the FibroTest[201], yet mostly for distinguishing incipient fibrosis (F0-F1) and significant fibrosis (F2-F4)[91].

Overall, serum markers have shown promising results in very particular scenarios, e.g. correlating with degree of fibrosis in patients with underlying HCV, or differentiating between mild and absent fibrosis in patients with alcohol related disease. Thus, it is believed that a combination of several markers might be used as puzzle pieces to complete the picture of diagnosing and staging fibrosis, but this has not yet proved successful[91]. To date, serum markers need comprehensive research to improve their reliability and suitability in staging liver fibrosis.

1.3.3 Imaging modalities

A number of medical imaging modalities have been utilised in assessing liver inflammation and fibrosis, by investigating structural or functional abnormalities. A distinctive category is molecular imaging, often employed with Single Photon Emission Computed Tomography (SPECT) or Positron Emission Tomography (PET). These modalities rely on the injection of a radioactive tracer that is usually designed to target the ECM or HSC. Substantial research has been done in a pre-clinical setting, on rat models, where some tracers have shown correlation with stages of liver fibrosis[283]. However, clinical human studies are more limited. Some promising results have been obtained in differentiating early stages of fibrosis, by targeting the hepatic glucose metabolism[253]. Likewise, liver uptake of some radiotracers can lead to differentiation between cirrhotic and non-cirrhotic patients[92]. However, currently no good discrimination between all stages of fibrosis has been achieved[18,142].

Computed tomography (CT) is a frequently used diagnostic modality that relies on a multitude of X-ray beams in order to produce a 3D image. Due to its high spatial resolution, it provides detailed structural images. Hence, many liver fibrosis CT stud-

ies focus on morphological changes occurring during liver disease. Such a study was conducted retrospectively by Huber et al.[112], who compared the sum of the diameters of the three main liver veins (hepatic artery, vena cava and portal vein) to the ratio of widths of the right and caudate lobes. This method was capable of differentiating between healthy, fibrosis (F1-F3) and cirrhotic (F4) patients, but not between intermediate stages of fibrosis. Several studies have employed a measure of the liver surface nodularity, based on the smoothness of the liver edge[125,198]. This measure was found to be correlated with stages of liver fibrosis, but needs further research in order to improve the staging accuracy[234]. Similarly, liver segmental volume ratio was found to increase with fibrosis[197], but no clear stage discrimination was achieved. Recently, deep learning was employed with contrast enhanced CT liver images[37]. With a tested accuracy of ≈80% in differentiating fibrosis stages, the prospects in this direction look promising.

The main drawback of the modalities reviewed above (PET/SPECT/CT) is the use of radiation. The diagnosis benefits are considered to outweigh the radiation related risks, yet this limits the use of these scanning methods in longitudinal studies and treatment progression assessments.

Ultrasound (US) is a widely available modality, advantageous due to its portability and reduced costs (compared to other scanning methods). It produces 2D images by sending high frequency acoustic impulses through a probe and mapping the echo's return time. Multiple images can be obtained from different perspectives, by manoeuvring the probe on the surface of the body. In liver disease, US can be employed to investigate solid structure features (e.g. nodularity, volume), or vasculature, by injecting microbubble contrast agent[237]. In both cases, abnormalities are identified once cirrhotic stage is reached. However, characterisation of early and mild fibrosis stages remains challenging[14,101]. The most promising US methods in detecting and staging liver fibrosis rely on stiffness elastography measurements, which will be discussed in the next section.

Among MRI methods, diffusion weighted imaging (DWI) was employed in order to measure the apparent diffusion coefficient (ADC) of water in fibrosis patients. It was found that the ADC correlated negatively with fibrosis stage[129,140], showing better predictive value towards the higher grades of fibrosis. However, other studies found no correlation[21,98]. It is hypothesised that perfusion might alter the ADC measurements, as an animal study found that the ADC to fibrosis correlation disappeared after death, although diffusion effects should still be present post mortem[2]. Another assessment method is dynamic contrast enhanced MRI, which was also employed in liver fibrosis studies. Thus, hepatocyte uptake of a gadolinium based contrast was investigated in patients with fibrosis[186]. Findings suggest that there is a difference in the uptake between low and high fibrosis stages (F0-F2 and F3-F4), but more research needs to be done in this direction. Other MRI measures investigated were T1 and T2 liver maps[33,93], with mediocre results in staging fibrosis. Nevertheless, improved results were

obtained when considering multiparametric measures, like iron corrected T1 maps and T2* maps[9,192]. In all cases, discrimination of intermediate stages of fibrosis remains a challenge.

1.4 Elastography as an assessment method

Tissue health can sometimes be investigated by manual palpation. In accessible organs like breast or skin, this approach is used to detect abnormal structures through changes in elasticity[181,265]. For internal organs, elastography emerged as a modern medical imaging technique that can quantitatively estimate tissue mechanical properties. Since fibrosis is categorised according to severity, elastography aims to establish a relationship between measured stiffness values and degree of fibrosis. Moreover, as inflammation and fibrosis define different structural changes (cellular accumulation and ECM deposition), different tissue mechanical properties might be investigated in order to attempt differentiation of the two conditions (e.g. wave speed, attenuation, etc).

Generally, elastography imaging is employed with US or MRI, and it relies on quantifying the tissue strain response to travelling shear waves. In the case of US, the waves are transient, whereas MRE uses harmonic waves.

One possible application of transient elastography (TE) with US is Fibroscan, which produces one-dimensional (1D) stiffness measurements. Briefly, the US probe is sending a short mechanical impulse in the tissue, which converts into a low frequency propagating shear wave. The wave velocity is recorded by the high frequency US waves produced from the same probe, and transformed into stiffness[285]. The measurements cannot be anatomically mapped, and only give an overview along the propagation path of the shear wave, up to a depth of ≈ 5 cm.

Another US elasticity application is known as acoustic radiation force impulse (ARFI). In this method, a focused acoustic wave, acting like a longitudinal push, causes the tissue to displace radially around the focus point, creating shear waves. The US probe captures the shear wave displacement at several user defined locations on an US anatomical image. This leads to the reconstruction of the wave speed[183]. Studies have shown a positive correlation between ARFI wave speed measurements and fibrosis stages[79,141], with some groups achieving excellent prediction of the high fibrosis stages (F3-F4)[60], which remains to be further validated. Overall, ARFI is superior to 1D TE by allowing anatomical localisation, which permits reproducibility and further investigation of the same area of interest in the liver[247].

Shear wave elastography (SWE) is another emerging elastography method for US. This is related to ARFI, but it relies on exciting multiple focus points along a beam. Then, the displacements of the sequentially produced shear waves are captured. Thus, a

2D image can be obtained, where the shear wave propagation speed is defined. This method offers the largest region of interest in which tissue mechanical properties can be estimated. A study comparing US elastography methods shows that SWE outperforms 1D TE in categorising liver fibrosis patients[58]. Further studies investigating the relationship between SWE measurements and fibrosis stage also found a positive correlation[220], yet with a lower predictive value[58]. As SWE is a relatively new method, introduced after 1D TE and ARFI, further validation studies are needed.

The best TE method remains to be identified. Nevertheless, among US modalities, it is the imaging sub-field which shows the most discriminative results in characterising liver fibrosis.

MRE relies on the propagation of harmonic waves in the organ of interest. These waves are obtained via a vibrating transducer[216] which is placed, in the case of liver imaging, on the right lateral part of the abdomen, on the rib cage. The vibrations propagate inside the body, generating shear and compressional waves. *In vivo* frequencies are low ($30 - 80$ Hz), in order to optimise wave penetration and wavelength[214]. The frequency of the transducer is synchronised with the MRI's motion encoding gradients (MEG). Multiple phase offsets of the wave are encoded, which leads to determining the wave displacements[157]. During one vibration sequence, a single component of the displacements is encoded. Nevertheless, the vibrations can be restarted and the MEGs can be adjusted to acquire the remaining orthogonal components of the 3D displacements. Sometimes, a fourth vibration sequence is acquired without motion encoding, and is called the reference phase/scan. This is then subtracted from the three orthogonal acquisitions[216]. Hence, MRE allows for a 3D acquisition of the wave displacements in a volume of interest. The data is post processed into stiffness maps, using reconstruction algorithms[62].

MRE was shown to be a reliable method for evaluating liver fibrosis, with a good correlation between liver elasticity and non-incipient fibrosis stages. In a study of 140 patients, MRE and 1D TE were performed on the same set of patients[116]. It was shown that MRE had a higher accuracy in staging liver fibrosis. Other independent or review studies, investigating MRE results of several patient cohorts, found that MRE provides an excellent tool in predicting advanced fibrosis and cirrhosis[43,228]. Additionally, when gathered into groups encompassing several fibrosis stages (e.g. F0-F1 vs F2-F4), MRE also provided a good discrimination value[43,232]. However, differentiation of individual stages, particularly the incipient fibrosis stages ($\leq$F2), needs further clinical investigation.

Compared to other methods presented in section 1.3, liver elastography, in particular MRE, is considered to be the most reliable noninvasive method for assessing liver fibrosis[159]. Aside the promising results, the main advantages of elastography imaging are its non-invasiveness and use of non-ionising radiation. Nonetheless, elastography

measurements of fibrosis may be overestimated by co-existing diseases, e.g. inflammation[177,258]. There is ongoing research in this regard, trying to differentiate the mechanical properties influenced by inflammation and fibrosis (e.g. wave attenuation and speed[232]).

Between the two elastography imaging methods presented, US is quick to perform, cheaper, and more widely available than MRE. However, MRE is more suitable for obese patients, with the condition that they fit into the scanner, whose bore size is also limited by the additional transducer. As the underlying cause of fibrosis is often related to fatty liver disease in the western world, this is an important advantage of the method. Moreover, MRE examines 3D waves in a volume, which enables more comprehensive data acquisition and sampling. Currently, elastography measurements are not directly comparable between US and MRE, with US yielding larger stiffness values[116]. Furthermore, stiffness measurements were shown to increase with increasing frequency[148,157]. This points towards a frequency dependence of the liver behaviour in *in vivo* measurements, and subsequently towards the importance of characterising the liver constitutive behaviour.

1.5 Biomechanics of liver

Continuum mechanics provides the framework for modelling liver tissue behaviour, employing conservation laws of mass and momentum. In this setting, a key component is the relationship between body forces and strain, which needs to be determined empirically. Constitutive equations are used to model the experimental measurements. However, precise quantification is difficult to attain. This is partly due to simplifying the characteristics of liver tissue, which microscopically is complex and diverse, but macroscopically is regarded as a homogeneous solid. Nonetheless, such a simplification can still provide a qualitative description of the tissue behaviour, and is easier to employ in practical situations.

Liver constitutive equations are essential in a wide range of applications. For example, the transportation industry is concerned with the biomechanical behaviour of the liver, as it is the abdominal organ with the highest injury frequency in frontal and side impacts[279]. Hence, determining the liver's injury tolerance limit helps to design safer vehicles[122]. In the medical field, a 3D liver model can be used in computer simulations of surgeries (e.g. pressing, cutting, puncturing), whether for training purposes or outcome prediction[158]. Here, the underlying reason for investigating liver constitutive behaviour is to improve MRE liver characterisation.

MRE employs biomechanical models in order to reconstruct stiffness measurements. Often, linear viscoelastic models are used, which, at small deformations, provide a linear relation between stress and strain. In the context of small amplitude waves propagating through an undeformed tissue, this yields satisfactory results. However, it is difficult to

say which is the liver's rest state, and whether its linear elastic limit is exceeded when it is deformed by respiratory motion. Thus, for a better understanding of liver behaviour, it is useful to investigate information gained by classical mechanical tests (rheology). These are performed on *ex vivo* samples where deformation can be controlled, hence the reference and deformed configurations can be assessed, and the boundary forces can be measured. This enables the characterisation of stress tensors and consequently of constitutive models. The liver is often being regarded as a hyperelastic solid, although some experimental studies have probed its viscoelastic behaviour. A review of studies considering both hyperelastic and viscoelastic models is presented below.

1.5.1 Previous work in liver constitutive modelling

The ultimate goal in mechanical characterisation of liver tissue - and materials in general - is determining a constitutive law that can encompass the tissue's response to every type of deformation. This seems distant, however, mechanical testing methods continue to evolve, allowing for incremental improvements in characterisation of the liver.

An established method in conducting mechanical testing is rheology. This is widely used in material testing, and has been adopted for biological tissues as well. Liver testing often involves bovine or porcine excised livers obtained from the butcher. This is due to the practicality in obtaining liver specimens, but also due to the structural similarities between human and porcine livers[243]. Thus, *ex vivo* liver samples are prepared and tested in a controlled environment. Tan et al.[246] provides a brief review of some testing protocols, concluding that the test conditions affect the measured properties. Efforts are being made in improving the reproducibility of *in vivo* conditions, e.g. reducing the post-mortem testing time, hydrating the samples and immersing them in a saline solution[182], or devising a system that can maintain liver perfusion[120].

One of the first comprehensive works in tissue mechanical testing was performed by Fung[66] on rabbit mesentery. The study documented the nonlinear viscoelastic behaviour of the tissue, and focused on modelling its elastic part. An exponential form was employed in order to describe the stress-strain relationship, which represented a turning point in modelling soft tissue behaviour.

In the liver, Wang et al.[259] demonstrated the viscoelastic behaviour of the tissue, using indentation tests. The study investigated the relaxation behaviour under a constant strain, and illustrated the relaxation curves at various indentation depths. Moreover, the study also showed that cirrhotic and non-cirrhotic pig liver exhibit different biomechanical properties.

Despite the evidence on the viscoelasticty of the liver tissue, many subsequent studies focused on characterising the liver's nonlinear elastic behaviour. Hence, most studies have employed large uniaxial tests. These tests exhibit an initial quasilinear elasticity, after which a sudden increase in stiffness is manifested. Chui et al.[39] examined

the performance of several hyperelastic models in capturing the stress-strain response of porcine liver tissue samples in tension and compression. Polynomial models (e.g. Mooney-Rivlin[175,208], but also extended versions), exponential and logarithmic[245], as well as Ogden based models were compared. Moreover, models involving a combination of exponential and polynomial form[254] were also considered, and the authors even proposed a combined logarithmic-polynomial form. The models' performance was ranked according to the root mean squared error (RMSE) in capturing the data. The authors suggest that combined logarithmic-polynomial outperform logarithmic, exponential and Ogden models, while the Mooney-Rivlin model was inadequate to model the entire data range. However, some data analysis aspects are missing from the study. Exemplified model curves against the data are not provided, and it is unclear whether some models might have been over-defined by a large number of parameters. Despite these drawbacks, this study provided a good case study incorporating multitude of hyperelastic models proposed in literature for tissue modelling.

Gao et al.[70] also performed experiments on porcine liver tissue samples in uniaxial tension and compression. The conditions of the tension were varied, by considering tissue samples that were either glued or clamped to the testing device. This difference was shown to lead to a distinct stress-strain behaviour, as the clamped samples required a higher stretch in order to exhibit nonlinear behaviour. The study proposed combined Ogden-exponential and Ogden-logarithmic models, which were shown to qualitatively capture the tested liver behaviour in compression and tension.

In order to better replicate *in vivo* conditions, Jordan et al.[120] ensured the perfusion of the liver through a system providing arterial and venous pressure flow. Thus, whole porcine livers were tested in cyclic indentation. The liver exhibited nonlinear viscoelastic, strain-rate dependent behaviour. Models based on viscoelastic rheological configurations of various complexities were considered. It was shown that the standard linear solid model (a spring connected in series with a parallel spring-dashpot configuration) cannot capture the liver behaviour in large indentation. However, by changing the elastic spring characterisation from linear to exponential, the configuration was able to describe the data acquired. Added nonlinearity in the dashpot component further improved the results, albeit complicating the model. Thus, nonlinear viscoelastic liver behaviour was once again probed.

The perfused liver device was also used by Kerdok et al.[123] in comparing tissue properties between *in vivo* (anaesthetised pigs), *ex vivo* perfused, *ex vivo* post perfusion and *ex vivo* excised samples. Thus, *in vivo* and *ex vivo* excised samples showed a consistent behaviour in creep analysis employing a constant load of 20 g. Nonetheless, compliance and damping measurements indicated that the *ex vivo* excised tissue appears stiffer and more viscous than *in vivo*. Histological analysis revealed that the *ex vivo* excised samples showed cellular swelling, which might be related to the difference observed in the biomechanical properties. By contrast, the perfused tissue was similar to the *in*

vivo tissue in regards to creep, compliance and damping behaviour, despite showing cellular contraction in the histological analysis. Thus, perfusion is thought to play an important role in defining the biomechanical properties of liver, indicating that classical *ex vivo* mechanical tests might lead to different measured properties than the actual *in vivo* organ properties. Nonetheless, in constitutive modelling, this might lead to differences in the model parameters, but not in the form employed by the model. In this study, the authors used a five parameter viscoelastic model in order to capture the liver characteristics in all testing conditions, and were able to do so by varying the model parameters.

The above mentioned studies investigated the liver tissue by employing uniaxial deformations, in a direction normal to the tissue surface. However, shear properties of the liver were also examined using rheometry. Thus, Liu et al[146] used small cylindrical liver samples of bovine provenance in a rotational oscillatory rheometer. The shear tests revealed that the relaxation modulus depends on the strain level, thus indicating a nonlinear viscoelastic behaviour. Additionally, the shear stress showed differences between strain rates, thus pointing towards a frequency dependence of the liver tissue response. The model proposed by the authors involves a five component generalised Maxwell configuration. This is rather complex, as it necessitates 10 parameters.

Tan et al.[246] tested the effect of combined loading. Thus, bovine liver samples were subjected to deformations comprising simultaneous large compression and shear strain. It was shown that the preload level influences the measured shear properties. The shear storage modulus was demonstrated to increase with compressional preload, while the linear viscoelastic limit decreased. The data in this study will later on be modelled in chapter 5.

Combined compressional and shear loading was also employed by Perepelyuk et al.[195] on rat livers. Additionally, the livers presented various degrees of fibrosis, from healthy to early cirrhosis. Similarly to the study performed by Tan et al.[246], the compressional preload led to an increased measured shear storage modulus. Moreover, the differences between healthy, incipient fibrosis and early cirrhosis became more apparent with an increased preload. This is consistent with findings from other studies that showed that human liver tumours exhibit increased strain hardening compared to healthy liver (i.e. exhibit more nonlinearity)[277], and that differences between healthy, inflamed and fibrotic rat bowels increase with increasing strain[272]. This has promising implications for *in vivo* stiffness measurements, as loading (e.g. from respiration or externally applied) could be used to better distinguish between fibrosis stages. Conversely, healthy tissue compressed to a 10% level appears almost as stiff as cirrhotic uncompressed tissue. Thus, loading conditions must be carefully assessed in order to accurately stage liver disease. Another aspect highlighted by the study is a softening effect observed in shear strain deformation. The authors suggested that this might be due to cell-ECM bonds that can break and re-form, but a lack of preconditioning could also have a

similar effect. The study determined that the liver is viscoelastic, but that the viscous effects are less dominant than the elastic ones. Thus, the data was modelled using a two component power law elastic model, encompassing the deviatoric and volumetric changes. However this needs further validation, as the parametrisation process is unclear.

With the liver being highly vascularised and perfusion carrying an important role, Kerdok et al.[124] have considered a poro-viscoelastic model in order to model the liver behaviour. In this case, parameters related to both solid phase and flow are required. This is highly complex, with many parameters being estimated from literature reported values, rather than experimentally identified. An MRE study on the brain[168] concluded that poro-viscoelastic models add value when using low frequency MRE (1 Hz). However, at 50 Hz, viscoelastic models were more suitable. Although these results were obtained in brain, similar findings could apply to liver tissue. Thus, poro-viscoelastic models would be more suitable in investigating low frequency scenarios, maybe high impact cases, whereas for typical liver MRE, which is usually performed at 40-80 Hz, viscoelastic models would suffice.

Overall, the liver has been shown to be a nonlinear viscoelastic strain-rate dependent tissue. A range of constitutive models have been investigated in order to describe its behaviour or parts of it. Hyperelastic models are widely utilised, usually employing polynomial, exponential, logarithmic and Ogden forms, or combinations. Viscoelastic modelling is more limited, with models requiring a large number of parameters. Moreover, the associated history dependence leads to a computational burden. Finally, poro-viscoelasticity has also been considered, but the added benefits might not be enough to account for the added complexity. Thus, one of the aims of this thesis is to identify a nonlinear viscoelastic law that can capture the rheological liver behaviour and is convenient to use with MRE.

1.6 Thesis outline

MRE assessment of liver disease relies on biomechanical models for reconstructing stiffness measurements. Linear viscoelasticity is often assumed, but the linear limit may be insufficient in the context of liver undergoing respiratory deformation. Thus, MRE measurements may be blurred by deformation effects. In order to address this challenge, it is essential to model the nonlinear viscoelastic behaviour of the liver and integrate it with MRE. Therefore, the objective of this thesis is to investigate the *in vivo* mechanical properties of the liver at different respiratory states, using MRE. In order to build up towards understanding the complex nature of the liver, part of the work is carried out on hydrogel (polymer) phantoms. Afterwards, the focus shifts towards *ex vivo* bovine liver sample, and concludes with *in vivo* liver assessment.

Chapter 2: The aim of this chapter is to briefly introduce the continuum mechanics

theory. This is needed in order to be able to characterise the MRE wave propagation in a body, which may be at rest or under deformation (e.g. liver under respiratory motion). Thus, finite and infinitesimal deformations are presented, along with mathematical formulations of constitutive liver models employed in the literature. Although liver hyperelasticity is predominant in the literature, viscoelasticity is also discussed, as the aim is to integrate a viscoelastic liver model into MRE.

Chapter 3: Here, the objective is to introduce fractional viscoelasticity as a way of modelling tissue behaviour, which employs a simpler form compared to other viscoelastic literature models. This is done using the Caputo formulation of fractional derivatives. A recursive computational method is introduced in order to efficiently approximate the Caputo derivatives, hence reducing the computational burden associated with viscoelasticity in biomechanical modelling.

Chapter 4: As the liver is moving and deforming under respiratory motion, or can be externally loaded, it is important to understand the impact that such deformations could have on MRE wave propagation. Thus, in this chapter, the bias introduced by large deformations is probed in PVA phantoms. A pipeline is set up, which employs knowledge on the deformation and material behaviour in order to undo the loading bias on the MRE measurements. The material behaviour information is gained from rheological experiments, while the deformation is known due to the controlled nature of the MRE experiment.

Chapter 5: The material behaviour plays a central role in the pipeline established in chapter 4. In order to be able to implement this framework in liver tissue, it is thus essential to identify a viscoelastic constitutive liver model. Therefore, this chapter addresses the mechanical characterisation of liver tissue using rheology. Bovine liver samples are tested under simultaneous compression and shear (data from Tan et al.[246], courtesy of Prof. Lynne Bilston), and their behaviour is represented using fractional viscoelastic formulations of polynomial, exponential and Ogden models.

Chapter 6: With a material model attained in chapter 5, this chapter provides the remaining complementary elements that build the framework presented in chapter 4. Thus, MRE is performed on *ex vivo* liver samples under load (experiments performed by Dr. Lauriane Jugé, data courtesy of Prof. Lynne Bilston). While the viscoelastic model derived in the previous chapter is able to predict the MRE measurements in undeformed samples, the complex nature of the loading poses additional complications, which are exemplified in simulated data.

Chapter 7: The focus of this chapter is on *in vivo* MRE liver measurements of healthy volunteers and patients. Data was acquired in both expiration and inspiration, aiming to compare the differences arising between the two states. Although the patient cohort size is small, a positive trend between fibrosis and stiffness measurements can be observed. The influence of co-existing inflammation and deformation on the MRE

measurements is discussed.

Chapter 8: The work in this thesis is reviewed in the last chapter. The focus is on the contribution it brings to MRE assessment of liver fibrosis, but also on the limitations encountered. However, as this is an interdisciplinary work - integrating nonlinear mechanics, MRE imaging and liver constitutive modelling - other potential applications beyond the path presented here are discussed.

2 Theory of continuum mechanics

Biomechanical properties of the liver change as a result of inflammation and fibrosis. Measuring these changes is important because it can benefit clinical medicine by enabling the development of more accurate diagnosis tools. In this thesis, mathematical modelling is used to describe and quantify mechanical properties of the liver and other tissue-mimicking materials.

The underlying assumption is that the liver and other mimicking materials are bodies defined in a continuum and governed by classical conservation laws. Large deformations (finite strains) are investigated, as the liver is deformed by respiratory motion *in vivo*, or an external load *ex vivo*. Additionally, small deformations (infinitesimal strains) are considered, as MRE relies on the propagation of small amplitude shear waves. Hence, these two types of deformation are examined in the context of perturbations being applied to a body under load. A comprehensive analysis of deformation in continuum mechanics can be found in[19,135,189,244].

This chapter provides a general overview of important kinematic quantities (section 2.1) and stresses (section 2.2) which are relevant in defining the deformation process. The transformation of a body under deformation obeys conservation laws (section 2.3), which ensure mass and motion equilibrium. Furthermore, a deformed body stores internal strain energy, which is modelled using constitutive relations (section 2.5). Often, soft tissues and mimicking materials are regarded as elastic or hyperelastic. However, in the context of high frequency MRE (50 - 150 Hz), we must extend our discussion to viscoelastic solids (section 2.5.2). Lastly, the linear viscoelasticity assumption in MRE is examined in section 2.6.

2.1 Kinematics

In this section we are briefly reviewing the basic kinematics in large deformation mechanics. More complete dispositions can be found in[19,83,104,156,189,260]. Motion and deformation are at the core of the problems investigated in this thesis. For this, kinematics is used to express a body's evolution in space and time, as a response to strain metrics. Throughout this work, space dimensionality ($d = 3$) is generally considered. Thus, let the reference configuration $\Omega_0 \subset \mathbb{R}^d$ denote a body at rest, comprising points

whose initial coordinates are denoted $\boldsymbol{X} \in \Omega_0$. Under the action of spatio-temporal deformation, denoted by the displacement field $\boldsymbol{U} : \Omega_0 \times [0, T] \to \mathbb{R}^d$, the body transforms to its physical configuration Ω_t (Fig. 2.1.1). Reference points $\boldsymbol{X}$ deform to their physical counterparts $\boldsymbol{x} \in \Omega_t$ via a bijective map[19] $\boldsymbol{\phi} : \Omega_0 \times [0, T] \to \Omega$:

$$\boldsymbol{x} = \boldsymbol{\phi}(\boldsymbol{X}, t) = \boldsymbol{U}(\boldsymbol{X}, t) + \boldsymbol{X}, \quad \forall \boldsymbol{X} \in \Omega_0, \ \forall t \in [0, T]. \tag{2.1.1}$$

Hence, the physical domain is defined as

$$\Omega_t = \{\boldsymbol{x} \in \mathbb{R}^d | \boldsymbol{x} = \boldsymbol{\phi}(\boldsymbol{X}, t), \ \boldsymbol{X} \in \Omega_0\}. \tag{2.1.2}$$

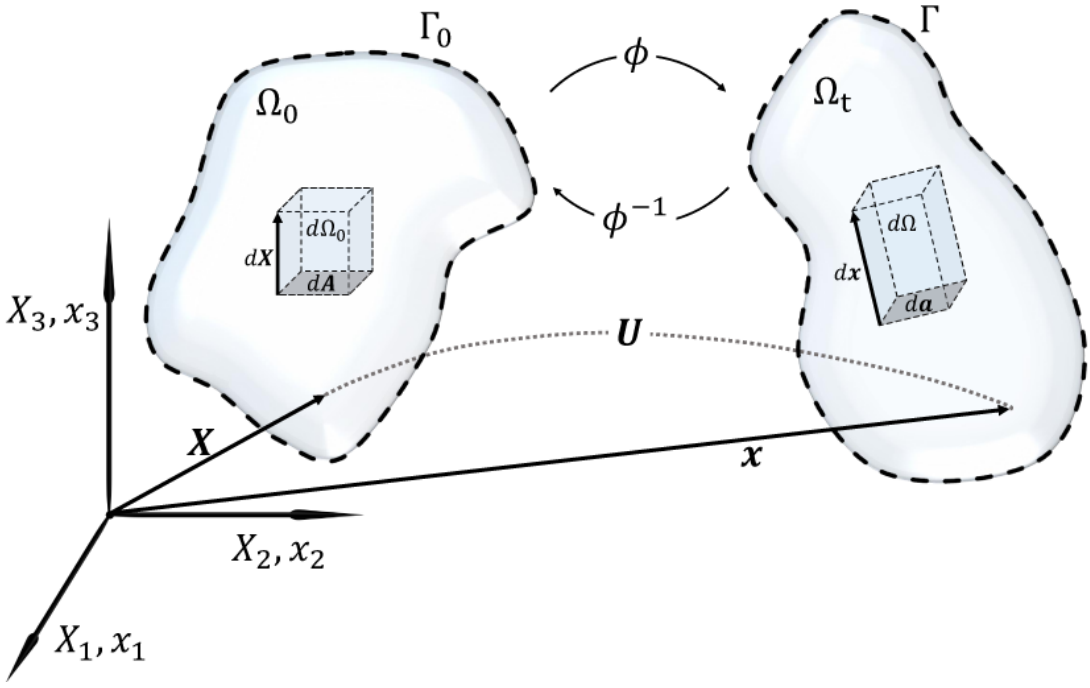

Figure 2.1.1 *Motion of a deformed body; the reference domain Ω_0, bounded by Γ_0, and physical domain Ω_t, bounded by Γ, are linked via the deformation map ϕ.*

Some generic quantities q characterising the body can be described with respect to either the reference or physical configurations[19]. The former is also known as the material (Lagrangian) description and is used to express the evolution of q attached to a fixed reference point $\boldsymbol{X}$, irrespective of its new physical location $\boldsymbol{x}$, as $q = q(\boldsymbol{X}, t)$. The latter is also known as the spatial (Eulerian) description and is used to express changes in q corresponding to a fixed spatial position $\boldsymbol{x}$, irrespective of which initial point $\boldsymbol{X}$ is located at this position, as $\hat{q} = \hat{q}(\boldsymbol{x}, t)$.

In this work, it is considered that at time $t = 0$, the body is in its undeformed configuration. For $t > 0$, the body is being subjected to motion and deformation.

2.1.1 Deformation gradient

The fundamental quantity in large deformation mechanics is the deformation gradient, $\boldsymbol{F}$. This is used to relate changes in infinitesimal distances between body points before and after deformation[19], and is defined as the gradient of map $\boldsymbol{\phi}$ with respect to the reference domain:

$$\boldsymbol{F} = \frac{\partial \boldsymbol{\phi}}{\partial \boldsymbol{X}} = \frac{\partial \boldsymbol{x}}{\partial \boldsymbol{X}} = \nabla_{\boldsymbol{X}} \boldsymbol{u} + \boldsymbol{I}, \tag{2.1.3}$$

with subscript $\boldsymbol{X}$ on the gradient operator, $\nabla_{\boldsymbol{X}}$, indicating the reference frame. Hence, considering an infinitesimal vector $d\boldsymbol{X}$ in the reference domain, this can be transformed into its physical domain counterpart as $d\boldsymbol{x} = \boldsymbol{F} d\boldsymbol{X}$, with $\boldsymbol{F}$ bridging the two domains. Likewise, $d\boldsymbol{X} = \boldsymbol{F}^{-1} d\boldsymbol{x}$, where the inverse deformation gradient

$$\boldsymbol{F}^{-1} = \frac{\partial \boldsymbol{\phi}^{-1}}{\partial \boldsymbol{x}} = \frac{\partial \boldsymbol{X}}{\partial \boldsymbol{x}} \tag{2.1.4}$$

exists due to $\boldsymbol{\phi}$ being bijective.

While the deformation gradient encodes changes in vector length and orientation, other tensors can be constructed to quantify changes in length. As a starting point, consider, for example, the squared magnitude (L_2 norm) of a vector $d\boldsymbol{x}$ in the physical frame, which can be cast in terms of the undeformed vector $d\boldsymbol{X}$ as

$$\|d\boldsymbol{x}\|_2^2 = d\boldsymbol{x}^T d\boldsymbol{x} = (\boldsymbol{F} d\boldsymbol{X})^T (\boldsymbol{F} d\boldsymbol{X}) = d\boldsymbol{X}^T \boldsymbol{F}^T \boldsymbol{F} d\boldsymbol{X} = d\boldsymbol{X}^T \boldsymbol{C} d\boldsymbol{X}, \tag{2.1.5}$$

where $\boldsymbol{C} = \boldsymbol{F}^T \boldsymbol{F}$ is known as the right Cauchy-Green deformation tensor. Conversely, starting by considering the squared magnitude of the reference vector $d\boldsymbol{X}$, then

$$\|d\boldsymbol{X}\|_2^2 = d\boldsymbol{X}^T d\boldsymbol{X} = (\boldsymbol{F}^{-1} d\boldsymbol{x})^T (\boldsymbol{F}^{-1} d\boldsymbol{x}) = d\boldsymbol{x}^T \boldsymbol{F}^{-T} \boldsymbol{F}^{-1} d\boldsymbol{x} = d\boldsymbol{x}^T \boldsymbol{B}^{-1} d\boldsymbol{x}, \tag{2.1.6}$$

where $\boldsymbol{B} = \boldsymbol{F}\boldsymbol{F}^T$ is the left Cauchy-Green strain tensor. Both $\boldsymbol{C}$ and $\boldsymbol{B}$ quantify changes in squared lengths between the reference and physical states.

The deformation gradient also relates infinitesimal volumes before and after deformation. The volumetric change between the reference ($d\Omega_0$) and physical ($d\Omega$) configurations[19] is

$$J \, d\Omega_0 = d\Omega, \tag{2.1.7}$$

where $J = \det \boldsymbol{F}$ is the determinant of the deformation gradient. Incompressible materials conserve their volume throughout deformation, thus being characterised by $J = 1$. For completeness, a reference area element dA is transformed into its physical counterpart da by

$$da \, \boldsymbol{n} = J \boldsymbol{F}^{-T} dA \, \boldsymbol{N}, \tag{2.1.8}$$

where $\boldsymbol{N}$ and $\boldsymbol{n}$ are the normal vectors to the surface in undeformed and deformed configurations. Equation (2.1.8) is also known as Nanson's formula[189].

2.1.2 Invariants

By construction, $\boldsymbol{C} = \boldsymbol{C}^T$ is a symmetric positive definite tensor[20], as long as $J > 0$. Likewise, $\boldsymbol{B}$ holds the same properties. This implies that the eigenvalues of $\boldsymbol{C}$ and $\boldsymbol{B}$ are positive. For generalisation purposes, let $\boldsymbol{A}$ be a second order symmetric positive definite tensor, with eigenvalues λ_i, $i = 1, ...d$, denoting the strains in the principal directions. These remain constant under coordinate rotation, and can be grouped to form three invariant quantities of $\boldsymbol{A}$:

$$I_{\boldsymbol{A}} = \sum_{i=1}^{d} \lambda_i = tr(\boldsymbol{A}) = \boldsymbol{A} : \boldsymbol{I}, \tag{2.1.9a}$$

$$II_{\boldsymbol{A}} = \sum_{i=1}^{d} \lambda_i^2 = tr(\boldsymbol{A}\boldsymbol{A}^T) = \boldsymbol{A} : \boldsymbol{A}, \tag{2.1.9b}$$

$$III_{\boldsymbol{A}} = \prod_{i=1}^{d} \lambda_i = \det(\boldsymbol{A}), \tag{2.1.9c}$$

where the double contraction ":" of two second order tensors $\boldsymbol{A}$ and $\boldsymbol{B}$ is defined as in[19], namely $\boldsymbol{A} : \boldsymbol{B} = \sum_{i,j=1}^{d} A_{ij}B_{ij}$. An alternative way of defining the second invariant is $II_{\boldsymbol{A}} = \frac{1}{2}I_{\boldsymbol{A}} - \boldsymbol{A} : \boldsymbol{A}$, but in this thesis the definition[19] given in Eq. (2.1.9b) will be used.

Generally, invariants are a convenient way to characterise the motion of an isotropic body, as they capture the overall body deformation. Furthermore, they satisfy the objectivity requirement by remaining constant under frame rotation.

2.1.3 Isochoric kinematic quantities and invariants

Deformation effects can be categorised into volumetric and deviatoric (change in shape). Being different in nature, it is often useful to separate the two components. Thus, here are presented isochoric alternatives (denoted by "$\hat{}$") of the kinematic quantities discussed in the previous sections:

$$\hat{\boldsymbol{F}} = III_{\boldsymbol{F}}^{-1/d}\boldsymbol{F} = J^{-1/d}\boldsymbol{F}, \tag{2.1.10a}$$

$$\hat{\boldsymbol{C}} = III_{\boldsymbol{C}}^{-1/d}\boldsymbol{C} = J^{-2/d}\boldsymbol{C}, \tag{2.1.10b}$$

$$\hat{\boldsymbol{B}} = III_{\boldsymbol{B}}^{-1/d}\boldsymbol{B} = J^{-2/d}\boldsymbol{B}, \tag{2.1.10c}$$

with $\det \hat{\boldsymbol{F}} = 1$, meaning that $\hat{\boldsymbol{F}}$, $\hat{\boldsymbol{C}}$ and $\hat{\boldsymbol{B}}$ are independent of changes in volume. Their invariants are

$$I_{\hat{\boldsymbol{F}}} = J^{-1/d}I_{\boldsymbol{F}}, \quad II_{\hat{\boldsymbol{F}}} = J^{-2/d}II_{\boldsymbol{F}}, \quad III_{\hat{\boldsymbol{F}}} = 1, \tag{2.1.11a}$$

$$I_{\hat{\boldsymbol{C}}} = J^{-2/d}I_{\boldsymbol{C}}, \quad II_{\hat{\boldsymbol{C}}} = J^{-4/d}II_{\boldsymbol{C}}, \quad III_{\hat{\boldsymbol{C}}} = 1, \tag{2.1.11b}$$

$$I_{\hat{\boldsymbol{B}}} = J^{-2/d}I_{\boldsymbol{B}}, \quad II_{\hat{\boldsymbol{B}}} = J^{-4/d}II_{\boldsymbol{B}}, \quad III_{\hat{\boldsymbol{B}}} = 1. \tag{2.1.11c}$$

It is notable that the invariants of $\boldsymbol{C}$ and $\boldsymbol{B}$, and their isochoric variants, respectively, are equal: $I_{\boldsymbol{C}} = I_{\boldsymbol{B}}$, $II_{\boldsymbol{C}} = II_{\boldsymbol{B}}$, $III_{\boldsymbol{C}} = III_{\boldsymbol{B}}$, $I_{\hat{\boldsymbol{C}}} = I_{\hat{\boldsymbol{B}}}$ and $II_{\hat{\boldsymbol{C}}} = II_{\hat{\boldsymbol{B}}}$.

2.2 Stress tensors

Section 2.1 discussed the mathematical concepts needed to characterise the motion and deformation problem, without relating them to the cause. This section introduces forces as source of deformation, further leading to mechanical stresses.

The most intuitive understanding of stress is force per unit area. As such, this gives the definition of the core stress tensor in solid mechanics, the Cauchy stress tensor $\boldsymbol{\sigma}$. This tensor determines the relationship between a surface normal vector $\boldsymbol{n}$ and traction $\boldsymbol{t}$ per unit area, as:

$$\boldsymbol{t} = \boldsymbol{\sigma} \cdot \boldsymbol{n}, \tag{2.2.1}$$

where $\boldsymbol{t}, \boldsymbol{\sigma}$ and $\boldsymbol{n}$ are defined in the physical configuration. However, stress can also be characterised in the reference domain, by involving the deformation gradient. Hence, let $\boldsymbol{P}$ be introduced as the first Piola-Kirchhoff (PK1) stress tensor

$$\boldsymbol{P} = J\boldsymbol{\sigma}\boldsymbol{F}^{-T}. \tag{2.2.2}$$

This definition can also be understood as relating reference areas to force vectors in the deformed domain. To fully characterise stress in the reference domain, then the second Piola-Kirchhoff (PK2) tensor can be introduced as

$$\boldsymbol{S} = J\boldsymbol{F}^{-1}\boldsymbol{\sigma}\boldsymbol{F}^{-T}. \tag{2.2.3}$$

Similar to $\boldsymbol{F}$, $\boldsymbol{P}$ connects the reference and physical domains. Contrarily, $\boldsymbol{\sigma}$ and $\boldsymbol{S}$ are defined exclusively in one of the domains and, due to conservation of angular momentum (section 2.3.3), are symmetric.

The Cauchy and Piola-Kirchhoff stress tensors are particularly useful for the characterisation of the constitutive properties of a body. Constitutive equations are usually determined empirically, by linking motion to stress. In order to avoid complications arising from deformed geometry, which may be difficult to determine, the use of the PK2 tensor $\boldsymbol{S}$ is preferred in this work, as it exists entirely in the reference configuration.

2.3 Conservation laws

The bodies discussed in this thesis are approximated in the continuum framework, thus their properties need to be characterised by continuous functions[156]. These ensure that an isolated mechanical system is always in balance. Here, continuous functions that are of interest and need to be satisfied are conservation of mass, linear momentum and

angular momentum.

2.3.1 Conservation of mass

In a closed system, mass cannot be created or destroyed through deformation. It may only be displaced, but its quantification over the body's initial volume Ω_0 or deformed volume Ω remains constant.

Consider $\Omega_0' \subseteq \Omega_0$ to be any arbitrary volume in the reference configuration, which has an equivalent in the physical configuration $\Omega' \subseteq \Omega$ given by the mapping $\boldsymbol{\phi}$. The corresponding mass M is given below on both configurations:

$$M(0) = \int_{\Omega_0'} \rho_0(\boldsymbol{X}, t)\, \mathrm{d}\Omega_0' \quad \text{on } \Omega_0, \qquad M(t) = \int_{\Omega'} \rho(\boldsymbol{x}, t)\, \mathrm{d}\Omega' \quad \text{on } \Omega, \tag{2.3.1}$$

where ρ_0 is the density associated to the undeformed body, and ρ is the density of the body after deformation. Due to conservation of mass, $M(t) - M(0) = 0$. Casting $M(t)$ into the reference domain by performing a change of variable (using Eqs. (2.1.1) and (2.1.7)), it follows that

$$M(t) - M(0) = \int_{\Omega_0'} \rho(\phi(\boldsymbol{X}, t), t) J\, \mathrm{d}\Omega_0' - \int_{\Omega_0'} \rho_0(\boldsymbol{X}, t)\, \mathrm{d}\Omega_0' = 0 \tag{2.3.2}$$

and subsequently

$$\rho J = \rho_0. \tag{2.3.3}$$

For the bodies considered here, the density is often assumed to remain constant through spatiotemporal deformation. Recalling that Ω_0' is any arbitrary volume, including infinitesimal volumes $\Omega_0' \to 0$, it must hold that

$$J - 1 = 0, \ \forall \boldsymbol{X} \in \Omega_0, \tag{2.3.4}$$

which is known as the incompressibility constraint.

2.3.2 Conservation of linear momentum

In classical mechanics, Newton's second law states that within an inertial reference frame, the sum of forces acting on the object is equal to its mass multiplied by its acceleration. As a generalisation in continuum mechanics, the sum of all forces acting on an arbitrary volume $\Omega' \subseteq \Omega(t)$ (Fig. 2.1.1) and boundary Γ' equals the rate of change of the total linear momentum:

$$\int_{\Gamma'} \boldsymbol{t}\, \mathrm{d}\Gamma' + \int_{\Omega'} \boldsymbol{f}\, \mathrm{d}\Omega' = \frac{\mathrm{d}}{\mathrm{d}t} \int_{\Omega'} \rho \boldsymbol{v}\, \mathrm{d}\Omega', \tag{2.3.5}$$

where $\boldsymbol{t}$ are the traction forces per unit area on the boundary, $\boldsymbol{f}$ are the body forces per unit volume and $\boldsymbol{v}$ is the velocity vector of the body. Recalling Eq. (2.2.1) and using

Gauss's theorem, which relates changes through a closed surface to changes through the volume enclosed by the surface, it follows that

$$\int_{\Gamma'} \boldsymbol{t}\, \mathrm{d}\Gamma' = \int_{\Gamma'} \boldsymbol{\sigma} \cdot \boldsymbol{n}\, \mathrm{d}\Gamma' = \int_{\Omega'} \nabla_{\boldsymbol{x}} \cdot \boldsymbol{\sigma}\, \mathrm{d}\Omega'. \tag{2.3.6}$$

Additionally, the momentum effects can be transformed, using Eq. (2.1.7), as

$$\begin{aligned} \frac{\mathrm{d}}{\mathrm{d}t} \int_{\Omega'} \rho \boldsymbol{v}\, \mathrm{d}\Omega' &= \int_{\Omega'_0} \frac{\mathrm{d}}{\mathrm{d}t} \left(\rho \boldsymbol{v} J\right)\, \mathrm{d}\Omega'_0 \\ &= \int_{\Omega'_0} \frac{1}{J} \frac{\mathrm{d}}{\mathrm{d}t} \left(\rho \boldsymbol{v} J\right) J\, \mathrm{d}\Omega'_0 \\ &= \int_{\Omega'} \frac{1}{J} \frac{\mathrm{d}}{\mathrm{d}t} \left(\rho \boldsymbol{v} J\right)\, \mathrm{d}\Omega'. \end{aligned} \tag{2.3.7}$$

Thus, it follows that the sum of forces equals the change in momentum, which is also known as Cauchy's first law of motion:

$$\nabla_{\boldsymbol{x}} \cdot \boldsymbol{\sigma} + \boldsymbol{f} = \frac{1}{J} \frac{\mathrm{d}}{\mathrm{d}t} (\rho \boldsymbol{v} J), \quad \forall \boldsymbol{x} \in \Omega. \tag{2.3.8}$$

When incompressibility is assumed, it follows that

$$\nabla_{\boldsymbol{x}} \cdot \boldsymbol{\sigma} + \boldsymbol{f} = \rho \frac{\mathrm{d}\boldsymbol{v}}{\mathrm{d}t}, \quad \forall \boldsymbol{x} \in \Omega. \tag{2.3.9}$$

Note that Eq. (2.3.8) holds in the physical configuration Ω, with $\nabla_{\boldsymbol{x}}$ denoting spatial differentiation with respect to the physical frame. To write Cauchy's first law of motion in the reference frame, a similar derivation can be employed. Thus, let us employ Eqs. (2.1.7) and (2.2.1) to transform Eq. (2.3.5) into the reference domain Ω_0:

$$\int_{\Gamma'_0} \boldsymbol{\sigma} \cdot J \boldsymbol{F}^{-1} \boldsymbol{N}\, \mathrm{d}\Gamma'_0 + \int_{\Omega'_0} J \boldsymbol{f}\, \mathrm{d}\Omega'_0 = \frac{\mathrm{d}}{\mathrm{d}t} \int_{\Omega'_0} \rho \boldsymbol{v} J\, \mathrm{d}\Omega'_0. \tag{2.3.10}$$

Let us rewrite the Cauchy tensor in terms of the PK2 tensor as

$$\boldsymbol{\sigma} = \frac{1}{J} \boldsymbol{F} \boldsymbol{S} \boldsymbol{F}^T, \tag{2.3.11}$$

leading to

$$\int_{\Gamma'_0} \boldsymbol{F} \boldsymbol{S} \cdot \boldsymbol{N}\, \mathrm{d}\Gamma'_0 + \int_{\Omega'_0} J \boldsymbol{f}\, \mathrm{d}\Omega'_0 = \int_{\Omega'_0} \frac{\mathrm{d}}{\mathrm{d}t} (\rho \boldsymbol{v} J)\, \mathrm{d}\Omega'_0. \tag{2.3.12}$$

As the above equation holds point-wise, then Cauchy's first equation of motion in the reference domain becomes

$$\nabla_{\boldsymbol{X}} \cdot (\boldsymbol{F} \boldsymbol{S}) + J \boldsymbol{f} = \frac{\mathrm{d}}{\mathrm{d}t} (\rho \boldsymbol{v} J), \quad \forall \boldsymbol{X} \in \Omega_0, \tag{2.3.13}$$

with incompressibility leading to

$$\nabla_{\boldsymbol{X}} \cdot (\boldsymbol{F}\boldsymbol{S}) + J\boldsymbol{f} = \rho J \frac{\mathrm{d}\boldsymbol{v}}{\mathrm{d}t}, \quad \forall \boldsymbol{X} \in \Omega_0. \tag{2.3.14}$$

2.3.3 Conservation of angular momentum

The rotational equilibrium is the correspondent of linear balance in a rotational setting. For an arbitrary volume, this is achieved if the angular momentum of the body and traction forces within the volume are zero[19], where the angular momentum is given by the cross product of the force with the position vector $\boldsymbol{x}$:

$$\int_{\Gamma'} \boldsymbol{x} \times \boldsymbol{t} \, \mathrm{d}\Gamma' + \int_{\Omega'} \boldsymbol{x} \times \boldsymbol{f} \, \mathrm{d}\Omega' = \frac{\mathrm{d}}{\mathrm{d}t} \int_{\Omega'} (\boldsymbol{x} \times \rho \boldsymbol{v}) \, \mathrm{d}\Omega'. \tag{2.3.15}$$

Recalling Eq. (2.2.1), then

$$\int_{\Gamma'} \boldsymbol{x} \times (\boldsymbol{\sigma} \cdot \boldsymbol{n}) \, \mathrm{d}\Gamma' + \int_{\Omega'} \boldsymbol{x} \times \boldsymbol{f} \, \mathrm{d}\Omega' = \frac{\mathrm{d}}{\mathrm{d}t} \int_{\Omega'} (\boldsymbol{x} \times \rho \boldsymbol{v}) \, \mathrm{d}\Omega'. \tag{2.3.16}$$

After applying Gauss' theorem and carrying the algebraic calculations[19], it follows that

$$\int_{\Omega'} \boldsymbol{x} \times (\nabla_{\boldsymbol{x}} \cdot \boldsymbol{\sigma}) \, \mathrm{d}\Omega' + \int_{\Omega'} \boldsymbol{\mathcal{E}} : \boldsymbol{\sigma}^T \, \mathrm{d}\Omega' + \int_{\Omega'} \boldsymbol{x} \times \boldsymbol{f} \, \mathrm{d}\Omega' = \frac{\mathrm{d}}{\mathrm{d}t} \int_{\Omega'} (\boldsymbol{x} \times \rho \boldsymbol{v}) \, \mathrm{d}\Omega'. \tag{2.3.17}$$

In a 3-dimensional setting, $\boldsymbol{\mathcal{E}}$ is the third order alternating tensor, with

$$\mathcal{E}_{ijk} = \begin{cases} 1 & \text{if permutation } \{i,j,k\} \text{ is even} \\ -1 & \text{if permutation } \{i,j,k\} \text{ is odd} \\ 0 & \text{if permutation } \{i,j,k\} \text{ has repeated indices.} \end{cases} \tag{2.3.18}$$

Rewriting Eq. (2.3.17) in the static case as

$$\int_{\Omega'} \boldsymbol{x} \times (\nabla_{\boldsymbol{x}} \cdot \boldsymbol{\sigma} + \boldsymbol{f}) \, \mathrm{d}\Omega' + \int_{\Omega'} \boldsymbol{\mathcal{E}} : \boldsymbol{\sigma}^T \, \mathrm{d}\Omega' = \boldsymbol{0} \tag{2.3.19}$$

and using the linear momentum conservation Eq. (2.3.8) assuming static equilibrium, it follows that

$$\int_{\Omega'} \boldsymbol{\mathcal{E}} : \boldsymbol{\sigma}^T \, \mathrm{d}\Omega' = \boldsymbol{0}. \tag{2.3.20}$$

Over an arbitrary volume $\Omega' \to 0$, this equation holds point-wise, thus

$$\boldsymbol{\mathcal{E}} : \boldsymbol{\sigma}^T = \boldsymbol{0}. \tag{2.3.21}$$

Investigating the components of the above contraction

$$\boldsymbol{\mathcal{E}} : \boldsymbol{\sigma}^T = \begin{pmatrix} \sigma_{32} - \sigma_{23} \\ \sigma_{13} - \sigma_{31} \\ \sigma_{21} - \sigma_{12} \end{pmatrix} \tag{2.3.22}$$

leads to concluding the symmetry of the Cauchy stress tensor:

$$\boldsymbol{\sigma} = \boldsymbol{\sigma}^T. \tag{2.3.23}$$

This is the rotational equivalent of Cauchy's first law of motion. Note that the symmetry of $\boldsymbol{\sigma}$ entails the symmetry of $\boldsymbol{S}$, but not the symmetry of $\boldsymbol{P}$.

2.4 Perturbed balance equations

Having the equations governing the finite deformation of a body, it is timely to introduce infinitesimal strains as additive deformation. These are examined for the purpose of understanding MRE wave propagation in media under large deformation.

Before starting the perturbation analysis, let us first recall that two domains can be considered: the reference (subscript $\boldsymbol{X}$) and physical (subscript $\boldsymbol{x}$) frames. For later use, here we list the identities that can be used to transform scalars and tensors between the two domains:

$$J\nabla_{\boldsymbol{x}} w = \nabla_{\boldsymbol{X}} \cdot [wJ\boldsymbol{F}^{-T}], \tag{2.4.1}$$

which transforms the gradient of a scalar[96] w,

$$J\nabla_{\boldsymbol{x}} \cdot \boldsymbol{A} = \nabla_{\boldsymbol{X}} \cdot [J\boldsymbol{A}\boldsymbol{F}^{-T}], \tag{2.4.2}$$

which transforms the divergence[96] of a second order tensor $\boldsymbol{A}$, and

$$\nabla_{\boldsymbol{x}} \boldsymbol{y} = (\nabla_{\boldsymbol{X}} \boldsymbol{y})\boldsymbol{F}^{-1}, \tag{2.4.3}$$

which transforms the gradient[189] of a vector $\boldsymbol{y}$.

To proceed with perturbation analysis, start now by considering an incompressible body under equilibrium, characterised by the conservation of mass and linear momentum Eqs. (2.3.4) and (2.3.13) in the reference frame Ω_0 assuming zero body forces:

$$\rho\partial_t(J\boldsymbol{v}) - \nabla_{\boldsymbol{X}} \cdot (\boldsymbol{F}\boldsymbol{S}) = \boldsymbol{0} \quad \text{on } \Omega_0, \tag{2.4.4a}$$

$$J - 1 = 0 \quad \text{on } \Omega_0, \tag{2.4.4b}$$

where J refers to $J(\boldsymbol{U})$ and $\boldsymbol{S}(\boldsymbol{F}, P)$ depends on deformation and hydrostatic pressure

P (detailed later in section 2.5). Additionally, high frequency low amplitude waves characterised by the state variables $\boldsymbol{u}^\varepsilon : \Omega_0 \times I \to \mathbb{R}^d$ and $p^\varepsilon : \Omega_0 \times I \to \mathbb{R}$ are imposed on the body during the time interval $I \subseteq [0, T]$. Here it is assumed that the introduced perturbations do not interfere in the course of the large deformation, enabling to describe the entire deformation process by using

$$\boldsymbol{U}^\varepsilon(\boldsymbol{X}, t) = \begin{cases} \boldsymbol{U}(\boldsymbol{X}, t) & t \in [0, T] \setminus I \\ \boldsymbol{U}(\boldsymbol{X}, t) + \boldsymbol{u}^\varepsilon(\boldsymbol{X}, t) & t \in I \end{cases} \tag{2.4.5a}$$

$$P^\varepsilon(\boldsymbol{X}, t) = \begin{cases} P(\boldsymbol{X}, t) & t \in [0, T] \setminus I \\ P(\boldsymbol{X}, t) + p^\varepsilon(\boldsymbol{X}, t) & t \in I \end{cases} \tag{2.4.5b}$$

where $\boldsymbol{U}$ and P satisfy Eq. (2.4.4). Let us define the velocity vectors

$$\boldsymbol{v} = \partial_t \boldsymbol{U}, \quad \boldsymbol{v}^\varepsilon = \partial_t \boldsymbol{U}^\varepsilon. \tag{2.4.6}$$

The quantities $\boldsymbol{v}^\varepsilon$ and P^ε are subject to a new, perturbed version of the same set of equations:

$$\rho \partial_t (J^\varepsilon \boldsymbol{v}^\varepsilon) - \nabla_{\boldsymbol{X}} \cdot (\boldsymbol{F}^\varepsilon \boldsymbol{S}^\varepsilon) = \boldsymbol{0} \quad \text{on } \Omega_0, \tag{2.4.7a}$$

$$J^\varepsilon - 1 = 0 \quad \text{on } \Omega_0. \tag{2.4.7b}$$

Superscript $^\varepsilon$ indicates dependency on the perturbed state, with the perturbed deformation gradient and its determinant being

$$\boldsymbol{F}^\varepsilon = \nabla_{\boldsymbol{X}} (\boldsymbol{U} + \boldsymbol{u}^\varepsilon) + \boldsymbol{I}, \qquad J^\varepsilon = \det \boldsymbol{F}^\varepsilon. \tag{2.4.8}$$

2.4.1 Linearisation of the perturbed equations of motion

In order to simplify the perturbed Eq. (2.4.7) of motion, a linearisation of the expansion around $\boldsymbol{U}$ can be developed. Before doing so, note that the directional derivative of a function of functions f is a generalisation to the derivative operator on a space of functions:

$$\mathrm{D}_{\boldsymbol{x}}[f][\boldsymbol{u}] = \lim_{\varepsilon \to 0} \frac{f(\boldsymbol{x} + \varepsilon \boldsymbol{u}) - f(\boldsymbol{x})}{\varepsilon}, \tag{2.4.9}$$

where ε is a scaling parameter.

Firstly, consider the perturbed deformation gradient (Eq. (2.4.8)), whose expansion

about the current state $\boldsymbol{U}$ becomes

$$\begin{aligned}\boldsymbol{F}^{\varepsilon} =& \nabla_{\boldsymbol{X}} \boldsymbol{U} + \boldsymbol{I} + \nabla_{\boldsymbol{X}} \boldsymbol{u}^{\varepsilon} \\ =& \boldsymbol{F} + \nabla_{\boldsymbol{X}} \boldsymbol{u}^{\varepsilon}.\end{aligned} \tag{2.4.10}$$

Proceeding with the linearisation of the Jacobian J^{ε}, chain rule can be used to obtain:

$$\begin{aligned}J(\boldsymbol{U} + \boldsymbol{u}^{\varepsilon}) &\approx J + \mathrm{D}_{\boldsymbol{U}}[J][\boldsymbol{u}^{\varepsilon}] \\ &\approx J + \mathrm{D}_{\boldsymbol{U}}[J(\boldsymbol{F})][\boldsymbol{u}^{\varepsilon}] \\ &\approx J + \frac{\partial J}{\partial \boldsymbol{F}} : \mathrm{D}_{\boldsymbol{U}}[\boldsymbol{F}][\boldsymbol{u}^{\varepsilon}] \\ &\approx J + \frac{\partial J}{\partial \boldsymbol{F}} : \nabla_{\boldsymbol{X}} \boldsymbol{u}^{\varepsilon},\end{aligned} \tag{2.4.11}$$

where second order terms $\mathcal{O}(\varepsilon^2)$ have been truncated. Since[19] $\frac{\partial J}{\partial \boldsymbol{F}} = J\boldsymbol{F}^{-T}$, it follows that

$$J(\boldsymbol{U} + \boldsymbol{u}^{\varepsilon}) \approx J + J\boldsymbol{F}^{-T} : \nabla_{\boldsymbol{X}} \boldsymbol{u}^{\varepsilon}. \tag{2.4.12}$$

With the incompressibility condition being satisfied for both $J - 1 = 0$ and $J^{\varepsilon} - 1 = 0$, as in Eqs. (2.4.4) and (2.4.7), considering the above first order approximation to hold strongly, then

$$J(\boldsymbol{U} + \boldsymbol{u}^{\varepsilon}) - 1 = (J - 1) + J\boldsymbol{F}^{-T} : \nabla_{\boldsymbol{X}} \boldsymbol{u}^{\varepsilon} = 0 \quad \text{on } \Omega_0, \tag{2.4.13}$$

leading to $\boldsymbol{F}^{-T} : \nabla_{\boldsymbol{X}} \boldsymbol{u}^{\varepsilon} = 0$ and implicitly to $J^{\varepsilon} \approx J$. This leads to the simplification of the momentum term in Eq. (2.4.7a) as

$$\rho J^{\varepsilon} \partial_{tt} \boldsymbol{U}^{\varepsilon} = \rho J \partial_{tt} \boldsymbol{U}^{\varepsilon} + \mathcal{O}(\varepsilon^2). \tag{2.4.14}$$

Before performing the linearisation of the perturbed PK2 tensor $\boldsymbol{S}^{\varepsilon}$, note that it depends on the perturbed hydrostatic pressure P^{ε}, which is linearised as

$$P^{\varepsilon} = P + p^{\varepsilon}. \tag{2.4.15}$$

This allows now to execute the linearisation of $\boldsymbol{S}^{\varepsilon}$ around $\boldsymbol{U}$ and P:

$$\begin{aligned}\boldsymbol{S}^{\varepsilon} &\approx \boldsymbol{S} + \mathrm{D}_{\boldsymbol{U}}[\boldsymbol{S}][\boldsymbol{u}^{\varepsilon}] + \mathrm{D}_{P}[\boldsymbol{S}][p^{\varepsilon}] \\ &\approx \boldsymbol{S} + \nabla_{\boldsymbol{F}} \boldsymbol{S} : \delta \boldsymbol{F} + (\partial_P \boldsymbol{S}) : \delta P + \mathcal{O}(\varepsilon^2) \\ &\approx \boldsymbol{S} + \nabla_{\boldsymbol{F}} \boldsymbol{S} : \nabla_{\boldsymbol{X}} \boldsymbol{u}^{\varepsilon} + p^{\varepsilon} (\partial_P \boldsymbol{S}) + \mathcal{O}(\varepsilon^2) \\ &\approx \boldsymbol{S} + \nabla_{\boldsymbol{F}} \boldsymbol{S} : \nabla_{\boldsymbol{X}} \boldsymbol{u}^{\varepsilon} - J p^{\varepsilon} \boldsymbol{C}^{-1} + \mathcal{O}(\varepsilon^2),\end{aligned} \tag{2.4.16}$$

where $\partial_P \boldsymbol{S} = -J\boldsymbol{C}^{-1}$, as it will be seen from the definition of $\boldsymbol{S}$ in section 2.5.1. Combining Eqs. (2.4.10) and (2.4.16), the first order approximation of the total stress

tensor $\boldsymbol{F}^\varepsilon \boldsymbol{S}^\varepsilon$ becomes

$$\boldsymbol{F}^\varepsilon \boldsymbol{S}^\varepsilon \approx \boldsymbol{F}\boldsymbol{S} + [\boldsymbol{F}\nabla_{\boldsymbol{F}}\boldsymbol{S} + \boldsymbol{\mathcal{I}}\boldsymbol{S}] : \nabla_{\boldsymbol{X}}\boldsymbol{u}^\varepsilon - Jp^\varepsilon \boldsymbol{F}^{-T} + \mathcal{O}(\varepsilon^2), \tag{2.4.17}$$

where $\boldsymbol{\mathcal{I}}_{ijkl} = \delta_{ik}\delta_{jl}$, the derivative of a 2$^{\text{nd}}$ order tensor $\boldsymbol{A}$ with respect to another one ($\boldsymbol{B}$) is defined as

$$(\nabla_{\boldsymbol{B}}\boldsymbol{A})_{ijkl} = \frac{\partial A_{ij}}{\partial B_{kl}},$$

and the contraction of a 4$^{\text{th}}$ order tensor $\boldsymbol{\mathcal{A}} \in \mathbb{R}^{3\times3\times3\times3}$ and a 2$^{\text{nd}}$ order tensor $\boldsymbol{B}$ yields a 2$^{\text{nd}}$ order tensor in $\mathbb{R}^{3\times3}$

$$(\boldsymbol{\mathcal{A}} : \boldsymbol{B})_{ij} = A_{ijkl}B_{kl}.$$

Considering all the derivations above, the linearised momentum balance Eq. (2.4.7) can be split between macro-deformation (first square bracketed term) and micro-deformation components, as

$$\begin{aligned}&[\rho\partial_t(J\boldsymbol{v}) - \nabla_{\boldsymbol{X}} \cdot (\boldsymbol{F}\boldsymbol{S})]+\\ &\rho\partial_t(J\boldsymbol{v}^\varepsilon) - \nabla_{\boldsymbol{X}} \cdot \left([\boldsymbol{F}\nabla_{\boldsymbol{F}}\boldsymbol{S} + \boldsymbol{\mathcal{I}}\boldsymbol{S}] : \nabla_{\boldsymbol{X}}\boldsymbol{u}^\varepsilon - Jp^\varepsilon \boldsymbol{F}^{-T}\right) = \boldsymbol{0} \quad \text{on } \Omega_0.\end{aligned} \tag{2.4.18}$$

Note that the first square bracketed term satisfies the unperturbed motion Eq. (2.4.4). Hence, the set of perturbed balance Eq. (2.4.7) becomes

$$\rho\partial_t(J\boldsymbol{v}^\varepsilon) - \nabla_{\boldsymbol{X}} \cdot \left([\boldsymbol{F}\nabla_{\boldsymbol{F}}\boldsymbol{S} + \boldsymbol{\mathcal{I}}\boldsymbol{S}] : \nabla_{\boldsymbol{X}}\boldsymbol{u}^\varepsilon - Jp^\varepsilon \boldsymbol{F}^{-T}\right) = \boldsymbol{0} \quad \text{on } \Omega_0, \tag{2.4.19a}$$

$$\boldsymbol{F}^{-T} : \nabla_{\boldsymbol{X}}\boldsymbol{u}^\varepsilon = 0 \quad \text{on } \Omega_0. \tag{2.4.19b}$$

2.4.2 Harmonic wave perturbations

Up to this point, generic infinitesimal displacements $\boldsymbol{u}^\varepsilon$ were considered to perturb the macrostate of the body. For this work, it is relevant to focus on further investigating these small displacements as harmonic waves. This is particularly relevant in the application of MRE high frequency / low amplitude wave propagation in deformed materials. Here, the small wave deformation and pressure are assumed to behave as[135]

$$\boldsymbol{u}^\varepsilon = \mathrm{Re}\{\boldsymbol{u}_c e^{i\omega t}\}, \qquad p^\varepsilon = \mathrm{Re}\{p_c e^{i\omega t}\}, \tag{2.4.20}$$

where $\boldsymbol{u}_c = \boldsymbol{u}_r + i\boldsymbol{u}_i$ ($\boldsymbol{u}_r, \boldsymbol{u}_i : \Omega_0 \to \mathbb{R}^d$) and $p_c = p_r + ip_i$ ($p_r, p_i : \Omega_0 \to \mathbb{R}$) give the complex periodic steady-state behaviour and subscripts r and i denote the real and imaginary parts, respectively. The second time derivative becomes $\partial_{tt}\boldsymbol{u}^\varepsilon = -\omega^2\mathrm{Re}\{\boldsymbol{u}_c e^{i\omega t}\}$. Since Eq. (2.4.19) has to hold at every time point $t \gg 0$, then $\boldsymbol{u}_c$ and p_c have to satisfy

periodic nonlinear wave equations in the reference domain Ω_0:

$$-\rho J\omega^2 \boldsymbol{u}_c - \nabla_{\boldsymbol{X}} \cdot \left([\boldsymbol{F}\nabla_{\boldsymbol{F}}\boldsymbol{S} + \boldsymbol{\mathcal{I}}\boldsymbol{S}] : \nabla_{\boldsymbol{X}}\boldsymbol{u}_c - p_c J\boldsymbol{F}^{-T} \right) = \boldsymbol{0} \quad \text{on } \Omega_0, \tag{2.4.21a}$$

$$\boldsymbol{F}^{-T} : \nabla_{\boldsymbol{X}}\boldsymbol{u}_c = 0 \quad \text{on } \Omega_0. \tag{2.4.21b}$$

2.4.3 Periodic nonlinear wave equations in the physical domain

As MRE is defined in the physical domain, the set of Eq. (2.4.21) can also be expressed in the physical frame. Firstly, the gradient operator can be converted using Eq. (2.4.3), leading to

$$\begin{aligned} [\boldsymbol{F}\nabla_{\boldsymbol{F}}\boldsymbol{S} + \boldsymbol{\mathcal{I}}\boldsymbol{S}] : \nabla_{\boldsymbol{X}}\boldsymbol{u}_c &= [\boldsymbol{F}(\nabla_{\boldsymbol{F}}\boldsymbol{S}) + \boldsymbol{\mathcal{I}}\boldsymbol{S}] : [\nabla_{\boldsymbol{X}}\boldsymbol{u}_c\boldsymbol{F}^{-1}\boldsymbol{F}] \\ &= [\boldsymbol{F}(\nabla_{\boldsymbol{F}}\boldsymbol{S})\boldsymbol{F}^T + \boldsymbol{\mathcal{I}}\boldsymbol{S}\boldsymbol{F}^T] : \nabla_{\boldsymbol{x}}\boldsymbol{u}_c \end{aligned} \tag{2.4.22}$$

and

$$\begin{aligned} \boldsymbol{F}^{-T} : \nabla_{\boldsymbol{X}}\boldsymbol{u}_c &= \boldsymbol{F}^{-T} : [\nabla_{\boldsymbol{X}}\boldsymbol{u}_c\boldsymbol{F}^{-1}\boldsymbol{F}] \\ &= \boldsymbol{I} : \nabla_{\boldsymbol{x}}\boldsymbol{u}_c \\ &= \nabla_{\boldsymbol{x}} \cdot \boldsymbol{u}_c. \end{aligned} \tag{2.4.23}$$

Then, the divergence of the stress term can be transformed using Eq. (2.4.2):

$$\nabla_{\boldsymbol{X}} \cdot \left([\boldsymbol{F}(\nabla_{\boldsymbol{F}}\boldsymbol{S})\boldsymbol{F}^T + \boldsymbol{\mathcal{I}}\boldsymbol{S}\boldsymbol{F}^T] : \nabla_{\boldsymbol{x}}\boldsymbol{u}_c \right) = J\nabla_{\boldsymbol{x}} \cdot (\boldsymbol{\mathcal{C}} : \nabla_{\boldsymbol{x}}\boldsymbol{u}_c), \tag{2.4.24}$$

where the fourth order tensor $\boldsymbol{\mathcal{C}}$ is

$$\boldsymbol{\mathcal{C}} = \frac{1}{J}(\boldsymbol{F}\nabla_{\boldsymbol{F}}\boldsymbol{S} + \boldsymbol{\mathcal{I}}\boldsymbol{S})\boldsymbol{F}^T\boldsymbol{F}^T. \tag{2.4.25}$$

Lastly, the gradient of the scalar pressure p_c can be recast using Eq. (2.4.1) and some algebraic manipulations:

$$\nabla_{\boldsymbol{X}} \cdot (Jp_c\boldsymbol{F}^{-T}) = J\nabla_{\boldsymbol{x}} \cdot (p_c\boldsymbol{I})\,. \tag{2.4.26}$$

Bringing together the above transformations, it follows that the set of periodic nonlinear wave equations in the physical domain is

$$\rho\omega^2 \boldsymbol{u}_c + \nabla_{\boldsymbol{x}} \cdot \left(\boldsymbol{\mathcal{C}} : \nabla_{\boldsymbol{x}}\boldsymbol{u}_c + \frac{p_c}{J}\boldsymbol{F}(\partial_P\boldsymbol{S})\boldsymbol{F}^T \right) = \boldsymbol{0} \quad \text{on } \Omega, \tag{2.4.27a}$$

$$\nabla_{\boldsymbol{x}} \cdot \boldsymbol{u}_c = 0 \quad \text{on } \Omega. \tag{2.4.27b}$$

2.5 Constitutive equations

In the previous section, finite and infinitesimal deformation analysis led to the identification of a set of equations that constrain a perturbed body under load. The equations are complete once the stress term, be it $\boldsymbol{\sigma}$, $\boldsymbol{P}$ or $\boldsymbol{S}$, takes a functional form. However, this is a complex task, as the stress tensor needs to be determined empirically. In this work, isothermal conditions are assumed, such that the stress tensor is modelled based only on strain, and later on its time rate. The model represents the constitutive behaviour of the body.

2.5.1 Hyperelastic solids

A hyperelastic material's behaviour may be described using a strain energy function which quantifies the energy stored by the body under deformation. This is a scalar function $W : \mathbb{R}^{d\times d} \to \mathbb{R}$ which depends on strain metrics that incorporate the deformation path (e.g. $\boldsymbol{F}$, $\boldsymbol{C}$, $\boldsymbol{B}$) and describes the body's tendency to return to its undeformed state once the loading ceases. For many solids, including liver tissue, it is considered that the strain energy is zero in the absence of mechanical loading. In general, this may not always be true, as there may be residual stresses[54]. In this thesis, as well as in liver constitutive models in literature, residual stress is not part of the analysis, as this would lead to additional complications. Nevertheless, the positivity constraint $W \geq 0$ must hold, as W quantifies the amount of energy necessary to deform the body.

In this thesis, it is presumed that the liver tissue and other mimicking materials are homogeneous, isotropic and incompressible. For such solids, the PK2 tensor is determined to be[19]

$$\boldsymbol{S} = 2\frac{\partial W}{\partial \boldsymbol{C}}. \tag{2.5.1}$$

The total PK2 tensor comprises an elastic and a hydrostatic part, which can be separated as $\boldsymbol{S} = \boldsymbol{S}_e + \boldsymbol{S}_p$. To ensure that $\boldsymbol{S}_e$ encompasses only the deviatoric part, then $\boldsymbol{S}_e : \boldsymbol{C} = 0$. This allows us to compute the hydrostatic pressure as $P = \frac{1}{d}J^{-1}\boldsymbol{S} : \boldsymbol{C}$, leading to the hydrostatic pressure tensor $\boldsymbol{S}_p = JP\boldsymbol{C}^{-1}$.

2.5.2 Viscoelastic solids

A viscoelastic material is characterised by both elastic and viscous elements. The elastic component is responsible for the restoration to the original state, while the viscous component characterises the resistance to deformation in a time-dependent manner. A viscoelastic material exhibits hysteresis in the stress-strain response (memory on the deformation path), stress relaxation and creep. Although creep and relaxation are two phenomena that are sometimes used interchangeably, they are different in nature. Creep is the slow/plastic strain produced under constant stress, while relaxation is a decrease in stress under constant strain. They can both produce permanent deformations. Thus, for a viscoelastic material, its constitutive law will include elastic components, given

by a dependency on the strain, and time-dependent viscous components, usually given by a dependency on the strain rate.

Rheological components can be used to explain a material's behaviour. Elasticity is described using springs, while viscosity is introduced by dashpots, which have a damping effect. Typically, these components are described by linear relationships. Thus, the spring is generally modelled as

$$\sigma_e = E\epsilon, \tag{2.5.2}$$

where σ_e is the elastic stress, ϵ is the applied strain and E is an elasticity constant, also known as Young's modulus. Similarly, the dashpot is modelled as

$$\sigma_v = \eta \frac{\mathrm{d}\epsilon}{\mathrm{d}t}, \tag{2.5.3}$$

where σ_v is the viscous stress which depends on the rate of change of strain ϵ via a viscosity constant η. In these rheological elements, nonlinear stress-strain relationships may also be considered.

Viscoelasticity can be obtained by combining a spring and a dashpot. Thus, for a series configuration, the Maxwell model is obtained. This system is described by

$$\frac{1}{E}\frac{\mathrm{d}\sigma}{\mathrm{d}t} + \frac{\sigma}{\eta} = \frac{\mathrm{d}\epsilon}{\mathrm{d}t}, \tag{2.5.4}$$

where $\sigma = \sigma_e = \sigma_v$ is the total stress, and ϵ is the total strain, which is distributed across the spring and dashpot[10]. A parallel configuration of these elements is also possible, leading to the Kelvin-Voigt model:

$$\sigma = E\epsilon + \eta \frac{\mathrm{d}\epsilon}{\mathrm{d}t}. \tag{2.5.5}$$

Here, the total stress σ is divided between the spring and dashpot, whereas the total strain ϵ is equivalent to the strain in both elements.

Inherently, the Maxwell model has a limitation in modelling creep, whereas the Kelvin-Voigt model is not suitable for modelling relaxation[156]. To overcome these drawbacks, these models can be combined into what is known as the standard linear solid model. This is obtained by arranging a spring in series with the Kelvin-Voigt model or, conversely, by arranging a spring in parallel with the Maxwell model. Moreover, the complexity of the standard linear solid model can be increased by continuing adding Kelvin-Voigt or Maxwell configurations, respectively (i.e. generalised Kelvin-Voigt / Maxwell models). As these become increasingly complex to handle, fractional viscoelasticity may be considered. One such approach is more broadly discussed in chapter 3.

2.5.3 Liver hyperelastic constitutive equations in literature

A range of hyperelastic models have been investigated in literature for capturing the

liver behaviour. Let us start by discussing a study by Chui et al.[39], who performed a comprehensive analysis on nonlinear hyperelastic models for porcine liver under uniaxial compression and elongation. Cylindrical samples of 7 mm diameter and less than 10 mm height, attached to rheometer plates using surgical bond, were examined. The deformations employed in the experiment lead to a deformation gradient given by

$$\boldsymbol{F} = \begin{pmatrix} \frac{1}{\sqrt{\lambda}} & 0 & 0 \\ 0 & \frac{1}{\sqrt{\lambda}} & 0 \\ 0 & 0 & \lambda \end{pmatrix}, \tag{2.5.6}$$

where λ is the compression or elongation ratio. Additionally, the material is considered to be incompressible ($\det \boldsymbol{F} = 1$). The P_{33} component of the PK1 tensor, which was used to model the experimental results, was then

$$P_{33} = 2\frac{\partial W}{\partial I_{\boldsymbol{C}}}\left(\lambda - \frac{1}{\lambda^2}\right) + 2\frac{\partial W}{\partial II_{\boldsymbol{C}}}\left(1 - \frac{1}{\lambda^3}\right). \tag{2.5.7}$$

This study investigated models from different functional forms that are usually employed in biomechanical modelling: polynomial, exponential, logarithmic and power-law forms, but also combined forms. The models' strain energy functions are given below, followed by a discussion on their suitability to model the data.

The first models considered were the polynomial ones. Three forms were employed, starting with the Neo-Hookean model:

$$W = C_1(I_C - 3), \tag{2.5.8}$$

then a Mooney-Rivlin[175,208] model:

$$W = C_1(I_{\boldsymbol{C}} - 3) + C_2(II_{\boldsymbol{C}} - 3), \tag{2.5.9}$$

and an extended model with 9 scaling parameters:

$$\begin{aligned} W = {} & C_1(I_{\boldsymbol{C}} - 3) + C_2(II_{\boldsymbol{C}} - 3) + C_3(I_{\boldsymbol{C}} - 3)^2 \\ & + C_4(I_{\boldsymbol{C}} - 3)(II_{\boldsymbol{C}} - 3) + C_5(II_{\boldsymbol{C}} - 3)^2 + C_6(I_{\boldsymbol{C}} - 3)^3 \\ & + C_7(I_{\boldsymbol{C}} - 3)^2(II_{\boldsymbol{C}} - 3) + C_8(I_{\boldsymbol{C}} - 3)(II_{\boldsymbol{C}} - 3)^2 + C_9(II_{\boldsymbol{C}} - 3)^3, \end{aligned} \tag{2.5.10}$$

The next class of models were the exponential and logarithmic ones, employing the following forms: the Fung exponential model[66]

$$W = \frac{C_1}{2C_2}(\mathrm{e}^{C_2(I_{\boldsymbol{C}} - 3)} - 1), \tag{2.5.11}$$

an exponential-polynomial model devised by Veronda and Westmann[254], adapted for

incompressible materials:

$$W = C_1(\mathrm{e}^{C_3(I_{\boldsymbol{C}}-3)} - 1) + C_2(II_{\boldsymbol{C}} - 3), \tag{2.5.12}$$

and a logarithmic form used by Takamizawa and Hayashi[245], adapted for isotropic materials:

$$W = -C_1(\ln(1 - C_2(I_{\boldsymbol{C}} - 3))). \tag{2.5.13}$$

Power law models were also considered, using the Ogden model[188] with the form presented by Zobitz[286]

$$W = \sum_{n=1}^{3} \frac{C_n}{\alpha_n} \left(\lambda_1^{0.5\alpha_n} + \lambda_2^{0.5\alpha_n} + \lambda_3^{0.5\alpha_n}\right), \tag{2.5.14}$$

where $\lambda_{1,2,3}$ are the eigenvalues of $\boldsymbol{F}$. Lastly, Chui proposed a combined logarithmic and polynomial function:

$$W = -\frac{C_1}{2} \ln\left(1 - C_2(I_{\boldsymbol{C}} - 3)\right) + C_3(I_{\boldsymbol{C}} - 3). \tag{2.5.15}$$

In all of the models listed above, the C and α terms are material parameters.

In Chui et al.[39], large uniaxial deformations were investigated, with the compression ratio reaching almost 0.6 and the maximum elongation ratio being 1.6. The liver behaviour followed a path similar to the representative curve presented in Fig. 2.5.1. Although there is no visual representation of the models being fit to the data, the errors are reported in numerical form. The first two polynomial models, Neo-Hookean and Mooney-Rivlin, could not capture well the entire deformation curve. The 9-parameter polynomial model (Eq. (2.5.10)) provided the best fit. However, fitting 9 parameters using only uniaxial deformation data is complex and possibly non-unique, with parameters $C_{1..9}$ being reported both in the positive and negative range. However, it is generally desirable to have positive parameters, such that contributions from different terms don't cancel out. The models involving exponential and logarithmic forms (Eqs. (2.5.11)–(2.5.13)) led to comparable errors, with no particular advantage of one form over the other. The power law model (Eq. (2.5.14)) was reported to have problems fitting the compression part of the data. The combined Chui form (logarithmic and polynomial, Eq. (2.5.15)) resulted in smaller errors than all other models except for the 9-parameter polynomial model. However, it also relied on the identification of negative parameters. Overall, although this study's parameter identification process is rather ambiguous, it provides a good overview of the main types of models that can be used for liver characterisation.

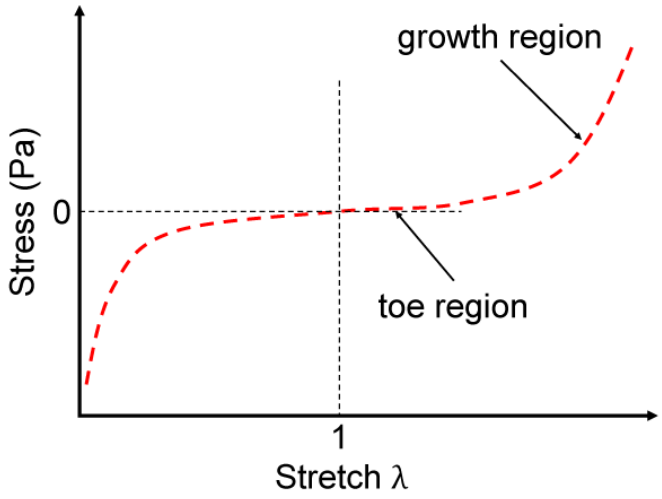

Figure 2.5.1 *Schematic of stress versus stretch (λ) in compression-elongation tests on liver samples*

Uniaxial tests have been extensively used in soft tissue rheology. However, added value can be obtained from varying the type of deformation. For example, Gao et al.[70] executed three tests on porcine liver tissue (see Fig. 2.5.2 for schematics): a tension (elongation) experiment similar to Chui et al.[39], where the samples were glued to the rheometer's plates and then stretched, a compression experiment, where samples were not fixed to the plate, thus being able to slide and consequently extend the area in contact with the plates, and a planar tension test, where short but wide samples were either glued to the plates or clamped and then stretched.

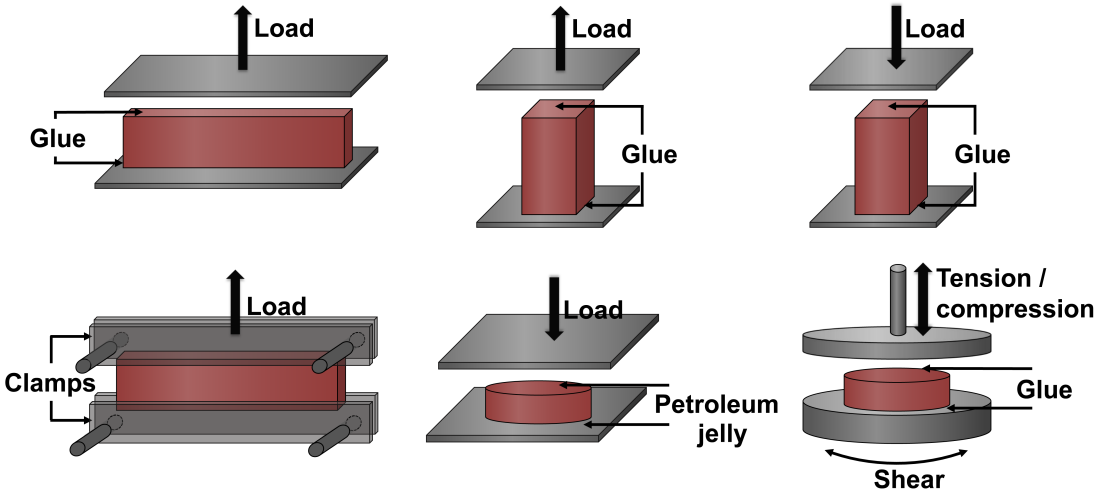

Figure 2.5.2 *Liver rheological testing configurations: (Top left) planar tension using glue to secure the sample; (Top middle) tensile test; (Top right) confined compression test; (Bottom left) planar tension using clamps to secure the sample; (Bottom middle) unconfined compression test; (Bottom right) shear test*

Two new models were employed in Gao et al.[70], based on the Ogden model, combined

with either an exponential or logarithmic term. Thus, the Ogden-exponential form

$$W = C_1 \left(\mathrm{e}^{C_2(\lambda_1^{\alpha_1} + \lambda_2^{\alpha_1} + \lambda_3^{\alpha_1} - 3)} - 1 \right), \tag{2.5.16}$$

and Ogden-logarithmic form

$$W = -C_1 \ln \left(1 - C_2(\lambda_1^{\alpha_1} + \lambda_2^{\alpha_1} + \lambda_3^{\alpha_1} - 3)\right), \tag{2.5.17}$$

were used, where $C_{1,2}$ and α_1 are material parameters and $\lambda_{1,2,3}$ are the stretches in the three directions.

The models in this study were not parametrised using a fitting algorithm. Instead, the parameters were approximated using certain regions of the deformation spectrum. The objective was to investigate the suitability of these models to represent the data and, as seen in Fig. 2.5.3, they can indeed capture the liver behaviour in tension and compression. Similar results are observed for the planar tension test.

This study incorporated the Ogden form in order to account for the stretches that occur in the different principal directions. This was mainly motivated by the planar tension test, where, due to the sample's large width, deformation in the width direction was considered minimal and hence one of the eigenvalues was set to 1. It would be interesting, however, to examine an exponential model based on invariants and determine its suitability to capture this data.

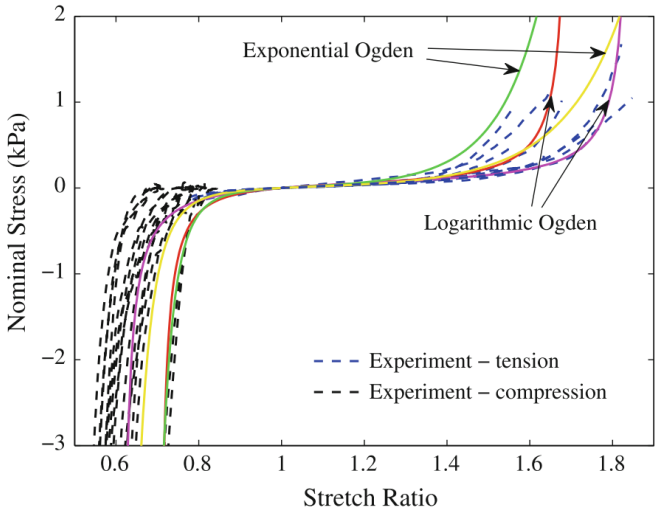

Figure 2.5.3 *Comparison of experimental nominal stress (P) - stretch (λ) behaviour (dashed line) with the theoretical prediction of the exponential Ogden and logarithmic Ogden prediction; figure reproduced from Gao et al.*[70]*, with permission*

A 3D deformation study was performed by Perepelyuk et al.[195], where cylindrical rat liver samples were examined in tension and under simultaneous compression and shear (Fig. 2.5.2, bottom right). The liver was considered to comprise a solid compressible

phase through which water (incompressible) could locally flow. Hence, under load, the sample could change its height but not its radius. The data were modelled using a power law model:

$$\sigma_{\lambda_i,J} = \begin{cases} C_1\left(1-\frac{1}{\lambda_i^{19}}\right)+C_2\left(1-\frac{1}{J^9}\right), & \lambda_i \geq 1 \\ \\ \frac{19C_1}{5J^5}(\lambda_i^5-1)+C_2\left(1-\frac{1}{J^9}\right), & \lambda_i < 1 \end{cases} \tag{2.5.18}$$

where $\sigma_{\lambda_i,J}$ were the stress components computed on the top surface in the three principal directions corresponding to eigenvalues λ_i. Within the ranges of tension and combined compression and shear applied in the experiments, the model generally fit well the observed stress response. However, some of the steps in determining the model were presented ambiguously, hence it would benefit from further validation.

The studies presented here are a representative sample which model the hyperelastic behaviour of liver tissue. Hence, let us summarise the strengths and limitations of the general polynomial, exponential, logarithmic and power law forms. Polynomial models are usually easy to handle, as they only involve material parameters that act as linear scaling (i.e. polynomial coefficients). This makes the parameter fitting process a reasonably simple one, and an example in this sense will be seen later in chapter 5. One drawback of polynomial models is that, for large strains, they have difficulties in capturing the entire deformation curve, whether it is in compression or elongation. Exponential models are more suitable in this sense, as the power parameter (e.g. C_2 in Eq. (2.5.11)) is variable and can be adjusted to control the growth portion, whereas the parameter acting as a linear scaling (e.g. C_1 in Eq. (2.5.11)) can be tweaked to model the toe region (see Fig. 2.5.1). However, those two parameters are coupled and cannot be managed independently, which leads to a complex parameter tuning process. Logarithmic models provide the same benefits as the exponential ones, with the two parametes (e.g. $C_{1,2}$ in Eq. (2.5.13)) easily adjusting to the toe and growth parts, but being coupled. Additionally, a pitfall occurs when $I_{\boldsymbol{C}} = 1/C_2 + 3$, which leads to $\ln 0$. This can be avoided by tuning the material parameters, but it shows a restriction of the model. Finally, power law models (e.g. Eqs. (2.5.14) and (2.5.18)) are well suited when deformations probe all three principal directions, as this is their added benefit over exponential models. However, these models have a time and cost limitation, as computation of eigenvalues is more complex and costly than that of invariants.

2.5.4 Liver viscoelastic constitutive equations in literature

Traditional liver models are hyperelastic, as seen from the wide range of models presented in section 2.5.3. For MRE purposes, however, it is important to incorporate viscoelasticity, as it operates at frequencies where tissue viscoelastic effects manifest ($\approx$ 50 Hz). In this section, we present liver viscoelastic constitutive models employed

in literature.

As described in section 2.5.2, mechanical components can be used to explain materials' behaviour. One such example is employed in a study by Liu and Bilston[147], who used a five component generalised Maxwell model to characterise the linear behaviour of bovine liver tissue at small strains:

$$\sigma = \gamma G_e + \gamma \sum_{i=1}^{n} \frac{\eta_i}{\tau_i} \mathrm{e}^{-t/\tau_i} \tag{2.5.19}$$

where G_e is the elastic modulus, γ is the shear strain and η_i and $\tau_i = \eta_i/G_i$ are the viscosity and relaxation time corresponding to the i^{th} element. With the shear strain γ depending on time, the stress σ becomes dependent on the deformation history. The model can capture the behaviour observed under shear strain sweep oscillation, relaxation and shear oscillations. However, it is only meant to model the linear limit, and its complexity would increase if considering larger strains.

The standard linear solid model has been investigated by Jordan et al. (Fig. 2.5.4, network configuration 2) in the context of identifying a minimal rheological configuration that can model porcine liver behaviour in cyclic indentation[120]. The classical form, with a linear elastic response in elements 2A and 2B ($\sigma^e = E\epsilon^e$, where E is the elastic modulus and ϵ^e is the elastic strain), and with a linear viscous response in element 2C ($\sigma^v = \eta\partial_t\epsilon$, where η is the viscous parameter), was shown to be insufficient, as the nonlinear response could not be met. Consequently, an exponential elastic law was considered for element 2A ($\sigma^e = A/b\left(\mathrm{e}^{b|\epsilon^e|} - 1\right)$, with parameters A and b); element 2B was kept linear; element 2C was changed to be governed by a nonlinear power law ($\partial_t\epsilon^v = \partial_t\epsilon_0^v\alpha/(|\epsilon^v| + \alpha)\,(\sigma^v/S_0)^n$, where S_0, n and α are model parameters and $\dot{\epsilon}_0^v = 1$ s^{-1}). The nonlinear considerations for the spring element 2A and dashpot element 2B were observed to significantly improve the model fit to the data.

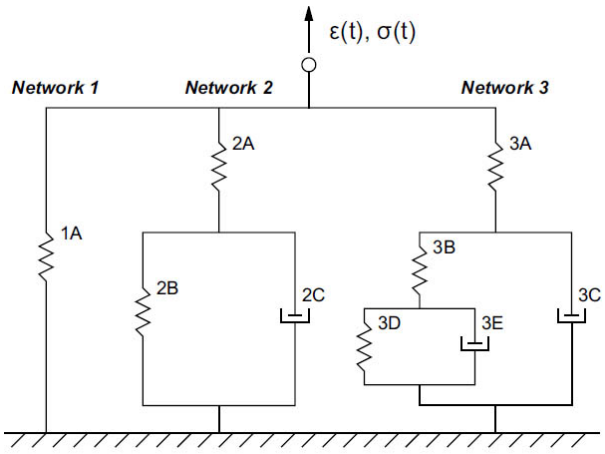

Figure 2.5.4 *Rheological schemes of increasing complexity; Network 2 depicts the standard linear model; figure reproduced from Jordan et al.*[120]*, with permission*

Other forms of viscoelastic liver models have been investigated. For example, a BKZ (Bernstein, Kearsley, Zapas) type model[13,174] was proposed by Nicolle et al.[217] in order to capture the behaviour of porcine liver in two types of tests: small strain rotational oscillation sweeps through the frequency range 0.1 - 10 Hz, and constant strain rate deformation until rupture (≈150% strain). Shear stress σ at the current configuration time t is designed to depend on the shear strain $\gamma(t)$, its time rate $\dot{\gamma}(t)$, and the entire strain history:

$$\sigma(t) = \int_{-\infty}^{t} G\left(t - t', \gamma(t) - \gamma(t')\right) \dot{\gamma}(t') \mathrm{d}t', \tag{2.5.20}$$

where $G(t, \gamma)$ is the strain dependent relaxation modulus, proposed to be defined as:

$$G(t, \gamma) = \frac{K}{\Gamma(1-n)} t^{-n} \left\{ 1 + \left(\frac{\gamma}{\gamma_{lim}} \right)^{p} \right\} + \eta \delta(t). \tag{2.5.21}$$

Γ is the Gamma function, $\delta(t)$ is the Dirac distribution, K, n, η , γ_{lim} and p are material constants. If $n = 0$ then the material becomes purely elastic, with elasticity K, whereas if $n = 1$ the material becomes purely viscous, with viscosity K. Any value of n in between the two limits gives a combined viscoelastic behaviour.

This model was able to capture the liver behaviour in both tests. Note, however, that the oscillatory test only employed small deformations, hence the viscoelastic effects of large deformations are unknown. Although large strain tests were employed, they were performed once, until rupture, thus preventing the investigation of the un-loading path, but also repeatability.

From the few models discussed above, it is obvious that introducing a viscous component is an intricate task. Models become convoluted, employ numerous material parameters, and depend on strain history, which can lead to unfeasible computational costs in large problems. An alternative for incorporating viscoelasticity is by considering fractional viscoelasticity. This approach introduces fractional derivatives in constitutive models / stress tensors. For example, on stress tensor $\boldsymbol{S}$ the fractional order derivative can be employed as defined by Caputo[31]:

$$D_t^{\alpha} \boldsymbol{S} = \frac{1}{\Gamma(1-\alpha)} \int_0^t \frac{1}{(t-z)^{\alpha}} \partial_t \boldsymbol{S}(z) \, \mathrm{d}z, \tag{2.5.22}$$

where α is the fractional order which ranges from 0 (leading to a purely elastic tensor $\boldsymbol{S}$) to 1 (leading to a purely viscous response, equivalent to $\partial_t \boldsymbol{S}$). This approach can greatly simplify the viscoelastic modelling process, as it can be applied to well-established, simple hyperelastic models. Compared to hyperelastic models, the added complexity lies only in the addition of parameter α. As for other viscoelastic models, the challenge remains in their dependence of stress on the entire time history. This can become problematic in terms of time efficiency and computational costs. Chapter 3 analyses this problem and introduces a computational method that can efficiently handle time history.

2.6 Linear viscoelasticity in MRE

MRE relies on the reconstruction of linear viscoelastic wave equations[62], which employ a form similar to

$$\rho\omega^2\boldsymbol{u}_c + \nabla_{\boldsymbol{x}} \cdot [G^* \left(\nabla_{\boldsymbol{x}}\boldsymbol{u}_c + \nabla_{\boldsymbol{x}}\boldsymbol{u}_c^T\right)] + \nabla_{\boldsymbol{x}} p_c = \boldsymbol{0}, \tag{2.6.1a}$$

$$\nabla_{\boldsymbol{x}} \cdot \boldsymbol{u}_c = 0. \tag{2.6.1b}$$

Density ρ is typically assumed to be that of water, ω is the angular frequency of the propagating waves, $\nabla_{\boldsymbol{x}}\boldsymbol{u}_c$ is the gradient of the measured wave displacements and p_c is the hydrostatic pressure which may be eliminated using various methods or remain an unknown to be solved. G^* is the unknown complex stiffness modulus defining the material investigated which needs to be reconstructed. This is usually separated as $G^* = G' + iG''$, where G' is the storage modulus (referred to as stiffness or elasticity) and G'' is the loss modulus (viscosity).

Equation (2.6.1a) is equivalent to the periodic nonlinear wave Eq. (2.4.27a) if no underlying macro-deformation exists. Thus, if $\boldsymbol{F} = \boldsymbol{I}$, then the deviatoric part of $\boldsymbol{S}$ simplifies to $G^*\boldsymbol{I}$, with G^* stemming from the constitutive model parameters used in the definition of $\boldsymbol{S}$. This further leads to the fourth order tensor $\boldsymbol{\mathcal{C}}$ to be equivalent to $G^*\boldsymbol{\mathcal{I}}$ and therefore to

$$\rho\omega^2\boldsymbol{u}_c + \nabla_{\boldsymbol{x}} \cdot (G^*\boldsymbol{\mathcal{I}} : \nabla_{\boldsymbol{x}}\boldsymbol{u}_c + p_c\boldsymbol{I}) = \boldsymbol{0}, \tag{2.6.2a}$$

$$\nabla_{\boldsymbol{x}} \cdot \boldsymbol{u}_c = 0, \tag{2.6.2b}$$

with $\boldsymbol{\mathcal{I}} : \nabla_{\boldsymbol{x}}\boldsymbol{u}_c = \nabla_{\boldsymbol{x}}\boldsymbol{u}_c + \nabla_{\boldsymbol{x}}\boldsymbol{u}_c^T$. We can thus see that, in the absence of macro-deformation, the periodic nonlinear wave equations are compatible with the linear viscoelastic wave equations employed in MRE. However, when deformation is present, the nonlinear behaviour of the material manifests, which leads to an intricate form of the fourth order tensor $\boldsymbol{\mathcal{C}}$. This is not compatible with standard MRE reconstruction methods, despite being often employed in practice.

3 An Efficient and Accurate Method for Modeling Nonlinear Fractional Viscoelastic Materials

The previous chapter introduced constitutive laws as the link between stress and deformation. In this work, it will be essential to determine constitutive laws of liver tissue and other mimicking materials. As we are interested in using these laws for MRE purposes, viscoelastic models need to be identified. Section 2.5.4 reviewed some viscoelastic models in literature, and introduced the Caputo fractional derivative (Eq. (2.5.22)).

This thesis relies exclusively on the Caputo fractional derivative as a means of introducing viscoelasticity in constitutive modelling. Therefore, it is important to discuss the methods employed to numerically approximate this derivative. In particular, chapter 4 utilises the Grünwald-Letnikov approach, while chapter 5 uses a Prony-based approach. These methods, along with other Caputo approximations employed in literature, are discussed in this chapter, in section 3.2. Aspects such as convergence, accuracy and computational costs are compared in sections 3.5–3.7, which present examples of polynomial functions, fractional differential equations and biomechanical models of liver tissue, respectively. A discussion and conclusions complete the study.

This chapter has been submitted as a self-standing article:
Will Zhang, Adela Capilnasiu, Gerhard Sommer, Gerhard A. Holzapfel, David A. Nordsletten. "An efficient and Accurate Method for Modeling Nonlinear Fractional Viscoelastic Biomaterials". *Computer Methods in Applied Mechanics and Engineering* (Submitted, 2019).
The candidate contributed to the analysis, interpretation of research data and drafting of section 3.7.

Abstract

Computational biomechanics plays an important role in biomedical engineering: using modeling to understand pathophysiology, treatment and device design. While experimental evidence indicates that the mechanical response of most tissues is

viscoelasticity, current biomechanical models in the computation community often assume only hyperelasticity. Fractional viscoelastic constitutive models have been successfully used in literature to capture the material response. However, the translation of these models into computational platforms remains limited. Many experimentally derived viscoelastic constitutive models are not suitable for three-dimensional simulations. Furthermore, the use of fractional derivatives can be computationally prohibitive, with a number of current numerical approximations having a computational cost that is $\mathcal{O}(N_T^2)$ and a storage cost that is $\mathcal{O}(N_T)$ (N_T denotes the number of time steps). In this paper, we present a novel numerical approximation to the Caputo derivative which exploits a recurrence relation similar to those used to discretize classic temporal derivatives, giving a computational cost that is $\mathcal{O}(N)$ and a storage cost that is fixed over time. The approximation is optimized for numerical applications, and the error estimate is presented to demonstrate efficacy of the method. The method is shown to be unconditionally stable in the linear viscoelastic case. It was then integrated into a computational biomechanical framework, with several numerical examples verifying accuracy and computational efficiency of the method, including in an analytic test, in an analytic fractional differential equation, as well as in a computational biomechanical model problem.

3.1 Introduction

Biomechanical analysis has become an area of increasing emphasis in biomedical engineering applications. It has been used for understanding a diverse range of complex problems, such as the surgical intervention strategies for arterial bifurcation[176], the impact of left ventricular assist devices[165,167], the risk of aortic aneurysm rupture[72,73], the repair of the mitral valve in the heart[47,206], as well as the surgical aids for brain surgeries[171]. Through biomechanics simulation, devices and procedures can be optimized and personalized to improve design, therapy and patient outcomes[35]. A key component to these types of biomechanical assessments is identifying appropriate constitutive equations that define the material response to physiological and extra-physiological loading. While hyperelastic material models have been developed to describe a range of tissues[67,109], viscoelasticity has been acknowledged as an important component of mechanical response in brain matter[143,219,238], connective tissues[55,136], fracturing of bone tissues[270], as well as many cardiovascular soft tissues[262], including arterial tissues[105] and myocardium[235,236]. Despite viscoelasticity in soft tissues being widely studied experimentally, its use in computational biomechanics simulations remains relatively uncommon, likely due, in part, to the challenges to its implementation.

Viscoelasticity and viscoelastic theory has been a topic of interest since the 19th century[164,266]. Early forms of viscoelastic constitutive models used spring and dashpot[267] constructs, e.g, the Maxwell[38] and the Kelvin-Voigt models[170]. To better explain experimental observations, authors began to combine these simple units in series and/or parallel to form more complex systems, such as the generalized Maxwell[266] or gen-

eralized Kelvin-Voigt models[34]. These early theoretical works were successfully used to explain the linear viscoelastic behavior in a number of materials, including muscle tissues[139]. A more generalized one dimensional theory was proposed by Green and Tobolsky[89] to explain relaxing media. Extension of these early concepts of viscoelasticity to nonlinear continuum mechanics was addressed by a number of analytic mechanicians, including Truesdell[249], Green and Rivlin[84,85] and Bernstein, Kearsley, and Zapas[13] (see[42] for a review on early works investigating viscoelasticity). Nonlinear viscoelastic theory has been applied to modelling of elastomers[38], rubber materials[149], fiber reinforced materials[107], myocardium[94] as well as brain tissue[27,28]. Extension of these approaches to computational mechanics has been in the works of Simo[227], Le Tallec[137], Holzapfel[94,105,107,110], and De Buhan and Frey[48] amongst others.

While much of the early developments in viscoelasticity and its numerical application focused on analogues to spring-dashpot systems, fractional viscoelastic behavior can be seen increasingly in modeling tissue properties[63,103,154]. Use of these models has been recently presented in lung tissue[17]. The advantage of fractional viscoelasticity is that the method provides a spectrum of relaxation times parameterized through the chosen fractional derivative order, α. A simplification of the generalized Maxwell approach with infinite Maxwell elements, the fractional approach has the advantage of being compact, requiring few parameters and being effective at characterizing hierarchical viscoelastic materials exhibiting power-law behavior[100,134,155,242]. These benefits are challenged by the need to numerically approximate the fractional derivative, which is often done using cumulative integral approximations that require the storage of all past values of stress and increasingly costly computations in time. Development of efficient approaches to approximating fractional derivatives by Yuan and Agrawal[280], Diethelm[53] and Birk and Song[16] have enabled the efficient extension of fractional models to solid mechanics[287]. However, how these approximations perform in a computational biomechanics context using finite elements presents additional challenges and questions.

In this work, we present a numerical formulation for the constitutive modeling of viscoelastic materials based on a novel and efficient recursive approximation to evaluate fractional viscoelasticity. The proposed approach, utilizes a Prony series (or generalized Maxwell model) as in[16,52,287] with an additional dashpot element and optimization process to making the computational and storage costs consistent with standard transient methods. An error estimate is derived for the class of Prony approximations, detailing the improved computational accuracy of the proposed method (as well as those previously proposed). The numerical method is then integrated into our finite element framework[138] and shown to be unconditionally stable in the linear viscoelastic setting. Results from this analysis are demonstrated through a series of numerical examples, demonstrating appropriateness of the developed bounds, accuracy and numerical efficiency. While demonstrated in a specific biomechanics setting, this generalized approach lends itself to a wide variety of modeling problems in soft tissues as well as

other fractional-time derivative problems.

The paper reviews current techniques for approximating the Caputo derivative, introduces our approximation as well as its error estimates (section 3.2). In section 3.3, the paper reviews mechanical formulations for viscoelasticity, including fractional approaches, for nonlinear mechanics. The introduced models and approximations are then integrated into a nonlinear mechanics finite element framework (section 3.4) which is shown to be unconditionally stable in the linear viscoelastic case (see Appendix 3.A). Convergence, accuracy and computational costs are then evaluated in an analytic example (section 3.5), a simplified fractional diffusion system (section 3.6) as well as in a biomechanical example of liver tissue (section 3.7). The paper finishes with a discussion of key results and conclusions.

3.2 Fractional Derivatives and their Approximations

3.2.1 Caputo fractional derivative

The concept of fractional calculus started with questions about about the generalization of integral and differential operators by L'Hospital and Leibniz[213] from the set of integers to the set of real numbers. Subsequently, many prominent mathematicians focused on fractional calculus (for reviews, see, Ross[213] and Machado[152]). Within the field, many different definitions for fractional differential and integral operators of arbitrary order have been introduced[199]. In this work, we focus on the Caputo definition where the fractional derivative, D_t^α (with $\alpha > 0$), of a n-times differentiable function f can be written as,

$$D_t^\alpha f = \frac{1}{\Gamma(\lceil\alpha\rceil - \alpha)} \int_0^t \frac{f^{\lceil\alpha\rceil}(s)}{(t-s)^{1+\alpha-\lceil\alpha\rceil}} \,\mathrm{d}s, \tag{3.2.1}$$

where $\lceil\alpha\rceil$ denotes the ceiling of α. The fractional derivative (for $\alpha \notin \mathbb{N}$), unlike integer derivatives, is a convolution of the past behavior of the function, making it particularly useful for constitutive modeling of viscoelastic materials. The Caputo form (which can be related to other formulations like the Riemann-Louiville fractional derivative) has the advantage that

$$D_t^\alpha c = 0, \qquad \text{for any constant } c \in \mathbb{R}. \tag{3.2.2}$$

For later analysis, we will instead assume that the functions f are continuous and $n+1$-times differentiable[51], which allows the use integration by parts to rewrite the Caputo derivative as

$$D_t^\alpha f = \frac{1}{\Gamma(1+n-\alpha)} \left(t^{n-\alpha} f^n(0) + \int_0^t (t-s)^{n-\alpha} f^{n+1}(s) \,\mathrm{d}s \right). \tag{3.2.3}$$

This form eliminates the weak singularity in the integrand of Eq. (3.2.1), which is convenient in our analysis.

3.2.2 Current methods for numerical approximation of the Caputo derivative

Fractional derivative operators and methods for approximating their effects are well studied in literature. For some recent review of this subject, readers may consider the works of Zeid[282], Guo[95], Weilbeer[264] and Podlubny[199]. Approaches in the literature can be categorized by their method of integration, either cumulative or recursive. Cumulative approaches approximate the Caputo derivative by directly numerically approximating the integrals in Eq. (3.2.1) or (3.2.2) using some form of a weighted sum over a set of discrete time points. In contrast, recursive approaches first approximate the Caputo derivative by transforming it into a series of ordinary differential equations that have standard discretizations.

Suppose we seek to approximate the α^{th}-order fractional derivative, $D_t^\alpha f$ $(0 < \alpha < 1)$, of a function $f : [0, T] \to \mathbb{R}$ at a series of N_T times points

$$0 = t_0 < t_1 < \cdots < t_{N_T} = T, \quad \text{where } t_n = n\Delta_t,$$

Δ_t denotes the time step size, and that $f_n = f(t_n)$ is easily computed given some prior information from previous time points. Considering cumulative approaches, a straightforward method to computing Caputo derivative is through a Riemann sum evaluated using the midpoint point (MP) rule, i.e.

$$\mathrm{D}^\alpha_{n,\mathrm{MP}} f = \frac{1}{\Gamma(1-\alpha)} \sum_{i=1}^{n} \frac{1}{\left(t - (i - \frac{1}{2})\Delta_t\right)^\alpha} (f_k - f_{k-1}). \tag{3.2.4}$$

Here the integral in Eq. (3.2.1) is approximated at the midpoint of each time interval with the derivative computed by central differences. The weights of integration decays temporally. Other cumulative methods differ by the choice of weights to improve accuracy or achieve higher order convergence.

Another common method for constructing the fractional order derivative is using the Grünwald-Letnikov (GL) derivative[222], which extends the standard finite difference definition for the derivative of functions. Using the definition from Scherer *et al.*[222], the GL derivative with corrections to match the Caputo derivative is

$$\mathrm{D}^\alpha_{n,\mathrm{GL}} f = \frac{1}{\Delta_t^\alpha} \left[f_n - \sum_{m=1}^{n} c_m^\alpha f_{n-m} \right] - \frac{t_n^{-\alpha}}{\Gamma(1-\alpha)} f_0, \tag{3.2.5}$$

where $C_m^\alpha = C_{m-1}^\alpha (1 - [\alpha + 1]/m)$, $C_1^\alpha = \alpha$, is the recursive definition of the real numbered binomial coefficient in the finite difference formula. Another example is

given by Diethelm *et al.*[50,51] where the trapezoidal rule was employed, i.e.

$$\begin{aligned} \mathrm{D}^{\alpha}_{n,D} f &= \left[\frac{\Delta_t^{-\alpha}}{\Gamma(2-\alpha)}\right] \sum_{m=0}^{n} a_{m,n} \left(f_{n-m} - \sum_{k=0}^{\lceil \alpha \rceil} \left[\frac{(n-m)^k \Delta_t^k}{k!}\right] f_0^{(k)} \right), \\ a_{m,n} &= \begin{cases} 1, & \text{if } m = 0, \\ (m+1)^{1-\alpha} - 2m^{1-\alpha} + (m-1)^{1-\alpha}, & \text{if } 0 < m < n, \\ (1-\alpha)n^{-\alpha} - n^{1-\alpha} + (n-1)^{1-\alpha}, & \text{if } m = n, \end{cases} \end{aligned} \tag{3.2.6}$$

where $a_{m,n}$ are the weights for the past values of f_n, and $f_0^{(k)}$ is the k-th derivative at 0. Richardson interpolation can also be used by selecting a subset for different size of Δ_t to improve accuracy. Gao *et al.*[69] developed a similar method for solving fractional diffusion equations, *i.e.*

$$\begin{aligned} \mathrm{D}^{\alpha}_{n,\mathrm{Gao}} f &= \frac{\Delta_t^{-\alpha}}{\Gamma(2-\alpha)} \left[a_0^{\alpha} f_n - \sum_{k=1}^{n-1} \left(a^{\alpha}_{k-i-1} - a^{\alpha}_{k-i} \right) f_i - a^{\alpha}_{k-1} f_0 \right], \\ a_i^{\alpha} &= (i+1)^{1-\alpha} - i^{1-\alpha}, \quad i \geq 1. \end{aligned} \tag{3.2.7}$$

Other cumulative methods have been presented by Murio *et al.*[178], Yang *et al.*[276] as well as Liu et al.[145], though many more have been published in the literature.

All the cumulative methods presented here require significant storage costs and have significant computational costs, especially for complex three dimensional tissue simulations. Storage/memory costs are typically $\mathcal{O}(N_T)$ and the computational complexity is often $\mathcal{O}(N_T^2)$, or by best reports $\mathcal{O}(N_T \log(N_T))$, due to the need to sum over the entire time domain. In contrasting, the computational cost of transient elasticity problems is independent of the number of time steps.

One strategy to cope with this limitation is to exploit the fact that the integration weights for numerical approximation of fractional derivatives exhibit a 'fading memory', where the weights tend to decay with the number of time steps (or length of time). Hence, some have proposed truncating the approximation, including only the last few weights. However, the accuracy of this approach is fundamentally dependent on the behavior of f and the fractional derivative order α. For example, the weights decay at slower rates for lower α values, requiring more and more terms to avoid inaccuracies due to truncation. More difficult is the dependence on the function f, which is not known *a priori* in computational simulations. A classic example is to consider a stress relaxation experiment, where an acute action occurring at the beginning of the experiment dictates the response over the entire time course.

Another strategy to reduce computational costs is by use of recursive methods. Such methods mostly follow a similar approach[287]. Namely, the Caputo derivative is first approximated using decaying exponentials (or, equivalently, a Prony-series). This ap-

proximation step is posited differently depending on the authors. However, a natural rationale for this approximation stems from the relationship between the relaxation spectrum of the Caputo derivative and decaying exponentials via the Laplace transform, i.e.

$$\frac{(t-s)^{-\alpha}}{\Gamma(1-\alpha)} = \int_0^\infty \left[\frac{\sin(\pi\alpha)z^{\alpha-1}}{\pi}\right] \exp[(s-t)z]\,\mathrm{d}z. \tag{3.2.8}$$

The integral above can be approximated by summation at a set of points z with the associated quadrature weights (in the bracketed term). Inserting into Eq. (3.2.1), we arrive at an equivalent form for a Prony-series comprised of decaying exponentials that can be recast as a series of ordinary differential equations (shown in the following section). One of the earlier works presenting a recursive method for approximating the Caputo derivative was by Yuan-Agarwal[280]. In this case, authors recast the integral based on the above and used Gauss-Laguerre quadrature for integration. Though they presented the idea in the context of a specific fractional differential equation, the idea was clearly generalizable.

The Yuan-Agrawal method has been critized for slow convergence for certain values of α. Investigation by Diethelm[53] found the integrand of the Yuan-Agrawal integrand method to be non-smooth at 0 for $\alpha \neq 1/2 + n$, contrary to the assumption made in the Gauss-Laguerre quadrature. This results in poor convergence for $\alpha \to 0$ and $\alpha \to \infty$. Instead, Diethelm suggested is his method[52] that Gauss-Laguerre be replaced by Gauss Jacobi integration by mapping the range of integration from $[0, \infty)$ to $[-1, 1]$ through a change of variables. Aiming for further improvements in the accuracy to these methods, Birk and Song[16] further extended the Diethelm method[52] by altering the mapping onto the $[-1, 1]$ interval and considering the Fourier transform of the fractional operator, showing generally comparable or superior results.

Although the quadrature scheme of these approaches covers the full range of frequency, this is not necessarily an advantage. The range of relevant frequencies can be limited based on the corresponding problem and by the size of Δ_t used for simulation. Moreover, as $\alpha \to 1$, the approximation must tend to approach the first order derivative, which becomes increasingly challenging to approximate. In the following sections, we expand on this Prony-based approach by formulating the error estimates, generalizing its form and proposing a new approach for optimizing parameters of the weights and time constants of the associated Prony series.

3.2.3 Prony approximation of the Caputo derivative

The Prony series approach has been used a number of times in literature[16,52,53,196,200,280]. Suppose that the fractional derivative can be approximated using N Maxwell elements in parallel, each with their own weight β_k and time constant τ_k $(k = 1 \dots N)$. Then a

Prony-based approximation $\hat{D}_t^\alpha f$ to $D_t^\alpha f$ can be written as,

$$\hat{D}_t^\alpha f := \beta_0 f'(t) + \sum_{k=1}^{N} \int_0^t \beta_k \exp\left[\frac{s-t}{\tau_k}\right] f'(s)\,\mathrm{d}s, \tag{3.2.9}$$

or equivalently as

$$\hat{D}_t^\alpha f := \beta_0 f'(t) + \sum_{k=1}^{N} q_k(t), \quad q_k'(t) + \frac{1}{\tau_k} q_k(t) = \beta_k f'(t), \tag{3.2.10}$$

where we introduce N intermediate variables q_k. While Eq. (3.2.9) requires further approximation of the integral over the time domain, Eq. (3.2.10) enables discretization of the intermediate variables q_k. Eq. (3.2.10) requires $2N+1$ parameters, $\boldsymbol{\theta}_\alpha = \{\tau_1, \ldots, \tau_N, \beta_0, \beta_1, \ldots, \beta_N\}$. The approximation error of equations (3.2.9) and (3.2.10) is shown in Lemma 1:

Lemma 1. *Let $f : [0,T] \to \mathbb{R}$ be a real function on the domain [0,T]. If $f'(0) < \infty$ and $f'' \in L^1(0,T)$, then*

$$(D_t^\alpha f - \hat{D}_t^\alpha f) = \varepsilon(t) f'(0) + \int_0^t \varepsilon(z) f''(t-z)\,\mathrm{d}z,$$

and for any $t \in [0,T]$

$$\left| D_t^\alpha f - \hat{D}_t^\alpha f \right| \leq \|\varepsilon\|_{0,\infty} \left[|f'(0)| + \|f''\|_{0,1} \right],$$

where the truncation error ε is defined as

$$\varepsilon(z) := \frac{z^{1-\alpha}}{\Gamma(2-\alpha)} - \beta_0 + \sum_{k=1}^{N} \beta_k \tau_k (\exp(-z/\tau_k) - 1). \tag{3.2.11}$$

Proof of Lemma 1 1. *Applying integration by parts to Eq.* (3.2.9)*, and the fundamental theorem of calculus to the leading first order derivative term, the Prony approximation to the fractional derivative can be re-written as,*

$$\hat{D}_t^\alpha f = \kappa(0,t) f'(0) + \int_0^t \kappa(s,t) f''(s) ds,$$

where $\kappa(s,t) = \beta_0 - \sum_{k=1}^{N} \beta_k \tau_k (\exp([s-t]/\tau_k) - 1)$. Subtracting this from Eq. (3.2.2)

leads to

$$\begin{aligned}(D_t^\alpha f - \hat{D}_t^\alpha f) &= \frac{1}{\Gamma(2-\alpha)}\left(t^{1-\alpha}f'(0) + \int_0^t (t-s)^{1-\alpha} f''(s)\,\mathrm{d}s\right) - \kappa(0,t)f'(0) - \\ &\quad \int_0^t \kappa(s,t) f''(s)\,\mathrm{d}s \\ &= \left(\frac{t^{1-\alpha}}{\Gamma(2-\alpha)} - \kappa(0,t)\right) f'(0) + \int_0^t \left(\frac{(t-s)^{1-\alpha}}{\Gamma(2-\alpha)} - \kappa(s,t)\right) f''(s)\,\mathrm{d}s \\ &= \left(\frac{t^{1-\alpha}}{\Gamma(2-\alpha)} - \kappa(0,t)\right) f'(0) + \int_0^t \left(\frac{z^{1-\alpha}}{\Gamma(2-\alpha)} - \kappa(0,z)\right) f''(t-z)\,\mathrm{d}z.\end{aligned}$$

We deduce that the error in the approximation can be written in terms of $\varepsilon(t) = t^{1-\alpha}/\Gamma(2-\alpha) - \kappa(0,t)$. *Hence,*

$$\begin{aligned}|D_t^\alpha f - \hat{D}_t^\alpha f| &= \left|\varepsilon(t)f'(0) + \int_0^t \varepsilon(z) f''(t-z)dz\right| \\ &\leq |\varepsilon(t)f'(0)| + \|\varepsilon\|_{0,\infty}\int_0^t |f''(t-z)|dz \\ &\leq \|\varepsilon\|_{0,\infty}\left[|f'(0)| + \|f''\|_{0,1}\right],\end{aligned}$$

where $\|\cdot\|_{0,\infty}$ *and* $\|\cdot\|_{0,1}$ *denote the* $L^\infty(0,T)$ *and* $L^1(0,T)$ *norms, respectively.*

Remark 1. *Assuming* $f'(0) = 0$ *and* $f'' \in L^2(0,T)$, *then*

$$\left|D_t^\alpha f - \hat{D}_t^\alpha f\right| \leq \|\varepsilon\|_0 \|f''\|_0,$$

where $\|\cdot\|_0$ *is the* $L^2(0,T)$ *norm.*

From Lemma 1, we observe that the error incurred, when re-writing the fractional derivative in terms of a finite series of Maxwell elements, is governed by ε as well as the behavior of the differentiated function f''. While for forward simulations in the time domain, the behavior of f is unknown, we can understand the impact of our approximation by directly evaluating ε over the time domain $(0,T)$.

3.2.4 Discrete Prony approximation of the Caputo derivative

The approximation shown in Eq. (3.2.10) lends itself to a straightforward discretized form by applying numerical updates to the intermediate variables q_k. We now approximate the first derivative using backward Euler and the integral term using a midpoint approximation, i.e.

$$\hat{\mathrm{D}}_n^\alpha f := \frac{\beta_0}{\Delta_t}\left(f^n - f^{n-1}\right) + \sum_{k=1}^N q_k^n, \quad q_k^n = e_k^2 q_k^{n-1} + e_k\beta_k\left(f^n - f^{n-1}\right), \tag{3.2.12}$$

where $e_k = \exp[-\Delta_t/(2\tau_k)]$. With this definition, we can examine the discretization error between the discrete operator $\hat{\mathrm{D}}_n^\alpha$ and its continuous counterpart $\hat{D}_t^\alpha$, as shown

in Lemma 2.

Lemma 2. *Let $f : [0,T] \to \mathbb{R}$ be a real function in the time domain [0,T] and let $f \in W^{3,\infty}(0,T)$. Assume the time interval $[0,T]$ is divided into equal divisions Δ_t, giving discrete time steps $\{t_1, \ldots, t_{N_T}\}$ with $t_k = k\Delta_t$ and $T = N_T\Delta_t$. The value $f^n = f(t_n)$ and the value q_k^n is our approximation to $q_k(t_n)$ based on Eq. (3.2.12). Here we assume $q_k^0 = q_k(0)$ for all $k = 1, \ldots, N$, and that $\beta_k, \tau_k \in \mathbb{R}^+$. Then for any $t_n \in \{t_1, \ldots t_N\}$*

$$|\hat{D}_{t_n}^{\alpha} f - \hat{\mathrm{D}}_n^{\alpha} f| \leq \Delta_t \left(\beta_0/2 + C(\boldsymbol{\beta}, \boldsymbol{\tau})\Delta_t\right) \|f\|_{W^{3,\infty}(0,T)},$$

where $C(\boldsymbol{\beta}, \boldsymbol{\tau}) > 0$ is a constant depending on the chosen β_k, τ_k for all $k = 1, \ldots, N$.

Proof of Lemma 2 2. *We start by manipulating the ordinary differential equation for q_k in Eq. (3.2.10). Applying an integration factor and integrating over a discrete time interval $[t_{n-1}, t_n]$, we can see that*

$$q_k(t_n) = \exp\left[-\frac{\Delta_t}{\tau_k}\right] q_k(t_{n-1}) + \int_{t_{n-1}}^{t_n} \beta_k \exp\left[\frac{s - t_n}{\tau_k}\right] f'(s)\, \mathrm{d}s.$$

Subtracting the discrete approximation shown in Eq. (3.2.12), we observe that

$$\begin{aligned}(q_k(t_n) - q_k^n) = &\exp\left[-\frac{\Delta_t}{\tau_k}\right] (q_k(t_{n-1}) - q_k^{n-1}) + \\ &\int_{t_{n-1}}^{t_n} \beta_k \exp\left[\frac{s - t_n}{\tau_k}\right] f'(s)\, \mathrm{d}s - e_k\beta_k \left(f^n - f^{n-1}\right).\end{aligned} \tag{3.2.13}$$

We recall the result that for $g \in W^{2,\infty}(0,T)$, one may derive the midpoint relation

$$\int_{t_{n-1}}^{t_n} g(s) - g(t_{n-\frac{1}{2}})\, \mathrm{d}s = \int_{t_{n-1}}^{t_n} \int_{t_{n-\frac{1}{2}}}^{s} (s - z) g''(z)\, \mathrm{d}z\, \mathrm{d}s, \tag{3.2.14}$$

as well as derive an inequality for the truncation error

$$\begin{aligned}\int_{t_{n-1}}^{t_n} g(s) - g(t_{n-\frac{1}{2}})\, \mathrm{d}s &= \int_{t_{n-\frac{1}{2}}}^{t_n} \int_{t_{n-\frac{1}{2}}}^{s} (s - z) g''(z)\, \mathrm{d}z\, \mathrm{d}s + \\ &\quad \int_{t_{n-1}}^{t_{n-\frac{1}{2}}} \int_{s}^{t_{n-\frac{1}{2}}} (z - s) g''(z)\, \mathrm{d}z\, \mathrm{d}s \\ &\leq \|g''\|_{L^\infty(t_{n-1}, t_n)} \left[\int_{t_{n-\frac{1}{2}}}^{t_n} \int_{t_{n-\frac{1}{2}}}^{s} |s - z|\, \mathrm{d}z\, \mathrm{d}s + \right. \\ &\quad \left. \int_{t_{n-1}}^{t_{n-\frac{1}{2}}} \int_{s}^{t_{n-\frac{1}{2}}} |z - s|\, \mathrm{d}z\, \mathrm{d}s \right] \\ &\leq \frac{\Delta_t^3}{24} \|g''\|_{L^\infty(t_{n-1}, t_n)}.\end{aligned}$$

Utilizing the midpoint relation, the second half of Eq. (3.2.13) *can be written as*

$$\begin{aligned}
&\int_{t_{n-1}}^{t_n} \beta_k \exp\left[\frac{s-t_n}{\tau_k}\right] f'(s)\,\mathrm{d}s - e_k\beta_k\left(f^n - f^{n-1}\right) \\
&\quad= \int_{t_{n-1}}^{t_n} \beta_k \exp\left[\frac{s-t_n}{\tau_k}\right] f'(s) - \beta_k e_k f'(t_{n-\frac{1}{2}})\,\mathrm{d}s - e_k\beta_k\left(f^n - f^{n-1} - \Delta_t f'(t_{n-\frac{1}{2}})\right) \\
&\quad= \int_{t_{n-1}}^{t_n} \beta_k \exp\left[\frac{s-t_n}{\tau_k}\right] f'(s) - \beta_k e_k f'(t_{n-\frac{1}{2}})\,\mathrm{d}s - e_k\beta_k \int_{t_{n-1}}^{t_n} f'(s) - f'(t_{n-\frac{1}{2}})\,\mathrm{d}s.
\end{aligned}$$

Note that each integral represents the truncation error of a midpoint approximation, i.e.

$$\begin{aligned}
&\left|\int_{t_{n-1}}^{t_n} \beta_k \exp\left[\frac{s-t_n}{\tau_k}\right] f'(s)\,\mathrm{d}s - e_k\beta_k\left(f^n - f^{n-1}\right)\right| \\
&\qquad\le \frac{\beta_k\Delta_t^3}{24}\left\|\left(\exp\left[\frac{s-t_n}{\tau_k}\right] f'(s)\right)''\right\|_{L^\infty(t_{n-1},t_n)} + \frac{e_k\beta_k\Delta_t^3}{24}\left\|f'''\right\|_{L^\infty(t_{n-1},t_n)} \\
&\qquad\le \frac{\beta_k\Delta_t^3}{24}\left(\frac{1}{\tau_k^2}\|f'\|_{L^\infty(t_{n-1},t_n)} + \frac{2}{\tau_k}\|f''\|_{L^\infty(t_{n-1},t_n)} + (1+e_k)\|f'''\|_{L^\infty(t_{n-1},t_n)}\right) \\
&\qquad\le \Delta_t^3 C_0(\beta_k,\tau_k)\|f\|_{W^{3,\infty}(t_{n-1},t_n)},
\end{aligned}$$

where $C_0(\beta_k,\tau_k) = (\beta_k/24)\max\{\tau_k^{-2},\tau_k^{-1},(1+e_k)\}$. *Inserting the truncation error into Eq.* (3.2.13), *we can see that*

$$\begin{aligned}
|q_k(t_n) - q_k^n| &\le e_k^2|q_k(t_{n-1}) - q_k^{n-1}| + \\
&\qquad \left|\int_{t_{n-1}}^{t_n} \beta_k \exp\left[\frac{s-t_n}{\tau_k}\right] f'(s)ds - e_k\beta_k\left(f^n - f^{n-1}\right)\right| \\
&\le e_k^2|q_k(t_{n-1}) - q_k^{n-1}| + \Delta_t^3 C_0(\beta_k,\tau_k)\|f\|_{W^{3,\infty}(t_{n-1},t_n)} \\
&\le e_k^2|q_k(0) - q_k^0| + C_0(\beta_k,\tau_k)\Delta_t^3\sum_{k=1}^{n}\|f\|_{W^{3,\infty}(t_{k-1},t_k)} \\
&\le C_0(\beta_k,\tau_k)T\Delta_t^2\|f\|_{W^{3,\infty}(0,T)},
\end{aligned}$$

making the update formula for q_k $\mathcal{O}(\Delta_t^2)$. *Subtracting the definition of* $\hat{D}_{t_n}^\alpha$ *from* $\hat{D}_n^\alpha$,

we can see that

$$\begin{aligned}
|\hat{D}^{\alpha}_{t_n} f - \hat{D}^{\alpha}_{n} f| &= \left| \beta_0 \left(f'(t_n) - \Delta_t^{-1}(f^n - f^{n-1}) \right) + \sum_{k=1}^{N} \left(q_k(t_n) - q_k^n \right) \right| \\
&\leq \beta_0 |f'(t_n) - \Delta_t^{-1}(f^n - f^{n-1})| + \sum_{k=1}^{N} |q_k(t_n) - q_k^n| \\
&\leq \beta_0 \left| \frac{1}{\Delta_t} \int_{t_{n-1}}^{t_n} (s - t_{n-1}) f''(s) ds \right| + C(\boldsymbol{\beta}, \boldsymbol{\tau}) \Delta_t^2 \|f\|_{W^{3,\infty}(0,T)} \\
&\leq \frac{\beta_0 \Delta_t}{2} \|f''\|_{L^{\infty}(t_{n-1}, t_n)} + C(\boldsymbol{\beta}, \boldsymbol{\tau}) \Delta_t^2 \|f\|_{W^{3,\infty}(0,T)}, \qquad (3.2.15)
\end{aligned}$$

where $C(\boldsymbol{\beta}, \boldsymbol{\tau}) = \sum_{k=1}^{N} C_0(\beta_k, \tau_k)$. *Generalizing for any time point completes the proof.*

From Lemma 2 we observe the typical discretization errors expected for backward Euler and midpoint based error estimates. The result shows that the discrete approximation converges to the approximate Prony series approximation with $\mathcal{O}(\Delta_t)$. Using backward Euler for the first-order derivative term is not necessary, and higher-order approximations could easily be used in Eq. (3.2.12). Here we select this form for ease and, in the context of biomechanics simulations, for stability considerations. Combining Lemmas 1 and 2, we can derive an error estimate for this Prony series-based approximation in Theorem 3.

Theorem 3. *Given the assumptions of Lemma 2, the error between* $\hat{\mathrm{D}}^{\alpha}_{n} f$ *and* $D^{\alpha}_{t_n} f$ *for any* $t_n \in \{t_1, \ldots, t_{N_T}\}$ *is given by*

$$|\hat{\mathrm{D}}^{\alpha}_{n} f - D^{\alpha}_{t_n} f| \leq \|\epsilon\|_{0,\infty} \left[|f'(0)| + \|f''\|_{0,1} \right] + \Delta_t \left(\beta_0/2 + C(\boldsymbol{\beta}, \boldsymbol{\tau}) \Delta_t \right) \|f\|_{W^{3,\infty}(0,T)}.$$

Proof of Theorem 3 1. *This is a straightforward result of the triangle inequality, Lemma 1 and 2.*

Based on this error estimate, we can see that a refinement with Δ_t eliminates the portion of error responsible for discretization, while the appropriate selection of the positive constants used in Eq. (3.2.12) can reduce the Prony approximation error given by the truncation ε (as we will later show). We note that decreasing Δ_t will eventually lead to a plateau in the error convergence based on how well the Prony series approximates the true fractional derivative. However, increasing the number of Prony terms N elicits a more complex response. For large Δ_t, the error can become dependent on the second term in Theorem 3 and, thus, the constant $C(\boldsymbol{\beta}, \boldsymbol{\tau})$. This constant, in general, grows with more Prony terms and can have truncation scale factors that grow larger with larger N. However, for sufficiently fine Δ_t, increasing the number of terms shifts the error onto ε and thus improves like the truncation error.

3.2.5 Optimizing the Numerical approximation $\hat{D}_t^\alpha$

The approximation introduced in Eq. (3.2.9) relies on the effective identification of the parameters $\boldsymbol{\theta}_\alpha$ that should be chosen to ensure optimal accuracy. Ideally, $\boldsymbol{\theta}_\alpha$ would be selected so as to minimize the error between the true Caputo derivative and the approximation in some suitable norm. For example, if we consider the $L^2(0,T)$ norm, then we would seek to minimize the squared error

$$F(f,\boldsymbol{\theta}_\alpha) = \frac{1}{2}\int_0^T [\hat{D}_t^\alpha f - D_t^\alpha f]^2 \ \mathrm{d}t, \tag{3.2.16}$$

where $F(f,\boldsymbol{\theta}_\alpha)$ gives the squared L^2-norm error between the approximate and the true Caputo derivatives for the given function f and set of parameters $\boldsymbol{\theta}_\alpha$. While the parameters $\boldsymbol{\theta}_\alpha$ could be chosen to minimize $F(f,\boldsymbol{\theta}_\alpha)$ this approach presents challenges as we often do not know f prior to simulation. Hence, instead, we must select our approximation to be suitably valid for all f, *i.e.* we find $\boldsymbol{\theta}_\alpha$ such that (for $0<\alpha<1$),

$$F(f,\boldsymbol{\theta}_\alpha,\alpha) := \left\{\min F(f,\boldsymbol{\varphi},\alpha),\ \boldsymbol{\varphi}\in\mathbb{R}^{2N+1}\right\}, \quad \text{for any } f\in L^\infty(0,T). \tag{3.2.17}$$

The problem posed in Eq. (3.2.17) is generally challenging to solve due to the flexibility in the behavior of f. In order to approximately minimize F, suppose we instead consider only those functions $f\in\mathcal{F}(M)$ where

$$\mathcal{F}(M) = \left\{ f\in L^2(0,T) \;\middle|\; f(t) = \mathrm{Re}\left\{\textstyle\sum_{k=1}^M C_k\exp(i\omega_k t)\right\},\ \text{for some } C_0,\dots,C_M\in\mathbb{E}\right\} \tag{3.2.18}$$

represents the set of functions that can be written using a Fourier basis[250]. Here we note that $\omega_k = k\omega^\star$, where $\omega^\star = 2\pi/T$ is the base frequency of f on the time interval $[0,T]$. In this context, our function f and its fractional derivative (for $t>>0$) can be written as

$$f(t) = \mathrm{Re}\left\{\sum_{k=1}^M C_k\exp(i\omega_k t)\right\}, \quad D_t^\alpha f(t) \approx \mathrm{Re}\left\{\sum_{k=1}^M C_k(i\omega_k)^\alpha\exp(i\omega_k t)\right\}. \tag{3.2.19}$$

In contrast, the approximate fractional derivative $\hat{D}_t^\alpha$ based on Eq. (3.2.9) can be written as,

$$\hat{D}_t^\alpha f(t) = \mathrm{Re}\left\{\sum_{k=1}^M C_k\left(\beta_0 i\omega_k + \sum_{m=1}^N \beta_m(\tau_m\omega_k)\frac{(\tau_m\omega_k+i)}{(\tau_m\omega_k)^2+1}\right)\exp\{i\omega_k t\}\right\}. \tag{3.2.20}$$

The difference between the true and approximate operators is then simply,

$$\hat{D}_t^\alpha f(t) - D_t^\alpha f(t) \approx \mathrm{Re}\left\{\sum_{k=1}^M C_k\exp(i\omega_k t)\left[\beta_0 i\omega_k + \sum_{m=1}^N \beta_m(\tau_m\omega_k)\frac{(\tau_m\omega_k+i)}{(\tau_m\omega_k)^2+1} - (i\omega_k)^\alpha\right]\right\}, \tag{3.2.21}$$

leaving the operator error dependent on the size of the complex number given in the brackets. This means that for us to obtain a good approximation for any $f \in \mathcal{F}(M)$, we must choose $\boldsymbol{\theta}_\alpha$ such that we minimize the bracketed term. Hence, we may reduce the minimization problem in Eq. (3.2.17) to an analogous normalised system where

$$\frac{1}{k^\alpha}\sum_{m=1}^{N}\hat{\beta}_m\frac{(k\hat{\tau}_m)^2}{(k\hat{\tau}_m)^2+1}=\cos\left(\frac{\pi\alpha}{2}\right),\quad \hat{\beta}_0k^{1-\alpha}-\frac{1}{k^\alpha}\sum_{m=1}^{N}\hat{\beta}_m\frac{k\hat{\tau}_m}{(k\hat{\tau}_m)^2+1}=\sin\left(\frac{\pi\alpha}{2}\right), \tag{3.2.22}$$

for $k = 1, \dots M$. Here, we note that parameters were normalized (with hats) to enable independence from the base frequency $\omega^\star$, with $\beta_0 = \hat{\beta}_0(\omega^\star)^{\alpha-1}$, $\beta_m = \hat{\beta}_m(\omega^\star)^\alpha$ and $\tau_m = \hat{\tau}_m/\omega^\star$ $(m = 1, \dots N)$. This leads to $2M$ constraint equations that, if hold, imply equivalence of the true and approximate Caputo derivative. Assuming that our function is composed of many more Fourier terms than the number of Prony terms (i.e. $M >> N$), Eq. (3.2.22) leads to a nonlinear over-constrained system that can be solved by optimization.

3.2.6 Numerical implementation

Resulting parameters for approximating different fractional derivatives can be found in the MATLAB[163] codes provided as supplementary material. Here optimized parameters can be returned for values of $N \in [3, 15]$ and $\alpha \in [0, 1]$ for a specified base frequency $\omega^\star$. Codes and examples are also provided showing how the approximation can be utilized for approximating the Caputo derivative. Other methods, such as the midpoint (MP) or Grünwald-Letnikov (GL) approximations, are also provided.

3.3 Large Deformation Viscoelastic Solid Mechanics

3.3.1 Review of kinematics and kinetics

In this section, we briefly review the kinematics and kinetics for hyperelastic materials. Let $\Omega_0 \subset \mathbb{R}^3$ denote the reference configuration of a three-dimensional solid (coordinates $\boldsymbol{X}$) and Γ_0 denote its boundary. The boundary is split into groups $\Gamma_0 = \Gamma_0^N \cup \Gamma_0^D$ based on either loading (subscript N) or displacement boundary conditions are applied (subscript D). Over a time interval $t \in [0, T]$, its configuration is $\Omega(t) \subset \mathbb{R}^3$, with physical coordinates $\boldsymbol{x}$. The coordinates are related by

$$\boldsymbol{x}(t) = \boldsymbol{u}(t) + \boldsymbol{X}, \qquad x_i(t) = u_i(t) + X_i. \tag{3.3.1}$$

This mapping in Eq. (3.3.1) is assumed to be bijective with $\boldsymbol{u} : \Omega_0 \times [0, T] \to \mathbb{R}^3$ denoting the material displacements. Note that $\boldsymbol{X}$ and $\boldsymbol{x}$ are the vector positions, with components X_i and x_i. The local deformation gradient $\boldsymbol{F}$ defines the local mapping of

infinitesimal vectors, which is given by

$$\boldsymbol{F} = \frac{\partial \boldsymbol{x}}{\partial \boldsymbol{X}} = \frac{\partial \boldsymbol{u}}{\partial \boldsymbol{X}} + \boldsymbol{I}, \qquad F_{ij} = \frac{\partial u_i}{\partial X_j} + \delta_{ij},$$

where $\boldsymbol{I}$ is the identity tensor. The determinant $J = \det \boldsymbol{F}$ defines the relative change in volumes, providing key information about material growth / decay. The right and left Cauchy-Green tensors[133], defining the material stretch, are

$$\boldsymbol{C} = \boldsymbol{F}^T \boldsymbol{F}, \qquad \boldsymbol{B} = \boldsymbol{F}\boldsymbol{F}^T.$$

The deformation gradient and the left and right Cauchy-Green tensors comprise a common set of measures used to characterize the constitutive behavior of a material. For a hyperelastic material, the strain-energy density function is given by $\Psi = \Psi(\boldsymbol{C})$, which defines the stored energy resulting from material deformations. From the second law of thermodynamics, the strain-energy function can be related to the second Piola-Kirchhoff stress tensor (PK2) as

$$\boldsymbol{S} = 2\frac{\partial \Psi(\boldsymbol{C})}{\partial \boldsymbol{C}}, \qquad S_{ij} = 2\frac{\partial \Psi(C_{ij})}{\partial C_{ij}}, \tag{3.3.2}$$

which, in turn, is related to the first Piola-Kirchhoff and Cauchy stress tensors ($\boldsymbol{P}$ and $\boldsymbol{\sigma}$, respectively) by push forward operations on PK2. In this case,

$$\boldsymbol{\sigma} = \frac{1}{J}\boldsymbol{F}\boldsymbol{S}\boldsymbol{F}^T = \frac{1}{J}\boldsymbol{P}\boldsymbol{F}^T. \tag{3.3.3}$$

For isotropic biomechanical materials, the strain-energy function is often defined using invariants of $\boldsymbol{C}$[19],

$$I = \boldsymbol{C} : \boldsymbol{I}, \quad II = \boldsymbol{C} : \boldsymbol{C}, \quad III = \det \boldsymbol{C} \tag{3.3.4}$$

with $\Psi = \Psi(I, II, III)$. For incompressible materials, the third invariant III is constrained to 1 by splitting the strain-energy function into a deviatoric (Ψ_d) and a volumetric components with $\Psi = \Psi_d + p(III^{1/2} - 1)$, where $p : \Omega \times [0, T] \to \mathbb{R}$ denotes the hydrostatic pressure. Often the strain-energy function takes exponential forms, as seen in the Fung model[67]. However, with many tissues exhibiting anisotropic material response[106], additional invariants have been introduced to denote stretch with respect to specific microstructural directions. These laws can be naturally extended, but for the purposes of this work, we will focus on more simple isotropic forms.

3.3.2 Extension of hyperelastic to viscoelastic models

For constitutive modeling of viscoelastic behavior, a number of model approaches have been presented in the literature. Fig. 3.3.1 illustrates some of the common models introduced, particularly for linear viscoelastic materials, using spring, dashpot or spring-pot elements. Extension of these forms toward nonlinear material models has become more

common, with models following the analogy presented in Fig. 3.3.1. For example, a nonlinear viscoelastic Maxwell model (Fig. 3.3.1A) could be written as

$$\boldsymbol{S} + \frac{\eta_1}{E_1}\dot{\boldsymbol{S}} = \eta_1 \dot{\boldsymbol{S}}_v \tag{3.3.5}$$

and the nonlinear viscoelastic Kelvin-Voigt model (Fig. 3.3.1B) as,

$$\boldsymbol{S} = E_0 \boldsymbol{S}_e + \eta_1 \dot{\boldsymbol{S}}_v. \tag{3.3.6}$$

Here $\boldsymbol{S}_e$ denotes a symmetric tensor denoting the hyperelastic response of the material, while $\boldsymbol{S}_v$ denotes the viscoelastic response. Note that these stresses denote the non-hydrostatic components, which can be included based on the application. Commonly, both take a similar form to hyperelastic materials commonly encountered in the literature. These models provide an exponential decay in the viscoelastic phenomena, which can yield viscoelastic response times that are incompatible with experimental data. Other formulations, such as introduced by Schapery et al.[221], provide a more generalized view for characterizing material response. Another example is the model developed by Freed and Diethelm[63], i.e.

$$\boldsymbol{S}(t) = \left(\mu_\infty + (\mu_0 - \mu_\infty)\right) G(t) \frac{\partial \Psi(\boldsymbol{E})}{\partial \boldsymbol{E}} + (\mu_0 - \mu_\infty) \int_0^t M(t-s) \frac{\partial \Psi(\boldsymbol{E})}{\partial \boldsymbol{E}} \, \mathrm{d}s, \tag{3.3.7}$$

where $G(t)$ is a relaxation function and $M(t)$ is a memory function for the history dependency.

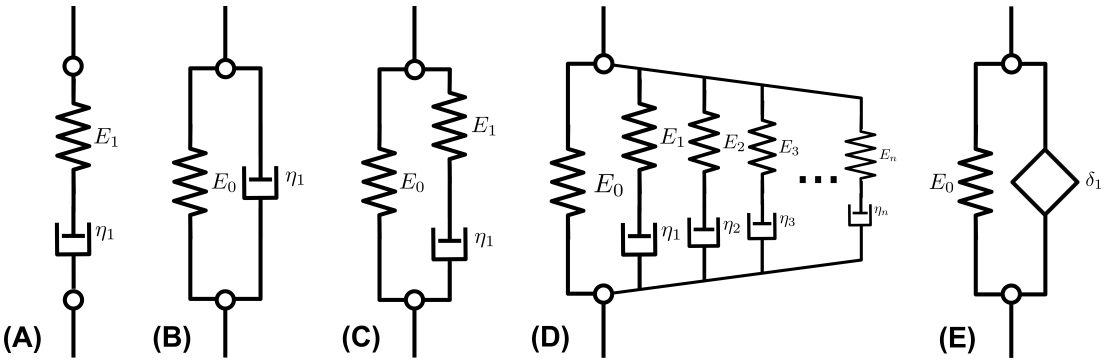

Figure 3.3.1 *Illustration of spring, dashpot and spring-pot elements used to compose viscoelastic models. Examples include the A) Maxwell, B) Kelvin Voigt, C) Standard Linear, D) Generalized Maxwell and E) Fractional Kelvin-Voigt models.*

An alternative approach, that has been successful in the experimental literature, is use of fractional elements[103,154]. This is due to the progressive memory that these models exhibit that follows a power spectrum commonly observed in biological tissues for moderate frequencies. In this case, we can envision development of nonlinear fractional viscoelastic models, such as the fractional Kelvin Voigt model (Fig. 3.3.1E), *e.g.*

$$\boldsymbol{S} = \boldsymbol{S}_e + D_t^\alpha \boldsymbol{S}_v. \tag{3.3.8}$$

Here $\alpha = 0$ reduces to a pure elastic response and $\alpha = 1$ converts the latter part of the equation to a purely viscous-like response. The advantage of this approach is the generality of its application and ability to capture the dynamic viscoelastic behavior of tissues with the addition of the fractional differential operator.

3.3.3 Conservation of mass and momentum

With an appropriately defined constitutive model, the conservation of mass and momentum for an incompressible solid material is given by[106],

$$\begin{aligned} \partial_t(\rho J \boldsymbol{v}) - \nabla_{\boldsymbol{X}} \cdot (\boldsymbol{F}\boldsymbol{S}) &= J\boldsymbol{b}, \quad \text{in } \Omega_0 \times [0,T], && (3.3.9) \\ J - 1 &= 0, \quad \text{in } \Omega_0 \times [0,T], && (3.3.10) \end{aligned}$$

where ∂_t is the Lagrangian derivative (taken with respect to fixed coordinates $\boldsymbol{X}$), ρ is the material density, $\boldsymbol{v} = \partial_t \boldsymbol{u}$ is the material velocity, and $[0,T]$ is the time interval of interest. The mechanical system is then subject to an initial condition and boundary conditions, e.g.

$$\begin{aligned} \boldsymbol{u}(\cdot,0) = \boldsymbol{u}_0, \qquad \boldsymbol{v}(\cdot,0) = \boldsymbol{v}_0 \quad \text{in } \Omega_0, && (3.3.11) \\ \boldsymbol{v}(\cdot,t) = \boldsymbol{v}_D, \quad \text{on } \Gamma_0^D \times [0,T], \qquad (\boldsymbol{F}\boldsymbol{S}) \cdot \boldsymbol{N} = \boldsymbol{t}_N \quad \text{on } \Gamma_0^N \times [0,T], && (3.3.12) \end{aligned}$$

where $\boldsymbol{u}_0, \boldsymbol{v}_0 : \Omega_0 \to \mathbb{R}^3$ are given initial conditions, $\boldsymbol{v}_D : \Gamma_0^D \to \mathbb{R}^3$ given information about the rate of deformation on the boundary Γ_0^D, and $\boldsymbol{t}_N : \Gamma_0^N \to \mathbb{R}^3$ is given information about the applied traction on boundary Γ_0^N. All examples considered herein assume that no history of deformation is present in the material for $t < 0$ (e.g., the fractional derivative is defined w.r.t. $t = 0$).

3.4 Finite Element Approximation for Viscoelastic Solid Models

This section reviews the integration of the nonlinear fractional viscoelastic model into a finite element solid mechanics framework. For development and discretization of the weakform system, we follow the typical mixed finite element $\boldsymbol{u} - p$ formulation[113,284] (section 3.4.1) and extend it to account for the discrete fractional order model (section 3.4.2). A summary of the implementation steps is provided in section 3.4.3. The linearized system is introduced in section 3.4.4, and stability estimates are proven for the discrete problem.

3.4.1 Continuous and Discrete Weakform System

The weak formulation for the mechanical system follows the typical procedure. Multiplying Eqs. (3.3.9)-(3.3.10) by test functions $\boldsymbol{w}$ and q, respectively, integrating and applying integration by parts, the weak problem can be written as: find $(\boldsymbol{u}(t), \boldsymbol{v}(t), p(t)) \in$

$\boldsymbol{\mathcal{U}} \times \boldsymbol{\mathcal{V}}_D \times \mathcal{P}$ such that,

$$(\partial_t(\rho \boldsymbol{v} J), \boldsymbol{y}) + (\boldsymbol{F}\boldsymbol{S}, \nabla_{\boldsymbol{X}} \boldsymbol{y}) - \left\langle \boldsymbol{t}_N, \boldsymbol{y} \right\rangle - (J\boldsymbol{b}, \boldsymbol{y}) + (q, J-1) + (\boldsymbol{v} - \partial_t \boldsymbol{u}, \boldsymbol{w}) = 0, \quad (3.4.1)$$

for all $(\boldsymbol{w}, \boldsymbol{y}, q) \in \boldsymbol{\mathcal{U}} \times \boldsymbol{\mathcal{V}}_0 \times \mathcal{P}$ and all times $t \in [0, T]$. Here, $\boldsymbol{\mathcal{U}}$, $\boldsymbol{\mathcal{V}}$ and $\mathcal{P}$ denote appropriate spaces[7], their subscripts D and 0 denote spaces equipped with appropriate Dirichlet or zero Dirichlet conditions on Γ_0^D, and the operators $(\cdot, \cdot)$ and $\left\langle \cdot, \cdot \right\rangle$ denote the inner products on Ω_0 and Γ_0^N, respectively.

A discrete-in-time discretization of Eq. (3.4.1) can be considered using Backward Euler for temporal derivative approximations. Here we define a series of time steps $\{t_n\}_{n=0}^{N_T}$ (as seen in section 3.2.2), and letting superscript n denote a variable quantity at time t_n, and define the Backward temporal operator, $\delta_t f^n = (f^n - f^{n-1})/\Delta_t$. Defining appropriate inf-sup compatible discrete spaces, denoted with the subscript h (in later results, we use $\mathbb{Q}^2 - \mathbb{Q}^2 - \mathbb{Q}^1$ Taylor-Hood elements[23]), the discrete weak form of Eq. (3.4.1) can be written as: find $(\boldsymbol{u}_h^n, \boldsymbol{v}_h^n, p_h^n) \in \boldsymbol{\mathcal{U}}^h \times \boldsymbol{\mathcal{V}}_D^h \times \mathcal{P}^h$ such that,

$$(\delta_t(\rho \boldsymbol{v}_h^n J^n), \boldsymbol{y}_h) + (\boldsymbol{F}^n \boldsymbol{S}^n, \nabla_{\boldsymbol{X}} \boldsymbol{y}_h) - \left\langle \boldsymbol{t}_N, \boldsymbol{y}_h \right\rangle + (q_h, J^n - 1) - (J^n \boldsymbol{b}^n, \boldsymbol{y}_h) + (\boldsymbol{v}_h^n - \delta_t \boldsymbol{u}_h^n, \boldsymbol{w}_h) = 0, \quad (3.4.2)$$

for all $(\boldsymbol{w}_h, \boldsymbol{y}_h, q_h) \in \boldsymbol{\mathcal{U}}^h \times \boldsymbol{\mathcal{V}}_0^h \times \mathcal{P}^h$ and all $n = 1, \dots N_T$. We note that, under the scheme presented, the solution for $\boldsymbol{u}_h^n$ can be implicitly defined based on $\boldsymbol{v}_h^n$ as

$$\boldsymbol{v}_h^n = \delta_t \boldsymbol{u}_h^n$$

at node points.

3.4.2 Stress Discretization and Integration with the Prony Approximation

Evaluation of the discrete finite element equation in Eq. (3.4.2) follows the typical procedure applied in mechanics. Namely, the weighted residual equations are evaluated using an appropriate form of quadrature based on the element type and computational complexity of the integrand. In the context of fractional viscoelastic models, as introduced in section 3.3.2, the only additional challenge is determining a scheme for handling the viscoelastic stress tensor. Using the prony approximation introduced in Eq. (3.2.12), the fractional Kelvin-Voigt model can be written as,

$$\boldsymbol{S}^n = \boldsymbol{S}_e^n + \beta_0 \delta_t \boldsymbol{S}_v^n + \sum_{k=1}^{N} \boldsymbol{Q}_k^n + p_h^n \boldsymbol{S}_p^n, \quad (3.4.3)$$

where $\boldsymbol{S}_e^n = \boldsymbol{S}_e(\boldsymbol{C}^n)$, $\boldsymbol{S}_v^n = \boldsymbol{S}_v(\boldsymbol{C}^n)$, $\boldsymbol{S}_p^n = J^n[\boldsymbol{C}^n]^{-1}$ and $\boldsymbol{Q}_k^n$ is defined by the update formula,

$$\boldsymbol{Q}_k^n = e_k^2 \boldsymbol{Q}_k^{n-1} + \beta_k e_k \Delta_t \delta_t \boldsymbol{S}_v^n.$$

The approximation for the current value of the second Piola Kirchhoff stress given in Eq. (3.4.3) introduces the intermediate variables, $\boldsymbol{Q}_k$, representing the evolution of the material history due to different Prony terms. Within a finite element discretization, Eq. (3.4.3) could be realized weakly, interpolating $\boldsymbol{Q}_k$ using basis functions. However, this form does not ensure equivalence to the original form observed in Eq. (3.4.2). Instead, the values of $\boldsymbol{Q}_k$ are *discretized* at quadrature points where the residual equation (and, consequently, the stress) must be evaluated. Fig. 3.4.1 illustrates this strategy for $\mathbb{P}^2 - \mathbb{P}^1$ mixed-problem set on triangles using an appropriate quadrature rule[150]. In Fig. 3.4.1B we see the mixed element showing node points for displacement and pressure and in Fig. 3.4.1C the quadrature points at which values of $\boldsymbol{Q}_k$ are stored.

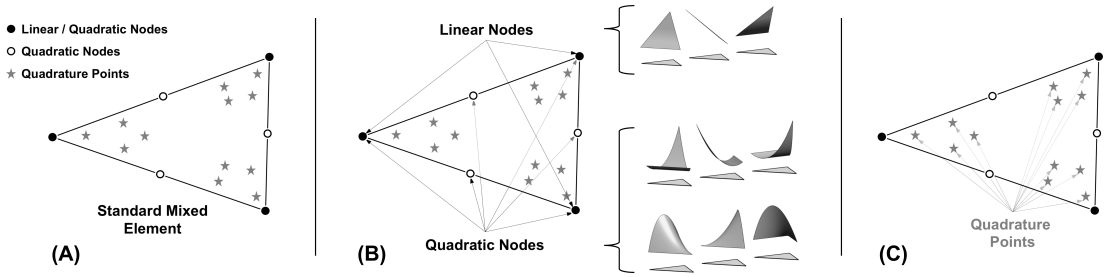

Figure 3.4.1 *Illustration of element level discretization for fractional viscoelasticity. (A) View of standard mixed $\mathbb{P}^2 - \mathbb{P}^1$ triangular finite element scheme and a corresponding quadrature set. (B) Selection of nodes for linear and quadratic triangle along with the corresponding nodal Lagrange basis functions. (C) Selection of quadrature used to approximate the viscoelastic intermediate variables, $\boldsymbol{Q}$.*

For practical implementation purposes, it is convenient to re-arrange Eq. (3.4.3) to consolidate terms based on their dependence on the current time step and past time step, *e.g.*

$$\boldsymbol{S}^n = \boldsymbol{S}_e^n + \gamma \boldsymbol{S}_v^n + p_h^n \boldsymbol{S}_p^n - \gamma \boldsymbol{S}_v^{n-1} + \sum_{k=1}^{N} e_k^2 \boldsymbol{Q}_k^{n-1}, \tag{3.4.4}$$

where $\gamma = \beta_0/\Delta_t + \sum_{k=1}^{N} \beta_k e_k$. From Eq. (3.4.4), the first three terms depend on n while the later two terms depend on variables at $n-1$. As a result, to iteratively solve Eq. (3.4.2), one needs to evaluate the last two terms once per time step. While the first three terms vary at each iteration, the complexity of computing these terms over a standard hyperelastic formulation is the addition of $\gamma \boldsymbol{S}_v^n$.

3.4.3 Solution procedure

The computational model framework presented was implemented into $\mathcal{C}$**heart**[138], a custom multiphysics finite element solver. The solution procedure follows the Shamanskii-Newton-Raphson (SNR) method[226] shown in Algorithm 1. Due to the formulation devised in section 3.4.1, the final linearized system is written for variables $\boldsymbol{v}_h^n$ and p_h^n with the current displacement calculated as discussed previously. In this case, our

residual functional can be written as,

$$R(\boldsymbol{v}_h^n, p_h^n; \boldsymbol{w}_h, q_h) := (\rho\delta_t(\boldsymbol{v}_h^n J^n), \boldsymbol{w}_h) + (\boldsymbol{F}^n \boldsymbol{S}^n, \nabla_{\boldsymbol{X}} \boldsymbol{w}_h) - \\ \langle \boldsymbol{t}_N, \boldsymbol{w}_h \rangle + (q_h, J^n - 1) - (J^n \boldsymbol{b}^n, \boldsymbol{w}_h). \tag{3.4.5}$$

Owing to the fact that $\boldsymbol{v}_h^n$ can be expressed as the weighted sum of vector basis functions (and similar for p_h^n, but using scalar basis functions), Eq. (3.4.5) can be written as

$$R(X^n; Y) = R(\Phi_{\boldsymbol{v}} V^n, \Phi_p P^n; \Phi_{\boldsymbol{v}} W, \Phi_p Q)$$

where $X^n = (V^n, P^n)$ denotes the coefficients of our solution and $Y = (W, Q)$ the weights of our test functions. Finally, the vector residual function can be expressed as the gradient with respect to Y, *e.g.*

$$\boldsymbol{R}(U^n) = \nabla_Y R(U^n, Y) = \boldsymbol{0}. \tag{3.4.6}$$

Algorithm 1 `Viscoelastic Mechanics Algorithm.`

Given initial condition X^0 (and $\boldsymbol{Q}^0$ at all quadrature points).
`Compute` $\boldsymbol{J}_\beta = \nabla_X \boldsymbol{R}(X^0)$, $[\boldsymbol{J}_\beta]^{-1}$.

for $(n = 1 : N)$ **do**

  `Set` $X^{n,0} = X^{n-1}$.
  `Compute` $\boldsymbol{R}(X^{n,0})$.
  `Compute` $r = \|\boldsymbol{R}(X^{n,0})\|$.
  `Set` $k = 0$.

  while $(r > TOL)$ **do**

    `Compute` $\delta X = -[\boldsymbol{J}_\beta]^{-1} \boldsymbol{R}(X^{n,k})$.
    `Find` $\min_{\alpha\in[0,1]} \|\boldsymbol{R}(X^{n,k} + \alpha\, \delta X)\|$.
    `Set` $X^{n,k+1} = X^{n,k} + \alpha\, \delta X$.
    if $(\|\boldsymbol{R}(X^{n,k+1})\| > \gamma\, r$ or $k > ITER)$ **then**
      `Compute` $\boldsymbol{J}_\beta = \nabla_X \boldsymbol{R}(X^{n,k+1})$, $[\boldsymbol{J}_\beta]^{-1}$.
    `Compute` $r = \|\boldsymbol{R}(X^{n,k+1})\|$.
    `Set` $k = k + 1$.
  `Update` $\boldsymbol{Q}^n = e_k^2 \boldsymbol{Q}_k^{n-1} + \beta_k e_k \Delta_t \delta_t \boldsymbol{S}_v^n$ at quadrature points.

3.4.4 Stability of the Discrete Weak form System

In this section, stability is analyzed for linear incompressible fractional viscoelastic materials shown in Eq. (3.4.7) and (3.4.7). The problem depends on parameters $\rho, E, \eta \in \mathbb{R}^+$ which, for ease, we take as positive spatiotemporal constants denoting the material density, elastic stiffness and fractional viscoelastic stiffness, respectively. Here $\boldsymbol{b}$ denotes body forces and $\boldsymbol{u}_0$ and $\boldsymbol{v}_0$ are given initial conditions. All examples

considered herein assume that no history of deformation (*e.g.* the fractional derivative is defined w.r.t. $t = 0$).

$$\rho\partial_t(\boldsymbol{v}) - \nabla_{\boldsymbol{X}} \cdot \boldsymbol{\Sigma} = \boldsymbol{b}, \qquad \text{in } \Omega_0 \tag{3.4.7}$$

$$\nabla_{\boldsymbol{X}} \cdot \boldsymbol{v} = 0, \qquad \text{in } \Omega_0 \tag{3.4.8}$$

$$\boldsymbol{u}(\cdot, 0) = \boldsymbol{u}_0, \qquad \boldsymbol{v}(\cdot, 0) = \boldsymbol{v}_0, \qquad \text{in } \Omega_0 \tag{3.4.9}$$

$$\boldsymbol{v} = \boldsymbol{0} \qquad \text{on } \Gamma_0^D, \quad \boldsymbol{\Sigma} \cdot \boldsymbol{N} = \boldsymbol{0}, \qquad \text{on } \Gamma_0^N \tag{3.4.10}$$

The constitutive model for the linear elastic material is given by

$$\boldsymbol{\Sigma} = E\boldsymbol{D}\boldsymbol{u} + \eta D_t^\alpha(\boldsymbol{D}\boldsymbol{u}) + p\boldsymbol{I}. \tag{3.4.11}$$

with $\boldsymbol{D}(\cdot) = \frac{1}{2}\left(\nabla_{\boldsymbol{X}}(\cdot) + \nabla_{\boldsymbol{X}}(\cdot)^T\right)$. Mirroring the discretization strategy of section 3.4, we can derive the discrete weakform equation for the problem in Eq. (3.4.7)-(3.4.10) as: For every $n = 1, \ldots, N_T$, find $(\boldsymbol{u}_h^n, \boldsymbol{v}_h^n, p_h^n) \in \boldsymbol{\mathcal{U}}^h \times \boldsymbol{\mathcal{V}}_0^h \times \mathcal{P}^h$ such that,

$$(\rho\delta_t\boldsymbol{v}_h^n, \boldsymbol{y}_h) + (\boldsymbol{\Sigma}^n, \nabla_{\boldsymbol{X}}\boldsymbol{y}_h) - (\boldsymbol{b}^n, \boldsymbol{y}_h) + (q_h, \nabla_{\boldsymbol{X}} \cdot \boldsymbol{v}_h^n) + (\boldsymbol{v}_h^n - \delta_t\boldsymbol{u}_h^n, \boldsymbol{w}_h) = 0 \tag{3.4.12}$$

for all $(\boldsymbol{w}_h, \boldsymbol{y}_h, q_h) \in \boldsymbol{\mathcal{U}}^h \times \boldsymbol{\mathcal{V}}_0^h \times \mathcal{P}^h$. Here we assume $\boldsymbol{u}_h^0 = \boldsymbol{u}_0$, $\boldsymbol{v}_h^0 = \boldsymbol{v}_0$, and $\boldsymbol{Q}_k^0 = \boldsymbol{0}$ for each $k = 1, \ldots, N$ (*e.g.* no history of deformation is assumed). $\boldsymbol{\Sigma}^n$ is given by Eq. (3.4.13), which utilizes the approximate fractional derivative denoted by $\hat{\mathrm{D}}_n^\alpha$.

$$\boldsymbol{\Sigma}^n = E\boldsymbol{D}\boldsymbol{u}_h^n + \eta\hat{\mathrm{D}}_n^\alpha(\boldsymbol{D}\boldsymbol{u}_h) + p_h^n\boldsymbol{I} \tag{3.4.13}$$

Examining the stability of Eq. (3.4.12), it can be shown that the state variables satisfy the stability estimates given in Lemma 4 and 5 in 3.A.

3.5 Approximation of Polynomial Functions

In this section, we aim to examine the accuracy and convergence of the Prony-based method (Eq. (3.2.12)) in comparison to a few other methods in the literature. For this purpose, we here consider a basic example of approximating the fractional derivative of a polynomial series, i.e.

$$p(t) = \sum_{k=1} b_k t^{k-1}, \quad D_t^\alpha p(t) = \sum_k b_k \Gamma(1-k)\frac{k-1}{k-\alpha}t^{k-1-\alpha}, \tag{3.5.1}$$

where b_k are the given parameters (given under Fig. 3.5.1). Different methods are used to approximate the fractional derivative of p, where the $L^2 -$ norm of the error with the analytic solution are then computed. All methods considered in this section were implemented in Matlab[163].

Table 3.1 compares the computation time of the Prony-based method in Eq. (3.2.12)

with a representative cumulative approach, in this case, the midpoint rule (Eq. (3.2.4)). From this, we observe that the computation time for the midpoint rule grows as $\mathcal{O}(N_T^2)$, with N_T denoting the number of time steps. As a consequence, the midpoint rule Eq. (3.2.4) takes $\approx$ 13 min to complete the problem with Δ_t =1e-5 in comparison to about 3s for the Prony-based method. This disparity stems from the use recursive updates of intermediate variables, q_k, in the Prony-based method relies to make the temporal scaling $\mathcal{O}(N_T)$. Minimal increase in compute time is observed with increasing Prony terms despite the N-dependent workload required for the computation of the fractional derivative operation (computation time grows 15% from $N = 3$ to $N = 12$). This likely stems from the efficiency of vectorized operations in Matlab.

Δ_t (s)	**Midpoint** (s)	**Prony** (s)			
		$N = 3$	$N = 6$	$N = 9$	$N = 12$
1e-4	8.16	0.28	0.27	0.30	0.33
5e-5	29.25	0.53	0.58	0.60	0.61
1e-5	785.14	2.58	2.64	2.87	3.01

Table 3.1 *Computational cost of approximating the fractional derivative of the polynomial in Eq.* (3.5.1) *with the midpoint rule versus the Prony-based method with* $N \in \{3, 6, 9, 12\}$. *Here the time interval for the calculation is* $[0, 0.9]$ *and* $\alpha = 0.4$.

For the Prony series parameters, we selected the optimized values from section 3.2.5 on a time scale of 9 seconds, 10 times the time domain. This can significantly improve the error estimates in Theorem 3 by reducing $\epsilon(z)$ and $C(\boldsymbol{\beta}, \boldsymbol{\tau})$, and being more inclusive of the frequencies of the Prony series that are larger than the time domain but still relevant to the problem (See Appendix 3.B for more details).

Fig. 3.5.2 illustrates the accuracy of the proposed, midpoint and Grünwald-Letnikov methods. Here the accuracy of the Prony approximation is examined for different α, N and Δ_t (Δ_t =1e-4 case shown in Fig. 3.5.1). Visibly, six or more Prony terms appear to perform well for the polynomial function, but three Prony terms generally yield noticeable errors. As predicted by the truncation error in Fig. 3.5.3, the accuracy of the Prony approximation deteriorates with increasing α, especially for $\alpha > 0.5$, limiting the Δ_t convergence as shown in Theorem 3. However, this deterioration is also observed in the midpoint method, where limited convergence with Δ_t is observed at $\alpha = 0.8$. The Grünwald-Letnikov method is significantly better in this regard, where convergence of the Grünwald-Letnikov method is on par or better than the Prony-based methods for $N = 12$ for sufficiently large N_T. However, as observed in Fig. 3.5.2, the Grünwald-Letnikov method seems to diverge as Δ_t approach 0. This is due to a singular behavior in the Grünwald-Letnikov method (Eq. (3.2.5)) when the number of time points N_T is small. Precisely, when $N_T = 0$, i.e. when taking the fractional derivative at time zero, the resulting value behaves as $f(0)/\Delta_t^\alpha$ (Fig. 3.5.1). This singularity is always present when N_T is small and decreases quickly with increases N_T, but this also indicates

the reliance of this method on knowing the value of the function being differentiated, making it unsuitable for solving differential equations without further corrections. The Prony-based method for $N > 3$ generally shows convergence for all α values, with errors plateauing based on the truncation error derived in Lemma 1 (see table 3.2). This is most visibly obvious for $\alpha = 0.1$ (Fig. 3.5.2A). For the $N = 3$ case, truncation errors vastly exceed time discretization errors, resulting in no appreciable convergence with time step refinement. It is noticeable that the Prony-based method performs better than the midpoint rule before reaching the truncation error in all cases tested. Larger number of Prony terms can significantly reduce this truncation error, illustrating the importance of choosing a sufficient number of terms for the problem depending on the required degree of accuracy.

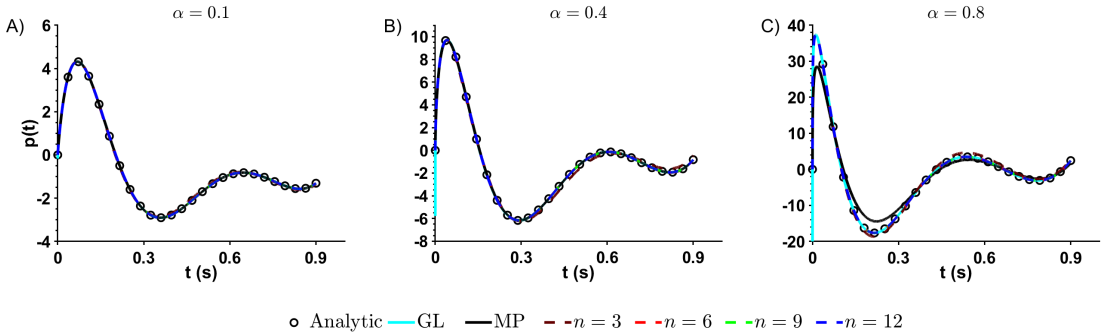

Figure 3.5.1 *Examples of approximating the fractional derivative of a polynomial (with* $\{b_1 \dots b_8\} = \{2.17,\ 101.54,\ -977.47,\ 3368.61,\ -5636.44,\ 4937.49,\ -2191.59,\ 398.40\}$ *) using the midpoint rule versus the Prony-based method with* $N \in \{3, 6, 9, 12\}$ *terms for A)* $\alpha = 0.1$*, B)* $\alpha = 0.4$ *and C)* $\alpha = 0.8$*.*

In addition to the midpoint rule, we also examined the method of Birk and Song[16], which also uses a Prony series approximation. The method presented in this work performs similarly or better for all α and N (see Table 3.2). This is consistent with our theoretical analysis in Fig. 3.5.3, which shows that the method presented here has better performance with $N > 3$ in nearly all scenarios. This improved performance stems from the increased error in the Prony approximation, causing errors to plateau with time step refinement earlier as predicted in Lemma 1 (see table 3.2). The performance gain is more significant for larger α and larger N as predicted. In the Prony-based method presented in this work, the integral is done with Prony terms with frequencies that are comparable with the domain of the simulation, whereas in the method of Birk and Song approximates the complete range of frequencies by Gauss-Jacobi weights (which need not be optimal). As a result, the method of Birk and Song does not see as much improvement in accuracy with an increases in N.

	Δ_t	**MP**	**GL**	**Prony**				**Birk and Song**			
				$N=3$	$N=6$	$N=9$	$N=12$	$N=3$	$N=6$	$N=9$	$N=12$
$\alpha=0.1$	1e-1	1.84e0	5.24e-1	5.07e-1	5.14e-1	5.14e-1	5.14e-1	4.73e-1	4.95e-1	5.12e-1	5.14e-1
	1e-2	2.64e-1	2.86e-2	4.96e-2	1.37e-2	1.49e-2	1.56e-2	2.99e-1	6.78e-2	2.77e-2	1.84e-2
	1e-3	2.76e-2	6.64e-3	5.04e-2	2.76e-3	4.45e-4	3.81e-4	3.01e-1	7.42e-2	2.23e-2	7.31e-3
	1e-4	2.81e-3	2.35e-3	5.04e-2	2.74e-3	3.03e-4	4.47e-5	3.01e-1	7.46e-2	2.24e-2	6.81e-3
	1e-5	2.86e-4	9.19e-4	5.04e-2	2.75e-3	3.13e-4	6.39e-5	3.01e-1	7.46e-2	2.24e-2	6.78e-3
	1e-6	2.93e-5	3.92e-4	5.04e-2	2.75e-3	3.14e-4	6.69e-5	3.01e-1	7.46e-2	2.24e-2	6.77e-3
	0	- -	- -	5.04e-2	2.75e-3	3.14e-4	6.71e-5	3.01e-1	7.46e-2	2.24e-2	6.77e-3
$\alpha=0.4$	1e-1	4.12e0	1.80e0	1.95e0	1.91e0	1.91e0	1.92e0	2.73e0	2.22e0	1.99e0	1.94e0
	1e-2	9.12e-1	2.36e-1	2.88e-1	2.25e-1	2.48e-1	2.58e-1	1.23e0	5.25e-1	3.34e-1	3.22e-1
	1e-3	1.43e-1	9.34e-2	2.21e-1	1.38e-2	1.08e-2	1.35e-2	1.21e0	4.74e-1	1.63e-1	7.59e-2
	1e-4	2.53e-2	6.46e-2	2.21e-1	1.14e-2	2.04e-3	9.88e-4	1.21e0	4.17e-1	1.43e-1	4.39e-2
	1e-5	5.27e-3	5.05e-2	2.21e-1	1.17e-2	2.76e-3	1.53e-3	1.21e0	4.12e-1	1.38e-1	4.31e-2
	1e-6	1.22e-3	4.42e-2	2.21e-1	1.18e-2	2.90e-3	1.68e-3	1.21e0	4.12e-1	1.37e-1	4.34e-2
	0	- -	- -	2.21e-1	1.18e-2	2.92e-3	1.69e-3	1.21e0	4.12e-1	1.37e-1	4.35e-2
$\alpha=0.8$	1e-1	1.13e1	8.46e0	8.14e0	8.37e0	8.42e0	8.47e0	8.22e0	9.10e0	9.38e0	9.36e0
	1e-2	6.42e0	1.84e0	2.27e0	2.79e0	2.92e0	3.06e0	4.54e0	5.35e0	5.90e0	5.53e0
	1e-3	3.54e0	5.66e-1	7.41e-1	3.52e-1	3.86e-1	4.71e-1	4.48e0	2.80e0	3.19e0	3.70e0
	1e-4	2.16e0	6.11e-1	6.75e-1	6.67e-2	6.50e-2	6.62e-2	3.98e0	1.71e0	2.41e0	2.07e0
	1e-5	1.36e0	1.14e0	6.75e-1	4.34e-2	2.98e-2	2.29e-2	2.85e0	1.70e0	1.13e0	1.42e0
	1e-6	8.56e-1	2.58e0	6.75e-1	4.90e-2	3.54e-2	2.76e-2	2.89e0	1.25e0	1.10e0	7.39e-1
	0	- -	- -	6.75e-1	4.98e-2	3.64e-2	2.87e-2	2.89e0	8.03e-1	2.63e-1	8.89e-2

Table 3.2 *Comparing the approximation error for the fractional derivative of polynomials when using the midpoint (MP) rule versus the Prony series. Here $\Delta_t = 0$ denotes the norm, $\|\varepsilon\|_0$, of the truncation error predicted in Lemma 1.*

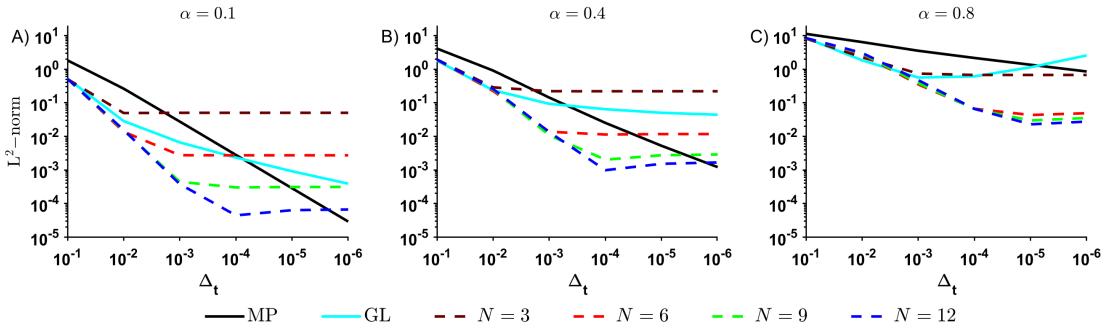

Figure 3.5.2 *The convergence of the approximation of the fractional derivative of polynomials when using the midpoint rule versus the Prony series for A)* $\alpha = 0.1$*, B)* $\alpha = 0.4$ *and C)* $\alpha = 0.8$*.*

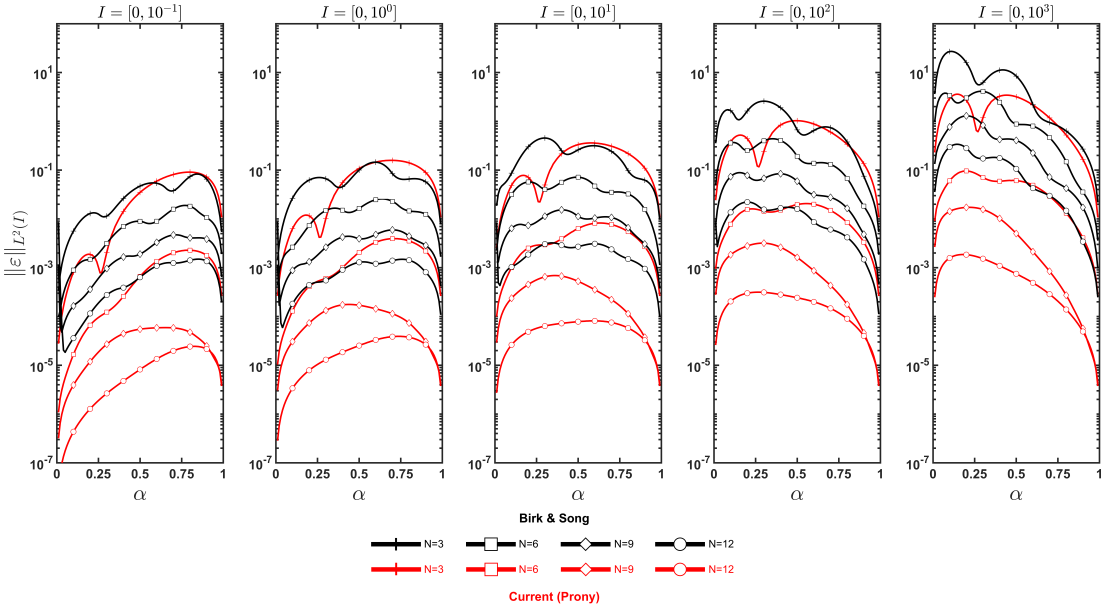

Figure 3.5.3 *Examination of the* $L^2(I)$ *norm error of the truncation error* ε *for different time intervals,* I*. Each plot shows parameters selected by the optimization approach here and the integral approach in Birk and Song*[16]*, for* $N \in \{3, 5, 6, 9, 12\}$*.*

3.6 FE approximation of fractional differential equations

While section 3.5 demonstrates the efficacy of the Prony approximation for given known differentiable functions, it does not give an indication of how well the method performs for solving a fractional differential equation. To examine this, we replicated Example

1 of Gao *et al.*[69], i.e.

$$\begin{aligned} D_t^\alpha u - \frac{\partial u}{\partial x^2} =& f(x,t), \quad \text{for } x \in [0,1], \quad t \in [0,1], \\ f(x,t) =& (x-1)^2 e^{-x} t^3 \left[\Gamma(4+\alpha)\frac{(x-1)^2}{6} - (21 - 10x + x^2)t^\alpha\right] - \\ & 4x^2(x-1)^2(14x^2 - 14x + 3), \\ u(x,0) =& x^4(x-1)^4, \\ u(0,t) =& t^{3+\alpha}, \quad u(1,t) = 0. \end{aligned}$$

The problem above has the unique analytic solution given in Eq. (3.6.1) and shown in Fig. 3.6.1. The major feature is a cubically growing source term at $x = 0$, which decays to 0 at $x = 1$ with a smaller concave quartic polynomial spanning $x \in [0, 1]$.

$$u(x,t) = (x-1)^4 \left(e^{-x} t^{3+\alpha} + x^4\right) \tag{3.6.1}$$

Following Gao *et al.*[69], Eq. (3.6.1) is solved using linear finite elements in space. Further, to make results comparable, we use the same error norm, i.e.

$$E(h, \Delta_t) = \max_{x\in[0,1]} \max_{t\in[0,1]} |u(x,t) - u_{\text{analytic}}(x,t)| \tag{3.6.2}$$

and replicate the results from Table 1 (temporal refinement) and Table 2 (spatial refinement) of Gao *et al.*[69] (see Tables 3.3 and 3.4, respectively). We also obtained Prony series parameters for the time scale of $[0, 100]$, by a factor of 100 times the time domain of the FE problem, to improve the error estimates (See Appendix 3.B). Spatiotemporal errors are also shown in Fig. 3.6.2 for $\Delta_t = 1/2500$, $h = 1/2500$ and a varying number of Prony terms. As expected, the error improves with an increasing number of Prony terms.

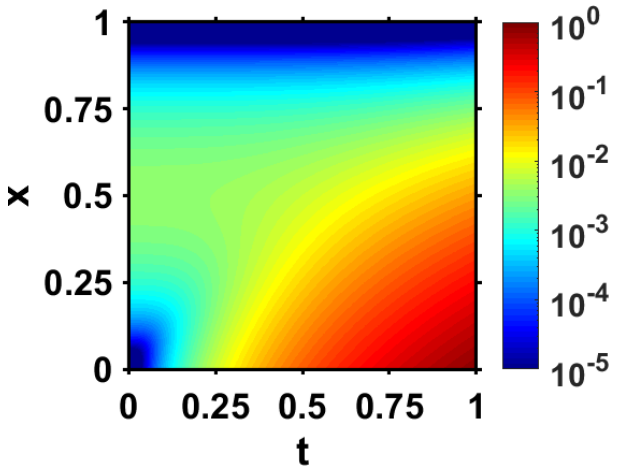

Figure 3.6.1 *The solution of the Prony series approximation of the fractional differential equation example Eq.* (3.6.1) *with three Prony terms,* $\alpha = 1/2$, $\Delta_x = 1/2500$ *and* $\Delta_t = 1/2500$.

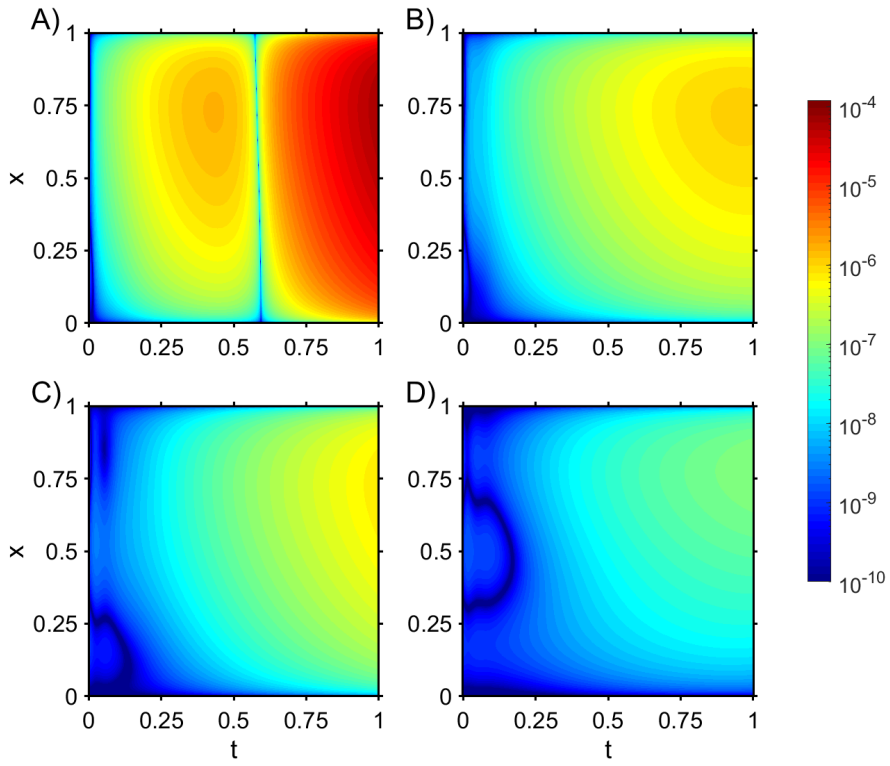

Figure 3.6.2 *The absolute value of the residuals from the Prony series approximation of the fractional differential equation example Eq.* (3.6.1) *shown in color with* $\alpha = 0.5$*,* $\Delta_t = 1/2500$*,* $\Delta_x = 1/2500$*, and A) 3, B) 6, C) 9, or D) 12 Prony terms in the approximation.*

Examining temporal refinement (with $h =$ 5e-5), the Prony-based method presented here has better convergence at smaller Δ_t; however, the results from Gao *et al.* show smaller initial errors (see Table 3.3). This improved error for larger Δ_t comes with additional computational expense requiring storage of the solution for all time points. Additionally, we observe that the truncation error due to the Prony approximation results in small errors, meaning that temporal convergence is observed even for $N = 3$ up to $\Delta_t > 1/160$. Further, at coarse time discretizations, the Prony-based method shows increasing errors for increasing N. While counter-intuitive, this is explained by Theorem 3. With increasing N, the discretization error is scaled by $C(\boldsymbol{\beta}, \boldsymbol{\tau})$ which generally grows with N. This results in slow convergence until the approximation errors asymptotically converges to the error bounds. However, optimal convergence is still achieved with Δ_t refinement.

			Gao et al.[69]		**Prony approximation**							
					$N = 3$		$N = 6$		$N = 9$		$N = 12$	
α	h	Δ_t	$E(h,\Delta_t)$	$\log_2$	$E(h,\Delta_t)$	$\log_2$	$E(h,\Delta_t)$	$\log_2$	$E(h,\Delta_t)$	$\log_2$	$E(h,\Delta_t)$	$\log_2$
1/2	1/20 000	1/10	8.48e-4	1.41	2.13e-3	1.62	3.33e-3	1.26	3.73e-3	0.96	3.96e-3	0.74
		1/20	3.19e-4	1.44	6.94e-4	1.54	1.39e-3	1.73	1.91e-3	1.53	2.36e-3	1.25
		1/40	1.17e-4	1.46	2.39e-4	1.03	4.17e-4	1.94	6.64e-4	1.86	9.94e-4	1.73
		1/80	4.26e-5	1.47	1.17e-4	0.44	1.09e-4	2.03	1.83e-4	1.98	3.00e-4	1.92
		1/160	1.53e-5	1.48	8.60e-5	0.14	2.67e-5	2.21	4.64e-5	2.08	7.92e-5	1.99
		1/320	5.49e-6	*	7.82e-5	*	5.79e-6	*	1.10e-5	*	2.00e-5	*
2/3	1/20 000	1/10	1.91e-3	1.26	4.52e-3	1.52	6.78e-3	0.99	7.40e-3	0.72	7.88e-3	0.56
		1/20	7.96e-4	1.29	1.58e-3	1.65	3.42e-3	1.58	4.51e-3	1.31	5.33e-3	1.00
		1/40	3.25e-4	1.31	5.04e-4	1.31	1.14e-3	1.90	1.82e-3	1.78	2.67e-3	1.59
		1/80	1.31e-4	1.32	2.04e-4	0.69	3.07e-4	2.07	5.28e-4	2.01	8.85e-4	1.91
		1/160	5.26e-5	1.32	1.26e-4	0.24	7.28e-5	2.53	1.31e-4	2.32	2.35e-4	2.13
		1/320	2.10e-5	*	1.07e-4	*	1.26e-5	*	2.64e-5	*	5.36e-5	*

Table 3.3 *Reproducing Table 1 from Gao et al.*[69] *using the Prony-based method Eq.* (3.2.12) *for refinement in time with a constant* $h =$ *5e-5.*

In the case with refinement in space (with $\Delta_t =$ 5e-5), both methods have similar convergence rates but the Prony-based approach has smaller initial errors due to better convergence with Δ_t (Table 3.4). Interestingly, but not unexpectedly, the number of Prony terms does not affect the convergence rate with refinement in space due to the fractional derivative being taken with respect to time only. However, additional Prony terms are still important, as an insufficient number of terms limits the lower bound of the errors, as seen for $N = 3$.

			Gao et al.[69]		**Prony approximation**							
					$N = 3$		$N = 6$		$N = 9$		$N = 12$	
α	h	Δ_t	$E(h,\Delta_t)$	$\log_2$	$E(h,\Delta_t)$	$\log_2$	$E(h,\Delta_t)$	$\log_2$	$E(h,\Delta_t)$	$\log_2$	$E(h,\Delta_t)$	$\log_2$
1/2	1/10	1/20 000	1.50e-2	2.00	5.95e-3	2.06	6.02e-3	2.01	6.02e-3	2.01	6.01e-3	2.01
	1/20		3.75e-3	2.00	1.43e-3	2.22	1.50e-3	2.00	1.50e-3	2.00	1.50e-3	2.00
	1/40		9.38e-4	2.00	3.07e-4	3.24	3.75e-4	1.99	3.75e-4	1.99	3.74e-4	2.00
	1/80		2.35e-4	2.00	3.25e-5	- 0.75	9.47e-5	1.95	9.44e-5	1.96	9.37e-5	2.00
	1/160		5.86e-5	*	5.47e-5	*	2.45e-5	*	2.43e-5	*	2.35e-5	*
2/3	1/10	1/20 000	1.37e-2	1.99	5.67e-3	2.08	5.77e-3	2.00	5.77e-3	2.00	5.77e-3	2.00
	1/20		3.44e-3	2.00	1.35e-3	2.31	1.44e-3	1.98	1.44e-3	1.97	1.44e-3	1.98
	1/40		8.61e-4	2.00	2.71e-4	3.33	3.66e-4	1.92	3.67e-4	1.90	3.67e-4	1.91
	1/80		2.15e-4	2.00	2.68e-5	- 1.58	9.67e-5	1.71	9.81e-5	1.66	9.75e-5	1.68
	1/160		5.37e-5	*	8.01e-5	*	2.96e-5	*	3.11e-5	*	3.05e-5	*

Table 3.4 *Reproducing Table 2 from Gao et al.*[69] *using the Prony-based method Eq.* (3.2.12) *for refinement in space with a constant* $\Delta_t =$ *5e-5.*

Fig. 3.6.3A, B and C shows spatiotemporal convergence for a range of time and discretizations. For fine spatial grids, we observe that errors approach the limit predicted by Lemma 2 and adhere to the results of Theorem 3. Coarsening spatial refinement, we can observe spatial errors shift the lower bound for higher values of N. Fig. 3.6.3D,

E, and F presents a similar analysis utilizing the weights from Birk and Song[16]. Once again, the Prony-based method presented in this work performs better, where the convergence rates are improved and lower bounds for the Prony-based approximation one ($N = 9$) to two ($N = 3$) orders of magnitude lower.

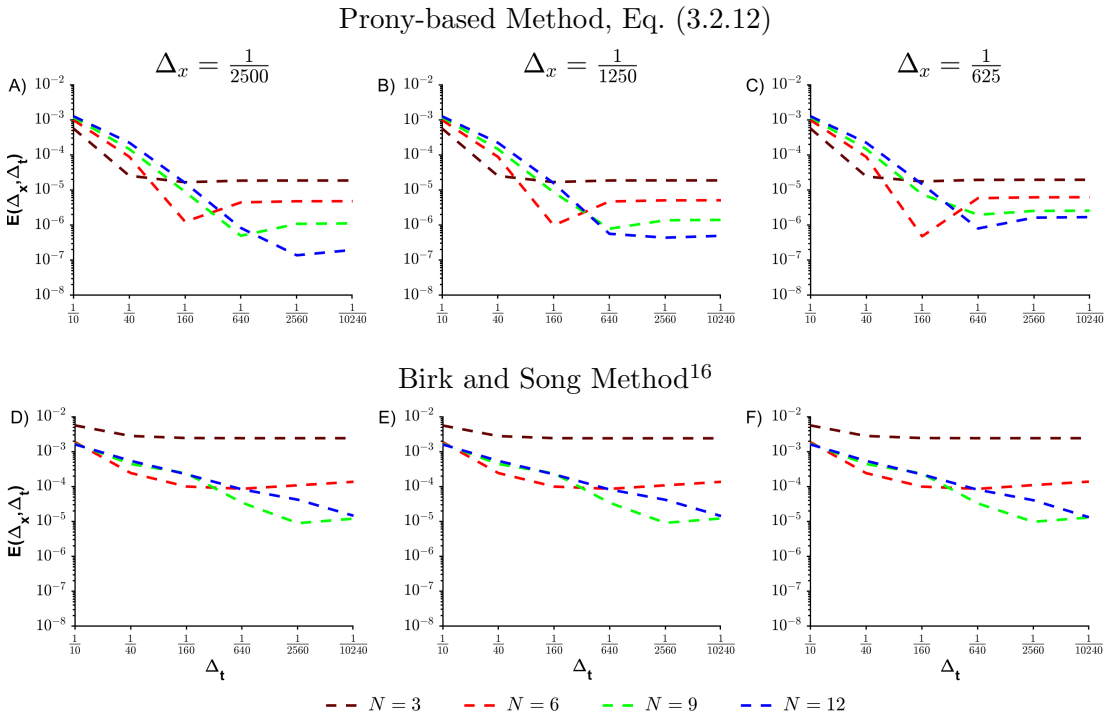

Figure 3.6.3 *Convergence of the solution of the fractional diffusion equation with* $\alpha = 0.3$ *using the Prony-based method Eq.* (3.2.12) *with refinement in time and A)*$\Delta_x = 1/2500$*, B)* $1/1250$ *and C)* $1/625$ *versus using the method of Birk and Song*[16] *with refinement in time and D)*$\Delta_x = 1/2500$*, E)* $1/1250$ *and F)* $1/625$*.*

3.7 Fractional Approximation applied to Biomechanics in the Liver

3.7.1 Finite element model for the mechanical testing of livers

In order to investigate the efficacy of the proposed method for simulating fractional viscoelasticity in soft tissues, here we model an experiment executed by Tan *et al.*[246] on *ex vivo* bovine liver tissue. Briefly, cylindrical liver samples of height $H = 2.7$mm and radius $R = 10$mm were tested in a rheometer at a range of compressions, shear strains and frequencies. The behavior of the *ex vivo* liver sample can be effectively modeled using a viscoelastic exponential model[29] of the form

$$\boldsymbol{S} = \delta \mathrm{Dev}\left[D_t^{\alpha} \boldsymbol{S}_v\right] + pJ\boldsymbol{C}^{-1}, \quad \boldsymbol{S}_v = \exp[b(II_{\boldsymbol{C}} - 3)]\boldsymbol{C}. \tag{3.7.1}$$

The first term denotes the deviatoric component of the stress depending on the frac-

tional derivative of $\boldsymbol{S}_v$ which follows a similar form to a typical hyperelastic material model of the right Cauchy-Green strain (see section 3.3.1). The second component denotes the hydrostatic stress, depending on the pressure variable, p. Here $J = 1$. Here $\text{Dev}[\boldsymbol{A}] = \boldsymbol{A} - (\boldsymbol{A} : \boldsymbol{C}/3)\boldsymbol{C}^{-1}$ denotes the deviatoric operator. The model can be fit to match the behavior of the *ex vivo* liver from[246] by three parameters: the linear scaling parameter δ, the nonlinear response parameter b, and the fractional derivative α. Following the parameterization process in[29], parameters $\alpha = 0.2$, $b = 1.5$ and $\delta = 126.4$Pa were observed to provide the best fit to the data (see Fig. 3.7.1).

Here we focus on a single test case, where a sample was compressed by 10% and subsequently sheared at a frequency of 1Hz around its axis with a shear strain amplitude of 25%. In this case, the reference domain is the cylindrical region $\Omega_0 = \{\boldsymbol{x} \in \mathbb{R}^3 | \sqrt{x_1^2 + x_2^2} \leq R, 0 \leq x_3 \leq H\}$. The boundary Γ_0 is split into a bottom surface, top surface, and side surface $\Gamma_0 = \Gamma_0^b \cup \Gamma_0^t \cup \Gamma_0^w$, respectively. Assuming pure compression and shear, the deformation can be described in analytic form as,

$$\boldsymbol{u}(t) = \begin{bmatrix} \frac{X_1}{\sqrt{\lambda(t)}}\cos(\psi(t)X_3) - \frac{X_2}{\sqrt{\lambda(t)}}\sin(\psi(t)X_3) - X_1 \\ \frac{X_1}{\sqrt{\lambda(t)}}\sin(\psi(t)X_3) + \frac{X_2}{\sqrt{\lambda(t)}}\cos(\psi(t)X_3) - X_2 \\ X_3\left(\lambda(t) - 1\right) \end{bmatrix}, \psi(t) = \frac{\gamma\lambda^{3/2}(t)\sin(2\pi f\hat{t})}{\sqrt{X_1^2 + X_2^2}}, \tag{3.7.2}$$

where the compression, λ, and the shear angle, ψX_3, were chosen to mimic the experimental conditions. Here compression took place over the first 1s, *e.g.* $\lambda(t) = 1 - 0.1\min(t, 1)$. Additionally, the angular displacement was applied after compression, $\hat{t} = \max(0, t - 1)$, with an oscillatory frequency $f = 1$Hz and a maximal shear strain of $\lambda\gamma$. Torque readings were acquired during the shearing process.

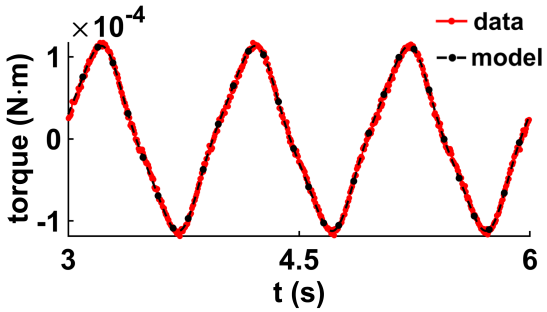

Figure 3.7.1 *Comparison of the model and experimental data from Tan* et al.*[246] at 10% compression and 25% shear strain, showing efficacy of the fractional viscoelastic model.*

This problem provides the ability to verify the finite element implementation outlined in section 3.4. The analytical stresses could be computed using Eq. (3.7.2)) and Eq. (3.7.1). Applying Eq. (3.3.3), the model predicted torque, τ, and normal traction,

t_N, can be calculated by

$$\tau(t) = \int_{\Gamma^t} \boldsymbol{e}_3 \cdot [\boldsymbol{x} \times (\boldsymbol{\sigma} \cdot \boldsymbol{n})] \; d\Gamma, \quad t_N(t) = \int_{\Gamma^t} \boldsymbol{e}_3 \cdot [\boldsymbol{\sigma} \cdot \boldsymbol{n}] \; d\Gamma, \tag{3.7.3}$$

where Γ^t is upper boundary of the physical domain Ω, $\boldsymbol{n} = \boldsymbol{e}_3$ the outward normal, and $\boldsymbol{e}_k$ is the k^{th}-base vector for rectangular-Cartesian coordinates. These quantities were computed in MATLAB R2018b and in-house software $\mathcal{C}$**heart**. In MATLAB, a reference solution for the torque and normal traction were computed using the Grünwald-Letnikov method[222] (Eq. (3.2.5)) with a small time-step Δ_t =1e-5. A sweep over time-step size and the number of Prony terms was also applied to examine computing times and computational accuracy.

For the finite element implementation in $\mathcal{C}$**heart**, a curvilinear hexahedral mesh (with $9,072$ elements) was used to approximate Ω_0. The inf-sup stable $\mathbb{Q}^2 - \mathbb{Q}^2 - \mathbb{Q}^1$ scheme was used to solve for $\boldsymbol{u}$, $\boldsymbol{v}$ and p (with $77,425$ quadratic nodes and $10,309$ linear nodes). Eq. (3.7.2) was applied as boundaries conditions on Γ_0^b and Γ_0^t with no boundary conditions applied on Γ_0^w. Model torque and normal traction were exported along with the solution.

3.7.2 Accuracy and convergence

The accuracy and convergence of the Grünwald-Letnikov and Prony approximations are shown in Table 3.5, with the latter examined for $N \in \{3, 6, 9, 12\}$. When the number of Prony terms is $N = 3$, there is little improvement in the stress accuracy with temporal refinement reflecting inherent limitations in the approximation quality with so few terms. However, increasing to $N = 6$, we see the stagnation in convergence shift to Δ_t =1e-3. Further increases to $N = 9$ and $N = 12$ exhibit continued convergence even for the finest time step size, as predicted from Theorem 3.

Δ_t (s)	**Prony error** (%)			
	$N = 3$	$N = 6$	$N = 9$	$N = 12$
1e-2	2.26e0	5.05e-1	6.51e-1	7.01e-1
5e-3	2.06e0	1.52e-1	2.50e-1	3.27e-1
1e-3	2.00e0	1.01e-1	1.30e-2	1.97e-2
5e-4	1.99e0	1.04e-1	8.79e-3	4.86e-3

Table 3.5 *Accuracy and convergence of the Prony approximation with Δ_t and N applied to the ideal analytic solution. Percentage errors were measured relative to the GL with a refined time-step size of Δ_t = 1e-5. The percentage errors reported in the table correspond to the $L^2(0,T)$ norm difference in (1,3)-Cauchy stress component normalized by the $L^2(0,T)$ norm of the (1,3)-Cauchy stress component predicted by the reference solution.*

The deformation and pressure from the FEM simulation can be observed in Fig. 3.7.2 (with $N = 9$ and Δ_t =1e-3). The simulated displacements were within 1e-6 of their

analytic counterparts. The FEM simulation was further verified against the Grünwald-Letnikov implementation in MATLAB. The torque and normal force from both implementations are shown in Fig. 3.7.2, showing both forward model and the analytically computed behavior are consistent. Here, an error of 1e-3 was observed for the torque and 2e-4 was observed in the normal traction force.

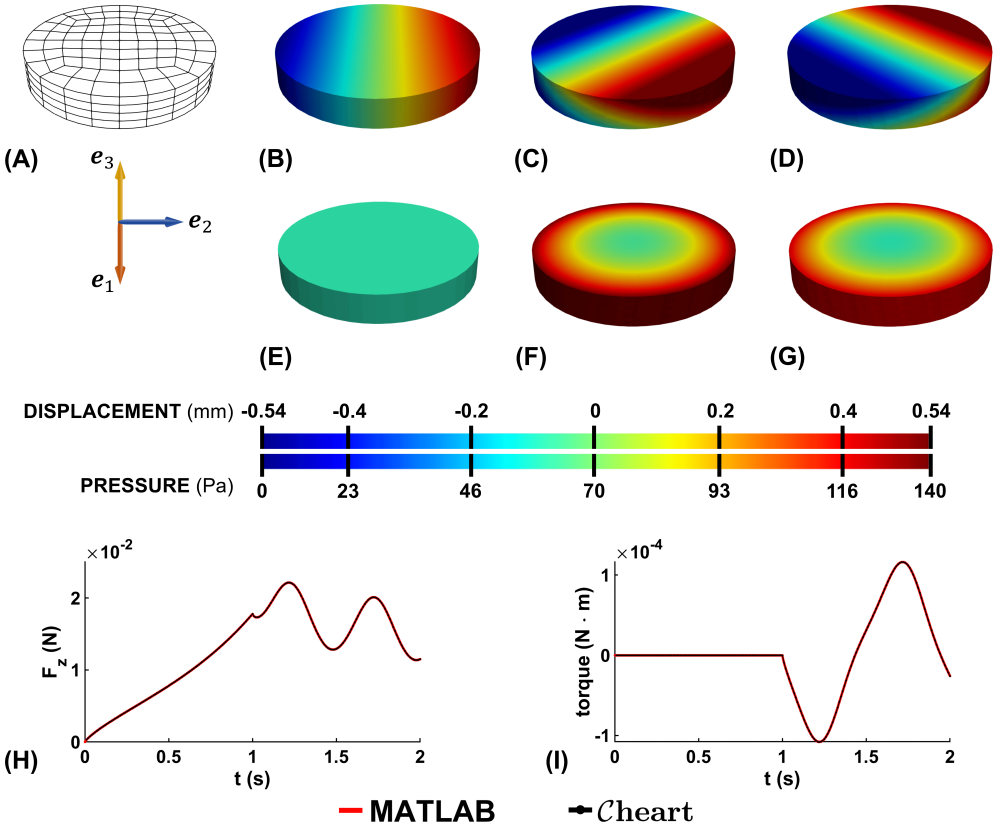

Figure 3.7.2 *Illustration of the FEM solution of the liver model under deformation and shear. A) Sample mesh; $\boldsymbol{u}_2$-component of the deformation at B) compressed state ($t = 1$ s) C) compressed and sheared state (counter-clockwise, $t = 1.25$ s) D) compressed and sheared state (clockwise, $t = 1.75$ s); Hydrostatic pressure at E) compressed state ($t = 1$ s) F) compressed and sheared state (counter-clockwise, $t = 1.25$ s) G) compressed and sheared state (clockwise, $t = 1.75$ s); The bottom panels show the force (H) and torque response (I) of a sample under compression and shear.*

3.7.3 Computational cost

Table 3.6 presents the cost performance of the Prony approximation (Eq. (3.2.12)) compared to the Grünwald-Letnikov method (Eq. (3.2.5)) over the time domain $t \in [0, 2]$. Time step Δ_t was chosen to vary between 1e-2 and 5e-5. For time steps larger than 1e-4, the the Grünwald-Letnikov and Prony approach (for $n = 3, 6, 9, 12$ terms) are comparably fast. However, as Δ_t shrinks further, the Grünwald-Letnikov approach becomes increasingly expensive to compute ($\mathcal{O}(N_T^2)$ versus $\mathcal{O}(N_T)$), with storage costs of $\mathcal{O}(N_T)$ vs $\mathcal{O}(N)$ (N is the number of Prony terms).

	Δ_t (s)	**GL** (s)	**Prony** (s)			
			$N = 3$	$N = 6$	$N = 9$	$N = 12$
$\alpha = 0.2$	1e-2	0.029	0.054	0.044	0.051	0.047
	5e-3	0.052	0.086	0.093	0.097	0.094
	1e-3	0.202	0.406	0.429	0.442	0.561
	5e-4	0.492	0.818	0.871	0.890	0.933
	1e-4	5.728	4.676	4.169	4.348	4.530
	5e-5	17.706	8.392	8.369	8.859	9.088
	1e-5	770.569	38.051	37.888	39.370	41.773

Table 3.6 *Comparison of solving speed for the Grünwald-Letnikov (GL) and Prony approximation methods (MATLAB implementation). The time results reported correspond to calculations for a single point on the outer edge of the cylinder. All methods were run in serial on a DELL PRECISION M4800 quad-core Intel(R) Core(TM) i7-4810MQ CPU @ 2.80 GHz.*

Finally, we sought to examine the added computational cost of simulating the viscoelastic model compared to a classical hyperelastic model (see Table 3.7). Here the compute time of the viscoelastic model in Eq. (3.7.1) was contrasted against the hyperelastic model resulting if $\alpha = 0$ in Eq. (3.7.1). It is notable that the computational time for both hyperelastic and viscoelastic material models does not increase with direct proportionality with the number of time steps, likely due to a reduction in the required number of Newton-Raphson iterations per time step. Further, while the computational cost of the viscoelastic model is larger, this does not lead to a significant increase in computational time, with the differences observed being within ≈16%. Additionally, varying the number of Prony terms does not significantly impact the computational time, as seen in Table 3.7. While increasing N increases the computational work, the added cost for residual and matrix calculations is minor relative to the basic computational expense for simulating large deformation mechanical systems.

Model $\backslash\Delta_t$	1e-2	1e-3	1e-4
Hyperelastic	170.43s	672.71s	2899.40s
Viscoelastic	190.24s	669.65s	3365.30s

Viscoelastic			
$N = 3$	$N = 6$	$N = 9$	$N = 12$
655.69s	684.74s	669.65s	677.85s

Table 3.7 *Comparison of compute times for a hyperelastic and fractional viscoelastic solutions in* ***Cheart*** *with (top) changes in Δ_t ($N = 9$) and (bottom) changes in N (Δ_t = 1e-3). All times are reported in seconds and based on simulations run using 16 cores on a 3.8 GHz Titan A399 AMD RYZEN Threadripper 32 core system.*

3.8 Discussion

3.8.1 Computational cost

The biggest advantage of this Prony based method for approximating Caputo fractional derivatives Eq. (3.2.12) is computational efficiency. The historical integral required typically leads to an accumulating computational cost and demands smaller time steps by introducing nonlinearity into the system in the form of the strain history, becoming a heavy burden in viscoelastic simulations. The method developed herein allows a bounded storage cost for the memory cost of the strain history by an approximation using Prony series. The parameters can be precomputed from the α values and are independent of the strain history itself, which only leaves the cost of summing over the Prony series at each time step, which is small. The number of Prony terms necessary is dependent on the required accuracy of the approximation. However, for the example we have tested, six or fewer terms are sufficient for a wide range of cases. We find this cost to be only a fraction of the cost of the overall simulation, but can reduce the cost of simulating later time steps by several magnitudes. A well-bounded cost for the historical integral also removes a limitation on the full duration of the simulation, making it applicable to a wider range of applications.

3.8.2 Accuracy and convergence

The number of terms to use in the Prony-based method (Eq. (3.2.12)) is the decision between the truncation error, lower-bound for the approximation, and the loss in accuracy at larger Δ_t due to the $C(\boldsymbol{\beta}, \boldsymbol{\tau})$ term. Increasing the number of Prony terms will lower the resulting truncation error at the cost of larger error terms. The Prony-based method has superior computational costs and better convergence rates when above the truncation error (Lemma 1) in comparison to classical non-recursive methods (Fig. 3.5.2). It is noted that in some cases, the discretization error introduced by the coefficient $C(\boldsymbol{\beta}, \boldsymbol{\tau})$ (Lemma 2) can cause the solution to be initially be less accurate at large Δ_t (Table 3.3 and 3.4). However, this factor remains to be small and the savings in the computational cost is the much more significant factor. Against competing methods such as the Birk and Song method[16], the Prony-based method has better convergence for six or more Prony terms or quadrature points and at higher α, and is competitive otherwise (Fig. 3.5.3) in examples tested.

3.8.3 Other methods

One common approach to improve the computational efficiency of traditional methods is by truncating the historical data. As noted by Diethelm et al.[51], it is typical that the weights in fractional derivative approximations exhibit some form of fading memory. For this reason, terms in the history are neglected to reduce computational costs. While it is true that terms that are further in the past will decay more, and in a way

becomes small enough to be negligible, the length of the history also increases. As such, truncation cannot be done negligently. For example, for $\alpha = 0.3$ and if the method presented by Diethelm et al.[51] in Eq. (3.2.6) is truncated to 12 terms, the sum of the absolute value of the first 12 weights on the domain $t \in [0, 1]$ is always 1.66353, independent of Δ_t (assuming $\Delta_t < 1/11$). In comparison, the sum of the remaining weights are 0.16037, 0.248329, 0.292299, and 0.314331 for Δ_t = 1e-2, 1e-3, 1e-4 and 1e-5 respectively. The weight of the truncated history actually increases faster than the rate of decay due to fading memories. This effect is more significant for lower values of α, and thus care must be taken for how the truncation is done. The number of terms to keep increases over time, depending on the problem.

Another similar method has been presented by Jiang et al.[119]. The major differences between the two methods are: i) the approximation of the integral in the discretized case and ii) the method of computing the parameters of the Prony series. For the approximation of the integral, this is largely a choice. However, we do note that in the method of Jiang *et al.*[119], by holding the input function constant will still lead to a small but non-zero increase in the history terms when the solution should be zero on a stationary pure viscoelastic body. Jiang *et al.*'s method of computing the Prony series parameters[119] is designed with the goal of targeting a desired error of the approximation. However, the bounds on the number of terms are typically in the hundred for even modest desired error (e.g., 1e-4). The algorithm provided by Jiang *et al.*[274] can reduce this number, but it is still larger than the Prony-based method. In addition, the algorithm presented can select from a list of frequencies based on Eigenvalues of the least squares system, which do not necessarily include the optimal frequencies. The method presented in this work (Eq. (3.2.12)) outputs a desired number of Prony terms, which is more desirable for ease of implementation and application.

3.8.4 Other applications

Although this method is described for the constitutive modeling of viscoelastic materials, fractional derivatives have a wide range of other applications. The most common application of fractional calculus in the literature is in regard to viscous fluid flows. The parallels to viscoelasticity are obvious and its use along with viscoelasticity to solve complex biomechanical systems is also very common. Also common is the application of acoustic waves traveling through viscous media. Another interesting and useful application is in edge detection in image analysis. The use of fractional derivatives can improve thin edge detection and tolorence to noises[162]. One other important application is in PID controllers, where the feedback loops are on fractional order. An interesting example of this is in path tracking of self driving vehicles[239]. Some other common and interesting applications are summarized by Dalir and Bashour[46].

3.8.5 Practical guidance

The cost of computing the parameters of the Prony series can be expensive and are best precomputed then imported at the time of use. However, since each of the parameters as a function of α is smooth, one method is to generate a set of Prony series parameters for well-spaced values of α, which can then be interpolated for more specific values of α. Indeed, we used this method for the Matlab and Cheart[138] implementations. The number of Prony terms to use is quite flexible. $N < 4$ is not recommended, but six is typically sufficient for most problems. Increasing N further will also not significantly negatively impact the solution and the computational cost of the problem. It should be noted that due to the necessity of approximating the derivative of the function to be uniform for each time interval, smaller time steps are necessary for the convergence of the solution in finite element simulations. One should choose step sizes such that the derivative is expected to be constant. Also, we have found that the velocity is unstable under second-order schemes in transient viscoelasticity simulations, but is stable under first-order schemes, as shown in 3.A.

3.9 Conclusion

In this work we present a novel method for the finite element approximation of fractional nonlinear viscoelastic materials. Application of fractional viscoelastic models can present computational challenges, with many methods requiring prohibitive storage and computational expense. To overcome these issues, a new approximation to the Caputo fractional derivative is introduced, resulting in a fixed storage cost and making the computational times scale linearly with the number of time steps. Error estimates are derived for this approximation, demonstrating the efficacy of the approximation. Estimates are demonstrated to be accurate through numerical examples, where comparable or better convergence behaviors with refinement in time are observed compared to current state-of-the-art methods. The fractional approximation was then introduced into a nonlinear transient finite element mechanics implementation. The numerical problem was shown to be unconditionally stable for simple linear fractional viscoelasticity, and observed stable for nonlinear viscoleasticity through verified numerical examples. The computational cost of this fractional derivative implementation is comparable to the standard hyperelastic model, despite the historical integral ($\sim$16% more), and it was able to accurately approximate the solution in all examples considered. This method can significantly simplify the implementation of fractional viscoelastic models in general, and provides a pathway for applications of viscoelastic soft tissue models for the efficient simulation of complex biomechanical systems. While developed in the context of viscoelastic modelling, the Caputo approximation introduced has potential applications in solving the many other problems involving fractional derivatives.

Supplementary materials

3.A Stability Analysis for Linear Fractional Viscoelastic Materials

Lemma 4 and 5 provide stability estimates for the linear viscoelastic mechanics problem introduced in Eq. (3.4.12). We note that the fractional derivative approximation follows the form discussed in section 3.2.4. Here N denotes the number of Prony terms, and $\beta_k, \tau_k \in \mathbb{R}^+$ denote the scaling and time scale of the k^{th} Maxwell element in the approximation (with β_0 being the scaling of a pure dashpot element). This approximation relies on intermediate variables $\boldsymbol{Q}_k^n$ which obey the update formula in Eq. (3.A.1).

$$\hat{\mathrm{D}}_n^{\alpha}(\boldsymbol{D}\boldsymbol{u}_h) = \beta_0 \boldsymbol{D}\boldsymbol{v}_h^n + \sum_{k=1}^{N} \boldsymbol{Q}_k^n, \quad \boldsymbol{Q}_k^n = e_k^2 \boldsymbol{Q}_k^{n-1} + \beta_k e_k \Delta_t \boldsymbol{D}\boldsymbol{v}_h^n \tag{3.A.1}$$

With this approximation in mind, we can derive the following stability estimate for the discrete solution showing that the discrete solution is unconditionally stable and bounded by given data.

Lemma 4. *Consider the linear incompressible fractional viscoelasticity problem shown in Eq.* (3.4.12) *and the update formula shown in Eq.* (3.A.1)*. Assuming that* $\boldsymbol{v}_h^0, \boldsymbol{u}_h^0 \in \boldsymbol{\mathcal{V}}_0^h$*, that* $\boldsymbol{Q}_k^0 = \boldsymbol{0}$*, and*

$$\boldsymbol{b} \in \boldsymbol{L}^{\infty}([0,T]; \boldsymbol{L}^2(\Omega_0)), \quad \sup_{t\in[0,T]} \|\boldsymbol{b}(t)\|_0 \leq K_{\boldsymbol{b}}$$

$$\varrho\|\boldsymbol{v}_h^n\|_0^2 + E\|\boldsymbol{D}\boldsymbol{u}_h^n\|_0^2 + \eta\beta_0 \sum_{m=1}^{n} \Delta_t \|\boldsymbol{D}\boldsymbol{v}_h^m\|_0^2 + \sum_{k=1}^{N} \frac{\eta}{\beta_k e_k} \|\boldsymbol{Q}_k^n\|_0^2 \leq \varrho\|\boldsymbol{v}_h^0\|_0^2 + E\|\boldsymbol{D}\boldsymbol{u}_h^0\|_0^2 + \frac{C_\Omega t_n K_{\boldsymbol{b}}}{\eta\beta_0}$$

for each $n = 1, \dots N_T$*.*

Proof of Lemma 4 3. *To prove Lemma 4, we choose* $\boldsymbol{w}_h = \boldsymbol{0}$*,* $\boldsymbol{y}_h = \boldsymbol{v}_h^n$ *and* $q_h = 0$

in Eq. (3.4.12) *resulting in the equation*

$$(\varrho\delta_t \boldsymbol{v}_h^n, \boldsymbol{v}_h^n) + (\boldsymbol{\Sigma}^n, \nabla_{\boldsymbol{X}} \boldsymbol{v}_h^n) - (\boldsymbol{b}^n, \boldsymbol{v}_h^n) = 0 \tag{3.A.2}$$

Rearranging the update formula for $\boldsymbol{Q}_k^n$ *in Eq.* (3.A.1)*, we note that*

$$\boldsymbol{D}\boldsymbol{v}_h^n = \frac{1}{\beta_k e_k \Delta_t}\left(\boldsymbol{Q}_k^n - e_k^2 \boldsymbol{Q}_k^{n-1}\right). \tag{3.A.3}$$

Focusing on the stress term in Eq. (3.A.2)*, noting the symmetry of* $\boldsymbol{\Sigma}^n$*,that* $\boldsymbol{v}_h^n$ *is weakly divergence free, the modified update formula of Eq.* (3.A.3)*, and the identity*

$$\begin{aligned}(\boldsymbol{a}-\boldsymbol{b})\cdot\boldsymbol{a} &= \frac{1}{2}\left(|\boldsymbol{a}|^2 - |\boldsymbol{b}|^2 + |\boldsymbol{a}-\boldsymbol{b}|^2\right), \qquad \text{for any } \boldsymbol{a},\boldsymbol{b}\in\mathbb{R}^d \\ (\boldsymbol{A}-\boldsymbol{B}):\boldsymbol{A} &= \frac{1}{2}\left(|\boldsymbol{A}|^2 - |\boldsymbol{B}|^2 + |\boldsymbol{A}-\boldsymbol{B}|^2\right), \qquad \text{for any } \boldsymbol{A},\boldsymbol{B}\in\mathbb{R}^{d\times d}\end{aligned} \tag{3.A.4}$$

we can observe that

$$\begin{aligned}(\boldsymbol{\Sigma}^n, \nabla_{\boldsymbol{X}}\boldsymbol{v}_h^n) =& (\boldsymbol{\Sigma}^n, \boldsymbol{D}\boldsymbol{v}_h^n) \\ =& \left(E\boldsymbol{D}\boldsymbol{u}_h^n + \eta\hat{D}_n^{\alpha}(\boldsymbol{D}\boldsymbol{u}_h) + p_h^n\boldsymbol{I}, \boldsymbol{D}\boldsymbol{v}_h^n\right) \\ =& \frac{E}{\Delta_t}\left(\boldsymbol{D}\boldsymbol{u}_h^n, \boldsymbol{D}[\boldsymbol{u}_h^n - \boldsymbol{u}_h^{n-1}]\right) + \eta\left(\beta_0\boldsymbol{D}\boldsymbol{v}_h^n + \sum_{k=1}^N \boldsymbol{Q}_k^n, \boldsymbol{D}\boldsymbol{v}_h^n\right) \\ =& \frac{E}{\Delta_t}\left(\boldsymbol{D}\boldsymbol{u}_h^n, \boldsymbol{D}[\boldsymbol{u}_h^n - \boldsymbol{u}_h^{n-1}]\right) + \eta\beta_0\|\boldsymbol{D}\boldsymbol{v}_h^n\|_0^2 + \\ & \sum_{k=1}^N \frac{\eta}{\beta_k e_k\Delta_t}\left(\boldsymbol{Q}_k^n, \boldsymbol{Q}_k^n - e_k^2\boldsymbol{Q}_k^{n-1}\right) \\ =& \frac{E}{2\Delta_t}\left(\|\boldsymbol{D}\boldsymbol{u}_h^n\|_0^2 - \|\boldsymbol{D}\boldsymbol{u}_h^{n-1}\|_0^2 + \|\boldsymbol{D}(\boldsymbol{u}_h^n - \boldsymbol{u}_h^{n-1})\|_0^2\right) + \eta\beta_0\|\boldsymbol{D}\boldsymbol{v}_h^n\|_0^2 + \\ & \sum_{k=1}^N \frac{\eta}{2\beta_k e_k\Delta_t}\left(\|\boldsymbol{Q}_k^n\|_0^2 - \|e_k^2\boldsymbol{Q}_k^{n-1}\|_0^2 + \|\boldsymbol{Q}_k^n - e_k^2\boldsymbol{Q}_k^{n-1}\|_0^2\right)\end{aligned} \tag{3.A.5}$$

Applying Eq. (3.A.4) *and the equality in Eq.* (3.A.5) *to Eq.* (3.A.2)*,*

$$\begin{aligned}&\frac{\varrho}{2}\left(\|\boldsymbol{v}_h^n\|_0^2 - \|\boldsymbol{v}_h^{n-1}\|_0^2 + \|\boldsymbol{v}_h^n - \boldsymbol{v}_h^{n-1}\|_0^2\right) + \\ &\frac{E}{2}\left(\|\boldsymbol{D}\boldsymbol{u}_h^n\|_0^2 - \|\boldsymbol{D}\boldsymbol{u}_h^{n-1}\|_0^2 + \|\boldsymbol{D}(\boldsymbol{u}_h^n - \boldsymbol{u}_h^{n-1})\|_0^2\right) + \\ \eta\beta_0\Delta_t\|\boldsymbol{D}\boldsymbol{v}_h^n\|_0^2 + \sum_{k=1}^N \frac{\eta}{2\beta_k e_k}&\left(\|\boldsymbol{Q}_k^n\|_0^2 - \|e_k^2\boldsymbol{Q}_k^{n-1}\|_0^2 + \|\boldsymbol{Q}_k^n - e_k^2\boldsymbol{Q}_k^{n-1}\|_0^2\right) - \\ &\Delta_t\left(\boldsymbol{b}^n, \boldsymbol{v}_h^n\right) = 0.\end{aligned} \tag{3.A.6}$$

Examining the final term in Eq. (3.A.6)*, noting through both Korn and Poincaré in-*

equalities there exists a $C_\Omega > 0$ *such that,*

$$\|\boldsymbol{v}_h^n\|_0 \leq C_\Omega \|\boldsymbol{D}\boldsymbol{v}_h^n\|_0$$

and applying Young's inequality (with $\epsilon = \eta\beta_0/C_\Omega$*), then*

$$\begin{aligned}(\boldsymbol{b}^n, \boldsymbol{v}_h^n) &\leq \frac{1}{2\epsilon}\|\boldsymbol{b}^n\|_0^2 + \frac{\epsilon}{2}\|\boldsymbol{v}_h^n\|_0^2 \\ &\leq \frac{C_\Omega}{2\eta\beta_0}\|\boldsymbol{b}^n\|_0^2 + \frac{\eta\beta_0}{2}\|\boldsymbol{D}\boldsymbol{v}_h^n\|_0^2 \end{aligned} \tag{3.A.7}$$

Combining Eq. (3.A.6) *and* (3.A.7) *and re-arranging terms, we observe that*

$$\begin{aligned}&\varrho\|\boldsymbol{v}_h^n\|_0^2 + E\|\boldsymbol{D}\boldsymbol{u}_h^n\|_0^2 + \eta\beta_0\Delta_t\|\boldsymbol{D}\boldsymbol{v}_h^n\|_0^2 + \sum_{k=1}^{N}\frac{\eta}{\beta_k e_k}\|\boldsymbol{Q}_k^n\|_0^2 \\ &\qquad \leq \varrho\|\boldsymbol{v}_h^{n-1}\|_0^2 + E\|\boldsymbol{D}\boldsymbol{u}_h^{n-1}\|_0^2 + \sum_{k=1}^{N}\frac{\eta}{\beta_k e_k}\|e_k^2\boldsymbol{Q}_k^{n-1}\|_0^2 + \Delta_t\frac{C_\Omega}{\eta\beta_0}\|\boldsymbol{b}^n\|_0^2\end{aligned}$$

Noting that $e_k \leq 1$*, applying induction, noting* $\boldsymbol{Q}_k^0 = \boldsymbol{0}$ *and utilizing the boundedness of* $\boldsymbol{b}$*, we arrive at the stability estimate.*

To show stability for the pressure, p_h^n, we assume that the spaces $\boldsymbol{\mathcal{V}}_0^h$ and $\mathcal{P}^h$ are inf-sup stable, satisfying the condition $(\beta > 0)$[204],

$$\forall q_h \in \mathcal{P}^h \;\; \exists\, \boldsymbol{w}_h \in \boldsymbol{\mathcal{V}}_0^h,\; \boldsymbol{w}_h \neq \boldsymbol{0} : \quad (q_h, \nabla_{\boldsymbol{X}} \cdot \boldsymbol{w}_h) \geq \beta\|q_h\|_0\|\boldsymbol{w}_h\|_1. \tag{3.A.8}$$

In addition, we assume there is a $\boldsymbol{v}_h^{-1} \in \boldsymbol{\mathcal{V}}_0^h$ satisfying

$$\|\Delta_t^{-1}(\boldsymbol{v}_h^0 - \boldsymbol{v}_h^{-1})\| \leq K \tag{3.A.9}$$

for some $K \geq 0$ (independent of Δ_t) and that the initial conditions satisfy the discrete weakform (with $\boldsymbol{Q}_k^{-1} = \boldsymbol{0}$ for $k = 1, \ldots N$),

$$\left(\varrho\delta_t\boldsymbol{v}_h^0, \boldsymbol{y}_h\right) + (\boldsymbol{\Sigma}^0, \nabla_{\boldsymbol{X}}\boldsymbol{y}_h) - (\boldsymbol{b}^0, \boldsymbol{y}_h) = 0 \tag{3.A.10}$$

for all weakly divergence free $\boldsymbol{w}_h \in \boldsymbol{\mathcal{V}}_{0,Div}^h$, with the space

$$\boldsymbol{\mathcal{V}}_{0,Div}^h = \left\{\boldsymbol{w}_h \in \boldsymbol{\mathcal{V}}_0^h \;\middle|\; (q_h, \nabla_{\boldsymbol{X}} \cdot \boldsymbol{v}_h^n) = 0, \quad \forall q_h \in \mathcal{P}^h\right\}.$$

With these assumptions, we can prove unconditional stability for the discrete model pressure.

Lemma 5. *Suppose the assumptions of Lemma 4 hold. Assuming there is a* $\boldsymbol{v}_h^{-1} \in \boldsymbol{\mathcal{V}}_0^h$

satisfying Eq. (3.A.9)*, that* $\boldsymbol{Q}_k^{-1} = \mathbf{0}$*, that*

$$\boldsymbol{b} \in \boldsymbol{W}^{1,\infty}([0,T];\boldsymbol{L}^2(\Omega_0)), \quad \sup_{t\in[0,T]} \|\boldsymbol{b}(t)\|_0 + \sup_{t\in[0,T]} \|\partial_t \boldsymbol{b}\|_0 \leq K'_{\boldsymbol{b}},$$

and that the spaces $\boldsymbol{\mathcal{V}}_0^h$ *and* $\mathcal{P}^h$ *are inf-sup stable, then* p_h^n *satisfies the stability estimate,*

$$\|p_h^n\|_0 \leq \frac{C}{\beta}\left(K + K_{\boldsymbol{b}} + t_n^{1/2}K'_{\boldsymbol{b}} + \|\boldsymbol{v}_h^0\|_0 + \|\boldsymbol{D}\boldsymbol{u}_h^0\|_0 + \|\boldsymbol{D}\boldsymbol{v}_h^0\|_0\right)$$

for a constant $C > 0$ *(independent of* h *and* δ_t*) and for each* $n = 1, \dots N_T$*.*

Proof of Lemma 5 4. *Looking at Eq.* (3.4.12)*, we first separate components of* $\boldsymbol{\Sigma}^n$*, choose* $\boldsymbol{w}_h = \mathbf{0}$ *and* $q_h = 0$ *and rearrange the equation. Applying Cauchy-Schwartz inequality, we can arrive at the following inequality.*

$$\begin{aligned}(p_h^n, \nabla_{\boldsymbol{X}} \cdot \boldsymbol{y}_h) =& (\boldsymbol{b}^n, \boldsymbol{w}_h) - \varrho\left(\delta_t \boldsymbol{v}_h^n, \boldsymbol{y}_h\right) - (E\boldsymbol{D}\boldsymbol{u}_h^n + \eta \hat{D}_n^{\alpha}(\boldsymbol{D}\boldsymbol{u}_h), \nabla_{\boldsymbol{X}}\boldsymbol{y}_h) \qquad (3.A.11)\\ \leq& \|\boldsymbol{b}^n\|_0\|\boldsymbol{y}_h\|_0 + \varrho\|\delta_t\boldsymbol{v}_h^n\|_0\|\boldsymbol{y}_h\|_0 + \|E\boldsymbol{D}\boldsymbol{u}_h^n + \eta\hat{D}_n^{\alpha}(\boldsymbol{D}\boldsymbol{u}_h)\|_0\|\nabla_{\boldsymbol{X}}\boldsymbol{y}_h\|_0\\ \leq& \left(\|\boldsymbol{b}^n\|_0 + \varrho\|\delta_t\boldsymbol{v}_h^n\|_0 + E\|\boldsymbol{D}\boldsymbol{u}_h^n\|_0 + \eta\beta_0\|\boldsymbol{D}\boldsymbol{v}_h^n\|_0 + \sum_{k=1}^{N}\eta\|\boldsymbol{Q}_k^n\|_0\right)\|\boldsymbol{y}_h\|_1\end{aligned}$$

Noting that the spaces of discrete solutions satisfy the inf-sup condition, the inequality in Eq. (3.A.11) *can be simplified to provide an upper bound on the pressure,* p_h^n*.*

$$\|p_h^n\|_0 \leq \frac{1}{\beta}\left(\|\boldsymbol{b}^n\|_0 + \varrho\|\delta_t\boldsymbol{v}_h^n\|_0 + E\|\boldsymbol{D}\boldsymbol{u}_h^n\|_0 + \eta\beta_0\|\boldsymbol{D}\boldsymbol{v}_h^n\|_0 + \sum_{k=1}^{N}\eta\|\boldsymbol{Q}_k^n\|_0\right) \qquad (3.A.12)$$

On the RHS of Eq. (3.A.12)*, the terms involving* $\boldsymbol{b}$ *remain bounded due to the implicit assumption that* $\boldsymbol{b} \in \boldsymbol{W}^{1,\infty}([0,T];\boldsymbol{L}^2(\Omega_0))$*. Moreover, from Lemma 4, we know there exists a* $C_0 > 0$ *(independent of* h *and* Δ_t*) such that,*

$$E\|\boldsymbol{D}\boldsymbol{u}_h^n\|_0 + \sum_{k=1}^{N}\eta\|\boldsymbol{Q}_k^n\|_0 \leq C_0\left(\|\boldsymbol{v}_h^0\|_0 + \|\boldsymbol{D}\boldsymbol{u}_h^0\|_0 + t_n^{1/2}K_{\boldsymbol{b}}\right). \qquad (3.A.13)$$

The stability estimate in Eq. (3.A.12) *relies on the boundedness of the discrete time derivative of* $\boldsymbol{v}_h^n$ *as well as the symmetric derivative of* $\boldsymbol{v}_h^n$*. To ensure these quantities remain bounded independent of* Δ_t*, we return to Eq.* (3.4.12)*. Subtracting the equation for* t_{n-1} *from that for* t_n*, letting* $\delta(\cdot)^n = (\cdot)^n - (\cdot)^{n-1}$*, and selecting the test functions* $\boldsymbol{w}_h = \mathbf{0}$*,* $\boldsymbol{y}_h = \delta\boldsymbol{v}_h^n$ *and* $q_h = 0$ *yields*

$$(\varrho\delta(\delta_t\boldsymbol{v}_h^n), \delta\boldsymbol{v}_h^n) + (\delta\boldsymbol{\Sigma}^n, \nabla_{\boldsymbol{X}}\delta\boldsymbol{v}_h^n) - (\delta\boldsymbol{b}^n, \delta\boldsymbol{v}_h^n) = 0 \qquad (3.A.14)$$

Applying the same approach as in Lemma 4 we can arrive at the following bound.

$$\begin{aligned}\varrho\|\delta\boldsymbol{v}_h^n\|_0^2 + E\|\boldsymbol{D}(\delta\boldsymbol{u}_h^n)\|_0^2 + \eta\beta_0\Delta_t\|\boldsymbol{D}(\delta\boldsymbol{v}_h^n)\|_0^2 + \sum_{k=1}^{N}\frac{\eta}{\beta_k e_k}\|\delta\boldsymbol{Q}_k^n\|_0^2 \\ \leq \varrho\|\delta\boldsymbol{v}_h^{n-1}\|_0^2 + E\|\boldsymbol{D}(\delta\boldsymbol{u}_h^{n-1})\|_0^2 + \sum_{k=1}^{N}\frac{\eta}{\beta_k e_k}\|e_k^2\delta\boldsymbol{Q}_k^{n-1}\|_0^2 + \Delta_t\frac{C_\Omega}{\eta\beta_0}\|\delta\boldsymbol{b}^n\|_0^2 \\ \leq \varrho\|\delta\boldsymbol{v}_h^0\|_0^2 + E\|\boldsymbol{D}(\delta\boldsymbol{u}_h^0)\|_0^2 + \sum_{m=1}^{n}\Delta_t\frac{C_\Omega}{\eta\beta_0}\|\delta\boldsymbol{b}^m\|_0^2 \end{aligned} \tag{3.A.15}$$

Dividing by Δ_t^2 *and noting* $\delta_t\boldsymbol{u}_h^n = \boldsymbol{v}_h^n$ *for any* n*, we observe that the remaining terms in Eq.* (3.A.12) *are bounded by given data,* e.g.

$$\varrho\|\delta_t\boldsymbol{v}_h^n\|_0^2 + E\|\boldsymbol{D}\boldsymbol{v}_h^n\|_0^2 \leq \varrho K^2 + E\|\boldsymbol{D}\boldsymbol{v}_h^0\|_0^2 + \sum_{m=1}^{n}\Delta_t\frac{C_\Omega}{\eta\beta_0}\|\delta_t\boldsymbol{b}^m\|_0^2. \tag{3.A.16}$$

Combining these results, along with bounds on $\boldsymbol{b}$ *and it's derivative, we arrive at the stability estimate.*

3.B Optimal Prony Series Parameters for Approximating the Caputo Fractional Derivative

In section 3.2.5, we presented the method for optimizing the parameters of the Prony series for a defined time scale proportional to the duration of the simulation. In practice, we observed in our examples (section 3.5 and 3.6) that better convergence rates can be achieved by scaling the time scale for which the Prony series parameters were mapped to. In every case, the convergence rates were significantly improved by lengthening the time scale by a factor of 10 or even 100. This was first observed as a consequence of the Geo et al. example (section 3.6), where the convergence response can be worse initially as the number of Prony terms increase. This is a results of the increase in value of $C(\boldsymbol{\beta}, \boldsymbol{\tau})$, which results in slow convergence until the approximation error hits the bounds of the error estimate in Theorem 3. Numerical, lengthening the time scale for mapping the Prony series parameters increases the time constants τ_k and decreases the weights β_k. We can observe from Theorem 3 that the error bound, specific β_0 and $C(\boldsymbol{\beta}, \boldsymbol{\tau})$ reduces as a response, decreasing the overall error of the approximation.

As this effect appears to be problem dependent (more significant in Gao et al. Example 1[69]), we tested this in more detail using two polynomial examples: 1) the decaying oscillating function like polynomial presented in Fig. 3.5.1, which behaves with short variable base frequencies and 2) a polynomial that's monotonically increasing with highly exponential behavior, which behaves with single long base frequency (i.e. fitted to $e^{6*t} - 1$). The convergence response was tested for $\alpha \in \{0.1, 0.4, 0.8\}$ and $N \in \{3, 6, 9, 12\}$ with time scaling of 1, 10, and 100.

The overall response is quite similar. Most important is that lengthening the time scale by a factor of 10 always results in better convergence and overall error, sometimes by two order of magnitude. Results from scaling by a factor of 100 is more variable. Most noticeably, the lower-bound with a scaling of 100 can be much worse at larger N. However, the convergence at larger Δ_t can be significantly better. Most noticeably, the L^2-norm in the example 2 can be 3 magnitude better at $\Delta_t = 10^-3$ for $\alpha = 0.8$ and N = 12 with a a scaling of 100. However, also note that with a scaling of 10, the L^2-norm eventually surpasses the scaling of 100 after it has plateaued. Here, the gain in convergence at large Δ_t surpasses the 1 magnitude gain in the lowerbound as a result of the truncation error (Lemma 1), which requires 1.5 more magnitude in Δ_t refinement. In contrast, for example 1, we observe that the gain in convergence initially is much less significant, and the truncation error is around 2 magnitudes larger.

Clearly, these results are also problem dependent. Part of this dependency can be observed from Theorem 3, by the weights of $[|f'(0)| + \|f''\|_{0,1}]$ and $\|f\|_{W^{3,\infty}(0,T)}$ on ϵ and $C(\boldsymbol{\beta}, \boldsymbol{\tau})$ respectively. Example 1 starts at zero, increasing quickly then oscillating until it decay exponentially to zero. Thus, $[|f'(0)| + \|f''\|_{0,1}]$ is large and $\|f\|_{W^{3,\infty}(0,T)}$, which is the norm on the last time step is small, emphasizing the importance of ϵ in the error estimate. Thus, scaling the time scale, which improves the $C(\boldsymbol{\beta}, \boldsymbol{\tau})$ terms, sees much less benefit. In contrast, examples 2 increase exponentially from zero, resulting in $\|f\|_{W^{3,\infty}(0,T)}$ being very large, allowing it to see more benefit from scaling the time scale. Another more physical reason is that example one oscillating during the duration of the simulation, with base frequencies on par with the time domain of the simulation, where as example two increase monotonically, with base frequencies much greater than the time domain of the simulation.

In summary, the optimal Prony terms from section 3.2.5 can still be improved. However, the choice of further optimizing these parameters are quite subjective. The choice dependent strongly on the Δ_t used in the simulation and even behavior of the function being differentiated. We, in our examples, observed that scaling the time scaling by 10 almost always improves the results. More optimal scalings remain to be investigated. For this reason, we have chosen to a time scaling of 10 for the polynomial example (section 3.5) and 100 for the Gao *et al.* example (section 3.6).

4 MRE in Nonlinear Viscoelastic Materials Under Load

The main challenge that this thesis aims to address is, in essence, the impact of large deformations on MRE measurements in the liver. This chapter is of paramount importance in this regard, as it addresses this challenge in a tissue-mimicking material (poly-vinyl alcohol, PVA).

Perturbation theory is used to relate low amplitude wave propagation to large deformations (section 4.2.1), leading to a new set of equations of motion that can be used in MRE analysis. This derivation is similar to the one presented in section 2.4, but it additionally incorporates viscoelasticity. Furthermore, simple examples are considered (section 4.2.1.3), in order to provide a more intuitive understanding. As for the classical Eq. (2.4.4) of motion, the new equations are complete only by incorporating knowledge on the deformation and material constitutive law. The complexity that the deformation problem can pose is reduced by focusing on simple uniaxial compressions, which allow for an easy identification of the deformation gradient. The constitutive law, however, requires in depth investigation of the material in a rheological setup, which is addressed in section 4.2.2. MRE experiments that investigate wave propagation in compressed PVA (section 4.2.3) shown that measurements are biased by the deformation. However, this bias can be successfully accounted for by combining the knowledge on deformation and material constitutive model (section 4.3).

Overall, the study here demonstrates the effect that large deformations have on MRE measurements, both theoretically and empirically. Furthermore, it builds a pipeline that can be used to undo the deformation bias, with three main components: the theoretical part, which may differ slightly to the one presented here (e.g. when considering non-viscoelastic materials), the deformation part, which can become intricate in complex loading problems, and the constitutive model part, which is specific to the material used.

This chapter has been published as a self standing-article in Capilnasiu et al.[30]. The candidate contributed to the design of the experiments, analysis and interpretation of research data, and drafting the manuscript. A supplementary material (section 4.C)

has been included at the end of the chapter. This additional section briefly presents some obstacles encountered when handling a range of tissue-mimicking materials, with the purpose of sharing insights into MRE phantom design.

Abstract

Characterisation of soft tissue mechanical properties is a topic of increasing interest in translational and clinical research. Magnetic Resonance Elastography (MRE) has been used in this context to assess the mechanical properties of tissues *in vivo* non-invasively. Typically these analyses rely on linear viscoelastic wave equations to assess material properties from measured wave dynamics. However, deformations that occur in some tissues (*e.g.* liver during respiration, heart during the cardiac cycle, or external compression during a breast exam) can yield *loading bias*, complicating the interpretation of tissue stiffness from MRE measurements. In this paper, it is shown how combined knowledge of a material's rheology and loading state can be used to eliminate loading bias and enable interpretation of *intrinsic* (unloaded) stiffness properties. Equations are derived utilising perturbation theory and Cauchy's equations of motion to demonstrate the impact of loading state on periodic steady-state wave behaviour in nonlinear viscoelastic materials. These equations demonstrate how loading bias yields apparent material stiffening, softening and anisotropy. MRE sensitivity to deformation is demonstrated in an experimental phantom, showing a loading bias of up to 2 fold. From an unbiased stiffness of 4910.4 ± 635.8 Pa in unloaded state, the biased stiffness increases to 9767.5 ± 1949.9 Pa under a load of $\approx 34\%$ uniaxial compression. Integrating knowledge of phantom loading and rheology into a novel MRE reconstruction, it is shown that it is possible to characterise intrinsic material characteristics, eliminating the loading bias from MRE data. The framework introduced and demonstrated in phantoms illustrates a pathway that can be translated and applied to MRE in complex deforming tissues. This would contribute to a better assessment of material properties in soft tissues employing elastography.

4.1 Introduction

Diagnosis and therapy planning often depend on developing an accurate understanding of the state of a patient's disease. Complex alterations occur in diseased tissue, depending on a range of factors such as changes to protein isoforms, alterations in protein density, extracellular matrix reorganization, inflammation, etc. These modifications fundamentally impact tissue mechanical properties, triggering changes in stiffness, elasticity and viscosity[8,277,278]. The ability to detect changes in tissue mechanical properties *in vivo* has the potential to significantly benefit clinical medicine, enabling a more thorough assessment of pathology as well as monitoring of treatment progression. This potential has led to the development of a number of approaches for the non-invasive assessment of tissue mechanics.

Manual palpation is a classical approach of inspecting tissue for changes in elasticity in accessible organs[181,265]. Advancements in medical imaging have led to the development

of elastography – a modern quantitative technique for assessing the mechanical properties of internal organs. Elastography imaging is usually achieved using Ultrasound or Magnetic Resonance Imaging (see[32] for a review), enabling the determination of tissue properties *in vivo*. Elastography imaging focuses on observing waves as they traverse through tissues, thus allowing quantification of strain response due to an excitation. In the case of Magnetic Resonance Elastography (MRE), low amplitude harmonic waves ($10 - 1000$ Hz, $30 - 80$ Hz *in vivo*) are produced on the body and subsequently imaged in three-dimensions[62,157]. Harmonic wave motion is then related to local tissue properties, in most cases, through linear viscoelastic wave equations[77]. MRE has been successfully employed for a range of tissues – including brain[88,128,223], liver[114–116,128] and breast[229,230,233,252] – showing contrast between diseased and healthy tissue as well as providing resolution of apparent tissue anisotropy[203]. More recently, it has also been applied to heart[44,56,57,130–132,209,231], skeletal muscles[86,87], and other soft tissues, reviewed in[62,157,159].

While interpreting stiffness measures in organs, such as the liver, has shown diagnostic value, a challenge yet to be addressed is the impact of macroscale deformations on wave propagation behaviour. Broadly, by looking at the 1D wave equation $\partial^2 u/\partial t^2 = c^2 \partial^2 u/\partial x^2$, term $c = \sqrt{T/\rho}$ depends on tension T and linear density ρ and is scaling the spatial second derivative of displacement u. The resultant force term on the right-hand side balances the acceleration term on the left hand side, leading to the phase velocity increasing with higher tension. Elastic, hyperelastic and viscoelastic nonlinear materials would exhibit this effect. This is relevant in the context of tissues that undergo natural deformations (e.g: the heart muscle during the cardiac cycle[7], the liver during respiration[179], etc) and tissues that undergo imposed deformations (e.g. breast during MRE scans[230,233]). As many tissues are known to exhibit significant nonlinearity[70,78,108,146,180,185,244] under physiological conditions, both natural and imposed deformation can result in *loading bias* – an apparent stiffness that is a conglomerate measure of the intrinsic material properties and current kinematic state. For instance, the nonlinearity arising from compressive strain was quantified in ex-vivo bovine liver samples using MRE measurements[40]. Hence, mixtures of patient-specific kinematics and intrinsic tissue properties are non-trivial and presumably result in a reduction of clinical specificity.

In this paper, the harmonic perturbation of Cauchy's equations of motion for a general incompressible nonlinear viscoelastic material is examined, in order to understand the links between intrinsic properties and kinematics in MRE. From this analysis, a set of governing equations are derived, illustrating the general impact of large deformation on the motion of harmonic waves. Importantly, these equations enable the elimination of loading bias and therefore retrieval of intrinsic properties when large-scale deformation and constitutive behaviour are known. Theoretical test cases are presented, showing the ability of deformation to yield apparent increase, decrease and anisotropy

in materials. In order to demonstrate the applicability of these perturbed equations, experiments were performed in polyvinyl alcohol (PVA) phantoms. Rheological tests were performed to characterise material behaviour, and loaded phantoms were imaged using MRE. Results show the capacity of these equations to correct for the complex dynamics of wave motion in deformed materials. To the authors' knowledge, this is the first cross-validation study linking mechanical characterisation of a material in rheology with wave motion through the deformed material in MRE. The developments presented provide a key step towards improving the estimation of material properties in soft tissues, using elastography.

As a starting point, section 4.2.1 presents perturbation theory employed within Cauchy's equations of motion. The perturbed equations are analysed in the context of a general viscoelastic material under load, further leading to the derivation of apparent stiffness moduli influenced by large deformations and material constitutive law. For exemplification purposes, an idealised case of harmonic wave motion traversing a uniformly compressed Neo-Hookean material is presented. Experiments are employed to test the theoretical ground developed. In section 4.2.2, PVA phantoms are tested in a rheological setup, to determine the material governing law. In section 4.2.3, MRE data is acquired in PVA phantoms at different uniaxial compression levels. The knowledge on rheological behaviour and deformation are integrated into MRE data analysis, in order to undo the loading bias. The experimental results are presented in section 4.3. Particularly, the estimation of the intrinsic stiffness of PVA is presented in section 4.3.3. The theoretical framework presented in this study could be extended to *in vivo* MRE data analysis.

4.2 Materials and Methods

4.2.1 Harmonic Wave Motion in Deformed Nonlinear Viscoelastic Materials

MRE relies on the analysis of small amplitude harmonic waves traversing through materials. As materials undergo deformation, wave behaviour is impacted[248]. One option to understand the relationship between large scale deformation and small scale wave behaviour is perturbation analysis. After covering notation in section 4.2.1.1, this section reviews perturbation results for Cauchy's equations (section 4.2.1.2) considering the particular case of a nonlinear viscoelastic material. Example cases are then highlighted (section 4.2.1.3), illustrating the impact of load on the apparent stiffness characteristics stemming from MRE waves.

4.2.1.1 Kinematics, Harmonic Wave Motion and Notation

Here we briefly review the basic kinematics in large deformation mechanics in order to later describe the macroscale deformation of phantom and tissue material subjected to

MRE. For more complete dispositions, see for example[19,83,104,156,260]. The motion of a solid body, denoted by the region, $\Omega_0 \subset \mathbb{R}^d$, is characterised by the displacement field $\boldsymbol{U} : \Omega_0 \times [0,T] \to \mathbb{R}^d$. In this case, any reference point $\boldsymbol{X} \in \Omega_0$ may be deformed to its physical position by the diffeomorphic Lagrangian mapping $\mathcal{L} : \Omega_0 \times [0,T] \to \mathbb{R}^d$ so that its position at a time $t \in [0,T]$ is given by

$$\boldsymbol{x} = \mathcal{L}(\boldsymbol{X}, t) = \boldsymbol{U}(\boldsymbol{X}, t) + \boldsymbol{X}, \quad \forall \boldsymbol{X} \in \Omega_0.$$

Due to the Lagrangian mapping, note that any m-dimensional function $\boldsymbol{v} : \Omega_0 \times [0,T] \to \mathbb{R}^m$ can be written as a function of the deformed domain $\Omega(t)$, e.g. $\widetilde{\boldsymbol{v}} : \Omega \to \mathbb{R}^m$, with the understanding that $\widetilde{\boldsymbol{v}}(\boldsymbol{x}, t) = \boldsymbol{v}(\mathcal{L}^{-1}(\boldsymbol{x}, t), t)$. For ease of notation, the $\widetilde{\cdot}$ is dropped where there is clear distinction.

The stresses resulting from material deformation can be separated into deviatoric and hydrostatic components. For the latter, the effect is quantified using the hydrostatic pressure P, which ensures some constraint on the volume or pressure-volume relation. The deviatoric components are, in turn, related to shape changes (or strains and strain history).

Important quantities for mechanics are the deformation gradient tensor $\boldsymbol{F}$ and its determinant J:

$$\boldsymbol{F} = \nabla_0 \boldsymbol{U} + \boldsymbol{I}, \quad J(\boldsymbol{F}) = \det \boldsymbol{F}.$$

Here ∇_0 refers to the gradient operator taken with respect to coordinates of Ω_0, so that $(\nabla_0)_k = \partial / \partial X_k$. For later use, $J = J(\boldsymbol{F})$ is implied.

When relating kinematics and kinetics, the right or left Cauchy Green strains

$$\boldsymbol{C} = \boldsymbol{F}^T \boldsymbol{F}, \quad \boldsymbol{B} = \boldsymbol{F} \boldsymbol{F}^T$$

are often considered. These may also be defined in terms of their isochoric variants[19,189] as

$$\hat{\boldsymbol{F}} = J^{-1/d} \boldsymbol{F}, \quad \hat{\boldsymbol{C}} = \hat{\boldsymbol{F}}^T \hat{\boldsymbol{F}}, \quad \hat{\boldsymbol{B}} = \hat{\boldsymbol{F}} \hat{\boldsymbol{F}}^T,$$

which are invariant to changes in volumetric properties of the material, *i.e.* $\hat{\boldsymbol{C}}(a\boldsymbol{F}) = \hat{\boldsymbol{C}}(\boldsymbol{F})$ for a real positive scalar $a \in \mathbb{R}^+$[104].

A set of invariants is associated with these quantities. Here the first and second invariants of any 2nd order tensor $\boldsymbol{A} \in \mathbb{R}^{m \times m}$ are defined as in[19]

$$I_{\boldsymbol{A}} = \boldsymbol{A} : \boldsymbol{I}, \quad II_{\boldsymbol{A}} = \boldsymbol{A} : \boldsymbol{A}.$$

For later clarity, the double contraction ':' is used as defined in[19], *e.g.* the contraction

of 2nd order square tensors $\boldsymbol{A}, \boldsymbol{B} \in \mathbb{R}^{m\times m}$ becomes a scalar [1]

$$\boldsymbol{A} : \boldsymbol{B} = A_{ij}B_{ij},$$

and the contraction of a 4th order tensor $\boldsymbol{\mathcal{A}} \in \mathbb{R}^{m\times m\times m\times m}$ and a 2nd order tensor $\boldsymbol{B}$ yields a 2nd order tensor in $\mathbb{R}^{m\times m}$ [2]

$$(\boldsymbol{\mathcal{A}} : \boldsymbol{B})_{ij} = A_{ijkl}B_{kl}.$$

For further use throughout the paper, the multiplication of 2nd and 4th order tensors $\boldsymbol{A\mathcal{A}}$ or $\boldsymbol{\mathcal{A}B}$ is defined to take place over the last index of the first quantity and first index of the second quantity, *i.e.*

$$(\boldsymbol{A\mathcal{A}})_{ijkl} = A_{is}\mathcal{A}_{sjkl}, \qquad (\boldsymbol{\mathcal{A}B})_{ijkl} = \mathcal{A}_{ijks}B_{sl}. \tag{4.2.1}$$

Finally, the derivative of a 2nd order tensor with respect to another is defined as

$$(\nabla_{\boldsymbol{B}}\boldsymbol{A})_{ijkl} = \frac{\partial A_{ij}}{\partial B_{kl}}.$$

MRE relies on the propagation of shear waves through the body, assumed to reach a harmonic steady state. Being wave motion, these deformations are assumed to be linear and small. The large deformation $\boldsymbol{U}$ is perturbed by these small wave deformations

$$\boldsymbol{u}^{\varepsilon} : \Omega_0 \times [0,T] \to \mathbb{R}^d, \tag{4.2.2}$$

where the scale of the perturbations is much smaller than the dominant length scale of the body or the large displacement it undergoes. When the perturbations are periodic-in-time and have reached a steady-state, the deformations and pressures can be written as

$$\boldsymbol{u}^{\varepsilon} = \mathrm{Re}\{\boldsymbol{u}_c e^{i\omega t}\}, \qquad p^{\varepsilon} = \mathrm{Re}\{p_c e^{i\omega t}\}, \tag{4.2.3}$$

where $\boldsymbol{u}_c = \boldsymbol{u}_r + i\boldsymbol{u}_i$ $(\boldsymbol{u}_r, \boldsymbol{u}_i : \Omega_0 \to \mathbb{R}^d)$ and $p_c = p_r + ip_i$ $(p_r, p_i : \Omega_0 \to \mathbb{R})$ give the complex periodic steady-state behaviour with real and imaginary parts given by subscripts r and i, respectively.

4.2.1.2 Perturbation of Cauchy's Equations of Motion

For an incompressible body, at any time $t \in [0,T]$, motion of Ω_0 satisfies Cauchy's first law (conservation of momentum) and conservation of mass shown in Eq. (4.2.4), respectively (see[19,104,156,189]):

[1] Einstein summation over repetitive indices is assumed.

[2] Only dimensionality m was used as this case is relevant to this work, particularly $m = 3$.

$$\rho J \partial_{tt} \boldsymbol{U} - \nabla_0 \cdot (\boldsymbol{F}\boldsymbol{S}) = \boldsymbol{0} \quad \text{on} \quad \Omega_0, \tag{4.2.4a}$$

$$J - 1 = 0 \quad \text{on} \quad \Omega_0. \tag{4.2.4b}$$

Here, ρ is the material density, ∂_{tt} is the second time derivative and $\boldsymbol{S}_e = \boldsymbol{S}(P, \boldsymbol{C})$ is the second Piola-Kirchhoff (PK2) stress tensor depending on the hydrostatic pressure, P, and the right Cauchy-Green tensor, $\boldsymbol{C}$.

The PK2 stress can be characterised as elastic, hyperelastic, viscoelastic, etc., depending on the constitutive relation that describes the material. A hyperelastic material, for example, can be written as a function of $\boldsymbol{C}$ (or other strain metrics) and space ($\boldsymbol{X}$). In contrast, a viscoelastic material additionally depends on time (t). We recall briefly that, for hyperelastic materials – such as those commonly applied in biomechanics – $\boldsymbol{S}_e$ is given as the derivative of a governing hyperelastic strain energy function, $W = W_e(\boldsymbol{C})$[19], with respect to the right Cauchy Green tensor $\boldsymbol{C}$, *i.e.*

$$\boldsymbol{S}_e = 2\nabla_{\boldsymbol{C}} W_e, \quad S_{e,ij} = 2\frac{\partial W_e}{\partial C_{ij}}. \tag{4.2.5}$$

This model is extensively applied in nonlinear biomechanics – for example in simulations of the heart[97,166,167,184,261], breast[68,205,207], arterial wall[74,99,104], etc. – where specific material response is usually defined through biorheological experiments.

The simplest material models are purely elastic, based on spring rheological elements. Complementary, pure viscosity is based solely on dash-pot elements. Biological tissues usually exhibit viscoelasticity, hence a suitable tissue model should consider a combination of these springs and dash-pots. For instance, the Maxwell model is formed by considering a spring and dash-pot connected in series, whereas the Kelvin-Voigt model is formed by considering a spring and dash-pot connected in parallel. These types of models have been analysed in literature[10,15,147], but have shortcomings in predicting creep (Maxwell model) or stress relaxation (Kelvin-Voigt model)[10,146]. While the Maxwell constitutive equation was found to be better suited for modelling fluids[230,251], the Kelvin-Voigt constitutive equation was employed for purposes similar to ours, modelling soft tissues subjected to elastography testing[114,116,230,233] (albeit not considering the effects of large deformations on the wave behaviour). However, the Kelvin-Voigt model is not able to accurately capture the power-law dependence on frequency that is usually observed in tissues[39,182,217,233]. Thus, an adaptation of this model is commonly used, which replaces the dash-pot with a spring-pot. This form was observed to describe tissue better[127].

To capture the viscoelastic behaviour exhibited generally by tissues and polymers, we proceed by assuming that the PK2 stress can be decomposed into an additive sum of

elastic, viscoelastic and hydrostatic components, *i.e.*

$$\boldsymbol{S} = \boldsymbol{S}_e + \boldsymbol{S}_p + D_t^\alpha \boldsymbol{S}_v. \tag{4.2.6}$$

The elastic part $\boldsymbol{S}_e$ is defined through a hyperelastic strain energy function $W_e(\boldsymbol{C})$ as in Eq. (4.2.5), the hydrostatic part as $\boldsymbol{S}_p = JP\boldsymbol{C}^{-1}$, and the viscoelastic part is defined using the Caputo formulation[31] of the fractional order derivative:

$$D_t^\alpha \boldsymbol{S}_v = \frac{1}{\Gamma(1-\alpha)} \int_0^t \frac{1}{(t-z)^\alpha} \partial_t \boldsymbol{S}_v(z)\, \mathrm{d}z.$$

Here, $\boldsymbol{S}_v$ depends on a viscoelastic strain energy function such as $\boldsymbol{S}_v = 2\nabla_{\boldsymbol{C}} W_v$. Considering the coefficient of derivation α to be 0, then the viscoelastic stress $\boldsymbol{S}_v$ acts as a hyperelastic term, while $\alpha = 1$ indicates the first order derivative $\partial_t \boldsymbol{S}_v$. Intermediate values of α would lead to non-trivial transitional results between $\boldsymbol{S}_v$ and $\partial_t \boldsymbol{S}_v$. Therefore, this formulation of the viscoelastic term leads to a fractional nonlinear Kelvin-Voigt type of model and the PK2 tensor for our viscoelastic material becomes

$$\begin{aligned} \boldsymbol{S} &= 2\nabla_{\boldsymbol{C}} W_e + 2D_t^\alpha(\nabla_{\boldsymbol{C}} W_v) + JP\boldsymbol{C}^{-1}, && \text{(4.2.7a)} \\ S_{ij} &= 2\frac{\partial W_e}{\partial C_{ij}} + 2D_t^\alpha\left(\frac{\partial W_v}{\partial C_{ij}}\right) + JPC_{ij}^{-1}. && \text{(4.2.7b)} \end{aligned}$$

In order to investigate the effect of deformation on wave behaviour, we consider the case where high frequency / low amplitude harmonic waves (see Eq. (4.2.2)) are imposed onto our body that satisfies the set of Eq. (4.2.4). For our purposes, we assume that the introduction of these micro-deformations $\boldsymbol{u}^\varepsilon$ does not disrupt the natural state of macro-deformation $\boldsymbol{U}$, such that the total observed state $(\boldsymbol{U}^\varepsilon, P^\varepsilon)$ can be characterised by

$$\begin{aligned} \boldsymbol{U}^\varepsilon(\boldsymbol{X}, t) &= \boldsymbol{U}(\boldsymbol{X}, t) + \boldsymbol{u}^\varepsilon(\boldsymbol{X}, t), \\ P^\varepsilon(\boldsymbol{X}, t) &= P(\boldsymbol{X}, t) + p^\varepsilon(\boldsymbol{X}, t), \end{aligned} \tag{4.2.8}$$

with $(\boldsymbol{U}, P)$ satisfying the original Eq. (4.2.4) (without perturbation conditions) and with $(\boldsymbol{U}^\varepsilon, P^\varepsilon)$ satisfying a perturbed version of Eq. (4.2.4), *i.e.*

$$\begin{aligned} \rho J^\varepsilon \partial_{tt} \boldsymbol{U}^\varepsilon - \nabla_0 \cdot (\boldsymbol{F}^\varepsilon \boldsymbol{S}^\varepsilon) = \boldsymbol{0} \quad \text{on} \quad \Omega_0, && \text{(4.2.9a)} \\ J^\varepsilon - 1 = 0 \quad \text{on} \quad \Omega_0, && \text{(4.2.9b)} \end{aligned}$$

where superscript ε indicates quantities dependent on the perturbed state variables.

A simplification of the set of Eq. (4.2.9) can be achieved by expanding about the state

variable $\boldsymbol{U}$ and then linearising with respect to the small perturbations $\boldsymbol{u}^{\varepsilon}$, $p^{\varepsilon 248}$. For completeness, details about the expansion and linearisation processes can be found in Appendix 4.A. Considering the case of harmonic waves, a set of periodic nonlinear viscoelastic wave equations can be derived in the reference domain Ω_0. By re-casting the reference frame gradient and divergence operators into their physical domain counterparts, the set of Eq. (4.2.9) can be transformed into the physical domain as:

$$-\rho\omega^2\boldsymbol{u}_c - \nabla\cdot[(\boldsymbol{\mathcal{G}}' + i\boldsymbol{\mathcal{G}}'') : \nabla\boldsymbol{u}_c + p_c\boldsymbol{I}] = \boldsymbol{0}, \tag{4.2.10a}$$

$$\nabla\cdot\boldsymbol{u}_c = 0, \tag{4.2.10b}$$

where $\nabla = \partial/\partial\boldsymbol{x}$ on Ω. Here $\boldsymbol{\mathcal{G}}'$ and $\boldsymbol{\mathcal{G}}''$ are the real and imaginary stiffness moduli influencing the apparent wave dynamics of $\boldsymbol{u}_c$ and taking the form of 4^{th} order tensors:

$$\mathcal{G}'_{ijml} = \frac{1}{J}\Big[\boldsymbol{F}\nabla_{\boldsymbol{F}}(\boldsymbol{S}_e + \omega^{\alpha}\cos\Big(\frac{\pi\alpha}{2}\Big)\boldsymbol{S}_v + \boldsymbol{S}_p) + \boldsymbol{\mathcal{I}}\boldsymbol{S}\Big]_{ismn}F_{ln}F_{js}, \tag{4.2.11a}$$

$$\mathcal{G}''_{ijml} = \frac{\omega^{\alpha}}{J}\sin\Big(\frac{\pi\alpha}{2}\Big)\left(\boldsymbol{F}\nabla_{\boldsymbol{F}}\boldsymbol{S}_v\right)_{ismn}F_{ln}F_{js}, \tag{4.2.11b}$$

where $\boldsymbol{F}$, $\boldsymbol{S}_e$, and $\boldsymbol{S}_v$ depend on the unperturbed macro-deformation $\boldsymbol{U}$ and hydrostatic pressure and P. In the absence of deformation, under the assumption of an isotropic material defined by a standard law (*e.g.* a neo-Hookean model for $\boldsymbol{S}_e$ and $\boldsymbol{S}_v$), these stiffness moduli are simply given by $\boldsymbol{\mathcal{G}}'+i\boldsymbol{\mathcal{G}}'' = G^*(\boldsymbol{\mathcal{I}}+\widetilde{\boldsymbol{\mathcal{I}}})$, where G^* is the true complex shear modulus characterising the material, $\mathcal{I}_{ijkl} = \delta_{ik}\delta_{jl}$ and $\widetilde{\mathcal{I}}_{ijkl} = \delta_{il}\delta_{jk}$. The wave dynamics become symmetric, since $(\boldsymbol{\mathcal{I}} + \widetilde{\boldsymbol{\mathcal{I}}}) : \nabla\boldsymbol{u}_c = \nabla\boldsymbol{u}_c + \nabla\boldsymbol{u}_c^T$. However, under deformation, the components of $\nabla\boldsymbol{u}_c$ are scaled in a non-trivial way. By understanding the form of the scaling, influencing the $\boldsymbol{\mathcal{G}}'$ and $\boldsymbol{\mathcal{G}}''$ moduli, the bias introduced by deformation on the wave behaviour can be predicted. Furthermore, the deformation can be undone, that is, the moduli that reflect the undeformed state can be recovered.

4.2.1.3 Loading Bias of Planar Shear Waves in Pure Compression

For an intuitive illustration, let us consider the case of a simple isotropic neo-Hookean material described by the strain energy function

$$W_e(P, \boldsymbol{F}) = \frac{\mu_e}{2}(I_{\hat{\boldsymbol{C}}} - 3),$$

where μ_e is the elastic material parameter. The elastic stress is derived to be

$$\boldsymbol{S}_e = \frac{\mu_e}{J^{2/3}}\left(\boldsymbol{I} - \frac{I_{\boldsymbol{C}}}{3}\boldsymbol{C}^{-1}\right).$$

The viscous term is assumed to be zero, i.e. $\boldsymbol{S}_v = \boldsymbol{0}$. Under these assumptions, the

real modulus $\boldsymbol{\mathcal{G}}'$ becomes

$$\mathcal{G}'_{ijml} = \frac{1}{J}\Bigg[\mu_e \hat{B}_{lj}\delta_{im} - \frac{2\mu_e}{3}(\hat{B}_{ij}\delta_{ml} + \hat{B}_{ml}\delta_{ij}) \\ +\delta_{ml}\delta_{ij}\left(\frac{2\mu_e I_{\hat{\boldsymbol{B}}}}{9} + PJ\right) + \delta_{mj}\delta_{il}\left(\frac{\mu_e I_{\hat{\boldsymbol{B}}}}{3} - PJ\right)\Bigg]. \tag{4.2.12}$$

To better understand the changes introduced by large deformations $\boldsymbol{U}$ on the wave dynamics, we analyse the case of plane waves through a material under pure compression. Thus, considering a cuboid that is compressed along the height ($\boldsymbol{e}_3$ direction), imposing incompressibility, the deformation $\boldsymbol{U}$ is described by

$$\boldsymbol{U} = \left[(1/\sqrt{\lambda} - 1)X_1,\ (1/\sqrt{\lambda} - 1)X_2,\ (\lambda - 1)X_3\right]^T,$$

where λ is the ratio of the final height over the initial height (*i.e.* $\lambda < 1$). In this case, the hydrostatic pressure is a constant given by $P = \mu_e(1/\lambda - \lambda^2)/3$ and the kinematic tensors describing this deformation are

$$\boldsymbol{F} = \begin{pmatrix} \frac{1}{\sqrt{\lambda}} & 0 & 0 \\ 0 & \frac{1}{\sqrt{\lambda}} & 0 \\ 0 & 0 & \lambda \end{pmatrix}, \tag{4.2.13}$$

$$\boldsymbol{B} = \hat{\boldsymbol{B}} = \boldsymbol{C} = \hat{\boldsymbol{C}} = \begin{pmatrix} \frac{1}{\lambda} & 0 & 0 \\ 0 & \frac{1}{\lambda} & 0 \\ 0 & 0 & \lambda^2 \end{pmatrix},$$

with $J = 1$.

A pure shear wave which will perturb the macro deformation $\boldsymbol{U}$ can be written as

$$\boldsymbol{u}_c = \begin{pmatrix} u_1(x_2, x_3) \\ u_2(x_1, x_3) \\ u_3(x_1, x_2) \end{pmatrix}. \tag{4.2.14}$$

This form ensures that $\nabla \boldsymbol{u}_c$ has only off diagonal components, i.e. $\nabla \boldsymbol{u}_c : \boldsymbol{I} = 0$, thus satisfying the incompressibility assumption of the material. Since the deformation considered employs no shearing (*i.e* no off-diagonal components), then also $\boldsymbol{B} : \nabla \boldsymbol{u}_c = 0$ and therefore this wave form allows for simplifications when being contracted, as needed in Eq. (4.2.10), with the stiffness modulus by removing the terms containing δ_{ml} and $\hat{B}_{ml}$ from section 4.2.1.3:

$$\boldsymbol{\mathcal{G}}' : \nabla \boldsymbol{u}_c = \frac{1}{J}\Big[\mu_e \nabla \boldsymbol{u}_c \boldsymbol{B} + \nabla \boldsymbol{u}_c^T \Big(\frac{\mu_e I_{\hat{\boldsymbol{B}}}}{3} - PJ\Big)\Big].$$

Additionally, under the divergence operator, $\nabla \boldsymbol{u}_c^T$ vanishes (together with $I_{\hat{\boldsymbol{B}}}$, P and J, which are constant in space) and thus the elastic contribution can be further simplified to

$$\nabla \cdot (\boldsymbol{\mathcal{G}}' : \nabla \boldsymbol{u}_c) = \nabla \cdot (\mu_e \nabla \boldsymbol{u}_c \boldsymbol{B}). \tag{4.2.15}$$

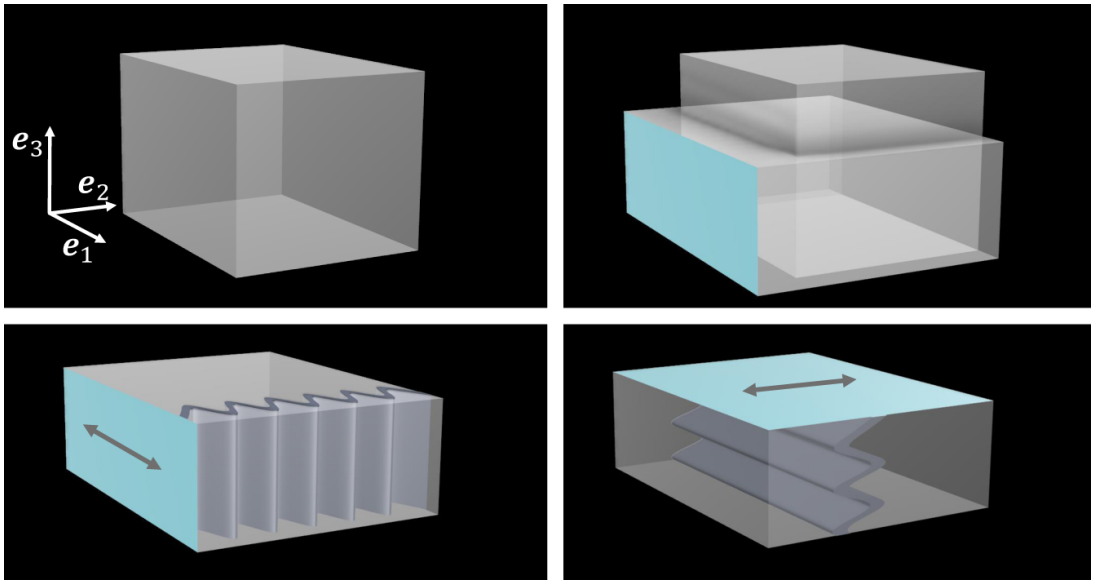

Figure 4.2.1 *Planar waves through a loaded phantom; (Top left) Phantom in undeformed state. (Top right) Phantom in compressed state, compared against the undeformed state. (Bottom left) Planar wave created by moving the front face of the phantom (in blue) along the* $\boldsymbol{e}_1$ *direction. (Bottom right) Planar wave created by moving the top face of the phantom (in blue) along the* $\boldsymbol{e}_2$ *direction*

Let us now analyse particular examples of shear waves - namely planar waves - travelling through the compressed cuboid. In the first case, consider that the front face of the cuboid is vibrated along the $\boldsymbol{e}_1$ direction (see Fig. 4.2.1), an idealised wave of the form

$$\boldsymbol{u}_c = \begin{pmatrix} u_1(x_2) \\ 0 \\ 0 \end{pmatrix} \tag{4.2.16}$$

is created, with the only non-zero entry in the wave displacement gradient being $(\nabla \boldsymbol{u}_c)_{12}$. Therefore, the deformation contribution in Eq. (4.2.15) simply becomes a scaling by $1/\lambda$:

$$\mu_e \nabla \boldsymbol{u}_c \boldsymbol{B} = \frac{\mu_e}{\lambda} \nabla \boldsymbol{u}_c.$$

As such, the loading bias is influencing the apparent stiffness of the cuboid, which appears to be μ_e/λ, whereas the intrinsic stiffness is μ_e. Thus, under this setup of the wave, the material stiffness appears to be higher, since $\lambda < 1$.

In the second case, consider a planar wave created by vibrating the top face of the cuboid, this time along the $\boldsymbol{e}_2$ direction (see Fig. 4.2.1). Then the idealised wave

displacements

$$\boldsymbol{u}_c = \begin{pmatrix} 0 \\ u_2(x_3) \\ 0 \end{pmatrix} \tag{4.2.17}$$

are probing the cuboid in the direction in which it was originally compressed, since the only non-zero component of the wave gradient is $(\nabla \boldsymbol{u}_c)_{23}$. This results in a stiffness scaling by λ^2, i.e.

$$\mu_e \nabla \boldsymbol{u}_c \boldsymbol{B} = \lambda^2 \mu_e \nabla \boldsymbol{u}_c.$$

With $\lambda < 1$, the biased stiffness $\lambda^2 \mu_e$ appears to be softer than the material's true stiffness μ_e.

From analysing these two simple instances of planar waves (Eqs. (4.2.16) and (4.2.17)), we gain an understanding of how the waves probing a material under compression experience different loading bias - stiffer in the expanded direction $\boldsymbol{e}_1$ and softer in the compressed direction $\boldsymbol{e}_3$. Had the waves been more complex, like in Eq. (4.2.14), then the effect of the loading would yield

$$\mu_e \nabla \boldsymbol{u}_c \boldsymbol{B} = \mu_e \begin{pmatrix} 0 & \frac{1}{\lambda}\frac{\partial u_1}{\partial x_2} & \lambda^2 \frac{\partial u_1}{\partial x_3} \\ \frac{1}{\lambda}\frac{\partial u_2}{\partial x_1} & 0 & \lambda^2 \frac{\partial u_2}{\partial x_3} \\ \frac{1}{\lambda}\frac{\partial u_3}{\partial x_1} & \frac{1}{\lambda}\frac{\partial u_3}{\partial x_2} & 0 \end{pmatrix}.$$

Thus, even under simplified conditions like an idealised shear wave travelling through a neo-Hookean material, we get a feeling for how biased the wave propagation becomes under pure compression. It can be presumed that, under less than ideal conditions (more complex materials and deformations), the harmonic wave motion becomes increasingly intricate.

4.2.2 Nonlinear Viscoelastic Characterisation of PVA

Experiments done in controllable media, where shapes and deformations are simple, constitute the first step in evaluating the theory explained in the previous section. A first key component is using a material with a known rheological behaviour, as this governs the effective loading bias (e.g. Eq. (4.2.7)). The following sections describe the fabrication process of PVA material and its testing in a rheological setup. A viscoelastic material law is also formulated. This law will then be later (section 4.2.3.2) integrated with deformation and MRE data.

4.2.2.1 PVA Phantom preparation

A material suitable for our purposes should be able to withstand large deformations without rupturing and to have low wave attenuation. For this, poly-vinyl alcohol cryogel (PVA-C) was selected, which is suitable for mimicking soft tissue properties and has a

high MR signal[230,240]. Following a protocol similar to the one described in[271], phantoms were created by mixing poly-vinyl alcohol powder (P1763 Sigma-Aldrich Company Ltd., UK) with deionised water in a concentration of 7%. A magnetic stirrer was used for 2 hours, in order to fully dissolve the powder into the water, while heating the concoction to 90°C. The mixture was covered throughout the process, to avoid evaporation, left to cool down at room temperature and poured into cuboid moulds of dimensions 64 × 48 × 42 mm. The moulds were then placed in a freezer at -20°C and underwent 3 cycles of freezing (14h) and thawing (10h) (F-T). These specifications ensured that the material was suitable for testing under large deformations. Laboratory experimentation with higher PVA concentrations (e.g. 10%) led to phantoms that were not easily deformable, whereas reducing the number of F-T cycles led to unstable phantoms that would leak water under loading.

During the freezing process, volumetric expansion occurred. Therefore, the phantoms' top was cut, in order to achieve cuboid shapes. This led to differences in the phantoms' height, which ranged between 32 and 42 mm. For a meaningful variance testing, 14 homogeneous phantoms were created, out of which 7 were used for rheological experiments and 7 for MRE experiments. However, one phantom was excluded in the rheological tests due to rupture. The time between phantom fabrication and testing in either rheology or MRE was within two weeks, to avoid potential material degradation.

4.2.2.2 Rheological testing of PVA phantoms

The phantoms allow for suitable examination methods that can test the theory developed in section 4.2.1. It was seen that, in order to account for the nonlinear complex stiffness moduli $\boldsymbol{\mathcal{G}}'$ and $\boldsymbol{\mathcal{G}}''$ (Eq. (4.2.11)), understanding of the nonlinear behaviour and frequency dependence of the material must be inferred. This can be done through rheological testing, which is used to characterise material behaviour by quantifying its response to different types of applied stress. As such, each of the 6 phantoms created for rheology experiments was tested in a Bose Electroforce 5500 test instrument, at constant room temperature. The setup, seen in Fig. 4.2.2, consisted of a supporting fixed platen and an adjustable upper platen, which was movable in the vertical direction. A load cell of capacity 225N measured the force required to ensure a user defined deformation.

For our aims, three types of tests were employed, with the purpose of assessing PVA's nonlinear behaviour. The first test was designed to investigate the material's response to dynamic micro-oscillations around a state of large static load. This design replicates closely the in-vivo MRE scenario, where low amplitude harmonic waves are propagating in an organ which may be subjected to large deformation. For reproducing the nonlinear behaviour, 4 different static loading states were investigated. Thus, the moving platen was programmed to compress the phantom by 2, 4, 6 and 8 mm respectively (∼5-20%

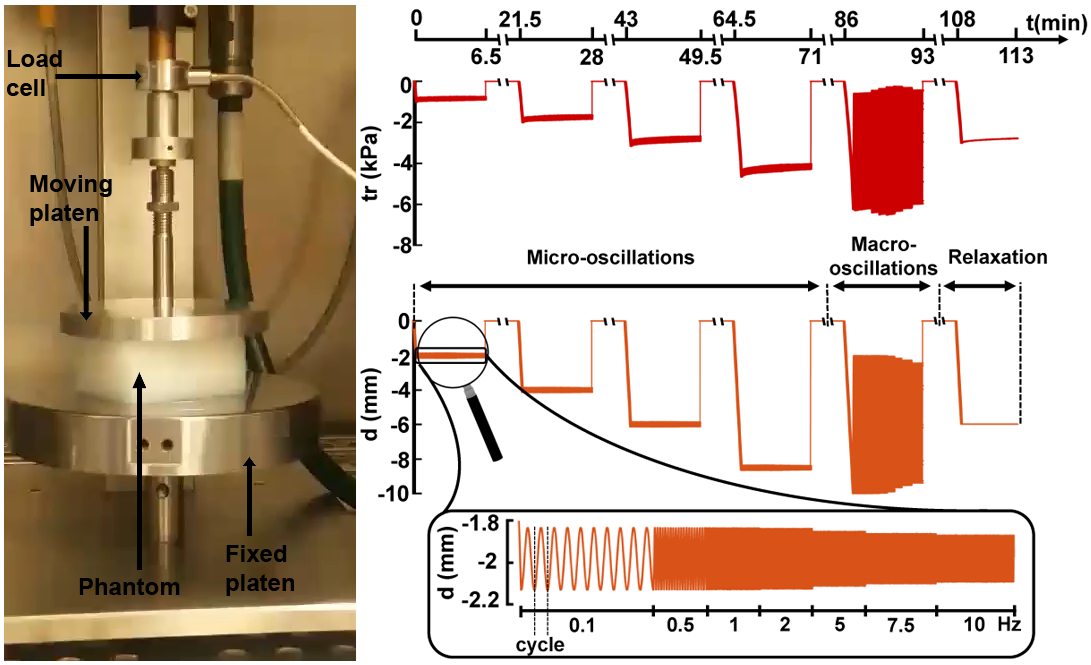

Figure 4.2.2 *Illustration of experimental setup, protocol and data in rheological tests. (Left) Phantom in the rheological instrument. The moving platen is compressing the phantom and oscillates vertically, while the loading cell records the force. (Right, top) The traction measurements in one phantom for the six tests: 4 micro-oscillations and 1 macro-oscillation (sweeping over frequencies) and a relaxation test. (Right, bottom) Platen displacements, corresponding to phantom compression levels. Zoomed panel: exemplification of a micro-oscillatory test displacements, showing the frequency sweep; Illustration of a cycle in the lowest frequency regime - one period, starting from the lowest point in the compression*

uniaxial compression), and then to oscillate with an amplitude of 0.15 mm (∼0.4%). This test will be referred to as the micro-oscillatory test.

The second test was designed to investigate the nonlinear large deformation response in time. As such, large oscillations were imposed around a state of large deformation: the platen compressed the phantom by 5.8 mm (∼15% uniaxial compression) and then oscillations of 4 mm (∼10%) amplitude were imposed. This test will be referred to as the macro-oscillatory test.

In both tests, oscillatory tests were carried under a frequency sweep, from 0.1 Hz to 10 Hz (the instrument's limit): 0.1, 0.5, 1, 2, 5, 7.5 and 10 Hz. A clear depiction of the testing protocol can be seen in Fig. 4.2.2. This was done to investigate the frequency response of PVA, with the aim of extrapolating it to the higher frequencies used in MRE. In all tests, but clearly noticeable in the macro-oscillatory one, the displacements' amplitude is decreasing with increasing frequency. This is probably due to the instrument's limitation which, in the faster frequency regime, cannot reach the instructed displacements.

At the higher frequencies ($\geq$ 5 Hz), it was observed that the moving platen gains acceleration and introduces a bias on the data. As such, calibration data was acquired, where the same protocol was followed, but with no sample in between the platens. Subtracting the calibration data from the phantom data eliminated the platen's momentum bias.

A final stress relaxation test was conducted by subjecting the material to a constant large deformation, in order to capture the specific viscoelastic effect. Hence, the phantoms were held under a compression of 11 mm ($\sim$28.5%) for 5 minutes.

Overall, each phantom underwent 6 tests: 4 micro-oscillations at different loads (with 7 different oscillatory states acquired), 1 macro-oscillation (with 7 different oscillatory states acquired) and 1 relaxation. In between tests, the phantoms were left to rest in water for 15-20 minutes, since PVA is best stored in water[240], for hydration reasons. This resting time allowed for an efficient testing protocol of the phantoms, and its duration was sufficient to observe reproducibility.

4.2.2.3 Constitutive Modelling of PVA

PVA and other hydrogels have been modelled, previously, as hyperelastic materials, employing laws that are generally used to describe rubber-like materials. Often, a Mooney-Rivlin type of model, employing two parameters, was found to be sufficient to capture the elastic behaviour of PVA[3,193]. Extension to viscoelasticity was sometimes accomplished by considering Maxwellian elements[3,126]. As such, here the aim is to model the PVA material as viscoelastic, yet using spring-pot elements.

Following previous investigations, we start the modelling process by considering the elastic part to be defined by a Mooney-Rivlin type of material law:

$$W_e(\boldsymbol{F}) = C_1(I_{\hat{\boldsymbol{C}}} - 3) + C_2(II_{\hat{\boldsymbol{C}}} - 3)^2, \tag{4.2.18}$$

where C_1 and C_2 (Pa) are material parameters. Considering the definition of the elastic part of the PK2 stress given, generally, as $\boldsymbol{S}_e = 2\nabla_{\boldsymbol{C}} W_e$, it follows that $\boldsymbol{S}_e$ has two elastic parts scaled by the material parameters C_1 and C_2:

$$\boldsymbol{S}_e(\boldsymbol{C}) = C_1\boldsymbol{S}_{e1} + C_2\boldsymbol{S}_{e2}.$$

The elastic terms are derived to be

$$\begin{aligned}
\boldsymbol{S}_{e1} &= \frac{2}{J^{2/3}}\left(\boldsymbol{I} - \frac{I_{\boldsymbol{C}}}{3}\boldsymbol{C}^{-1}\right), \\
\boldsymbol{S}_{e2} &= \frac{8}{J^{4/3}}(II_{\hat{\boldsymbol{C}}} - 3)\left(\boldsymbol{C} - \frac{II_{\boldsymbol{C}}}{3}\boldsymbol{C}^{-1}\right).
\end{aligned}$$

As previously mentioned in section 4.2.1.2, we consider the viscous part of PK2 to

depend on a fractional order derivative of a viscoelastic stress $\boldsymbol{S}_v$, which is defined here as the sum $\delta_1\boldsymbol{S}_{e1} + \delta_2\boldsymbol{S}_{e2}$. Hence, the PK2 tensor becomes

$$\boldsymbol{S} = C_1\boldsymbol{S}_{e1} + C_2\boldsymbol{S}_{e2} + D_t^{\alpha}(\delta_1\boldsymbol{S}_{e1} + \delta_2\boldsymbol{S}_{e2}) + \boldsymbol{S}_p. \tag{4.2.20}$$

Here α is the fractional derivative coefficient, with $\alpha = 0$ preserving the viscoelastic stress ($D_t^{\alpha}\boldsymbol{S}_e = \boldsymbol{S}_e$), which turns into a purely elastic contribution, and $\alpha = 1$ indicating the first order derivative, which becomes a purely viscous contribution. The hydrostatic stress $\boldsymbol{S}_p = JP\boldsymbol{C}^{-1}$ completes the definition of our PK2 tensor.

4.2.2.4 Rheology Data Analysis and Model Fitting

The viscoelastic model derived in the previous section (Eq. (4.2.20)) needs to be tailored to the PVA material used in the rheological experiments by finding appropriate parameters C_1, C_2, δ_1, δ_2 (Pa) and α.

As previously mentioned, the acquired rheological data consists of force measurements required to ensure a predefined displacement, each corresponding to a point in time. This was transformed into traction data in the $\boldsymbol{e}_3$ direction by dividing the force readings by the cuboid's top area adjusted to the deformation, *i.e.*

$$tr^d(t) = \frac{F(t)}{A(t)}, \quad A(t) = \frac{A_0 h_0}{h(t)}.$$

Here $tr^d(t)$ is the traction obtained from the data, $F(t)$ is the force reading and $A(t)$ is the area at time t, which depends on the initial top area A_0 and the ratio of initial cuboid height h_0 to the compressed height $h(t)$ (with $h(t) = h_0 - d(t)$).

Likewise, the traction in the $\boldsymbol{e}_3$ direction arising from the model (tr^m) was computed using

$$tr^m(t) = (\boldsymbol{\sigma}(t)\cdot\boldsymbol{n})_3, \quad \boldsymbol{\sigma} = \boldsymbol{F}\boldsymbol{S}\boldsymbol{F}^T,$$

where $\boldsymbol{\sigma}$ is the Cauchy stress and $\boldsymbol{n}$ is the normal to the surface (in our case, we are interested in the normal to the top surface, *i.e.* $\boldsymbol{n} = [0,\ 0,\ 1]^T$). Since the deformation at any point in time is given by

$$\boldsymbol{U}(t) = \begin{pmatrix} \left(\sqrt{\frac{h(t)}{h_0}} - 1\right) X_1 \\ \left(\sqrt{\frac{h(t)}{h_0}} - 1\right) X_2 \\ \left(\frac{h_0}{h(t)} - 1\right) X_3 \end{pmatrix},$$

the elastic and viscoelastic tensors $\boldsymbol{S}_{e1,2}$ and $D_t^{\alpha}\boldsymbol{S}_{e1,2}$ can be determined, together with their counterparts in the Cauchy stress. They take the form of diagonal 2$^{\text{nd}}$ order tensors. The hydrostatic pressure P can also be determined at each time point by noticing that the traction in the $\boldsymbol{e}_{1,2}$ directions is 0. Hence, P counteracts the elastic

and viscoelastic contributions in both the $\boldsymbol{e}_{1,2}$ directions, and can be used as such in computing the traction in the $\boldsymbol{e}_3$ direction. Thus, the only unknowns in the traction model are parameters C_1, C_2, δ_1, δ_2, α.

In broad terms, since α is the only nonlinear parameter of the model, the parameterisation process is done by iterating over fixed values of α and then solving a minimisation problem which yields a best fit of the remaining linear parameters. It is desired that all tests (micro-, macro-oscillations and relaxation) carry the same importance in the fitting process, and that the error is not dominated by certain tests (*e.g.* those done at higher compression levels, which employ larger tractions). As such, for each of the 6 tests (4 micro-oscillation, 1 macro-oscillation and 1 relaxation), the traction data and model were standardised according to the maximum traction value in the test, *i.e.*

$$\hat{tr}^d(t) = \frac{tr^d(t)}{\max_t |tr^d(t)|}, \qquad \hat{tr}^m(t) = \frac{tr^m(t)}{\max_t |tr^d(t)|}.$$

After the standardisation, the '$\hat{\cdot}$' notation is dropped for simplicity, to avoid addition of further notation.

Three characteristics were considered to be important when fitting the model to the data: the compression, relaxation and oscillatory response. Thus, the error to be minimised was designed to comprise two parts, the first one dealing with the compression and relaxation behaviour, and the second one with the oscillatory behaviour. For the first part, in order to ensure that the error is not dominated by compression only, but also by relaxation, it is important to consider the data broken down into cycles, *i.e.* one full oscillation starting from the lowest load state, equivalent to one period (see Fig. 4.2.2). Each of these cycles is confined within a generic time interval $[t_1, t_2]$. A mean traction value ($\bar{tr}^d$, $\bar{tr}^m$ for data and model, respectively) is defined as the integral of the traction over the cycle, *e.g.*

$$\bar{tr}^d_k = \int_{t1}^{t2} tr^d(t)\ \mathrm{d}t, \quad \bar{tr}^m_k = \int_{t1}^{t2} tr^m(t)\ \mathrm{d}t$$

over generic cycle k. This mean value captures the compression level and, by considering locally every cycle in a test, captures the relaxation behaviour. Hence, the first part of the error deals with the sum, over all cycles, of the mean traction value difference between the data and the model, normalised by the data:

$$\mathrm{err}_1 = \frac{\sum_k (\bar{tr}^d_k - \bar{tr}^m_k)^2}{\sum_k (\bar{tr}^d_k)^2}.$$

The second part of the error is designed to measure the difference in the oscillatory behaviour between data and model. Thus, the traction amplitude corresponding to a generic time point t_j in a cycle k is found as the difference between the traction value

and the traction mean over the cycle, *e.g.*

$$tr^d(t_j^k) - \bar{tr}_k^d, \qquad tr^m(t_j^k) - \bar{tr}_k^m.$$

The difference in amplitudes between the model and the data is investigated across all time points in a cycle, over all cycles, and is subsequently normalised by the data, as

$$\mathrm{err}_2 = \frac{\sum_k \sum_j \left[(tr^d(t_j^k) - \bar{tr}_k^d) - (tr^m(t_j^k) - \bar{tr}_k^m) \right]^2}{\sum_k \sum_j \left(tr^d(t_j^k) - \bar{tr}_k^d \right)^2}.$$

We note that the standardisation of the data was done over each of the 6 tests separately, to ensure that they carry equal importance within the error, while the normalisation was done over the tests altogether, to facilitate the interpretation of the error, which is finally outlined as

$$\mathrm{err} = \sqrt{\frac{\mathrm{err}_1 + \mathrm{err}_2}{2}}. \tag{4.2.21}$$

This form yields 0% for a perfect fit and 100% when C_1, C_2, δ_1, $\delta_2 = 0$ Pa, irrespective of α.

Having defined the error to be minimised, a more detailed parameter fitting process can be described. The nonlinear parameter α is iterated between 0.05 and 1 (close to the elastic and viscous limits, respectively), with an incremental step of 0.05. Since the PVA material used has a low viscoelastic response (and $\alpha = 0.05$ was observed to be the most suitable), the incremental step was refined to be 0.01 between 0.01 and 0.1. For each fixed α, the linear parameters C_1, C_2, δ_1, δ_2 were searched by solving the least squares problem corresponding to error Eq. (4.2.21), using the inbuilt function *lsqnonlin* of MATLAB and Statistics Toolbox Release 2015a, The MathWorks, Inc., Natick, Massachusetts, United States. The nonlinear solver was used in order to allow for a positivity constraint on the parameters. For each phantom, a full set of parameters was determined.

To ensure parameter uniqueness, once the best α value was determined, a new parameter search was performed. Thus, each individual linear parameter (C_1, C_2, δ_1 and δ_2, respectively) was fit using the process described above, but while imposing the remaining 3 linear parameters to be 0 Pa. This was done in order to gauge the value of each model component and to identify potential parameter coupling.

4.2.3 Harmonic Wave Motion in Deformed PVA

After characterising the PVA material through a viscoelastic model, the next essential element in estimating the intrinsic material parameters and bypassing the loading bias is merging the information on deformation and rheology with MRE data. Thus, in what follows, the MRE experimental features used to obtain simple deformations are described. The core component of integrating material behaviour and deformation

knowledge into the data analysis process is outlined.

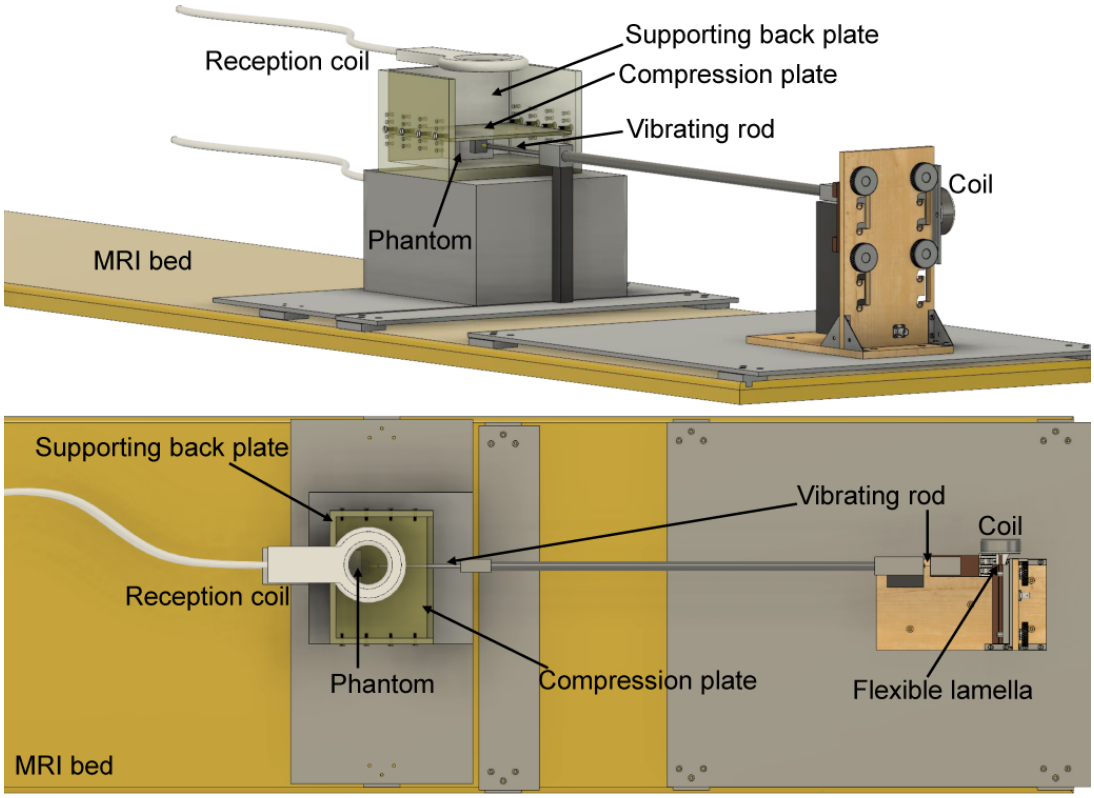

Figure 4.2.3 *Illustration of the MRE test setup. (Top) 3D view of the setup. A coil vibrating to the frequency established by the MRE sequence is connected to a flexible lamella, which causes an attached rod to vibrate longitudinally. A piston fit at the end of the rod is indenting the phantom, thus generating compressional waves. The phantom is resting on a smooth support and is in contact with the back support plate, which prevents the phantom from slipping and thus helps converting the compressional waves into shear waves. An upper plate compressing the phantom is kept in place by bolts fixed to the side plates. Reception coils are placed around the phantom, for signal enhancement. (Bottom) 2D top view of the setup*

4.2.3.1 MRE Experimental setup

When designing the MRE experiment, it was important to obtain shear waves that would propagate through the whole body of the phantom, while maintaining a fixed position of the phantom. The setup used is illustrated in Fig. 4.2.3. A transducer indenting the phantom transmits small amplitude compressional waves. Since the PVA material is aqueous, it could easily slide on a flat surface. For this reason, the phantom's back side was in contact with the support, ensuring no penetration, hence converting the compressional waves into shear waves. A large uniaxial deformation could be obtained by simply compressing the phantom with a smooth top plate, as seen in Fig. 4.2.3. Due to the sliding feature of the PVA material, the phantoms did not bulge under the uniaxial compression just described.

Using this setup inside the MR scanner, coronal wave data was recorded using MRE in undeformed and deformed configurations. Each phantom was scanned in the reference state (uncompressed), first deformation state consisting of uniaxial compression of ∼5mm (∼14%) and second deformation state consisting of uniaxial compression of ∼12mm (∼35%).

MR acquisition consisted of two primary scans. First, a geometric scan was acquired providing 55 cross-sectional slices with a field of view (FOV) of 96 × 96 mm (resolution of 96×96 pixels and slice thickness of 1 mm). Scan parameters were adjusted to enhance signal of the PVA material (TE/TR= 120.00 /5000.00 ms).

The second scan was a MRE eXpresso Gradient Echo sequence[71] providing 10 cross–sectional slices with a FOV of 96 × 96 mm (resolution 96 × 96 pixels and slice thickness of 2.0 mm). Driver frequency and motion encoding gradients were set, by turn, at 120, 130 and 140 Hz, and TE/TR at 6.91 /151.82 ms. The sequence encoded each of the three displacement component direction - $\boldsymbol{e}_1$, $\boldsymbol{e}_2$, $\boldsymbol{e}_3$ and a reference non-motion encoded image removing background phase shifts due to the MRI gradients.. Examples of the geometric and wave images can be seen in Fig. 4.2.4, for the undeformed and deformed configurations.

4.2.3.2 MRE data analysis

The geometric data acquired was used to provide detailed quantitative information of the geometrical configuration of the material in reference and deformed states. Assuming that the cuboid phantoms were compressed uniformly, then the deformation gradient can be written as in Eq. (4.2.13), where λ is the compression defined as the ratio of the compressed and uncompressed heights. Hence, due to the design of the MRE experiment, this form of the deformation gradient can be employed with the stiffness moduli given by Eq. (4.2.11).

From the recorded small amplitude displacements, two reconstruction methods were used. Firstly, a divergence free finite element reconstruction solving the set of Eq. (4.2.10)[61] was used to retrieve the stiffness of the PVA phantom, merging the datasets acquired at 120, 130 and 140 Hz, for a better signal to noise ratio. This method takes as input the material density ρ, frequency ω and wave displacements $\boldsymbol{u}_c$ and reconstructs the complex stiffness modulus G^* by assuming

$$\boldsymbol{\mathcal{G}}^* = G^*(\boldsymbol{\mathcal{I}} + \widetilde{\boldsymbol{\mathcal{I}}}). \tag{4.2.22}$$

This is usually separated into the (real) storage modulus G' and (imaginary) loss modulus G'' (where $G^* = G' + iG''$).

As explained in section 4.2.1.2, the form of $\boldsymbol{\mathcal{G}}^*$ presented in Eq. (4.2.22) holds true in the absence of deformation and under an isotropic standard material law, and the wave

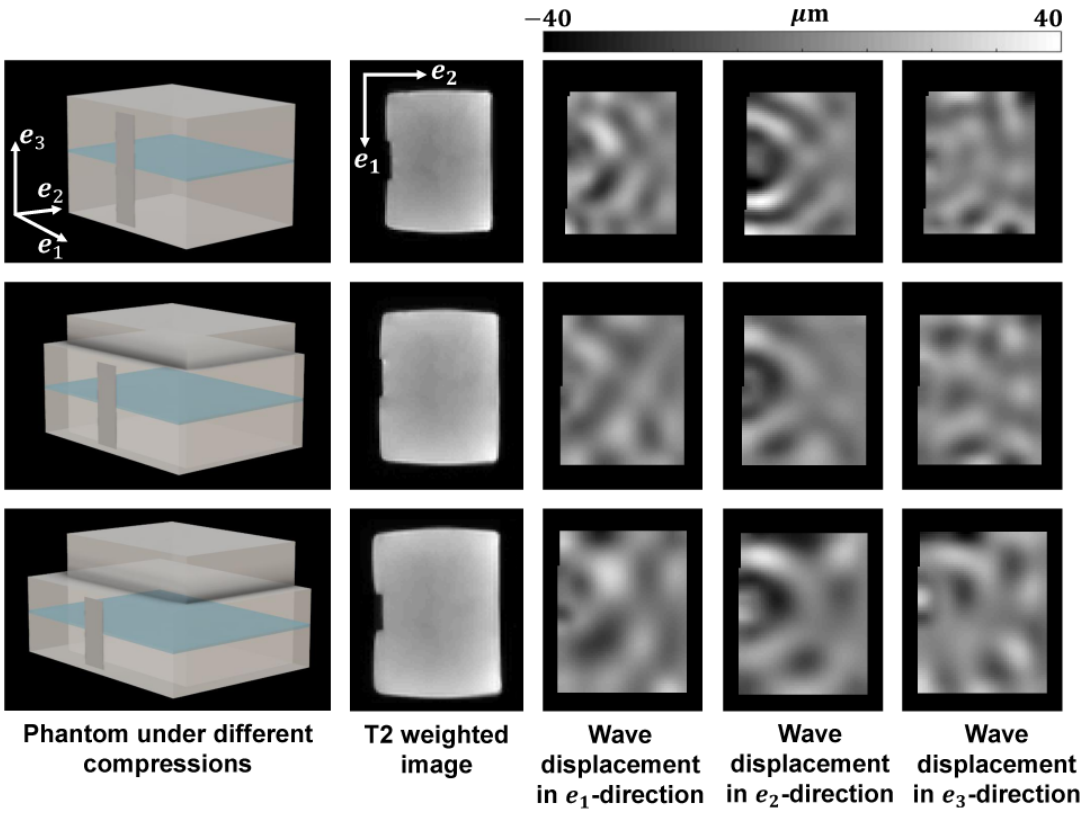

Figure 4.2.4 *Images corresponding to the uncompressed (top row) and compressed (middle and bottom rows) phantoms (here illustrated in phantom 12). (First column) Phantom depicted at the different deformation states. The uncompressed state is kept for reference. The piston (grey bar) is indenting the phantom perpendicularly during the MRE scan. Slices are acquired in the coronal plane (depicted in blue). (Second column) Cross sectional (coronal) view from the T2 weighted images. The piston indentation can be seen, as well as the expansion of the phantom in the* $\boldsymbol{e}_1 - \boldsymbol{e}_2$ *directions under compression. Wave displacements from the MRE imaging protocol can be seen in the* $\boldsymbol{e}_1$ *direction (third column), in the* $\boldsymbol{e}_2$ *direction (fourth column) and in the* $\boldsymbol{e}_3$ *direction (fifth column). It can be observed in the wave displacements, between the three rows, that the wavelength increases under compression. The wave images in the third, fourth and fifth columns have been cropped around the phantom area, to exclude the surrounding noise*

gradient contribution becomes symmetric, as $(\boldsymbol{\mathcal{I}} + \widetilde{\boldsymbol{\mathcal{I}}}) : \nabla \boldsymbol{u}_c = \nabla \boldsymbol{u}_c + \nabla \boldsymbol{u}_c^T$. Hence this method is suitable for reconstructing the stiffness modulus when no deformation is employed, but will lead to a biased result under deformation. Throughout the rest of the paper, this method will be referred to as uncorrected reconstruction (UR).

Secondly, the same reconstruction was adapted here, by integrating the formal definition of the real and imaginary stiffness moduli $\boldsymbol{\mathcal{G}}'$ and $\boldsymbol{\mathcal{G}}''$ (Eq. (4.2.11)) in order to account for the bias in apparent stiffness introduced by the deformations. Conceptually, instead of relying solely on the wave displacements and its gradient $\nabla \boldsymbol{u}_c$, the reconstruction integrates the scaling due to large deformations into the wave displacements gradient.

Hence, instead of solving for G^*, a modified form of the equations was developed, given below:

$$-\rho\omega^2\boldsymbol{u}_c - \nabla\cdot[M(\boldsymbol{\mathcal{G}}':\nabla\boldsymbol{u}_c)] - i\nabla\cdot[(N(\boldsymbol{\mathcal{G}}'':\nabla\boldsymbol{u}_c)] - \nabla\cdot p_c\boldsymbol{I} = \boldsymbol{0}, \quad (4.2.23a)$$

$$\nabla\cdot\boldsymbol{u}_c = 0, \quad (4.2.23b)$$

where a solution is sought for $M+iN$. This second approach will be referred to as the corrected reconstruction (CR).

As previously mentioned, within the UR the wave gradient is contracted with the 4^{th} order identity tensor scaled by the complex stiffness modulus, as $(G^*(\boldsymbol{\mathcal{I}}+\widetilde{\boldsymbol{\mathcal{I}}})):\nabla\boldsymbol{u}_c$. By contrast, the CR allows the wave to be contracted with two distinct 4^{th} order tensors, defined by the user. One is to be integrated with the real part and one with the imaginary part of the complex stiffness modulus, as $M(\boldsymbol{\mathcal{G}}':\nabla\boldsymbol{u}_c)+iN(\boldsymbol{\mathcal{G}}'':\nabla\boldsymbol{u}_c)$, where $M+iN$ is to be found. This is a novel way of analysing MRE data and is of utmost importance, since we saw, in Eq. (4.2.11), that the real and imaginary moduli $\boldsymbol{\mathcal{G}}'$ and $\boldsymbol{\mathcal{G}}''$ are non-trivial and change differently with deformation. These changes depend on metrics derived from the known deformation gradient $\boldsymbol{F}$ ($\boldsymbol{B}$, $I_{\boldsymbol{C}}$, etc), and, for our PVA material, are scaled by the parameters determining the viscoelastic Eq. (4.2.20). The specific form can be found in appendix 4.B, which is applicable to the PVA material used here. Thus, assuming that the viscoelastic model describes the data well, then $\boldsymbol{\mathcal{G}}'$ and $\boldsymbol{\mathcal{G}}''$ already incorporate the true real and imaginary stiffness moduli. Hence, it is predicted that M and N will be reconstructed as unity.

With this understanding of the newly developed CR, the PVA material model was parameterised, this time employing the MRE data. The reference and second compression states were used, and the left hand side of Eq. (4.2.23) was minimised over all pixels. That is, the linear model parameters were sought such that M and N were reconstructed as closely as possible to unity for each pixel, over all pixels. The nonlinear parameter α was fixed to be the one indicated by rheology tests. The set of parameters thus obtained from the reference and second compression states was tested against the first compression state, for prediction value. The error was measured as the pixel-wise difference between the reconstructed values M and unity in uncompressed and second compression case, normalised by the number of pixels, as

$$\text{err} = \sqrt{\frac{\sum_{k=1}^{n}(M_k-1)^2}{n}}, \quad (4.2.24)$$

where n is the total number of pixels considered and subscript k iterates over those pixels.

4.3 Results and Discussion

The first essential step in the experimental work was tailoring the viscoelastic law 4.2.20 to the PVA phantoms used in the rheology testing. The results of this process are presented in section 4.3.1 and help us understand the rheological behaviour of the PVA material used, which directly influences the loading bias. The deformation bias is shown in section 4.3.2, by investigating uniaxial compression in the MRE experimental setup. In section 4.3.3 it is shown that, by incorporating the information on rheology and deformation into the CR, the intrinsic stiffness of the PVA material can be retrieved from the loaded states of the phantoms.

4.3.1 Nonlinear Viscoelastic Model for PVA

The aim of the modelling process was to fit the viscoelastic model 4.2.20 to the PVA data acquired in the rheological setup. Hence, for each of the 6 phantoms used in the rheology experiment, the parameters were fit accounting for all oscillatory and relaxation tests simultaneously. It will be seen that the parameters cannot be uniquely identified, which stems from the fact that the PVA has a small viscoelastic response, as it will be explained shortly. As such, a model with a reduced number of parameters is sought, which ensures unique parameter estimation.

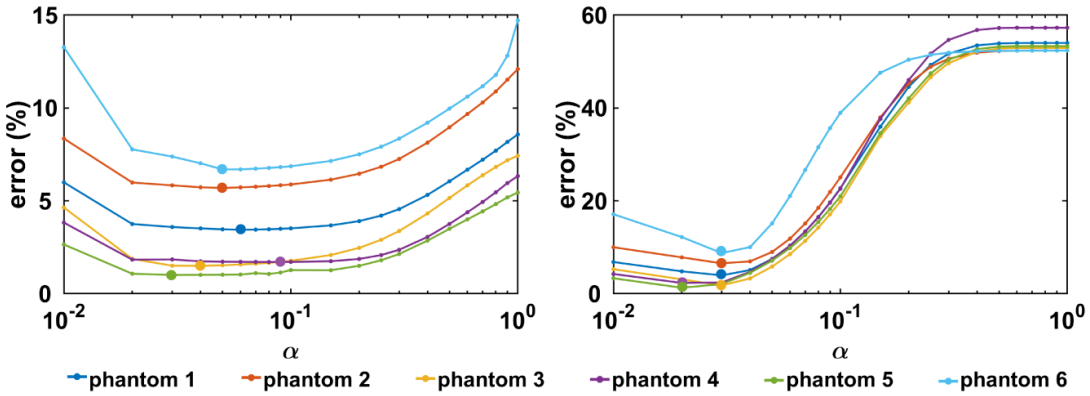

Figure 4.3.1 *The minimum error (per Eq.* (4.2.21)*) obtained by fitting the model to the data for each phantom, sweeping over fixed values of* α *between 0.01 and 1. (Left) The error for the 5-parameter model. (Right) The error for the 3-parameter model. The minimal error for each phantom, obtained by employing the parameters in Table 4.3.1 (5-parameter model) and Table 4.3.3 (3-parameter model), are enhanced*

Initially, the 5-parameter model described by Eq. (4.2.20) was fit to the data, considering α values between 0 and 1. Fig. 4.3.1 (left) depicts the errors for each of the 6 phantoms used in rheology. All phantoms yield a minimal error around an α value of 0.03-0.09. The minimal error increases only slightly at higher α values. The reason for the shallow changes in minimal error at high α values is that the 2 viscoelastic parameters δ_1 and δ_2 become very small, hence the data is fit mostly with the elastic parameters C_1 and C_2. Due to the PVA material having a small viscoelastic response,

employing only an elastic model is not highly detrimental to the model fit, hence the small errors even at $\alpha = 1$. The best parameter fit for each phantom is summarised in Table 4.3.1. The errors are small (less than ~ 7 %), which indicates that a good fit is ensured for each test. An example of the model fit can be seen in Fig. 4.3.2 (left). It can be observed that the compression level and relaxation behaviour are properly captured, while micro-oscillatory amplitudes are slightly underestimated. Notably, a large variability can be seen for all parameters with standard deviations around the mean spanning more than 100%. This can be explained by looking at the α parameter, which is generally small (0.03 - 0.09). These values indicate that the PVA has a very small viscoelastic response. Mathematically, if $\alpha = 0$, then the linear parameters $\{C_1, \delta_1\}$ and $\{C_2, \delta_2\}$ become pairwise redundant, since they scale the same component. Hence, with a very low α, a coupling of the parameters arises. For instance, it can be seen, in Table 4.3.1, that the phantoms for which a high δ_1 was yielded had a small C_1 and vice versa.

Phantom	C_1 (Pa)	C_2 (Pa)	δ_1 (Pa)	δ_2 (Pa)	α
p1 (3.44%)	1545.66	0.18	195.76	149.40	0.06
p2 (5.69%)	1683.89	11.55	0.47	275.13	0.05
p3 (1.50%)	1606.03	4.50	1457.86	193.03	0.04
p4 (1.71%)	2491.84	57.71	628.60	79.40	0.09
p5 (1.01%)	647.09	174.31	2259.66	2.00	0.03
p6 (6.69%)	1746.13	0.04	0.00	272.97	0.05
mean	1620.11	41.38	757.06	161.99	0.05
std dev	537.34	62.71	839.25	98.87	0.019

Table 4.3.1 *Best fit parameters for each PVA phantom; the error, computed as per Eq.* (4.2.21)*, can be seen in the first column (in brackets).*

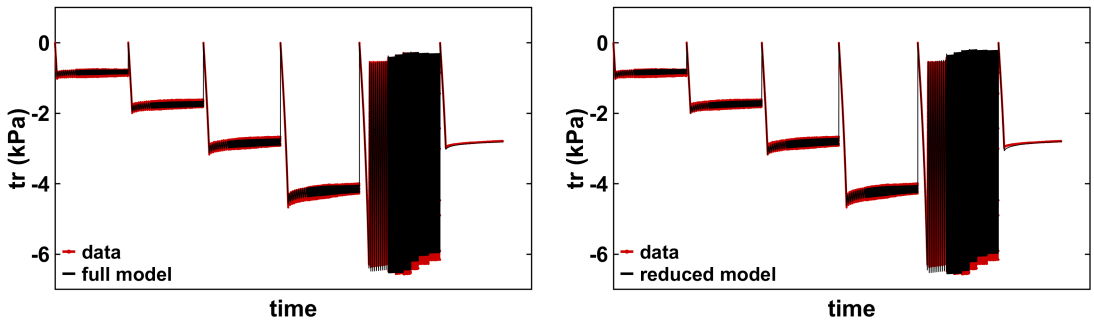

Figure 4.3.2 *Illustration of the model fit considering the 5-parameter model or 3-parameter model in phantom 3. (Left) The model fit to the data using all parameters:* C_1, C_2, δ_1, δ_2 *and* α *(with an error of* 1.50%*). (Right) The model fit to the data using a reduced number of parameters:* C_2, δ_1, *and* α *(with an error of* 1.78%*). The parameter values can be seen in Tables 4.3.1 and 4.3.3*

Due to the small viscoelastic response of the PVA phantoms, parameters $\{C_1, \delta_1\}$ and

$\{C_2, \delta_2\}$ tend to exhibit very similar features. As such, in order to identify each parameter contribution to the model, α was set to 0.03 (the best choice according to Fig. 4.3.1 (right)) and each of the linear parameters was fit individually. The effects of each individual parameter on the model are illustrated in Fig. 4.3.3. When considering only C_1, the model component considered is $\boldsymbol{S}_{e1}$, which is equivalent to the neo-Hookean elastic law. This parameter captures reasonably well the compression level of each test, indicating that the PVA material used has a dominant linearly elastic response. However, it lacks the ability to capture the changes in oscillatory amplitudes - in the 4 repetitions of the micro-oscillatory tests, the data indicates an increased amplitude at higher compression levels, whereas the model shows the same amplitude. The decrease in amplitude seen in the macro-oscillatory test is a direct result of the decrease in the actual displacement amplitude data, as seen in Fig. 4.3.3. This amplitude behaviour is entirely expected from the neo-Hookean model, and the mismatch between the model and data indicates that the PVA displays nonlinear characteristics. Lastly, no relaxation behaviour is displayed, which is also expected due to the model component being purely elastic. Conversely, the fractional derivative of the $\boldsymbol{S}_{e1}$ component, scaled by δ_1, is the viscoelastic counterpart of the neo-Hookean model. As such, investigating the value of δ_1 leads to similar observations as for C_1, with the obvious difference that it can capture the relaxation behaviour. It is stressed, once again, that the similarity occurs due to α being very small.

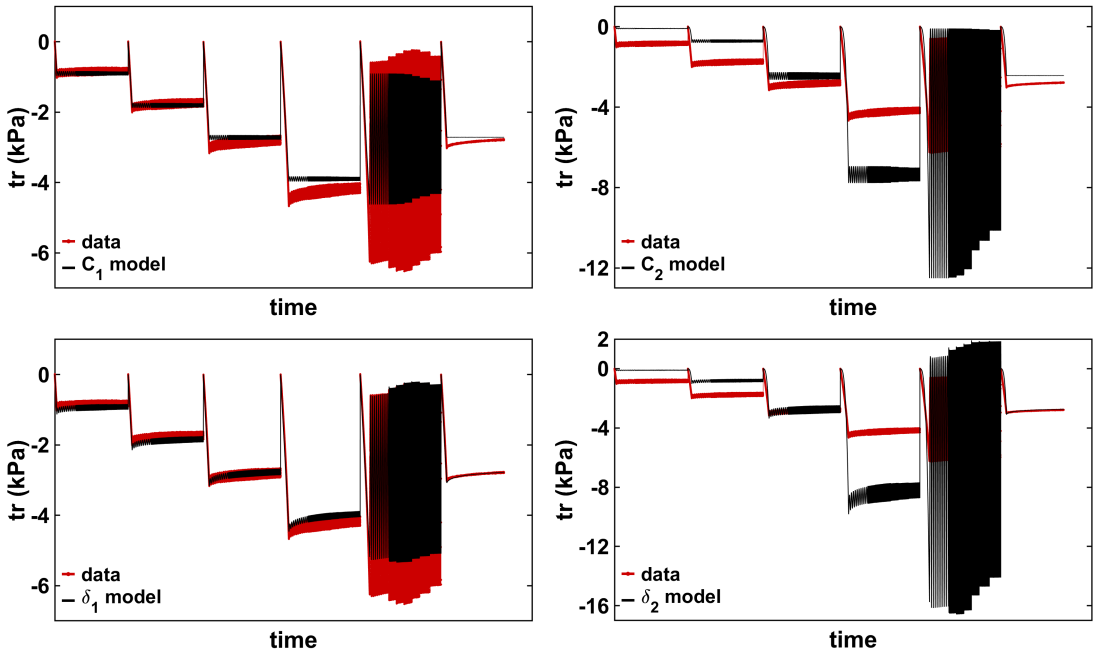

Figure 4.3.3 *Contribution of each parameter to the model (black) compared to the data (red) (here, in phantom 4). Each of the 4 linear parameters (C_1 (top left), C_2 (top right), δ_1 (bottom left), δ_2 (bottom right)) was fit to the data, while setting the other 3 to be 0 (α was kept constant at 0.03). In each quadrant, the traction is depicted along the y-axis and the time along the x-axis (waiting times between tests not plotted for convenience). The parameters and errors can be seen in Table 4.3.2*

When investigating C_2 , the nonlinearity of the $\boldsymbol{S}_{e2}$ component becomes obvious - a linear increase in the compression level (2 mm between the micro-oscillatory tests) leads to a nonlinear response in the traction force. Hence, this parameter alone provides an unsuitable fit to the data, however it adds value to the full model by being able to adjust for the increased amplitude in the 4 micro-oscillation tests. As before, the viscoelastic counterpart δ_2 captures the relaxation behaviour. Table 4.3.2 presents the best fit parameter for each PVA phantom. By investigating Fig. 4.3.3, it is expected that the C_1 and δ_1 parameters provide a better fit, and hence yield smaller errors than the C_2 and δ_2 parameters.

Having looked at each individual component, it is reasonable to conclude that 2 out of the 4 of the linear parameters - one elastic and one viscoelastic non-counterpart - are sufficient for describing the PVA material behaviour. By keeping either C_1 or δ_1, the compression level is ensured. By adding either δ_2 or C_2, the amplitude fit can be improved for both the micro- and macro-oscillations. The relaxation is ensured by considering either viscoelastic component - δ_1 or δ_2, although from the individual parameter fit it looks like δ_1 is more suitable for this aspect.

Phantom	C_1 (Pa)	C_2 (Pa)	δ_1 (Pa)	δ_2 (Pa)	α
p1	1835.42	685.33	2175.25	813.40	0.03
err (%)	11.69	53.97	9.80	58.12	
p2	1933.73	884.40	2318.04	1031.81	0.03
err (%)	17.78	52.34	15.18	59.42	
p3	3015.56	1190.96	3568.47	1433.38	0.03
err (%)	9.29	52.93	7.31	56.10	
p4	3036.63	1072.38	3585.49	1258.29	0.03
err (%)	7.89	57.27	6.24	60.80	
p5	2864.40	1132.68	3374.09	1346.91	0.03
err (%)	8.70	53.30	8.70	56.92	
p6	1934.22	890.65	2363.49	922.69	0.03
err (%)	22.35	52.31	15.39	65.47	
mean	2436.66	976.06	2897.47	1134.41	NA
std dev	590.75	189.85	677.24	248.31	NA

Table 4.3.2 *Best fit parameter for each PVA phantom; the error, computed as per Eq.* (4.2.21)*, can be seen below each parameter; Each parameter was fit considering the remaining three parameters to be 0.*

These observations indicate that the best parameters to fit are C_2 and δ_1, while setting C_1 and δ_2 to 0 Pa. Indeed, when investigating all pairwise tests (*i.e.* fitting either $\{C_1, \delta_1\}$, $\{C_1, \delta_2\}$, $\{C_2, \delta_1\}$ or $\{C_2, \delta_2\}$, with $\alpha = 0.03$), the smallest errors were obtained when considering C_2 and δ_1. Hence, the initial model was reduced to 3 parameters - C_2, δ_1 and α-, with δ_1 modelling the neo-Hookean viscoelastic component, and C_2 spanning the nonlinear behaviour. The simplified PK2 tensor that characterises the

PVA material becomes

$$\boldsymbol{S} = C_2\boldsymbol{S}_{e2} + \delta_1 D_t^{\alpha}\boldsymbol{S}_{v1} + \boldsymbol{S}_p. \tag{4.3.1}$$

The new set of parameters obtained for the 3-parameter model can be seen in Table 4.3.3. It is notable that the error increase is very small, thus the new parametrisation does not significantly deteriorate the quality of the fit. An example of the parameterised 3-parameter model fit to the rheology data can be seen in Fig. 4.3.2 (right). The error plot of the 3-parameter model can be seen in figure 4.3.1 (right). Each phantom indicated a best fit for a very small α (0.02 or 0.03). At low α values, the errors are generally small, since the PVA is only slightly viscoelastic. However, at high α values, there is a sharp increase in the minimal error, which eventually plateaus. This happens when the contribution of the viscoelastic parameter becomes insignificant (δ_1 becomes very small, to counteract the effect of α) and the only remaining parameter is thus C_2. In this case, as seen in Table 4.3.2 as well, the errors rise up to $\sim 30-35\%$. In the low α regime, employing the 3-parameter model increases the errors only slightly compared to the 5-parameter model, which is preferred due to reduced complexity.

Phantom	C_2 (Pa)	δ_1 (Pa)	α
p1 (3.95%)	118.94	1923.03	0.03
p2 (6.54%)	233.16	1900.25	0.03
p3 (1.78%)	169.10	3220.10	0.03
p4 (2.32%)	117.86	3143.31	0.02
p5 (1.28%)	176.42	2854.77	0.02
p6 (8.74%)	216.15	1973.74	0.03
	linear	linear	nonlinear
mean	171.94	2502.53	0.03
std dev	43.71	581.34	0.005

Table 4.3.3 *Best fit parameters for each phantom, restricting $C_1, \delta_2 = 0$ Pa; the error, computed as per Eq.* (4.2.21)*, can be seen in the first column, in brackets*

4.3.2 Loading Bias in Harmonic Wave Motion Under Pure Compression

In this study, the PVA phantom material is described by the moderately complex viscoelastic Eq. (4.3.1). Harmonic waves were designed to probe the PVA, as shown in Fig. 4.2.4 (columns 3-5).

With this experimental design, when reconstructing with UR the MRE phantom stiffness in the uncompressed and two compression states, it is observed that the material appears increasingly stiffer with increasing compression. This behaviour is observed in all 7 phantoms, as shown in Fig. 4.3.4 (columns 2 and 3). There it can be seen that, in the uncompressed case, the intrinsic stiffness is ∼4.5 kPa. At the first compression

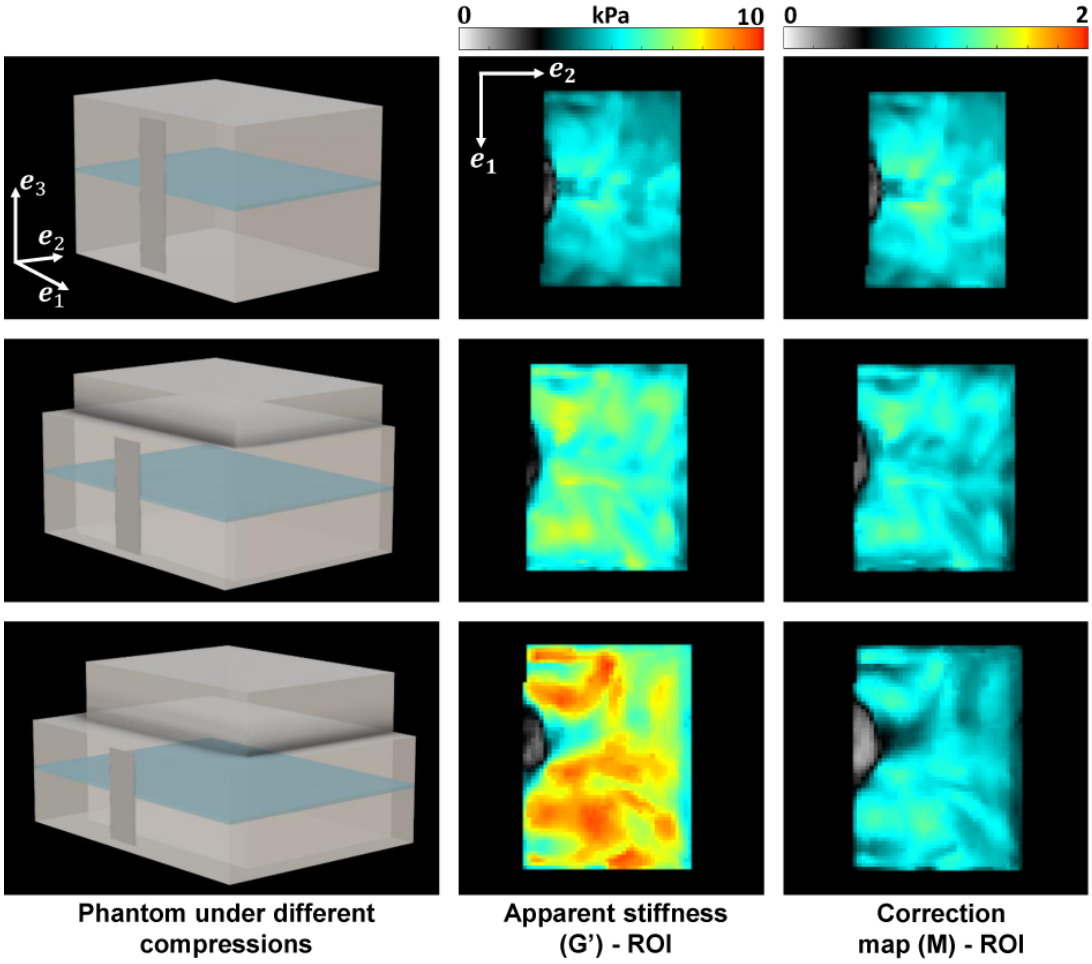

Figure 4.3.4 *Stiffness maps G' and corrected maps M corresponding to the uncompressed (top row) and compressed (middle and bottom rows) phantoms (here illustrated in phantom 12). (First column) Phantom depicted at the different deformation states. The uncompressed state is kept for reference. The piston (grey bar) is indenting the phantom perpendicularly during the MRE scan. Slices are acquired in the coronal plane (depicted in blue). (Second column) Stiffness estimates using the UR. The region of interest (ROI) of the apparent stiffness map G' was obtained by eroding the phantoms' margins. (Third column) Estimates of map M using the CR. The ROI of maps M was obtained by eroding the phantoms' margins*

level, the loading bias leads to an apparent stiffness of ∼6 kPa, and at the second compression level to an apparent stiffness of ∼7.5 kPa. A summary of the average stiffness of every phantom in each deformation state can be seen in Fig. 4.3.5. The statistics are based on a region of interest (as seen in Fig. 4.3.4) which excludes the phantom's margins, in order to avoid peculiar boundary effects. A nonlinear stiffening trend can be observed with increased compression. The standard deviations increase as well, from $\sim 10\%$ to $\sim 21\%$, suggesting a higher stiffness heterogeneity under compression, which could be a result of the complex wave behaviour. Since the phantom PVA material becomes apparently anisotropic under deformation, a shear wave (as in Eq. (4.2.14)) probing, locally, different directions would lead to higher variability in the

stiffness measurements.

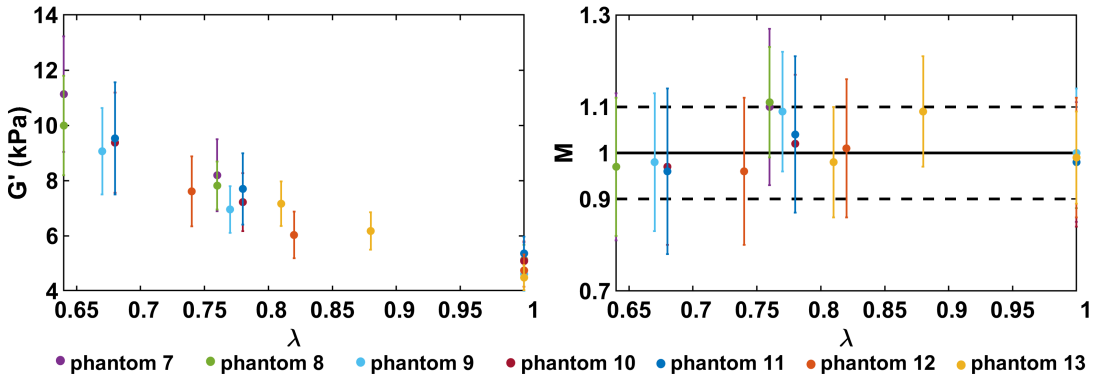

Figure 4.3.5 *Average of stiffness maps G' and corrected maps M over all pixels in a phantom (excluding boundaries), in all deformation states. (Left) Average of stiffness map G' obtained using UR (Eq.* (4.2.10)*) on the MRE data. In undeformed state, when $\lambda = 1$, the average stiffness of the phantoms lies within 4.5-5.3 kPa. With increased compression, the phantoms appear to be stiffer, following a nonlinear trend. (Right) Average of corrected maps M, obtained by employing CR (Eq.* (4.2.23)*) on the MRE data. The average value of the corrected maps M spans between 0.96 and 1.11. The standard deviation for all phantoms in all compression states cross the line at the ideal value $M = 1$*

Recall that in section 4.2.1.3 we discussed the motion of a planar shear wave through a compressed body in order to gain an intuition of the biasing effects of loading. It was seen that, for an idealised planar wave (like in Eq. (4.2.16)) moving through a compressed neo-Hookean body, the material appears to be stiffer. Although the MRE experiment employed in this study carries additional complexity compared to the idealised case (particularly in the type of material used and wave structure), the stiffening trend observed in PVA is in accordance with the simplified theoretical outcomes just summarised. The same stiffening effect was observed in an ultrasound study as well[75], under similar conditions (idealised planar wave and uniaxially compressed material).

4.3.3 Intrinsic Stiffness Estimation

By understanding how loading biases stiffness estimation, it is possible to estimate intrinsic stiffness values when using CR. This requires knowledge of the deformation employed and the material law. Since this study deals with pure compression, the deformation was estimated using Eq. (4.2.13). Rheological testing of the PVA led to a 3-parameter material law (Eq. (4.3.1)). It was seen, in section 4.3.1, that there is variation in estimating the linear parameters C_2 and δ_1, whereas the nonlinear parameter α is stable around 0.02-0.03. The optimisation performed in rheology was not repeated for MRE, as this was observed to lead to a parameter coupling between α and δ_1. Thus, α was fixed at 0.03, as indicated by the rheological tests, and C_2, δ_1 were estimated as described in the data analysis section 4.2.3.2. The resulting parameters are presented in

Table 4.3.4. It is notable that the C_2 parameter is generally lower in MRE (Table 4.3.4) than in rheology (Table 4.3.3), with the exception of phantom 13. This could be related to the degree of relative compression achieved. In rheology, the maximum relative compression is 28.5%. In MRE, however, relative compressions reach up to 35%, with the exception of phantom 13 (only 18%), as seen in Fig. 4.3.5. At lower deformation levels, the viscoelastic component is less employed, thus the purely elastic part becomes more dominant. As C_2 is scaling the elastic component, its estimate is higher when less uniaxial compression is achieved.

Phantom	C_2 (Pa)	δ_1 (Pa)	α
p7 (15.85%)	93.68	2119.92	0.03
p8 (15.86%)	83.15	2085.28	0.03
p9 (14.80%)	88.36	1878.05	0.03
p10 (16.64%)	94.83	2126.26	0.03
p11 (17.08%)	103.43	2235.11	0.03
p12 (18.27%)	106.27	1945.07	0.03
p13 (11.15%)	246.54	1848.72	0.03
	linear	linear	nonlinear
mean	120.43	2019.75	NA
std dev	56.96	139.60	NA

Table 4.3.4 *MRE minimisation parameters fixing $\alpha = 0.03$; the error, computed as per Eq.* (4.2.24)*, can be seen in the first column, in brackets*

Within each MRE phantom, experimental imperfections lead to variability between pixels. Looking at the apparent stiffness maps in Fig. 4.3.4, excluding the boundary area (as shown in column 3), a small degree of heterogeneity is observed, which accentuates under higher compressions. One reason behind this is speculated to lie in the crystallisation process during the F-T cycles of PVA. Assuming that the PVA freezes first at the mould edges and then in the centre, this could affect the local structures formed. Another reason could be that the top side of the phantoms is not perfectly flat, as it was cut manually. As such, the compression could have not been ideally uniform. Other arguments could revolve around the compression that the piston is exerting on the phantom, but an analysis in this sense is intricate and beyond the purpose of this study. Regardless of the underlying reasons, the small local variations in each phantom lead to the errors presented in Table 4.3.4, as slightly different pixels are attempted to be fit to the same measure. Although the errors are higher than in rheology (Table 4.3.3), the error metrics are not directly comparable. In rheology, a transient behaviour is investigated, that is, a data point is followed in time (Eq. (4.2.21)), whereas in MRE a large spatial sample size is examined - all the pixels across several slices of each phantom, in uncompressed and second compressed state (Eq. (4.2.24)).

The parameters obtained in Table 4.3.4 were sought by employing the CR on each phantom in uncompressed and second compression states, as previously described. Subsequently, they were used directly in reconstructing the corrected maps M for the first compression case, correspondingly for each phantom. The corrected maps M are illustrated, in a phantom, in Fig. 4.3.4 (column 4 and 5). Since the parameters are fit to best describe the data in uncompressed and second compressed states, it was indeed expected that the M map's average for these cases is close to unity. Additionally, the corrected map for the first compression case, whose average also lies close to unity, demonstrates the prediction value of the parameters.

The quantified average of map M for all phantoms in all deformation states (uncompressed, first compression and second compression) is shown in Fig. 4.3.5 (right). Same as for the apparent stiffness G', only a ROI was considered inside each phantom, to avoid boundary effects. Depending on each phantom's height, a variable compression λ describes the first or second compression. For instance, the data points on the graph corresponding to λ between 0.75 and 0.8 depict the first compression for taller phantoms and second compression for shorter phantoms. It is observed that the standard deviations are sizeable (10-19%) and tend to be higher at the larger compression levels. In the stiffness measurements, this observation was attributed to the apparent anisotropy effect and waves' local probing directions. In the corrected maps M, the apparent anisotropy effect is undone by incorporating the knowledge on the deformation gradient, given by Eq. (4.2.13). Since the variance does not decrease in the M maps compared to G' maps, it suggests that the predicted apparent anisotropy in compression is not the main cause of the increasing standard deviations. Instead, it could be due to experimental imperfections which are difficult to control. For instance, the slight unevenness of the phantoms' top or the compression induced by the piston indentation are unavoidable, yet for simplicity their effects are not accounted for in the deformation gradient, which employs an idealised form. Despite these, in all but one cases, the average of corrected map M lies within 10% of the ideal value of 1. This indicates that the model, parameterised with the values presented in Table 4.3.4, captures the bias induced by loading on the wave motion. This shows that the parameters found can describe the material at different deformation states and are suitable for estimating the intrinsic stiffness of the PVA material.

Integrating rheology and MRE is a difficult problem to tackle. While rheology can be employed to directly measure a material's stress-strain response, MRE relies on investigating the wave propagation behaviour in order to estimate material properties. Here, we tried to integrate the two methods by validating a viscoelastic model using rheological data and then using it to derive the $\boldsymbol{\mathcal{G}}'$ and $\boldsymbol{\mathcal{G}}''$ moduli to be used within CR of MRE data. The model was shown to capture the loading bias, thus proving the successful integration of the methods. Furthermore, model parameterisation was done separately for rheology and MRE, yet it is notable that the standard deviations

around the mean of the C_2 and δ_1 parameters are overlapping across the two experimental methods. This, together with the undoing of the loading bias, demonstrates the improvement that the newly developed CR brings in analysing MRE data.

4.3.4 Extension and Impact in Tissue

The theoretical framework presented in section 4.2.1.2 showed that the stiffness moduli are directly related to the material law and deformation. The work done in phantoms supports the theoretical concept. It was shown that, by incorporating the knowledge on material behaviour and deformation into the MRE reconstruction, the intrinsic stiffness can be estimated. This approach could be extended and applied in tissues. As a first step, a biomechanical model describing the tissue could be inferred and further adapted from animal rheological work. Additionally, by employing registration tools on anatomical images of an organ in undeformed and deformed states, deformations can be quantified. Together, a better characterisation of specific tissue rheology and large deformation recordings using MRI could enable proper interpretation of MRE data.

The most immediate extension of our approach could be breast MRE. This imaging technique relies on the breast being fixed in between two plates, which leads to tissue compression. In literature, the loading bias was observed in cases where the breast was fixed tightly, compared to cases where the breast was fixed more loosely[230], but was not accounted for. Undoing this bias using subject specific deformation would help in correcting the observed stiffness for both healthy and diseased areas. For instance, provided that the risk of breast cancer is associated with tissue stiffness[22], accounting for the loading bias would ensure that the risk assessment is not underestimated or overestimated. Clinically, this could improve the prognostic value and disease management.

Another extension of our study could be in the liver, which is subjected to motion due to respiration. While this results mainly in translational motion, parts of the liver can be strained[179]. This can be advantageous, since some liver pathologies were shown to become more apparent, compared to healthy tissue, under large strains (in ex-vivo)[277]. Measuring stiffness in strained tissue could increase diagnostic accuracy, but would require techniques to eliminate loading bias.

The heart is a particularly complex organ which presents structural anisotropy, has dynamic stiffness, and undergoes large motion during the cardiac cycle. The latter constitutes one of the many challenges in assessing the unbiased stiffness of the myocardium[77,132], since the effects of deformation non-trivially interfere with the intrinsic tissue properties. The framework presented in this study would constitute a step forward in assessing the tissue characteristics, by eliminating the deformation bias.

In order to follow this paper's proposed pathway of retrieving intrinsic material param-

eters from MRE data, one would have to consider Eq. (4.2.10) in the material frame as a starting point. Since the moduli $\boldsymbol{\mathcal{G}}'$ and $\boldsymbol{\mathcal{G}}''$ depend on constitutive behaviour and deformation (*e.g.* Eq. (4.2.11)), then knowledge on the PK2 tensor and deformation gradient is necessary. The material behaviour can be modelled by considering a constitutive equation for the strain energy function W, like in Eq. (4.2.18), from which tensor $\boldsymbol{S}$ can be derived, or by proposing an adaption for $\boldsymbol{S}$, *e.g.* Eq. (4.2.20). A formulation for the deformation gradient $\boldsymbol{F}$ is required, like the one presented in Eq. (4.2.13), which needs to describe the unperturbed macro-deformation that the body is undergoing. From these, a form of the moduli $\boldsymbol{\mathcal{G}}'$ and $\boldsymbol{\mathcal{G}}''$ can be inferred, which can be used within CR (Eq. (4.2.23)) to eliminate the loading bias.

4.3.5 Study Limitations

A limitation encountered during the analysis process of the data presented in this study was the estimation of the viscous modulus from MRE data. The rheological tests performed on PVA phantoms identified a very low α, indicating that there is little viscous response of the material. This is a consequence of choosing a highly elastic material, with low wave attenuation. As such, the characteristics of the viscous component were difficult to identify under MRE testing, leading to an overestimation of the reconstructed viscous modulus. This effect was already identified with the employed MRE reconstruction[61], where the overestimation of the viscous modulus was observed in a purely elastic phantom, particularly with increased noise. However, this drawback is predicted to disappear when using *in vivo* data, as tissue has a stronger viscous component. Nevertheless, in this phantom study, the bias due to the spectrum of stiffness prevented the characterisation of the full complex modulus, thus shifting the focus only on the real stiffness modulus.

This study provides the means through which a material's intrinsic characteristics can be retrieved, despite it experiencing loading. However, a reasonable quantification of intrinsic material parameters relies on a good estimation of the deformation state and on an appropriate constitutive material law. In more complex scenarios, like in-vivo measurements, these prerequisites are more challenging to attain. The deformation metrics would presumably need to rely on precise image registration techniques. As medical image registration is a greatly developed field, identification of suitable methods is surely attainable. However, the material constitutive law could be difficult to model, particularly in tissues which exhibit anisotropy. Nonetheless, much work has been done in this sense, as tissue models have been developed in many forms - polynomial, exponential, logarithmic, power laws, etc - and can be further improved and adapted. Undeniably, a model with increased complexity would lead to convoluted $\boldsymbol{\mathcal{G}}'$ and $\boldsymbol{\mathcal{G}}''$ moduli, yet they can be attained numerically (by contrast with the analytic form presented here, for PVA, in appendix 4.B). Hence, despite an increased computational cost, the use of a complex model would not be hindered.

4.4 Conclusions

This paper presents a framework for integrating knowledge on material constitutive behaviour and deformation into wave dynamics in order to retrieve intrinsic material stiffness properties. First off, a theoretical foundation was established by perturbing Cauchy's equations of motion and transcribing the resulting equations into material frame. This determined a form of the stiffness moduli which was seen to depend on the material model and deformation metrics. To support the theory, experiments on PVA phantoms were employed. The PVA material was tested in a rheological setup and its examined behaviour was modelled using a viscoelastic law. The same material was subjected to MRE experiments, where a known deformation (uniaxial compression) was employed. It was seen that, under the designed testing conditions, using standard MRE analysis, the material appeared to be stiffer with increasing compression. Thus, the known material model and deformation were integrated into the stiffness moduli and subsequently into the MRE reconstruction. By doing this, it was shown that intrinsic material stiffness parameters can be estimated, thus undoing the loading bias observed using standard analysis. Hence, this study provides a framework demonstrated to work in phantoms, which can be adapted and applied to MRE in more complex instances.

Conflict of Interest

The authors declare that they have no conflict of interest.

Supplementary materials

4.A Simplification to Linearised Elastic Wave Equations

Here we aim to simplify the total system of Eq. (4.2.9) by Perturbation theory, expanding about the current state $\boldsymbol{U}$.

Starting by linearising the mass conservation equation, using the matrix determinant multiplication rule[80], note that the first order ε terms of the Jacobian J^ε may be clustered as [3]

$$\begin{aligned} J(\boldsymbol{F}^\varepsilon) &= J + D_{\boldsymbol{u}}[J][\boldsymbol{u}^\varepsilon] \\ &= J + D_{\boldsymbol{u}}[J(\boldsymbol{F})][\boldsymbol{u}^\varepsilon] \\ &= J + \frac{\partial J}{\partial \boldsymbol{F}} : D_{\boldsymbol{u}}[\boldsymbol{F}][\boldsymbol{u}^\varepsilon] + \mathcal{O}(\varepsilon^2) \\ &= J + \frac{\partial J}{\partial \boldsymbol{F}} : \nabla_0 \boldsymbol{u}^\varepsilon + \mathcal{O}(\varepsilon^2). \end{aligned} \tag{4.A.1}$$

Since[19] $\frac{\partial J}{\partial \boldsymbol{F}} = J\boldsymbol{F}^{-T}$, it follows that

$$J(\boldsymbol{U} + \boldsymbol{u}^\varepsilon) \approx J + J\boldsymbol{F}^{-T} : \nabla_0 \boldsymbol{u}^\varepsilon. \tag{4.A.2}$$

This approximation, considered to hold strongly when truncated to the first order, reduces the mass balance in Eq. (4.2.9) to

$$\begin{aligned} J^\varepsilon - 1 = J(1 + \boldsymbol{F}^{-T} : \nabla_0 \boldsymbol{u}^\varepsilon) - 1 = \quad & 0 \\ \text{on} \quad & \Omega_0 \quad . \end{aligned} \tag{4.A.3}$$

Here note that J is assumed to satisfy the original balance law in Eq. (4.2.4), which

[3] Here we denote by

$$D_{\boldsymbol{x}}[f][\boldsymbol{u}] = \lim_{\varepsilon \to 0} \frac{f(\boldsymbol{x} + \varepsilon \boldsymbol{u}) - f(\boldsymbol{x})}{\varepsilon}$$

the directional derivative of f at a point $\boldsymbol{x}$ in the direction of increment $\boldsymbol{u}$.

leads section 4.A to become

$$\boldsymbol{F}^{-T} : \nabla_0 \boldsymbol{u}^\varepsilon \quad = \quad 0. \tag{4.A.4}$$

Using Eqs. (4.A.1) and (4.A.4), it is now clear that $J^\varepsilon = J + \mathcal{O}(\varepsilon^2)$, which simplifies the momentum term in Eq. (4.2.9a) to

$$\rho J^\varepsilon \partial_{tt} \boldsymbol{U}^\varepsilon = \rho J \partial_{tt} \boldsymbol{U}^\varepsilon + \mathcal{O}(\varepsilon^2). \tag{4.A.5}$$

To further reduce the momentum balance, we want to expand the stress term $\boldsymbol{F}^\varepsilon \boldsymbol{S}^\varepsilon$ in Eq. (4.2.9) using Taylor expansion in $(P, \boldsymbol{F})$. As a result, letting $\boldsymbol{S} = \boldsymbol{S}_e(\boldsymbol{C}(\boldsymbol{F})) + D_t^\alpha \boldsymbol{S}_v(\boldsymbol{C}(\boldsymbol{F})) + \boldsymbol{S}_p(\boldsymbol{C}(\boldsymbol{F}), P)$, using $\nabla_{\boldsymbol{F}}$ to denote the derivative with respect to $\boldsymbol{F}$, *i.e.*

$$(\nabla_{\boldsymbol{F}})_{ij} = \partial / \partial F_{ij},$$

and the deltas for the difference between the perturbed and unperturbed states, *i.e.*

$$\begin{aligned} \delta \boldsymbol{F} &= \boldsymbol{F}^\varepsilon - \boldsymbol{F} &= \nabla_0 \boldsymbol{u}^\varepsilon, \\ \delta P &= P^\varepsilon - P &= p^\varepsilon, \end{aligned} \tag{4.A.6}$$

we may focus on the deformation gradient expansion

$$\begin{aligned} \boldsymbol{F}^\varepsilon &= \boldsymbol{F} + \sum_{n=1}^{\infty} \big([\nabla_{\boldsymbol{F}}]^n \boldsymbol{F} \big) [: \delta \boldsymbol{F}]^n, \\ &\approx \boldsymbol{F} + \nabla_0 \boldsymbol{u}^\varepsilon + \mathcal{O}(\varepsilon^2), \end{aligned} \tag{4.A.7}$$

the hydrostatic part expansion

$$\begin{aligned} \boldsymbol{S}_p^\varepsilon &= \boldsymbol{S}_p + \sum_{n=1}^{\infty} \left(\big([\nabla_{\boldsymbol{F}}]^n \boldsymbol{S}_p \big) [: \delta \boldsymbol{F}]^n + \left(\frac{\partial^n}{\partial P^n} \boldsymbol{S}_p \right) [: \delta P]^n \right) \\ &\approx \big(\boldsymbol{S}_p + \nabla_{\boldsymbol{F}} \boldsymbol{S}_p : \nabla_0 \boldsymbol{u}^\varepsilon + p^\varepsilon J \boldsymbol{F}^{-T} \big) + \mathcal{O}(\varepsilon^2), \end{aligned} \tag{4.A.8}$$

the PK2 elastic part expansion

$$\begin{aligned} \boldsymbol{S}_e^\varepsilon &= \boldsymbol{S}_e + \sum_{n=1}^{\infty} \big([\nabla_{\boldsymbol{F}}]^n \boldsymbol{S}_e \big) [: \delta \boldsymbol{F}]^n, \\ &\approx \boldsymbol{S}_e + \nabla_{\boldsymbol{F}} \boldsymbol{S}_e : \nabla_0 \boldsymbol{u}^\varepsilon + \mathcal{O}(\varepsilon^2), \end{aligned} \tag{4.A.9}$$

and the PK2 viscoelastic part expansion

$$\begin{aligned} D_t^\alpha \boldsymbol{S}_v^\varepsilon &= D_t^\alpha \left(\boldsymbol{S}_v + \sum_{n=1}^{\infty} \left([\nabla_{\boldsymbol{F}}]^n \boldsymbol{S}_v \right) [: \delta \boldsymbol{F}]^n \right) \\ &\approx D_t^\alpha \left(\boldsymbol{S}_v + \nabla_{\boldsymbol{F}} \boldsymbol{S}_v : \nabla_0 \boldsymbol{u}^\varepsilon \right) + \mathcal{O}(\varepsilon^2) \\ &\approx \nabla_{\boldsymbol{F}} \boldsymbol{S}_v : D_t^\alpha \left(\nabla_0 \boldsymbol{u}^\varepsilon \right) + \mathcal{O}(\varepsilon^2), \end{aligned} \tag{4.A.10}$$

where it is assumed that $\boldsymbol{S}_v$ and $\nabla_{\boldsymbol{F}} \boldsymbol{S}_v$ are constant in time.

Hence, the components of the stress term $\boldsymbol{F}^\varepsilon \boldsymbol{S}^\varepsilon$ are given by

$$\begin{aligned} \boldsymbol{F}^\varepsilon \boldsymbol{S}^\varepsilon \approx\ & \boldsymbol{F}\boldsymbol{S} + \left(\boldsymbol{F}[\nabla_{\boldsymbol{F}}(\boldsymbol{S}_e + \boldsymbol{S}_p)] + [\boldsymbol{\mathcal{I}}]\boldsymbol{S} \right) : \nabla_0 \boldsymbol{u}^\varepsilon + \\ & \boldsymbol{F}[\nabla_{\boldsymbol{F}} \boldsymbol{S}_v] : D_t^\alpha \left(\nabla_0 \boldsymbol{u}^\varepsilon \right) + p^\varepsilon J \boldsymbol{F}^{-T} + \mathcal{O}(\varepsilon^2), \end{aligned}$$

where the square bracketed terms denote fourth-order tensors resulting from differentials of the PK2 stress tensor with respect to $\boldsymbol{F}$. For clarity, in indicial notation,

$$\begin{aligned} (F^\varepsilon S^\varepsilon)_{ij} =\ & F_{ik} S_{kj} + F_{ik} \frac{\partial (S_e + S_p)_{kj}}{\partial F_{mn}} \frac{\partial u_m^\varepsilon}{\partial X_n} + D_t^\alpha F_{ik} \frac{\partial (S_v)_{kj}}{\partial F_{mn}} \frac{\partial u_m^\varepsilon}{\partial X_n} + \frac{\partial u_i^\varepsilon}{\partial X_n} S_{nj} + \\ & p^\varepsilon J F_{ji}^{-1} + \mathcal{O}(\varepsilon^2). \end{aligned} \tag{4.A.11}$$

Thus, considering Eqs. (4.A.5) and (4.A.11), the conservation of momentum can be split between macro-deformation (in square brackets) and micro-deformation components, *i.e.*

$$\begin{aligned} & \left[\rho J \partial_{tt} \boldsymbol{U} - \nabla_0 \cdot (\boldsymbol{F}\boldsymbol{S}) \right] + \rho J \partial_{tt} \boldsymbol{u}^\varepsilon - \\ & \nabla_0 \cdot \left(\left[\boldsymbol{F} \nabla_{\boldsymbol{F}} (\boldsymbol{S}_e + \boldsymbol{S}_p) + \boldsymbol{\mathcal{I}}\boldsymbol{S} \right] : \nabla_0 \boldsymbol{u}^\varepsilon + [\boldsymbol{F} \nabla_{\boldsymbol{F}} \boldsymbol{S}_v] : D_t^\alpha \left(\nabla_0 \boldsymbol{u}^\varepsilon \right) + p^\varepsilon J \boldsymbol{F}^{-T} \right) = \boldsymbol{0}. \end{aligned} \tag{4.A.12}$$

Noting that the macro-deformation $\boldsymbol{U}$ satisfies Eq. (4.2.4), the first square bracketed term on the left-hand side is zero. Hence, a set of linearised elastic wave equations in the reference frame can be formulated:

$$\begin{aligned} \rho J \partial_{tt} \boldsymbol{u}^\varepsilon - \nabla_0 \cdot \Bigg(& \left[\boldsymbol{F} \nabla_{\boldsymbol{F}} (\boldsymbol{S}_e + \boldsymbol{S}_p) + \boldsymbol{\mathcal{I}}\boldsymbol{S} \right] : \nabla_0 \boldsymbol{u}^\varepsilon + \\ & [\boldsymbol{F} \nabla_{\boldsymbol{F}} \boldsymbol{S}_v] : D_t^\alpha \left(\nabla_0 \boldsymbol{u}^\varepsilon \right) + p^\varepsilon J \boldsymbol{F}^{-T} \Bigg) = \boldsymbol{0}, \end{aligned} \tag{4.A.13a}$$

$$\boldsymbol{F}^{-T} : \nabla_0 \boldsymbol{u}^\varepsilon = 0. \tag{4.A.13b}$$

While the set of Eq. (4.A.13) deals generically with small scale perturbations, in the case where the frequency is sufficiently high or the time interval sufficiently long, harmonic waves may be considered. Thus, inserting the wave form given by Eq. (4.2.3) into the set of Eq. (4.A.13), and noting the Laplace transform as $D_t^\alpha \left(e^{i\omega t} \right) \approx (i\omega)^\alpha e^{i\omega t}\ \forall t >> 0$,

it follows that

$$-\rho J\omega^2 \boldsymbol{u}_c -$$
$$\nabla_0 \cdot \Big([\boldsymbol{F}\nabla_{\boldsymbol{F}}(\boldsymbol{S}_e + (i\omega)^\alpha \boldsymbol{S}_v + \boldsymbol{S}_p) + \boldsymbol{\mathcal{I}}\boldsymbol{S}] : \nabla_0 \boldsymbol{u}_c + p_c J \boldsymbol{F}^{-T} \Big) = \boldsymbol{0}, \tag{4.A.14a}$$
$$\boldsymbol{F}^{-T} : \nabla_0 \boldsymbol{u}_c = 0. \tag{4.A.14b}$$

When comparing with real data, it is desirable to map the momentum equations into the physical frame. Using the property[189] that

$$\nabla \widetilde{\boldsymbol{y}} = (\nabla_0 \boldsymbol{y}) \boldsymbol{F}^{-1},$$

the gradients with respect to the reference frame can also be transformed into the current domain. Hence, the terms in the set of Eq. (4.A.14) become

$$\begin{aligned} &[\boldsymbol{F}\nabla_{\boldsymbol{F}}(\boldsymbol{S}_e + (i\omega)^\alpha \boldsymbol{S}_v + \boldsymbol{S}_p) + \boldsymbol{\mathcal{I}}\boldsymbol{S}] : \nabla_0 \boldsymbol{u}_c \\ &= [\boldsymbol{F}\nabla_{\boldsymbol{F}}(\boldsymbol{S}_e + (i\omega)^\alpha \boldsymbol{S}_v + \boldsymbol{S}_p) + \boldsymbol{\mathcal{I}}\boldsymbol{S}] : [\nabla_0 \boldsymbol{u}_c \boldsymbol{F}^{-1} \boldsymbol{F}] \\ &= [\boldsymbol{F}\nabla_{\boldsymbol{F}}(\boldsymbol{S}_e + (i\omega)^\alpha \boldsymbol{S}_v + \boldsymbol{S}_p)\boldsymbol{F}^T + \boldsymbol{\mathcal{I}}\boldsymbol{S}\boldsymbol{F}^T] : \nabla \boldsymbol{u}_c, \end{aligned} \tag{4.A.15}$$

and

$$\begin{aligned} \boldsymbol{F}^{-T} : \nabla_0 \boldsymbol{u}_c &= \boldsymbol{F}^{-T} : [\nabla_0 \boldsymbol{u}_c \boldsymbol{F}^{-1} \boldsymbol{F}] \\ &= \boldsymbol{I} : \nabla \boldsymbol{u}_c \\ &= \nabla \cdot \boldsymbol{u}_c. \end{aligned} \tag{4.A.16}$$

In indicial notation,

$$\begin{aligned} \Big([\boldsymbol{F}\nabla_{\boldsymbol{F}}(\boldsymbol{S}_e + (i\omega)^\alpha \boldsymbol{S}_v + \boldsymbol{S}_p) + \boldsymbol{\mathcal{I}}\boldsymbol{S}] : \nabla_0 \boldsymbol{u}_c \Big)_{ij} \quad = \\ F_{ik} \frac{\partial (S_e + (i\omega)^\alpha S_v + S_p)_{kj}}{\partial F_{mn}} \frac{\partial (u_c)_m}{\partial x_l} F_{ln} + \\ \delta_{im} S_{nj} \frac{\partial (u_c)_m}{\partial x_l} F_{ln}, \end{aligned}$$

and

$$\boldsymbol{F}^{-T} : \nabla_0 \boldsymbol{u}_c = \frac{\partial (u_c)_m}{\partial x_m}.$$

Moreover, by noticing the property linking the divergence of a tensor between the physical and reference domains[96]

$$J \nabla \cdot \widetilde{\boldsymbol{H}} = \nabla_0 \cdot [J \boldsymbol{H} \boldsymbol{F}^{-T}],$$

the divergence of the stress terms can be re-cast in terms of the physical gradient operator ∇, *i.e.*

$$\nabla_0 \cdot \Big([\boldsymbol{F}\nabla_{\boldsymbol{F}}(\boldsymbol{S}_e + (i\omega)^\alpha \boldsymbol{S}_v + \boldsymbol{S}_p)\boldsymbol{F}^T + \boldsymbol{\mathcal{I}}\boldsymbol{S}\boldsymbol{F}^T] : \nabla \boldsymbol{u}_c \Big) = J\nabla \cdot (\boldsymbol{\mathcal{C}} : \nabla \boldsymbol{u}_c), \tag{4.A.17}$$

where the 4^{th} order tensor $\boldsymbol{\mathcal{C}}$ encompasses

$$\mathcal{C}_{ijml} = \frac{1}{J}\left(F_{ik}\frac{\partial (S_e + (i\omega)^\alpha S_v + S_p)_{ks}}{\partial F_{mn}} + \frac{\partial F_{ik}}{\partial F_{mn}} S_{ks} \right) F_{ln} F_{js}. \tag{4.A.18}$$

Combining Eqs. (4.A.16) and (4.A.17) and noting the property linking the divergence of a scalar in the reference domain to the physical frame[96]

$$J\nabla \widetilde{w} = \nabla_0 \cdot [wJ\boldsymbol{F}^{-T}]$$

the equations analogous to the classical set of Eq. (4.2.4), may be written as,

$$\rho J\omega^2 \boldsymbol{u}_c - J\nabla \cdot \Big(p_c \boldsymbol{I} + \boldsymbol{\mathcal{C}} : \nabla \boldsymbol{u}_c \Big) = \boldsymbol{0}, \tag{4.A.19a}$$

$$\nabla \cdot \boldsymbol{u}_c = 0, \qquad \text{on } \Omega. \tag{4.A.19b}$$

Equation (4.A.19) can be written as

$$-\rho\omega^2 \boldsymbol{u}_c - \nabla \cdot [(\boldsymbol{\mathcal{G}}' + i\boldsymbol{\mathcal{G}}'') : \nabla \boldsymbol{u}_c + p_c \boldsymbol{I}] = \boldsymbol{0}, \tag{4.A.20a}$$

with the understanding that the real and imaginary scaling moduli $\boldsymbol{\mathcal{G}}'$ and $\boldsymbol{\mathcal{G}}''$ are given by $\boldsymbol{\mathcal{G}}' = \mathrm{Re}(\boldsymbol{\mathcal{C}})$, $\boldsymbol{\mathcal{G}}'' = \mathrm{Im}(\boldsymbol{\mathcal{C}})$, *i.e.*

$$\boldsymbol{\mathcal{G}}' = \frac{1}{J}\Big(\boldsymbol{F}\nabla_{\boldsymbol{F}}\boldsymbol{S}_e + \omega^\alpha \cos\Big(\frac{\pi\alpha}{2}\Big) \boldsymbol{F}\nabla_{\boldsymbol{F}}\boldsymbol{S}_v + \boldsymbol{F}\nabla_{\boldsymbol{F}}\boldsymbol{S}_p + \boldsymbol{\mathcal{I}}\boldsymbol{S} \Big) \boldsymbol{F}^T\boldsymbol{F}^T, \tag{4.A.21a}$$

$$\boldsymbol{\mathcal{G}}'' = \frac{\omega^\alpha}{J} \sin\Big(\frac{\pi\alpha}{2}\Big) \boldsymbol{F}(\nabla_{\boldsymbol{F}}\boldsymbol{S}_v)\boldsymbol{F}^T\boldsymbol{F}^T, \tag{4.A.21b}$$

where the index notation of $\boldsymbol{\mathcal{G}}'$ and $\boldsymbol{\mathcal{G}}''$ follows that of $\boldsymbol{\mathcal{C}}$, as presented in Eq. (4.A.18), and the tensor products are defined as in Eq. (4.2.1).

4.B Viscoelastic Moduli estimates for PVA material

In this section the aim is to understand the effect of macrodeformations on the wave behaviour in a viscoelastic material described by Eq. (4.2.20). So far general elastic and viscoelastic stresses $\boldsymbol{S}_e$ and $\boldsymbol{S}_v$ have been used. Recall that, for this work, they were considered to comprise two parts each, based on a Mooney-Rivlin type of law, as follows:

$$\begin{aligned} \boldsymbol{S}_e &= C_1\boldsymbol{S}_{e1} + C_2\boldsymbol{S}_{e2}, \\ D_t^\alpha \boldsymbol{S}_v &= \delta_1 D_t^\alpha \boldsymbol{S}_{e1} + \delta_2 D_t^\alpha \boldsymbol{S}_{e2}. \end{aligned}$$

Hence, the 4^{th} order tensor $\boldsymbol{\mathcal{C}}$ can be taken one step further and written as

$$\begin{aligned}\mathcal{C}_{ijml} =& \frac{1}{J}\Bigg\{ F_{ik}\Bigg[C_1\frac{\partial S_{e1,ks}}{\partial F_{mn}} + C_2\frac{\partial S_{e2,ks}}{\partial F_{mn}} + (i\omega)^{\alpha}\Big(\delta_1\frac{\partial S_{v1,ks}}{\partial F_{mn}} + \delta_2\frac{\partial S_{v2,ks}}{\partial F_{mn}}\Big) + \\ & \frac{\partial S_{p,ks}}{\partial F_{mn}}\Bigg] + \frac{\partial F_{ik}}{\partial F_{mn}}S_{ks}\Bigg\}F_{ln}F_{js}, \end{aligned} \tag{4.B.2}$$

while the $\boldsymbol{\mathcal{G}}'$ and $\boldsymbol{\mathcal{G}}''$ moduli become

$$\begin{aligned}\boldsymbol{\mathcal{G}}' =& \frac{1}{J}\Bigg\{\boldsymbol{F}\Big[C_1(\nabla_{\boldsymbol{F}}\boldsymbol{S}_{e1}) + C_2(\nabla_{\boldsymbol{F}}\boldsymbol{S}_{e2}) + \nabla_{\boldsymbol{F}}\boldsymbol{S}_p\Big] + \boldsymbol{\mathcal{I}}\boldsymbol{S}\Bigg\}\boldsymbol{F}^T\boldsymbol{F}^T + \\ & \frac{\omega^{\alpha}}{J}\cos\Big(\frac{\pi\alpha}{2}\Big)\,\boldsymbol{F}\Bigg\{\delta_1(\nabla_{\boldsymbol{F}}\boldsymbol{S}_{e1}) + \delta_2(\nabla_{\boldsymbol{F}}\boldsymbol{S}_{e2})\Bigg\}\boldsymbol{F}^T\boldsymbol{F}^T, \end{aligned} \tag{4.B.3a}$$

$$\boldsymbol{\mathcal{G}}'' = \frac{\omega^{\alpha}}{J}\sin\Big(\frac{\pi\alpha}{2}\Big)\,\boldsymbol{F}\Bigg\{\delta_1(\nabla_{\boldsymbol{F}}\boldsymbol{S}_{e1}) + \delta_2(\nabla_{\boldsymbol{F}}\boldsymbol{S}_{e2})\Bigg\}\boldsymbol{F}^T\boldsymbol{F}^T. \tag{4.B.3b}$$

The moduli $\boldsymbol{\mathcal{G}}'$ and $\boldsymbol{\mathcal{G}}''$ are influencing the wave dynamics $\nabla\boldsymbol{u}_c$, leading to an apparent wave dynamic. Now, considering the analytic formulation of the contraction $(\boldsymbol{\mathcal{G}}'+i\boldsymbol{\mathcal{G}}'') : \nabla\boldsymbol{u}_c$, consider that the wave $\nabla\boldsymbol{u}_c$ satisfies the harmonic wave motion described in section 4.2.1.1. After a cumbersome derivation and simplification process, the moduli defining the PVA material used can be formulated as

$$\begin{aligned}\boldsymbol{\mathcal{G}}' : \nabla\boldsymbol{u}_c =& \frac{1}{J}\Bigg\{C_1\Big[-\frac{4}{3}\boldsymbol{I}(\widehat{\boldsymbol{B}} : \nabla\boldsymbol{u}_c) + \frac{2}{3}I_{\widehat{\boldsymbol{C}}}\nabla\boldsymbol{u}_c^T + 2\nabla\boldsymbol{u}_c\widehat{\boldsymbol{B}}\Big] \\ & + 8C_2\Bigg[(\widehat{\boldsymbol{B}}^2 : \nabla\boldsymbol{u}_c)\left(4\widehat{\boldsymbol{B}}^2 + 4\boldsymbol{I} - \frac{8}{3}II_{\widehat{\boldsymbol{C}}}\boldsymbol{I}\right) + \\ & \Big(\widehat{\boldsymbol{B}}\nabla\boldsymbol{u}_c\widehat{\boldsymbol{B}} + (\widehat{\boldsymbol{B}}\nabla\boldsymbol{u}_c\widehat{\boldsymbol{B}})^T + \nabla\boldsymbol{u}_c\widehat{\boldsymbol{B}}^2 + \frac{II_{\widehat{\boldsymbol{C}}}}{3}\nabla\boldsymbol{u}_c^T\Big) \\ & \cdot (II_{\widehat{\boldsymbol{C}}} - 3)\Bigg] - JP\nabla\boldsymbol{u}_c^T + \\ & \omega^{\alpha}\cos\Big(\frac{\pi\alpha}{2}\Big)\cdot\Bigg(\delta_1\frac{2}{3}I_{\widehat{\boldsymbol{C}}}\big[\nabla\boldsymbol{u}_c + \nabla\boldsymbol{u}_c^T\big] + \\ & 8\delta_2\Bigg[(\widehat{\boldsymbol{B}}^2 : \nabla\boldsymbol{u}_c)\left(4\widehat{\boldsymbol{B}}^2 + 2\boldsymbol{I} - 2II_{\widehat{\boldsymbol{C}}}\boldsymbol{I}\right) + \\ & \Big(\widehat{\boldsymbol{B}}\nabla\boldsymbol{u}_c\widehat{\boldsymbol{B}} + (\widehat{\boldsymbol{B}}\nabla\boldsymbol{u}_c\widehat{\boldsymbol{B}})^T + \frac{II_{\widehat{\boldsymbol{C}}}}{3}\big(\nabla\boldsymbol{u}_c + \nabla\boldsymbol{u}_c^T\big)\Big)\cdot(II_{\widehat{\boldsymbol{C}}} - 3)\Bigg]\Bigg)\Bigg\}\end{aligned} \tag{4.B.4}$$

and

$$\boldsymbol{\mathcal{G}}'' : \nabla \boldsymbol{u}_c = \frac{1}{J}\Bigg\{\omega^{\alpha}\sin\left(\frac{\pi\alpha}{2}\right)\cdot\Bigg(\delta_1\frac{2}{3}I_{\widehat{\boldsymbol{C}}}\left[\nabla\boldsymbol{u}_c+\nabla\boldsymbol{u}_c^T\right]+ \\ 8\delta_2\Bigg[(\widehat{\boldsymbol{B}}^2:\nabla\boldsymbol{u}_c)\left(4\widehat{\boldsymbol{B}}^2+2\boldsymbol{I}-2II_{\widehat{\boldsymbol{C}}}\boldsymbol{I}\right)+ \\ \left(\widehat{\boldsymbol{B}}\nabla\boldsymbol{u}_c\widehat{\boldsymbol{B}}+(\widehat{\boldsymbol{B}}\nabla\boldsymbol{u}_c\widehat{\boldsymbol{B}})^T+\frac{II_{\widehat{\boldsymbol{C}}}}{3}\left(\nabla\boldsymbol{u}_c+\nabla\boldsymbol{u}_c^T\right)\right)\cdot(II_{\widehat{\boldsymbol{C}}}-3)\Bigg]\Bigg)\Bigg\}. \tag{4.B.5}$$

In the particular case when there exists no macro deformation, *i.e.* $\boldsymbol{F}=\boldsymbol{I}$, it follows that the real scaling modulus retains only the terms

$$\boldsymbol{\mathcal{G}}' : \nabla \boldsymbol{u}_c = \frac{1}{J}\Bigg\{2C_1\left(\nabla\boldsymbol{u}_c+\nabla\boldsymbol{u}_c^T\right)-JP\nabla\boldsymbol{u}_c^T+2\delta_1\omega^{\alpha}\cos\left(\frac{\pi\alpha}{2}\right)\left(\nabla\boldsymbol{u}_c+\nabla\boldsymbol{u}_c^T\right)\Bigg\}, \tag{4.B.6}$$

while the imaginary modulus reduces to

$$\boldsymbol{\mathcal{G}}'' : \nabla \boldsymbol{u}_c = \frac{2\delta_1\omega^{\alpha}}{J}\sin\left(\frac{\pi\alpha}{2}\right)\left(\nabla\boldsymbol{u}_c+\nabla\boldsymbol{u}_c^T\right). \tag{4.B.7}$$

4.C Supplement

In search of a suitable phantom for MRE measurements, an intricate and lengthy process followed. The aim of this supplementary material is to give some details into the challenges encountered during the phantom design stage, as this may provide some useful insights for the readers interested in this process.

4.C.1 Silicone phantom

Initially, a two agent silicone dielectric gel Sylgard 527 A & B (Dow Corning Corporation, Midland, MI, USA) was chosen to be investigated due to its intrinsic nonlinear properties under loading and suitability of mimicking tissue behaviour[4,153,173]. The two parts of the gel (A & B) were mixed in a volume ratio of 1:2 by manual stirring for approximately 10 minutes. The compound was then placed for 5 minutes in a vacuum pump for degassing. After being transferred in a cylindrical mould (3.9 cm diameter and 4.7 cm height), the mixture was placed in the oven to cure for 180 minutes at a temperature of 120°C, then left to cool down in the same oven. The phantom thus obtained was very slightly sticky but easy to handle. It had a well defined shape and was able to undergo large deformations ($\approx 30\%$) without obvious damage.

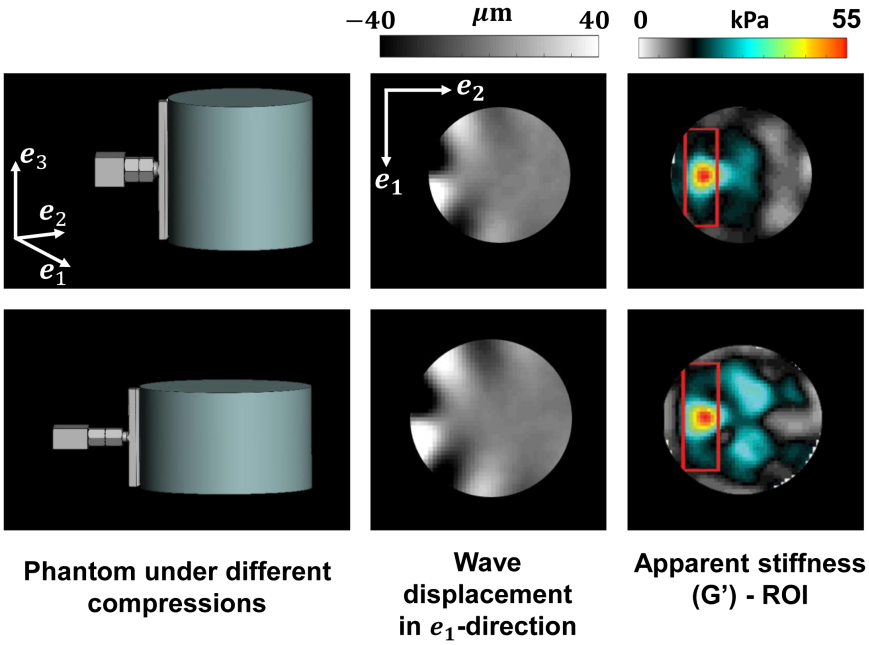

Figure 4.C.1 *Images corresponding to the uncompressed (top row) and compressed (bottom row) silicone phantom; (First column) Phantom depicted at the different deformation states. Harmonic deformations were driven by the piston on the left (grey bar). Slices were acquired in the coronal plane ($\boldsymbol{e}_1 - \boldsymbol{e}_2$). (Second column) Wave displacements from the MRE imaging protocol can be seen in the $\boldsymbol{e}_1$ direction ; (Third column) Stiffness estimates using the UR. The region of interest (ROI) of the apparent stiffness map G' was obtained by eroding the phantoms' margins.*

For MRE scanning purposes, the phantom was placed in a device similar to the one in Fig. 4.2.3, where the top and bottom plates were sprayed with a silicone spray, in order to facilitate phantom sliding under compression. Fig. 4.C.1 shows the phantom in uncompressed and compressed states, the wave propagation in the $\boldsymbol{e}_1$ direction and the reconstructed stiffness maps. It can be seen that the waves are highly attenuated, as they do not reach the part that is furthest away from the piston. This led to complications when reconstructing the stiffness map, leading to small areas with reliable stiffness estimates (shown by the red rectangles). Thus, it was deemed that the material was too highly attenuating, making it unsuitable for our MRE purposes.

4.C.2 PVA phantom

Following the procedure described in section 4.2.2.1, multiple PVA phantoms were created with varying concentrations. With 5% PVA, the phantom was soft and unstable, leaking water when being compressed. The same effect was observed for a 7% phantom that underwent only two freeze-thaw cycles instead of three. The 10% phantom was much stiffer, making it very difficult to be compressed at the desired $\approx 30\%$ level.

An additional challenge encountered when fabricating the PVA phantoms was the bulging that occurred due to freezing. This created an uneven top surface, which would not have allowed us to perform uniform compression across the sample. The solution was to cut the top part using a hacksaw. This had to be performed immediately after the third freezing cycle. It was not possible to obtain a flat surface by cutting a thawed phantom.

This summary provides a brief overview of the steps taken in order to obtain a phantom that was suitable for the study. Once the best phantom was identified, the fabrication process was standardised and multiple samples were produced.

5 Nonlinear viscoelastic constitutive model for bovine liver tissue

The previous chapter presented a study on PVA phantoms, which led to a framework for undoing the deformation bias in MRE measurements of loaded materials. In this sense, a corrected MRE reconstruction was employed, as described by Eq. (4.2.23), which relies on the identification of the 4^{th} order real and imaginary tensors $\boldsymbol{\mathcal{G}}'$ and $\boldsymbol{\mathcal{G}}''$. Subsequently, these depend on the deformation and material law.

The next goal is to employ a similar framework in liver tissue, in order to retrieve its intrinsic properties even when subjected to deformation. Hence, this chapter focuses on one part of the framework, namely the constitutive characterisation of liver tissue. Ideally, the constitutive law should be rate dependent, nonlinearly viscoelastic, in order to be utilised in MRE reconstruction of liver data (chapter 6).

This study is based on rheological data acquired by Tan et al.[246] at a range of large compressions (1-20%), shear strains (1-50%) and frequencies (0.5-2 Hz). The modelling of the experiment, which is similar to the one depicted in Fig. 2.5.2 (bottom right), is presented in section 5.2.2. For constitutive modelling, viscoelastic adaptions of three types of hyperelastic laws were considered: polynomial (modified Mooney-Rivlin), exponential and Ogden (section 5.2.3). These are fit to the data, using three different error norms (section 5.2.4), which contribute to a better understanding of the empirical observations, as presented in the results and discussion sections 5.3 and 5.4.

One important note regarding the modelling of the testing conditions is that the tissue was considered to be able to slide under compression (ideal compression). However, in the actual experiment, the contact surface was restricted (non-ideal compression). In order to understand the potential differences introduced by this assumption, simulations of both scenarios were run. The comparison of the ideal and non-ideal compressions is discussed in the supplementary section 5.B, appended at the end of this chapter.

This chapter has been submitted as a self-standing article:
Adela Capilnasiu, Lynne Bilston, Ralph Sinkus, David Nordsletten. "Nonlinear viscoelastic constitutive model for bovine liver tissue". *Biomechanics and modeling in mechanobiology* (Under review, 2019).

The candidate contributed to the analysis and interpretation of research data, and drafting of the manuscript.

Abstract

Soft tissue mechanical characterisation is important in many areas of medical research. Examples span from surgery training, device design and testing, sudden injury and disease diagnosis. The liver is of particular interest, as it is the most commonly injured organ in frontal and side motor vehicle crashes, and also assessed for inflammation and fibrosis in chronic liver diseases. Hence, an extensive rheological characterisation of liver tissue would contribute to advancements in these areas, which are dependent upon underlying biomechanical models. The aim of this paper is to define a liver constitutive equation that is able to characterise the nonlinear viscoelastic behaviour of liver tissue under a range of deformations and frequencies. The tissue response to large amplitude oscillatory shear (1-50%) under varying preloads (1-20%) and frequencies (0.5-2 Hz) is modelled using viscoelastic adapted forms of the Mooney-Rivlin, Ogden and exponential models. These models are fit to the data using classical or modified objective norms. Results show that all three models are suitable for capturing the initial nonlinear regime, with the latter two being capable of capturing, simultaneously, the whole deformation range tested. The work presented here provides a comprehensive analysis across several material models and norms, leading to an identifiable constitutive equation that describes the nonlinear viscoelastic behaviour of the liver.

5.1 Introduction

Biomechanical characterisation of tissues is essential in medical research. New surgery techniques, implants or devices are being tested *in silico*, *in vitro* and *in vivo*[41,81,158,187,212]. In these tests, it is critical to know the liver's response to a range of factors, such as puncturing, cutting, deformations and displacements, etc. For diagnosis purposes, elastography is a technique that depends on the underlying tissue properties in order to assess the presence of disease[62]. In vivo magnetic resonance elastography (MRE) has shown that the existence of liver inflammation and fibrosis gives higher stiffness measurements[114,232]. However, coexisting diseases[177] and the bias introduced by large deformations on elastography measurements[30] can further complicate the diagnosis. Comprehensive liver models could also benefit other research areas like transportation safety[255,279], where biomechanical tests for abdominal injury tolerance limits provide essential information in developing safer vehicles[122]. With the liver being the most frequently injured organ in frontal and side impacts[279], a finite element (FE) model could be used for prediction purposes, provided that it incorporates local and global liver tissue response to mechanical testing. Hence, improved knowledge of the nonlinear viscoelastic behaviour of the liver is needed.

Over the past decades, a range of rheological tests have been employed to characterise liver tissue, the most common being uniaxial deformation (either as small sample

loading or indentation on the full organ) and shearing. Both oscillatory shear and uniaxial deformation tests show that, at low strains, the liver exhibits quasi-linearity, with the nonlinear behaviour being exposed at higher strains[70,147,246]. Additionally, loading-unloading tests reveal that hysteresis effects are taking place[120], with the response being rate dependent[147,172]. Multi-frequency soft tissue measurements of the shear modulus G^* indicate a fractional order dependence on the angular frequency in the form of $G^* \propto \omega^{\alpha}$[102], with $\alpha \in [0.2, 0.35]$ (e.g. $\alpha \approx 0.23$[147], $\alpha \approx 0.26$[120,232], $\alpha \approx 0.32$[6]). Other biomechanical properties of the liver have also been investigated, such as relaxation[36,146] and creep[259].

Liver tissue rheology measurements have led to a range of biomechanical models. Hyperelasticity is often assumed, with polynomial, exponential and logarithmic forms being employed for compression and elongation data[39,70]. The general findings indicate that the exponential, logarithmic and power-law models offer more flexibility in capturing the different regions of the stress-strain curves. In order to probe viscoelasticity, cyclic deformations or relaxation tests usually need to be investigated. Some studies employed relaxation[146], shear oscillations[217] or cyclic indentation[120] over a range of frequencies, thus offering a broader picture of the biomechanical behaviour of liver. Among these, the K-BKZ model was proposed due to its awareness of the complete past time history, and was validated against small amplitude oscillatory shear and strain ramp[217]. Alternatively, viscoelasticity was modelled by introducing a Maxwell element. A complex differential model, with 10 model parameters, was investigated by Liu[146] against the relaxation behaviour at four strain levels. Jordan[120] considered increasingly complex networks of springs and dash-pots, arranged both in series and in parallel, in order to model the liver behaviour under cyclic indentation at different strain rates and relaxation. A power-law model considering solid-phase compressibility was employed by Perepelyuk[195], who, at large preload strains and small oscillatory shear, measured the storage modulus G'. While these models significantly contribute to our understanding of separate aspects of the viscoelastic behaviour of the liver, there remains a need for a comprehensive 3D model which can describe the tissue response under various deformation types and frequencies.

In this paper, we present a comparison of liver constitutive models based on the tissue's response to a range of large deformations and frequencies. A cross testing of uniaxial preloads (1-20%), shear strains (1-50%) and frequencies (0.5-2Hz) is considered[246], thus emphasising the rate dependent, nonlinearly viscoelastic behaviour of the liver. The testing protocol displays a strain softening effect, which is addressed by proposing a new error norm that allows for some degree of flexibility in fitting the linear parameters of the models. This analysis and model fitting procedure lead to the identification of simplified constitutive models, which retain the essential components needed for characterising the above mentioned properties of the liver exhibited under combined deformation and various frequencies. To the authors' knowledge, this is the first modelling study for

liver that bridges the gap between uniaxial loading, oscillatory shearing and frequency sweeping all within a three-dimensional nonlinear visoelastic model.

In what follows, a brief introduction to kinematics (section 5.2.1) precedes the outlining of the experimental design and modelling assumptions (section 5.2.2). Three different constitutive models are proposed, which are then fit to the data using a set of error norms that infer different model properties. Throughout section 5.3, the results of the model fitting process are going to be presented grouped by the norm investigated (sections 5.3.1–5.3.3), with the three models being compared within each subsection. This is followed by a discussion reviewing the findings and potential future applications (section 5.4).

5.2 Materials and Methods

The aim of this work is to characterise the constitutive behaviour of the liver under a range of combined deformations and frequencies. In order to achieve this, section 5.2.1 outlines the kinematics metrics that are needed throughout this paper (see[19,244]). Section 5.2.2 explains the testing protocol and its modelling characteristics. Three different types of models are proposed in section 5.2.3, which are due to be fit to the data using the methods described in section 5.2.4.

5.2.1 Kinematics background

Let the region $\Omega_0 \subset \mathbb{R}^d$ define a solid body which can be deformed in space and time using a displacement field $\boldsymbol{U} : \Omega_0 \times [0,T] \to \mathbb{R}^d$. A point in the reference domain, $\boldsymbol{X} \in \Omega_0$, corresponds at time $t \in [0,T]$ to a point in the physical domain Ω_t, by the mapping

$$\boldsymbol{x} = \boldsymbol{U}(\boldsymbol{X}, t) + \boldsymbol{X}, \qquad \boldsymbol{x} \in \Omega_t. \tag{5.2.1}$$

The deformation gradient tensor $\boldsymbol{F}$ relates the reference and physical domains via

$$\boldsymbol{F} = \nabla_{\boldsymbol{X}} \boldsymbol{x} = \frac{\partial \boldsymbol{x}}{\partial \boldsymbol{X}}, \qquad F_{ij} = \frac{\partial x_i}{\partial X_j}. \tag{5.2.2}$$

The volumetric changes between the two states are quantified by the determinant $J = \det \boldsymbol{F}$, with $J = 1$ implying incompressibility. From the deformation gradient $\boldsymbol{F}$, the right and left Cauchy Green strains are defined as

$$\boldsymbol{C} = \boldsymbol{F}^T \boldsymbol{F}, \quad \boldsymbol{B} = \boldsymbol{F}\boldsymbol{F}^T,$$

or, in their isochoric form[19], here indicated by the " ˆ " symbol, as

$$\hat{\boldsymbol{F}} = J^{-1/d}\boldsymbol{F}, \quad \hat{\boldsymbol{C}} = \hat{\boldsymbol{F}}^T\hat{\boldsymbol{F}}, \quad \hat{\boldsymbol{B}} = \hat{\boldsymbol{F}}\hat{\boldsymbol{F}}^T.$$

Some tensor quantities that remain unchanged under rotations are the first and second

invariants[19], obtained using the double contraction ":"

$$I_{\boldsymbol{A}} = \boldsymbol{A} : \boldsymbol{I}, \quad II_{\boldsymbol{A}} = \boldsymbol{A} : \boldsymbol{A}, \tag{5.2.3}$$

where $\boldsymbol{A}$ is a general $m \times m$ tensor. For clarity, in index notation, this is equivalent to

$$I_{\boldsymbol{A}} = \sum_{i=1}^{m}\sum_{j=1}^{m} A_{ij}\delta_{ij}, \quad II_{\boldsymbol{A}} = \sum_{i=1}^{m}\sum_{j=1}^{m} A_{ij}A_{ij}. \tag{5.2.4}$$

Constitutive equations can be used to describe a material's behaviour under deformation. Let $W(\boldsymbol{C})$ denote a strain energy function which depends on $\boldsymbol{C}$. The corresponding second Piola-Kirchhoff (PK2) tensor is obtained by taking the derivative of the strain energy function with respect to $\boldsymbol{C}$, as $\boldsymbol{S} = 2\nabla_{\boldsymbol{C}} W$[19]. For a viscoelastic material description, fractional order viscoelastic models have been successfully employed in modelling soft tissue behaviour[127]. Thus, here let $\boldsymbol{S}$ be defined as the sum of an elastic, fractional viscoelastic and hydrostatic part, as

$$\boldsymbol{S} = \boldsymbol{S}_e + D_t^{\alpha}\boldsymbol{S}_v + \boldsymbol{S}_p. \tag{5.2.5}$$

The elastic and viscoelastic parts are derivatives of elastic and viscoelastic strain energy functions (i.e. $\boldsymbol{S}_e = 2\nabla_{\boldsymbol{C}} W_e$ and $\boldsymbol{S}_v = 2\nabla_{\boldsymbol{C}} W_v$), and the hydrostatic part is defined as $\boldsymbol{S}_p = JP\boldsymbol{C}^{-1}$, where P is the hydrostatic pressure. The fractional order derivative, as defined by Caputo[31], is

$$D_t^{\alpha}\boldsymbol{S}_v = \frac{1}{\Gamma(1-\alpha)}\int_0^t \frac{1}{(t-z)^{\alpha}}\partial_t \boldsymbol{S}_v(z)\,\mathrm{d}z, \tag{5.2.6}$$

with $\alpha = 0$ leading to a hyperelastic contribution, and $\alpha = 1$ leading to a purely viscous contribution in the form $\partial_t \boldsymbol{S}_v$. In order to separate the deviatoric and hydrostatic stress components, we introduce the deviatoric operator

$$\mathrm{Dev}[\boldsymbol{A}] = \boldsymbol{A} - \frac{\boldsymbol{A} : \boldsymbol{C}}{3}\boldsymbol{C}^{-1}, \tag{5.2.7}$$

which ensures that $\mathrm{Dev}[\boldsymbol{A}] : \boldsymbol{C} = 0$. Having defined the PK2 tensor in the context of constitutive modelling, the Cauchy stress tensor can be related to the PK2 tensor using

$$\boldsymbol{\sigma} = \frac{1}{J}\boldsymbol{F}\boldsymbol{S}\boldsymbol{F}^T. \tag{5.2.8}$$

5.2.2 Nonlinear viscoelastic characterisation of liver tissue

In this paper, combined loading experiments are used to investigate the behaviour of liver tissue. The data presented here has been previously published in[246]. Here, we focus on the large amplitude oscillatory strain (LAOS) tests and briefly review the protocol.

5.2.2.1 Sample preparation

Fresh healthy bovine liver was collected from an abattoir, with the samples being tested within 6 hours post-mortem. Before testing, the samples were kept in ice, and then immersed in a saline solution. Cylindrical samples were cut to approximately 10 mm radius and 3 mm height. For more complete preparatory details see the original protocol published in[246].

5.2.2.2 Rheological experimental design

Tissues were tested using a rotational rheometer (Kinexus Pro KNX 2100, Malvern, United Kingdom), as illustrated in Fig. 5.2.1. The cylindrical samples were fit in between two serrated plates of 20 mm diameter, to avoid slipping. The bottom plate was fixed, while the upper plate was vertically adjusted and oscillated around the cylindrical axis. Torque measurements were acquired in combined loading tests, with shear strains of 1, 10, 25 and 50% being investigated under different uniaxial preload levels - 1, 10 and 20%, at a strain rate of 1 Hz. Additionally, shear strains of 1, 10 and 25%, at a preload of 10%, were investigated at strain rates of 0.5 and 2 Hz. Table 5.2.1 summarises the loading, shearing and frequency protocols employed.

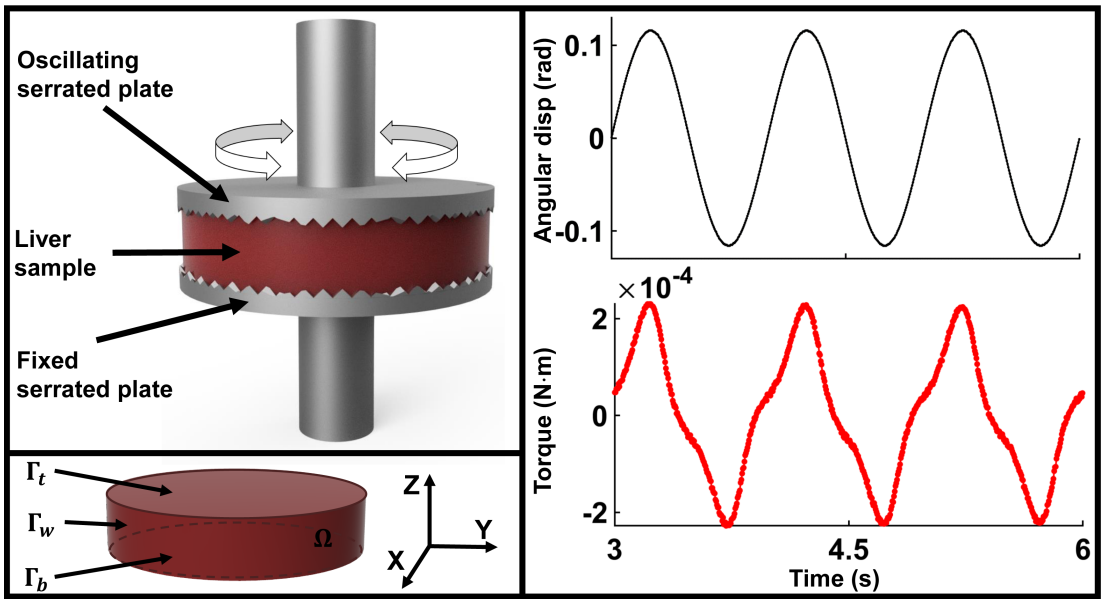

Figure 5.2.1 *Illustration of the experimental setup. (Top left) Liver tissue in the oscillatory rheological instrument. The plates were serrated, with the lower plate being fixed, while the upper plate could move vertically and rotate around the axis. (Bottom left) Axis and boundaries defined with respect to the liver sample. (Right) Example of angular displacement trace (sinusoidal) and torque response (non-sinusoidal) at CS 10%, γ 50%, 1 Hz.*

A total of 18 tests were carried out - 12 at 1 Hz and 3 at 0.5 and 2Hz, respectively. For each test, the data was averaged between at least four liver samples. For each test, the first eight cycles were used for pre-conditioning purposes, with the data being recorded

from the ninth cycle. Pre-conditioning was done sequentially and not directly at the maximum deformation level in order to avoid damaging tissue. Originally, two more shear strain levels were acquired - 80 and 100%[246], but this data was excluded here due to potential tissue damage.

	SS 1%	SS 10%	SS 25%	SS 50%
CS 1%	◯	◯	◯	◯
CS 10%	⊕	⊕	⊕	◯
CS 20%	◯	◯	◯	◯
Legend	| 0.5Hz	◯ 1Hz	− 2Hz	

Table 5.2.1 *Testing protocol across frequencies, compression and shear deformations.*

5.2.2.3 Modelling the experiment

Compressive and shear deformations were imposed onto the liver samples in order to investigate their 3D biomechanical response. Thus, denoting by H and R the undeformed height and radius of a sample, let h and r denote the height and radius deformed by compression. Let the ratio of the deformed to undeformed height be $\lambda = h/H$, which corresponds to each compression strain (CS) level via $\text{CS} = 1 - \lambda$. Here, ideal compression is assumed, which leads to the radius being deformed as $r = R/\sqrt{\lambda}$.

The shear strain, γ, is defined as the ratio between top plate rotational part of the displacement and inter plate gap, $\gamma = d/h$, with the rotational displacement depending on the angular displacement and radius. Having a predefined γ level, at frequency f the angular displacement on the top of the sample is given by

$$\psi(t) = \frac{\sin(2\pi f t) h\gamma}{r}, \tag{5.2.9}$$

with the maximum angular displacement being reached at $\psi = h\gamma/r$. Let $\Psi(t, X_3)$ define the angular displacement throughout the sample, as

$$\Psi(t, X_3) = \frac{\psi(t)}{H} X_3.$$

Hence, the compression and shearing lead to a body deformation[244] defined by

$$\boldsymbol{x}(t) = \begin{bmatrix} \frac{X_1}{\sqrt{\lambda}} \cos\left(\Psi(t, X_3)\right) - \frac{X_2}{\sqrt{\lambda}} \sin\left(\Psi(t, X_3)\right) \\ \frac{X_1}{\sqrt{\lambda}} \sin\left(\Psi(t, X_3)\right) + \frac{X_2}{\sqrt{\lambda}} \cos\left(\Psi(t, X_3)\right) \\ \lambda X_3 \end{bmatrix}. \tag{5.2.10}$$

Incorporating the above form into Eq. (5.2.2), the corresponding deformation gradient

takes the form

$$\boldsymbol{F}(t) = \begin{pmatrix} \frac{\cos\Psi(t,X_3)}{\sqrt{\lambda}} & -\frac{\sin\Psi(t,X_3)}{\sqrt{\lambda}} & -\frac{\Psi(t,X_3)}{H} r_{\boldsymbol{x}} \sin\theta(t) \\ \frac{\sin\Psi(t,X_3)}{\sqrt{\lambda}} & \frac{\cos\Psi(t,X_3)}{\sqrt{\lambda}} & \frac{\Psi(t,X_3)}{H} r_{\boldsymbol{x}} \cos\theta(t) \\ 0 & 0 & \lambda \end{pmatrix}, \tag{5.2.11}$$

where angle θ is related to spatial position and is given by $\theta(t) = \arctan(X_2/X_1) + \Psi(t, X_3)$ and $r_{\boldsymbol{x}}$ is the radial position throughout the sample. On the top surface, the deformation metrics can be found by replacing $\Psi(t, X_3)$ with $\psi(t)$.

In every test, torque measurements are acquired at the top plate level. Here, the torque on the top surface Γ_t (as identified in Fig. 5.2.1) is computed as

$$\boldsymbol{\tau} = \int_{\Gamma_t} \boldsymbol{r} \times \boldsymbol{t} \mathrm{d}\Gamma = \int_{\Gamma_t} \boldsymbol{r} \times (\boldsymbol{\sigma} \cdot \boldsymbol{n}) \mathrm{d}\Gamma_t, \tag{5.2.12}$$

where $\boldsymbol{n} = [0, 0, 1]^T$ is the normal to the top surface. Since the rotational forces are acting in plane, symmetrically around the Z-axis, then the only non-zero torque component is

$$\tau_3 = \int_{\Gamma_t} x_1\sigma_{23} - x_2\sigma_{13} \ \mathrm{d}\Gamma_t, \tag{5.2.13}$$

where the Cauchy stress components can be found from Eq. (5.2.8). Although the hydrostatic pressure P does not affect the torque computation, note that its value can be retrieved due to the zero normal traction on the wall boundary Γ_w. By combining Eqs. (5.2.5) and (5.2.8) into

$$\boldsymbol{\sigma} = \boldsymbol{F}(\boldsymbol{S}_e + D_t^{\alpha}\boldsymbol{S}_v)\boldsymbol{F}^T + JP\boldsymbol{I},$$

and knowing that $\boldsymbol{t} = \boldsymbol{\sigma} \cdot \boldsymbol{n} = \boldsymbol{0}$, P can be determined by balancing out the elastic and viscoelastic components in the traction normal on the wall, Γ_w.

5.2.3 Constitutive modelling of liver tissue

In this study, the nonlinear liver behaviour is investigated under combined large compressions and shear strains. An example of angular displacements employed is shown in Fig. 5.2.1. The observed torque behaviour is modelled using a viscoelastic adaption of three hyperelastic models commonly applied in soft tissue mechanics, with the aim of drawing a comparison between their suitability to model the data: polynomial (a modified form of the Mooney-Rivlin model, which will be indicated by vMR^*), Ogden (vOG) and exponential ($vEXP$).

5.2.3.1 Viscoelastic modified Mooney-Rivlin model

The simplest model considered here is a modified Mooney-Rivlin strain energy function,

which comprises two parts: $W_1 = (I_{\hat{\boldsymbol{C}}} - 3)/2$ and $W_2 = (II_{\hat{\boldsymbol{C}}} - 3)^2/8$. The first part is a linear neo-Hookean term, whereas the second term, compared to the original Mooney-Rivlin model, is quadratic, in order to trigger a more accentuated nonlinear response. This modified form has been previously employed in capturing polymer hyperelasticity[30], as the classical Mooney-Rivlin form was found to be unsuitable to model liver tissue hyperelasticity at large strains[39]. In this form, the PK2 tensors are derived to be

$$\boldsymbol{S}_e^1 = \frac{1}{J^{2/3}}\left(\boldsymbol{I} - \frac{I_{\boldsymbol{C}}}{3}\boldsymbol{C}^{-1}\right), \tag{5.2.14a}$$

$$\boldsymbol{S}_e^2 = \frac{1}{J^{4/3}}(II_{\hat{\boldsymbol{C}}} - 3)\left(\boldsymbol{C} - \frac{II_{\boldsymbol{C}}}{3}\boldsymbol{C}^{-1}\right). \tag{5.2.14b}$$

The above form provides a purely elastic part, and viscoelasticity is introduced by taking a fractional order derivative on the $\boldsymbol{S}_e^1$ tensor, as described in Eq. (5.2.5). Initially, a more extensive Mooney-Rivlin based model was considered (section 5.A, Eq. (5.A.1)), but it did not perform much better than a model with fewer parameters. Hence, the total PK2 tensor for the *vMR** law considered here is

$$\boldsymbol{S} = C\boldsymbol{S}_e^2 + \delta D_t^\alpha(\boldsymbol{S}_e^1) + \boldsymbol{S}_p, \tag{5.2.15}$$

with C, δ (Pa), and α (unitless) being material parameters. Note that C and δ act as linear scalings on the model components, whereas α triggers a nonlinear reponse.

5.2.3.2 Viscoelastic Ogden based model

The second type of model considered is the Ogden model, described by the strain energy function $W = (\lambda_1^b + \lambda_2^b + \lambda_3^b - 3)/(2b)$, and the corresponding PK2 tensor

$$\boldsymbol{S}_e^b = \sum_{i=1}^{3} \lambda_i^{b-1}\boldsymbol{v}_i \otimes \boldsymbol{v}_i. \tag{5.2.16}$$

Here, power b is a nonlinear parameter, λ_i are the three principal stretches, and $\boldsymbol{v}_i$ are the corresponding eigenvectors of tensor $\boldsymbol{C}$. A more comprehensive Ogden based model was initially considered (section 5.A, Eq. (5.A.2)), however, it did not perform significantly better than a single component model and made the parametrisation non-unique. Thus, the total PK2 stress considered here includes only a viscoelastic and a hydrostatic part:

$$\boldsymbol{S} = \delta D_t^\alpha(\boldsymbol{S}_e^b) + \boldsymbol{S}_p, \tag{5.2.17}$$

where δ (Pa) is a linear scaling parameter, while the fractional order derivative α and the eigenvalue power b (unitless) parameters act nonlinearly. This model will be referred to as the viscoelastic Ogden model *vOG*.

5.2.3.3 Viscoelastic Exponential model

The last type of model considered here is the isotropic exponential Fung-type model, described by the strain energy function $W = (\exp(b(II_{\boldsymbol{C}} - 3)) - 1)/(4b)$. The corresponding elastic PK2 tensor is derived to be

$$\boldsymbol{S}_e^b = \exp(b(II_{\boldsymbol{C}} - 3))\boldsymbol{C}, \tag{5.2.18}$$

with power b being a nonlinear scaling parameter. As before, viscoelasticity is introduced by the fractional order derivative $D_t^\alpha \boldsymbol{S}_e$. For this model, in order to ensure that the deviatoric and hydrostatic parts are separated after applying the time derivative, let the PK2 tensor be defined as

$$\boldsymbol{S} = \delta \mathrm{Dev}[D_t^\alpha \boldsymbol{S}_e^b] + \boldsymbol{S}_p, \tag{5.2.19}$$

where δ (Pa) is a linear scaling parameters and b (unitless) is a parameter that acts nonlinearly. Hence, Eq. (5.2.19) defines the viscoelastic exponential model *vEXP*. A more comprehensive form of the exponential model was also considered (section 5.A, Eq. (5.A.3)). However, similarly to the Ogden-based model, the extensive form did not perform significantly better and it led to non-unique parameter identification.

5.2.4 Data analysis and model fitting

Parameters from all models were tuned to match the experimental data. In this case, torque measurements (τ^d) were compared against the torque corresponding to the models (τ^m). In order to obtain τ^m, the PK2 stress tensor for each individual model (*vMR** - Eq. (5.2.15), *vOG* - Eq. (5.2.17), and *vEXP* - Eq. (5.2.19)) was used in Eq. (5.2.8) in order to quantify the Cauchy stress, and in Eq. (5.2.13) to quantify the torque. Then, the model parameters were adjusted to match the data by solving a minimisation problem. Three different objective functions were employed, which will be described later in this section.

5.2.4.1 Minimisation problem

Let $\boldsymbol{y}$ denote a set of M parameters that matches a model to the data. In order to find $\boldsymbol{y}$, a minimisation problem of the form

$$\theta = \underset{\boldsymbol{y} \in \mathbb{R}_+^M}{\arg\min}\, \mathcal{J}(\boldsymbol{y}, \boldsymbol{\tau}^d) \tag{5.2.20}$$

is posed, where $\mathcal{J}$ is a function to be minimised. For the models presented here, $\boldsymbol{y}$ comprises the nonlinear parameter α and, where applicable, b, C and δ. However, the m linear parameters can simply be found by inverting a system of linear equations, as

it will be seen shortly. This leads to a simplified minimisation problem

$$\theta^* = \underset{\boldsymbol{y}^* \in \mathbb{R}_+^{M-m}}{\arg\min}\ \mathcal{J}^*(\boldsymbol{y}^*, \boldsymbol{\tau}^d), \tag{5.2.21}$$

where $\boldsymbol{y}^*$ spans the nonlinear parameters only (α and, if applicable, b).

In this work, the minimisation problem θ^* is solved by carrying out a parameter sweep over the nonlinear parameters. Specifically, the fractional order α is iterated between 0.05 and 1 (with a step of 0.05), to ensure that the whole spectrum from elastic to viscous is captured. In the interval [0.15, 0.4], which is close to the literature range estimated for α, a finer step of 0.01 was used. Similarly, power b is examined over a range - $[0.1, 14]$ for the *vOG* model and $[0.1, 3]$ for the *vEXP* model, with coarse refinements, to see trends. Then, we focused on the range $[1, 14]$ for the *vOG* model, with refinements of 0.5, and on $[1, 1.5]$ for the *vEXP* model, with refinements of 0.1, to isolate parameter values.

For each combination of α and b considered, the best linear parameters C and δ can be found by solving a linear system of equations

$$\boldsymbol{A}\boldsymbol{x} = \boldsymbol{b}, \tag{5.2.22}$$

with the understanding that $\boldsymbol{A} = \boldsymbol{A}(\alpha, b)$ and $\boldsymbol{x} = \boldsymbol{x}(\alpha, b)$. The matrix $\boldsymbol{A}$ and vector $\boldsymbol{b}$

$$\boldsymbol{A} = \begin{bmatrix} [\tau_1^{m,e} & \tau_1^{m,v}] \\ [\tau_2^{m,e} & \tau_2^{m,v}] \\ \vdots & \vdots \\ [\tau_N^{m,e} & \tau_N^{m,v}] \end{bmatrix} \qquad \boldsymbol{b} = \begin{bmatrix} [\tau_1^d] \\ [\tau_2^d] \\ \vdots \\ [\tau_N^d] \end{bmatrix} \tag{5.2.23}$$

comprise the elastic (if applicable) and viscoelastic torque model components, and the torque data measurements, respectively. Subscripts 1 to N indicate the tests considered, which are vertically concatenated. Each block $[\tau_i^{m,e}\ \tau_i^{m,v}]$ comprises multiple time points. Vector $\boldsymbol{x} = [C\ \ \delta]^T$ contains the unknown linear parameters to be found. For further use throughout the section, subscript i denotes the block corresponding to test i, i.e.

$\boldsymbol{A}_i = \ [\tau_i^{m,e} \quad \tau_i^{m,v}]$ and $\boldsymbol{b}_i = [\tau_i^d]$.

Three different norms were employed in order to quantify the model fit to the data. Firstly, the classical L_2 norm is investigated. Further on, a point-wise scaling norm is introduced, which is an adaption of the L_2 norm. Lastly, a parameter-scaling norm is designed, where some constraints on the linear parameters are relaxed. The norms presented are constructed such that the error is 0% for a perfect fit and 100% when the linear parameters are set to 0 Pa. The contrasting nature of the norms leads to gathering different insights about the data, and thus contributes to an overall better

understanding of the liver tissue.

5.2.4.2 L_2 norm

The first norm relies on the MATLAB implemented linear solver "lsqnonneg". The linear parameters are found by minimising the remainder in a least squares (lsq) sense, using the L_2 norm ($||\cdot||_2$), i.e.

$$\mathcal{J}^*_{lsq} = \frac{||\boldsymbol{A}\boldsymbol{x} - \boldsymbol{b}||_2}{||\boldsymbol{b}||_2}. \tag{5.2.24}$$

While straightforward, this norm favours the tests that employ larger deformations and thus attain higher torque amplitudes.

5.2.4.3 Point-wise norm

An alternative to the classic L_2 norm is to scale values to ensure that all points carry equal importance in the fitting process. To achieve this, each point in the data and model is scaled by its corresponding amplitude in the data (point-wise scaling). In general form, this can be written as

$$(\boldsymbol{a};\boldsymbol{b})_{pw} = \sum_k \left(\frac{a_k}{\max(tol, |b_k|)}\right)^2, \tag{5.2.25}$$

where *tol* is a non-zero tolerance level, to avoid division by zero. Thus, the error measure, which is also the function to be minimised, becomes

$$\mathcal{J}^*_{pw} = \frac{\left(\sum_i (\boldsymbol{A}_i\boldsymbol{x} - \boldsymbol{b}_i;\boldsymbol{b}_i)_{pw}\right)^{1/2}}{\left(\sum_i (\boldsymbol{b}_i;\boldsymbol{b}_i)_{pw}\right)^{1/2}}. \tag{5.2.26}$$

This adapted norm leads to potentially higher L_2 norm errors, but it also ensures that the curve trends (e.g. the non-sinusoidal torque response in Fig. 5.2.1) are better matched, irrespective of their amplitude.

5.2.4.4 Parameter-scaling norm

Parameter variability can be encountered when analysing samples collected from different livers or different locations in the liver. Furthermore, the parametrisation process can be affected by shear softening - an effect which might be observed when a material is sheared at successive increasing levels[195]. Here, in order to accommodate for parameter variability due to sample location or shear softening, we introduce a norm that allows for flexibility in the linear scaling parameters.

Since a single frequency was investigated per sample (either 0.5, 1 or 2 Hz), this is

not sufficient to allow for variability in the fractional order α. Moreover, it is observed that the shape of the data curves tends to be preserved across samples, whereas the amplitude scaling changes. Hence, presuming that the nonlinear parameters govern the shape of the torque curves, α and b (if applicable) are assumed to be consistent across samples and shear softening. By contrast, the linear scaling parameters C and δ are assumed to vary, and their distribution will be examined in order to understand the amplitude behaviour of the data.

Firstly, consider the normalised

$$\boldsymbol{A}_i^* = \left[\frac{\tau_i^{m,e}}{n_i \left|\left|\tau_i^d\right|\right|_2} \quad \frac{\tau_i^{m,v}}{n_i \left|\left|\tau_i^d\right|\right|_2} \right] \text{ and } \boldsymbol{b}_i^* = \left[\frac{\tau_i^d}{n_i \left|\left|\tau_i^d\right|\right|_2} \right]$$

which make up normalised matrix $\boldsymbol{A}^*$ and vector $\boldsymbol{b}^*$. Here, n_i is the number of data points in test i. Additionally, let

$$\boldsymbol{x}^* = \boldsymbol{x}_i \beta_i \tag{5.2.27}$$

be a set of unique linear parameters $[C^* \ \delta^*]$ which can be transformed into the test specific parameters $\boldsymbol{x}_i$ by employing the scaling β_i. In order to find $\boldsymbol{x}^*$ and β, an iterative process is employed, starting with each $\beta_i = 1$:

$$\boldsymbol{x}^* = \underset{\boldsymbol{x}^*}{\arg\min} \left(\sum_{i=1}^{N} ||\boldsymbol{A}_i^* \boldsymbol{x}^* / \beta_i - \boldsymbol{b}_i^*||_2^2 \right)^{1/2}, \tag{5.2.28}$$

$$\beta_i = \underset{\beta_i}{\arg\min} \, ||\boldsymbol{A}_i^* \boldsymbol{x}^* - \boldsymbol{b}_i^* \beta_i||_2 \, . \tag{5.2.29}$$

The above sequence of minimisation equations is repeated until there is no change in the error $\mathcal{J}_{sc}^*$,

$$\mathcal{J}_{sc}^* = \frac{\left(\sum_{i=1}^{N} ||\boldsymbol{A}_i^* \boldsymbol{x}^* / \beta_i - \boldsymbol{b}_i^*||_2^2 \right)^{1/2}}{||\boldsymbol{b}^*||_2}. \tag{5.2.30}$$

Although the set of linear parameters $\boldsymbol{x}_i$ is different for every test considered, note that this is different than solving each test individually, as this norm ensures that the nonlinear parameters are fixed across all tests. Solving each test individually would yield similar results only if α and b were known a priori.

5.3 Results

This work is based on data acquired at a range of compression preloads, oscillatory shear strains and frequencies. At the smallest shear strain (1%), the data is close to linear viscoelasticity, with the nonlinearity becoming more evident at increased shear strains. Increasing the frequency also enhances the nonlinear behaviour of the liver tissue samples. Hysteresis effects manifest during all tests employed and they tend to increase slightly with increasing shear strain. Strain rate dependence is observed,

as both nonlinearity and hysteresis increase with frequency. These observations point towards a strain rate dependent, nonlinearly viscoelastic liver tissue behaviour.

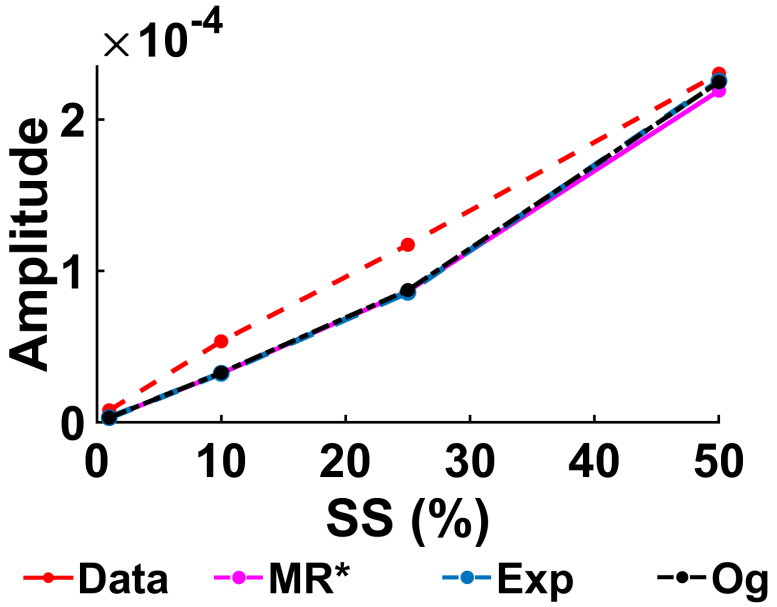

Figure 5.3.1 *Maximum torque amplitude across shear strain, exemplified in the data group acquired at 1 Hz, CS 10%.*

When investigating the acquired data, a strain softening effect is observed. That is, the more strained the tissue sample is, the less force is required to produce a strain increment. This is exemplified in Fig. 5.3.1 for shear strain (CS 10%, 1Hz), but a similar trend is exhibited for compressive strain as well. It can be seen that the data has a slight concave trend, indicating strain softening, while the models have a convex trend.

5.3.1 Viscoelastic models tailored with the L_2 norm

Fig. 5.3.2 presents the L_2 error norm for each α value investigated for the optimal set of all remaining parameters, with larger markers denoting the minimum. The data was grouped by compression strain and frequency, with each group comprising the corresponding shear strain tests (e.g. CS 10%, 1 Hz, $\gamma = 1, 10, 25, 50\%$). The best parameter set for each data group is presented in the corresponding tables.

Fig. 5.3.3 illustrates examples of the three models - vMR^*, vOG and $vEXP$ - fit to the data tests at 1 Hz and CS 10%. The three model curves were produced using the best fit parameters obtained when fitting the whole shear strain range (1-50%). Fig. 5.3.4 shows the Lissajous plots (torque readings depending on the angular displacement) corresponding to CS 10%, 1Hz. The continuous lines show the data readings, while the dashed lines show the $vEXP$ model fit.

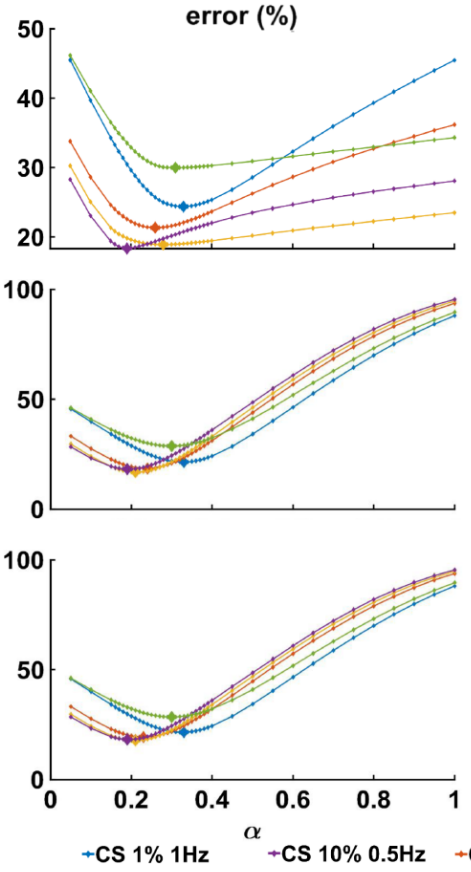

CS freq	1% 1Hz	10% 1Hz	20% 1Hz	10% 0.5Hz	10% 2Hz	mean ± SD
err(%)	24.40	21.35	18.92	18.36	29.99	
α	0.33	0.26	0.28	0.19	0.31	0.27±0.05
C(Pa)	10.16	35.28	38.96	0	67.68	30.42±26.56
δ(Pa)	80.2	95.78	62.88	328.12	166.44	146.68±108.79

CS freq	1% 1Hz	10% 1Hz	20% 1Hz	10% 0.5Hz	10% 2Hz	mean ± SD
err(%)	21.41	18.46	16.83	18.20	28.70	
α	0.33	0.24	0.21	0.19	0.3	0.25±0.06
b	3.5	4	4.5	2.5	6.5	4.2±1.48
δ(Pa)	17.86	24.19	23.02	243.44	13.84	64.47±100.14

CS freq	1% 1Hz	10% 1Hz	20% 1Hz	10% 0.5Hz	10% 2Hz	mean ± SD
err(%)	21.48	19.27	17.73	18.20	28.44	
α	0.33	0.23	0.21	0.19	0.3	0.25±0.06
b	0.1	0.1	0.1	0.1	1.2	0.32±0.49
δ(Pa)	82.26	149.85	177.70	438.22	184.56	206.52±135.69

Figure 5.3.2 *The minimum error for the L_2 norm (Eq. (5.2.24)), obtained for each data group, for fractional order α values between 0.05 and 1. Plots show minimal error obtained for* vMR* *(Top),* vOG *(Middle) and* vEXP *(Bottom) models, with the larger sized markers being obtained for the parameters presented in the corresponding tables.*

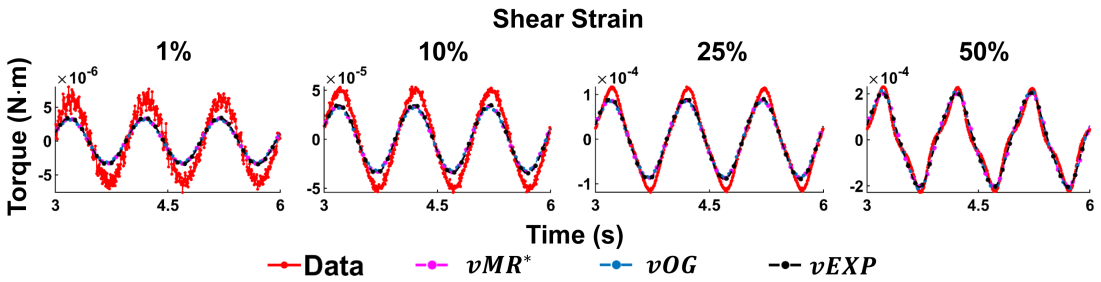

Figure 5.3.3 *Example of the three models fit to the data acquired at 1Hz, compression strain 10%, using the L_2 norm. The parameters employed to produce the models' curves can be found in column 2 (CS 10% 1Hz) of the corresponding tables in Fig. 5.3.2.*

5.3.2 Viscoelastic models tailored with the point-wise norm

The point-wise error norm behaviour with α is shown in Fig. 5.3.5 for the *vMR** (top), *vOG* (middle) and *vEXP* (bottom) models. The larger error markers identify the overall best parameter fit, obtained for the parameters presented in the corresponding tables.

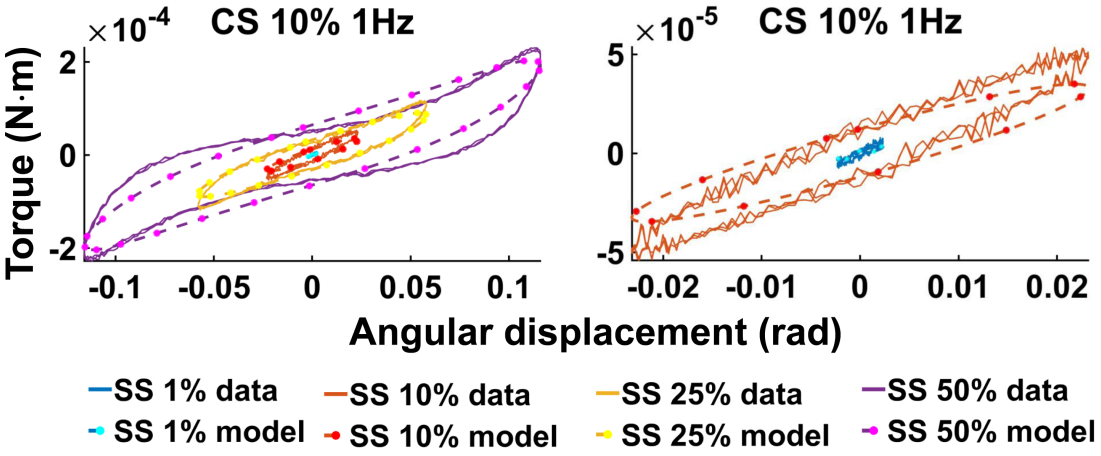

Figure 5.3.4 *Lissajous curve exemplifying the* vEXP *model fit to the data acquired at 1 Hz, compression strain 10%. The parameters employed to produce the model's curves can be found in column 2 (CS 10% 1 Hz) of the bottom table in Fig. 5.3.2. The curves corresponding to shear strains 1-10-25-50% are shown in the left panel, while the right panel zooms on shear strains 1-10%.*

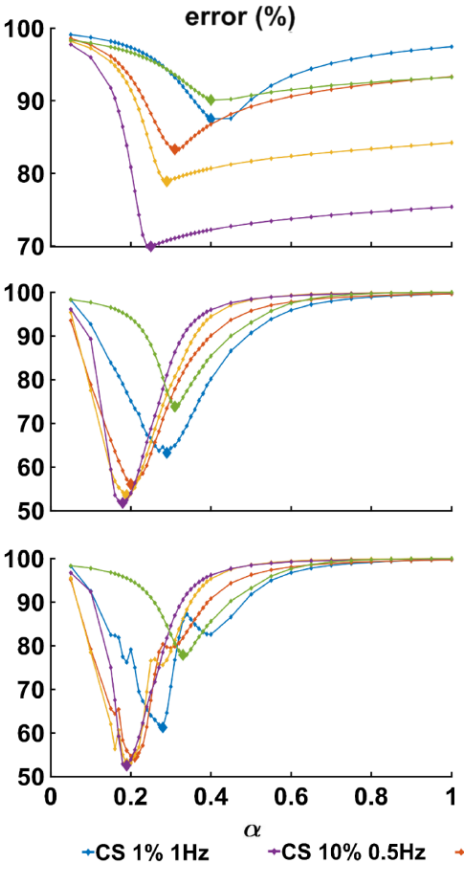

CS freq	1% 1Hz	10% 1Hz	20% 1Hz	10% 0.5Hz	10% 2Hz	mean ± SD
err(%)	87.51	83.31	78.90	69.95	90.12	
α	0.4	0.31	0.29	0.25	0.4	0.33±0.07
C(Pa)	0	0	0	18.93	0	3.79±8.47
δ(Pa)	22.30	34.36	34.24	184.45	35.30	62.13±68.59

CS freq	1% 1Hz	10% 1Hz	20% 1Hz	10% 0.5Hz	10% 2Hz	mean ± SD
err(%)	63.23	56.05	53.55	51.76	73.82	
α	0.29	0.2	0.19	0.18	0.31	0.23±0.06
b	7	8	8.5	12	14	9.9±2.97
δ(Pa)	2.48	3.93	3.56	5.58	1.26	3.36±1.62

CS freq	1% 1Hz	10% 1Hz	20% 1Hz	10% 0.5Hz	10% 2Hz	mean ± SD
err(%)	61.25	54.56	52.91	52.55	77.88	
α	0.28	0.21	0.19	0.19	0.33	0.24±0.06
b	1	1.2	1.4	3	3	1.92±1.00
δ(Pa)	55.08	89.73	63.98	235.39	71.20	103.07±75.05

Figure 5.3.5 *The minimum error for the point-wise scaling norm (Eq.* (5.2.26)*), obtained for each data group, for fractional order α values between 0.05 and 1. Plots show minimal error obtained for* vMR* *(Top),* vOG *(Middle) and* vEXP *(Bottom) models, with the larger sized markers being obtained for the parameters presented in the corresponding tables.*

Fig. 5.3.6 presents the best models' fit to the data acquired at 1 Hz, CS 10%. The models' parameters can be found in Fig. 5.3.5. The same dataset and the *vEXP* model fit are also conveyed in Lissajous curves in Fig. 5.3.7.

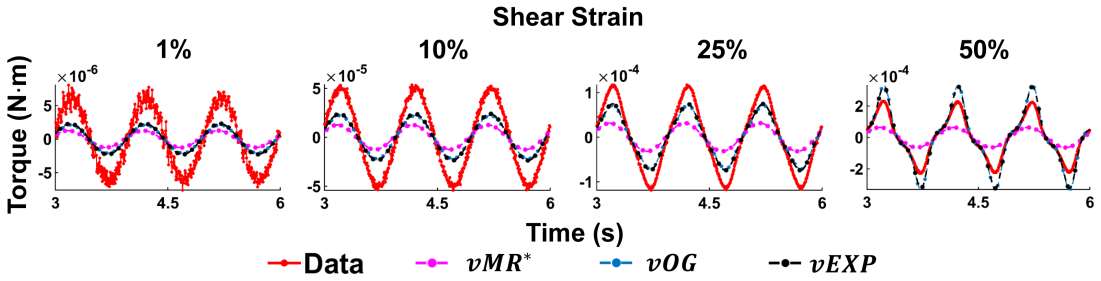

Figure 5.3.6 *Example of the three models fit to the data acquired at 1Hz, compression strain 10%, using the point-wise scaling norm. The parameters employed to produce the models' curves can be found in column 2 (CS 10% 1Hz) of the corresponding tables in Fig. 5.3.5.*

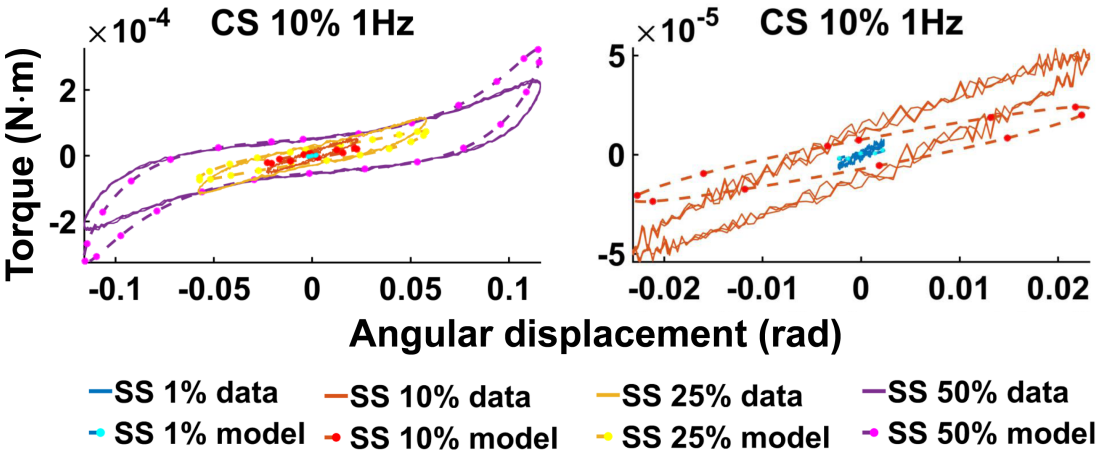

Figure 5.3.7 *Lissajous curve exemplifying the* vEXP *model fit to the data acquired at 1 Hz, compression strain 10%. The parameters employed to produce the model's curves can be found in column 2 (CS 10% 1 Hz) of the bottom table in Fig. 5.3.5. The curves corresponding to shear strains 1-10-25-50% are shown in the left panel, while the right panel zooms on shear strains 1-10%.*

5.3.3 Viscoelastic models tailored with the parameter-scaling norm

Fig. 5.3.8 shows the minimum parameter-scaling error norm corresponding to the models (*vMR**, *vOG*, *vEXP*), for every fractional order α investigated. All 18 tests were considered simultaneously, hence a single curve corresponding to each model, compared to the previous analogue Figs. 5.3.2 and 5.3.5, where subgroups of the data tests were considered. The smallest error across the α range is identified by the larger markers, and the set of parameters corresponding to these minima are found in the corresponding table.

Figs. 5.3.9 and 5.3.10 show all data tests acquired, and the three model fits. Fig. 5.3.9

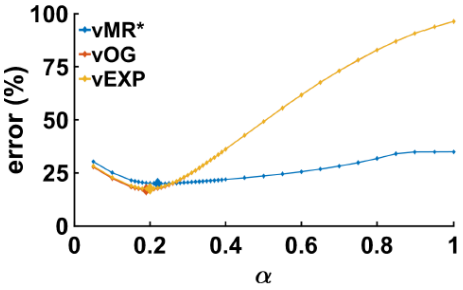

	err(%)	α	b	$C^*(Pa)$	$\delta^*(Pa)$
*vMR**	19.92	0.22	N/A	97.38	130.85
mean±SD				145.55±106.26	195.43±142.79
vOG	17.04	0.19	10	N/A	2.7
mean±SD					6.74±6.09
vEXP	17.52	0.2	1.5	N/A	113.99
mean±SD					231.02±198.43

Figure 5.3.8 *The minimum model error (*vMR***, vOG *and* vEXP*) for the parameter scaling norm (Eq.* (5.2.30)*), obtained for the tests altogether, for fractional order* α *values between 0.05 and 1. The minimal error across* α *is enhanced by the larger sized marker, obtained for the parameters presented in the corresponding table.*

shows all datasets acquired at a frequency of 1 Hz, while Fig. 5.3.10 shows datasets acquired under a compression strain of 10%. Example Lissajous curves are shown, for the data and *vEXP* model at 1 Hz, in Fig. 5.3.11. The top row shows all four shear strains (1-10-25-50%), while the bottom row zooms in on the 1 and 10% shear strains. Compression strain increases from the left column (1%) to middle (10%) and right (20%). In these figures, the models' curves were obtained by employing the starred parameters from Fig. 5.3.8, scaled according to Eq. (5.2.27). The test specific linear parameters can be seen, for all models, in Fig. 5.3.12, and their mean and standard deviation are shown in Fig. 5.3.8.

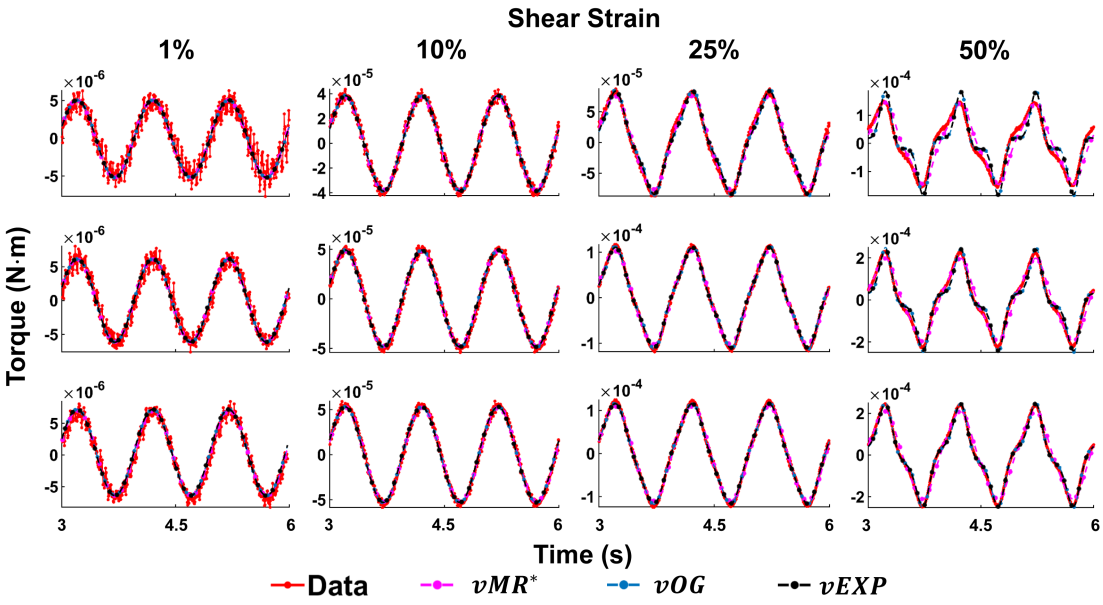

Figure 5.3.9 *The three models fit to the data acquired at 1Hz, using the parameter scaling norm. The first row illustrates the tests at CS 1%, the second row at CS 10% and the third row at CS 20%. The parameters employed to produce the models' curves can be found in the table corresponding to Fig. 5.3.8.*

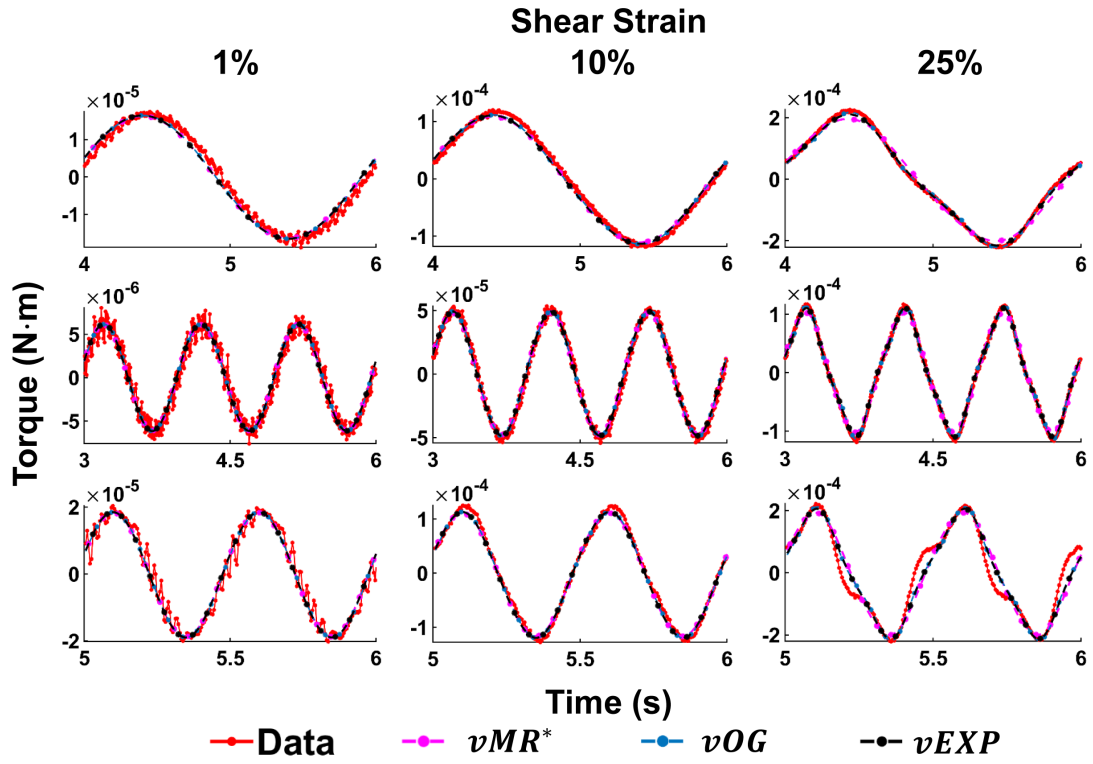

Figure 5.3.10 *The three models fit to the data acquired at CS 10%, using the parameter scaling norm. The first row illustrates the tests at 0.5 Hz, the second row at 1 Hz and the third row at 2 Hz. The parameters employed to produce the models' curves can be found in the table corresponding to Fig. 5.3.8.*

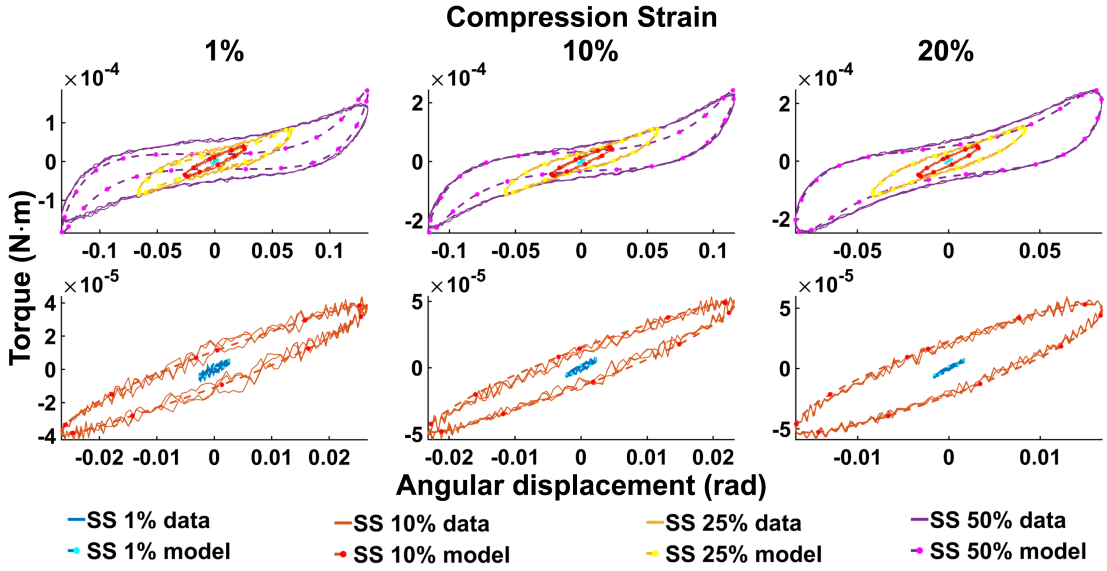

Figure 5.3.11 *Lissajous curve exemplifying the* vEXP *model fit to the data acquired at 1 Hz. The parameters employed to produce the model's curves can be found in the table corresponding to Fig. 5.3.8. The top row shows the curves corresponding to shear strains 1-10-25-50%, while the bottom row zooms on shear strains 1-10%. Compression strain increases from left (1%) to middle (10%) and right (20%).*

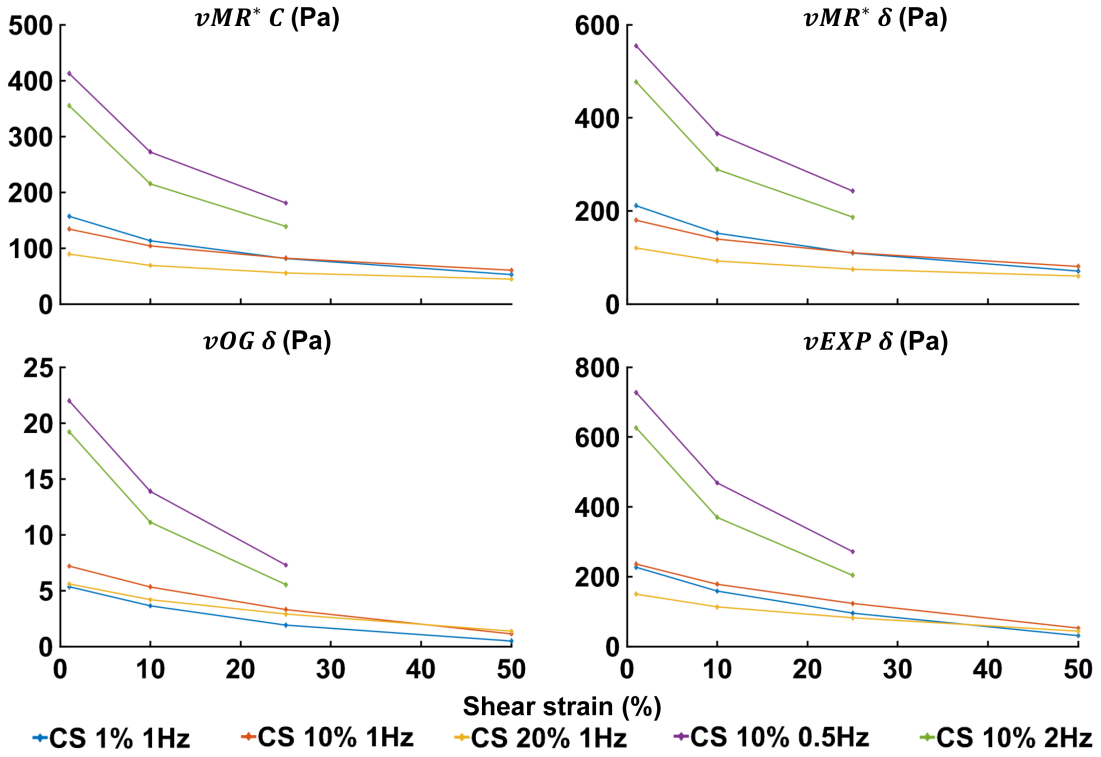

Figure 5.3.12 *Absolute linear parameters for the models, obtained by transforming the starred* relative parameters into their absolute counterparts using Eq.* (5.2.27)*. The top panels show the C and δ parameters scaling the elastic and viscoelastic components of the* vMR* *model. The bottom panels show the δ parameter scaling the viscoelastic component of the* vOG *and* vEXP *models, respectively.*

5.4 Discussion

When comparing the three models (*vMR**, *vOG* and *vEXP*) within the L_2 norm performance, it can be seen that the errors presented in Fig. 5.3.2 are very similar, with the *vMR** model errors being slightly higher (at most $\approx 3\%$). This is likely due to the fact that the other two models are more suitable to capture the nonlinear trends. However, it can be seen from Fig. 5.3.3 that all three models match the closest the data peaks at shear strain 50%. This is because the data in this study can vary even by two orders of magnitude, with the higher amplitude data having the largest impact on the L_2 norm. As a result, amplitudes in the other tests have lesser fidelity, as a consequence of the L_2 norm, which penalises less the discrepancies at smaller amplitudes. This mismatch is further accentuated by the strain softening effect. It can be seen that the data exhibits a shallower increase in amplitude with shear strain (1% to 50%) than the models are. The bias of the L_2 norm towards the higher amplitude points can also be observed in Fig. 5.3.4, where the *vEXP* model fit well the peak at shear strain 50%, yet the rest of the model torque curve looks idealised (almost perfectly elliptic) and does not follow the data curve.

In order for the models to better follow the data curve trends throughout the entire deformation, a point-wise scaling norm (Eq. (5.2.26)) was designed, which penalises discrepancies between data and models, across all points considered, evenly. For this norm, the errors for the *vOG* and *vEXP* models are similar, with the *vMR** model performing significantly worse ($\approx$ 20%, as seen in Fig. 5.3.5). This is because the *vMR** model cannot recreate the nonlinear trends exhibited. Hence, this norm drives the model peak points to match closely the lower amplitude data points (Fig. 5.3.6), by forcing a delayed response (higher α values, as seen in the top table of Fig. 5.3.5, compared to the middle and bottom tables).

Fig. 5.3.6 shows that the *vOG* and *vEXP* models are able to capture the data trends; however, there is a data-model amplitude discrepancy for all tests. This discrepancy is more accentuated than for the L_2 norm (Fig. 5.3.3) because the models employ a higher nonlinear parameter b - 8 to 4 for *vOG*, as seen in the middle tables of Figs. 5.3.2 and 5.3.5, and 1.2 to 0.1 for *vEXP*, as seen in the bottom tables of the same figures. This determines a steeper increase in the models' amplitude. Fig. 5.3.7 clearly shows that this norm leads to a better model match of the data curve trend, at the cost of discrepancy in the peaks.

In the models, the nonlinear parameter α determines the phase delay between the shear strain input and torque output. The nonlinear parameter b controls the shape and amplitude of the torque curve, where $b = 0$ leads to a linear response (i.e. sinusoidal output as a result of a sinusoidal input) and higher values lead to an increased nonlinear response. The linear parameters C and δ amplify the contribution of the model components. Comparing the results of the L_2 and point-wise norms, it can be concluded that the data curve trends can only be captured by accentuating the nonlinear characteristics of the models (e.g. increasing the b parameter). However, this deteriorates the peak amplitude match, as the data exhibits a sublinear, concave trend (Fig. 5.3.1), due to strain softening.

Due to the fact that the data could not be described using a set of fully consistent parameters, the parameter-scaling norm was designed so that the set of linear parameters can be adjusted according to each test, by scaling the models' amplitude response. Hence it is expected that the errors, computed using Eq. (5.2.30), are small. Indeed, as per Fig. 5.3.8, the parameter-scaling norm leads to the smallest quantified errors, compared to the L_2 and point-wise scaling norms. Comparing the three models, it can be observed that error behaviour with α (Fig. 5.3.8) is almost identical for the *vOG* and *vEXP* models. For the *vMR** model, the minimum error curve is shallow for α values between 0.15 and 0.4, leading to a less precise parameter identifiability.

With the three models reaching a similar minimum error, it is expected that they behave similarly, as seen in Figs. 5.3.9 and 5.3.10. The *vOG* and *vEXP* models are better at capturing the data nonlinearity at the larger shear strains. One notable test

where the *vMR** model performs better than the other two is at compression strain 1%, shear strain 50%, 1 Hz (top right panel in Fig. 5.3.9). There, *vMR** captures the data amplitude and does not exhibit the exaggerated nonlinearity of the other two models, however, it performs inferiorly in other tests (e.g compression strain 10%, shear strain 25%, 0.5 Hz - top right panel in Fig. 5.3.10).

The models' curves in Figs. 5.3.9–5.3.11 were produced using the parameters presented in Fig. 5.3.8. All three models employ a similar fractional order derivative, between 0.19 and 0.22, which is in good agreement with the literature[6,120,147,232]. It is notable that for the *vOG* and *vEXP* models, the nonlinear parameters α and b presented in Fig. 5.3.8, are similar to the parameter means presented in Fig. 5.3.5, obtained using the point-wise norm. This reinforces the suitability of the parameter-scaling norm to be employed with this study's data, as its main effect is facilitating the amplitude match.

The linear parameters δ^* and, if applicable, C^*, are scaled according to each data test, leading to the test-specific parameters depicted in Fig. 5.3.12. It can be observed that for all three models, the linear parameters decrease with increasing shear strain, which reflects the shear strain softening effect. Interestingly, it appears that three data groups can be identified, which correspond to the frequency groups - 0.5, 1 and 2 Hz. Since the linear parameters do not have a monotonic trend with frequency, with the parameters at 0.5 and 2 Hz being larger than the ones at 1 Hz, it is unlikely that this reflects a parameter-frequency coupling. Instead, this might be explained by a dependency on the sample location, as different samples were tested across the frequency tests. Additionally, the standard deviation of these parameters reaches up to 90% of their mean, as presented in Fig. 5.3.8, indicating a high linear parameter variability introduced by sample location and strain softening.

5.4.1 Overview

In this work, three constitutive equations were proposed for modelling the behaviour of liver tissue under a range of deformations and frequencies, being parametrised by three error norms. For the data employed here, the L_2 norm proved to be unsuitable, as it was biased by the larger amplitude points. However, this is a straightforward norm that is convenient to use when analysing data of comparable magnitude. The point-wise norm was introduced in order to equalise the weight of each data point in the models' fitting process. The *vMR** model performed particularly poor with this norm, however the *vOG* and *vEXP* models followed the data curve trends better than for the L_2 norm. Hence, this norm offered better insights into the nonlinearity of the data. With the shear strain softening leading to amplitude mismatches, the parameter scaling norm was designed to allow for flexibility in the set of linear parameters and thus facilitate the model to data amplitude match. In this case, the models' fit was significantly improved, with all three models performing similarly in capturing the data

particularities.

The choice of constitutive law for modelling the liver behaviour depends on the complexity desired. The vMR^* model provided a marginally less suitable fit compared to the vOG and $vEXP$ models; however, it is very practical due to its simple form, requiring only the computation of invariants and identifying a single nonlinear parameter. Nevertheless, for the data presented here, the shallow minima of the error norm across the nonlinear parameter α reveals a non ideal parameter identifiability process. As an alternative, the vOG and $vEXP$ models can be employed if more accuracy is required, as they lead to the identification of a clear minima and also provide an improved fit. They are more complex, involving two nonlinear parameters. Furthermore, the vOG model relies on the computation of eigenvalues, which is more computationally expensive.

Considering this study's findings, the $vEXP$ model provides a good balance between model complexity and data fit. The use of the parameter-scaling norm was essential in ensuring a good overall model fit. Nevertheless, note that this norm was employed in order to overcome strain softening effect. Ideally, this effect would be mitigated by pre-conditioning the samples at the highest strain applied, but here, due to the very large strains, is avoided in order to avoid tissue damage to the samples during early testing.

5.4.2 Extension and impact in-vivo and in-silico

The transportation industry is particularly concerned with the study of liver's response to sudden large impacts, as it is the most exposed abdominal organ in frontal and side crashes. Having a model that is able to capture its behaviour at large deformations as well as rate-dependent effects enables the determination of injury tolerance limits and hence can guide the design of seatbelts, airbags, children car seats, etc.

In the medical research field, in-silico simulations are used in order to test new devices, provide surgery training, predict diagnosis and treatment response, etc. These simulations need to be able to gauge the nonlinear viscoelastic tissue response to a range of mechanical stimuli, e.g. cutting, puncturing, pressing. The models discussed here are suitable for in-silico work, with the $vEXP$ model performing better than the vMR^* model and being computationally cheaper than vOG.

A different possible application of the models discussed is in the medical elastography area, which provides noninvasive in-vivo measurements of an organ's stiffness in order to assess disease severity. These measurements rely on assumptions about an underlying biomechanical model. In general, simple models are considered (e.g. Neo-Hookean), but frequency dependent nonlinear viscoelastic models, like the ones presented here, could lead to a better identification and staging of pathology. With the liver being one of the most imaged organs using elastography, the 3D liver models proposed here could

be translated and investigated in the context of small amplitude shear waves probing the liver at various deformation states imposed by the respiratory motion[179].

5.4.3 Study limitations

The aim of this paper is to define a frequency dependent nonlinear viscoelastic law that is able to characterise the liver tissue under a range of combined deformations and frequencies. The results presented advocate for the suitability of all three models employed, with *vEXP* in particular, to capture the liver behaviour, yet some limitations remain to be addressed by further research.

One of the main difficulties in this study was to overcome strain softening effect encountered, which was emphasised by the testing procedure. Given that large deformations were investigated, the pre-conditioning protocol had to be applied sequentially with the measurements. That is, at each deformation level, few oscillations were carried before acquiring the data. However, the tissue samples were not strained to the maximum deformation level before starting the data acquisition, as that could have damaged the samples' microstructure and lead to non-representative measurements at low strains. In order to address this effect, an initial pre-conditioning would need to be done at the highest deformation level, or measurements would need to be acquired in reverse, from the highest to the lowest strain. This would also require determination of the maximal deformation allowed avoiding material damage.

One of the assumptions made in the modelling process is the idealised compression employed. In the experiments, however, the samples bulged under compression. Likely, the viscoelastic model response would change when considering a non idealised compression. Investigations in simulated 3D models indicate that there is a torque amplitude difference between the idealised and non idealised compression. However, this would have an impact only on the linear parameters of the models, which would need to be upscaled by ≈ 16. The normal force, nonetheless, would be the most affected, as simulations show a qualitative difference between ideal and non ideal compression.

5.5 Conclusions

This paper investigates the suitability of three models - *vMR**, *vOG* and *vEXP* - to capture the nonlinear viscoelastic liver response at a range of large deformations. Their performance is gauged using three norms - the L_2 norm, a point-wise scaling norm, which ensures even contributions from each data point, and a novel parameter-scaling norm, which allows for flexibility in determining the linear parameters. This norm was introduced in order to overcome the strain softening effect, and its implementation leads to significant improvements in fitting the models to the data, with the *vOG* and *vEXP* models being able to better capture the nonlinear particularities. Among the forms presented here, the *vEXP* model is able to recreate the data trends, while identifying

a clear minima across the fractional order α. Furthermore, it relies on strain metrics that are cheap to compute, making it advantageous to use.

Acknowledgements

The authors would like to thank Kirsty Tan for acquiring the data.

Conflict of Interest

The authors declare that they have no conflict of interest.

Supplementary materials

5.A Extended models

The models presented in this study may be extended to include more components. This could allow for more flexibility in the modelling process. For example, consider the extended version of the vMR^* model (vMR^*_{ext}) to be

$$\boldsymbol{S} = C_1\boldsymbol{S}_e^1 + C_2\boldsymbol{S}_e^2 + \delta_1 D_t^\alpha(\boldsymbol{S}_e^1) + \delta_2 D_t^\alpha(\boldsymbol{S}_e^2) + \boldsymbol{S}_p, \tag{5.A.1}$$

where $S_e^{1,2}$ are defined as in the set of Eq. (5.2.14). Similarly, the extended vOG model (vOG_{ext}) would be characterised as

$$\boldsymbol{S} = C_1\boldsymbol{S}_e^{b_1} + \delta_1 D_t^\alpha(\boldsymbol{S}_e^{b_2}) + \boldsymbol{S}_p, \tag{5.A.2}$$

with S_e^b given by Eq. (5.2.16). Lastly, the extended $vEXP$ model ($vEXP_{ext}$) would be defined as

$$\boldsymbol{S} = C_1\mathrm{Dev}[\boldsymbol{S}_e^{b_1}] + \delta_1\mathrm{Dev}[D_t^\alpha\boldsymbol{S}_e^{b_2}] + \boldsymbol{S}_p, \tag{5.A.3}$$

where S_e^b is characterised by Eq. (5.2.18). For all three extended models, the material parameters C and δ are linearly scaling the elastic and viscoelastic contributions, respectively.

5.A.1 Results employing the extended models

Employing the extended models with the parameter-scaling norm leads to smaller errors compared to the initial models. Fig. 5.A.1 summarises the minimum errors and best parameter set for each model. The vMR^*_{ext} model leads to a better fit (≈4% error improvement) compared to vMR^*. For the other two extended models, the error improvement is less than ≈1%. However, in Fig. 5.A.1 it can be seen that the minima is shallow, whereas when using the initial models vOG and $vEXP$ (Fig. 5.3.8), the minima is more clearly identified. This is because the vOG_{ext} and $vEXP_{ext}$ models offer more flexibility in fitting the data, by adding a purely elastic component. This becomes dominant, while the viscoelastic part is used for fine-tuning of the nonlinear behaviour, which is why the error curve is shallow across α values. Given the data range used in this study, the extended models do not lead to a clear parameter identifiability.

Nevertheless, they might be suitable in modelling more complex experimental data or different materials.

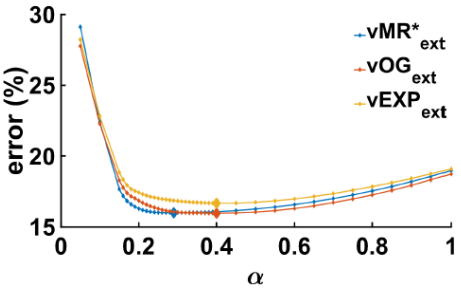

	α	b_1	b_2	C_1^*	C_2^*	δ_1^*	δ_2^*
vMR^*_{ext} (err 15.99%)	0.29	N/A	N/A	47.58	49.02	9.12	140.11
vOG_{ext} (err 15.95%)	0.4	7	11	5.39	N/A	0.73	N/A
$vEXP_{ext}$ (err 16.67%)	0.4	1.5	2	54.23	N/A	33.01	N/A

Figure 5.A.1 *The minimum model error (*vMR^*_{ext}*,* vOG_{ext} *and* vEXP_{ext}*) for the parameter scaling norm (Eq.* (5.2.30)*), obtained for the tests altogether, for fractional order* α *values between 0.05 and 1. The minimal error across* α *is enhanced by the larger sized marker, obtained for the parameters presented in the corresponding tables.*

5.B Supplement

This supplementary material aims to investigate the differences arising from considering ideal or non-ideal compression. For this, **$\mathcal{C}$heart** was used to solve the mechanical problem posed in section 5.2.2.3. The same modelling approach as in section 3.7 was followed, in order to replicate the experiment as accurately as possible. Briefly, a cylindrical sample of radius $R = 10$ mm and height $H = 2.7$ mm was compressed by 10% and, here, sheared up to 1, 10, 25 and 50% level, at a frequency of 1 Hz. The exponential model (Eq. (5.2.18)) was employed, with the linear scaling $\delta = 20$, the nonlinear parameter $b = 1.5$ and the fractional power $\alpha = 0.2$. The uniform compression was prescribed at the top and bottom surfaces as in Eq. (3.7.2), while the non-ideal compression was prescribed as

$$\boldsymbol{u}(t) = \begin{bmatrix} X_1\cos(\psi(t)X_3) - X_2\sin(\psi(t)X_3) - X_1 \\ X_1\sin(\psi(t)X_3) + X_2\cos(\psi(t)X_3) - X_2 \\ X_3\left(\lambda(t) - 1\right) \end{bmatrix}, \quad \psi(t) = \frac{\gamma\lambda^{3/2}(t)\sin(2\pi f\hat{t})}{\sqrt{X_1^2 + X_2^2}}. \tag{5.B.1}$$

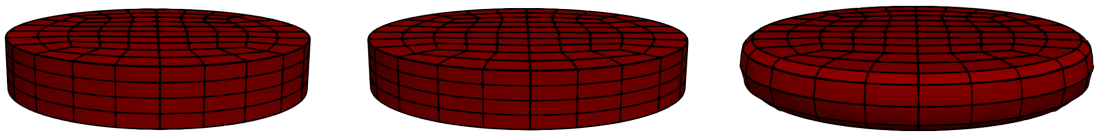

Figure 5.B.1 *Simulations of liver sample compression; (Left) Liver in undeformed state; (Middle) Liver under 10% ideal compression; (Right) Liver under 10% non-ideal compression*

The liver under ideal and non-ideal 10% compression is illustrated in Fig. 5.B.1. It can be seen that, under non-ideal compression, the sample is bulging. Simulations of

the normal force on the top surface and torque are presented in Fig. 5.B.2. For the normal force, the ideal case was upscaled by a factor of 100, for a clearer comparison. It is observed that the ramp-up part between 0 and 1s, corresponding to the compression part, has a very accentuated exponential behaviour in the non-ideal compression. Additionally, the shearing part decays much faster than in the ideal compression case. For the torque, an upscale of the ideal curves makes them match their non-ideal counterparts. The factors used for upscaling are 10.0155, 10.2447, 10.9682 and 12.2721 for shear strains 1, 10, 25 and 50%, respectively. The match is not perfect, with the L_2 normalised errors being quantified as 3.62, 3.16, 2.56 and 2.29%, respectively. Hence, the differences would likely fall within the noise level of the data.

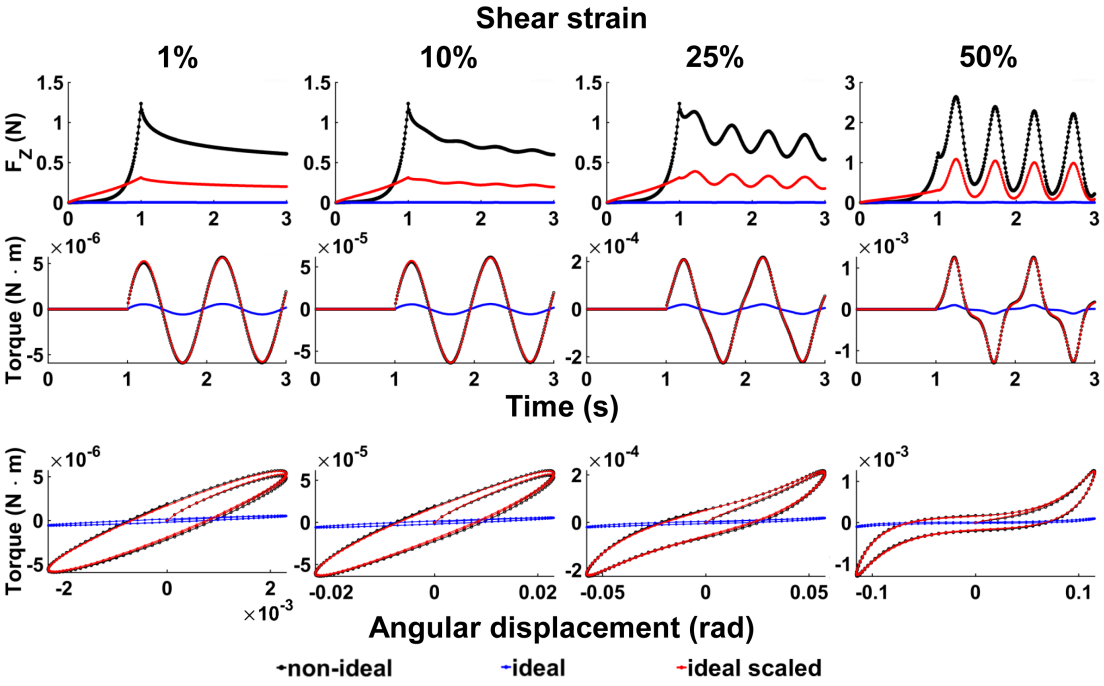

Figure 5.B.2 *Simulations of ideal and non-ideal compression; The simulations were carried at compression strain 10% and shear strain 1% (first column), 10% (second column), 25% (third column) and 50% (fourth column). The top row shows the normal force on the top surface, the middle row shows the torque versus time, and the bottom row shows the torque versus angular displacement. The black curves show the non-ideal compression, the blue curves show the ideal compression, and the red curves show the scaled ideal compression, as follows: by a factor 100 for normal force, and by factors 10.0155 (SS 1%), 10.2447 (SS 10%), 10.9682 (SS 25%) and 12.2721 (SS 50%) for torque.*

The normal force simulations show the most striking differences between the two compression types. However, this did not affect the study, since the exponential model presented in this chapter was fit to torque data only. Although there is a scale factor that needs to be applied to the torque simulations between ideal and non-ideal compression, this only affected the identification of the linear parameters presented in Figs. 5.3.8 and 5.3.12 because the parameter scaling norm (Eq. (5.2.30)) allowed for

the linear parameters to be adjusted according to each test. Despite this, it can be concluded that the exponential model (Eq. (5.2.18)) with nonlinear parameters, presented in Fig. 5.3.8, is suitable for capturing the constitutive behaviour of liver tissue.

6 Ex vivo MRE liver characterisation

The aim of this thesis is to investigate the effects of large deformations on MRE liver measurements. This is done in order to advise on the bias that elastography measurements may exhibit at different loading states, but also to gain more insight by performing measurements at different respiratory states. In this sense, chapter 4 provided a proof of concept in PVA phantoms. There it was shown that large deformations led to the measurement of apparent changes in material properties, thus demonstrating that MRE measurements incur loading bias. However, by providing a pipeline that uses knowledge of the material's constitutive behaviour and loading state, the loading bias can be eliminated. This enables the interpretation of intrinsic material properties. In order to translate the above pipeline in a tissue setting, *ex vivo* liver sample experiments were devised. Thus, chapter 5 investigated the rheology behaviour of liver tissue. Several constitutive models were considered, with a viscoelastic exponential model being preferred for describing the liver's biomechanical behaviour.

The work in this chapter takes the method developed in chapter 4 and applies it to *ex vivo* liver samples assuming the *vEXP* model devised in chapter 5. Similar to the phantom experiments, the liver samples are examined under different compression levels, using MRE. Again, the aim is to assess the impact that the loading exerts on the wave propagation in the tissue. This is a crucial step towards the next chapter which examines *in vivo* cases where the liver is deformed by respiratory motion.

In this chapter, the analysis is performed under the consideration that the liver is a nonlinear viscoelastic material, described by the *vEXP* model determined from the rheological investigations. Thus, the set of stiffness moduli that influence the wave dynamics is determined in section 6.1.1. These can be used in understanding the data obtained from MRE experiments, whose design is detailed in section 6.1.1.2, by following the analysis described in section 6.1.1.3. While the liver tissue is generally regarded as homogeneous, in section 6.1.2 we examine the implications of unpressurised large blood vessels, which can introduce additional complexity in the analysis process. Additionally, registration techniques are considered for determining the deformations undergone by the liver samples (section 6.1.3). Finally, results are presented and dis-

cussed in section 6.2. Two supplementary materials are included, one presenting the detailed mathematical derivation of the stiffness moduli (section 6.A), and the other investigating the performance of the registration method (section 6.B).

The experiments in this chapter were performed by Dr. Lauriane Jugé, and the data was obtained courtesy of Prof. Lynne Bilston. The candidate performed the entire analysis.

6.1 Materials and methods

6.1.1 Harmonic wave motion in loaded liver samples

The aim of this study is to investigate the effect of deformation on wave behaviour in loaded liver samples. Hence, we need to analyse the perturbed equations of motion, given in Eq. (2.4.7). In order to relate those to linear viscoelasticity used in MRE, a linearisation around the macro-deformation state has to be employed, as exemplified in section 2.4.1. Subsequently, the perturbations considered take the form of harmonic waves (section 2.4.2), leading to periodic nonlinear wave equations. Finally, these equations need to be expressed in the physical domain, in order to use them for MRE data interpretation. This can be done following the steps presented in section 2.4.3, leading to the periodic nonlinear wave equations recalled here:

$$-\rho\omega^2\boldsymbol{u}_c - \nabla\cdot[(\boldsymbol{\mathcal{G}}' + i\boldsymbol{\mathcal{G}}'') : \nabla\boldsymbol{u}_c + p_c\boldsymbol{I}] = \boldsymbol{0}, \tag{6.1.1a}$$

$$\nabla\cdot\boldsymbol{u}_c = 0. \tag{6.1.1b}$$

Here, in the context of a viscoelastic material model like the one presented in Eq. (5.2.19), the real and imaginary stiffness moduli take the form

$$\boldsymbol{\mathcal{G}}' = \frac{1}{J}\left(\left\{\boldsymbol{F}\left(\omega^\alpha\cos\left(\frac{\pi\alpha}{2}\right)\mathrm{Dev}\left[\nabla_{\boldsymbol{F}}\boldsymbol{S}_e^b\right] + \nabla_{\boldsymbol{F}}\boldsymbol{S}_p\right) + \boldsymbol{\mathcal{I}}\boldsymbol{S}_p\right\}\right)\boldsymbol{F}^T\boldsymbol{F}^T, \tag{6.1.2a}$$

$$\boldsymbol{\mathcal{G}}'' = \frac{\omega^\alpha}{J}\sin\left(\frac{\pi\alpha}{2}\right)\boldsymbol{F}\mathrm{Dev}\left[\nabla_{\boldsymbol{F}}\boldsymbol{S}_e^b\right]\boldsymbol{F}^T\boldsymbol{F}^T. \tag{6.1.2b}$$

These were obtained following a detailed analysis performed in section 6.A.1. All the quantities defining the moduli, i.e. $\boldsymbol{F}, \boldsymbol{S}_e^b$ and $\boldsymbol{S}_p$, depend on the unperturbed macro-deformation.

Briefly, let us recall that if there is no underlying macro-deformation (i.e. $\boldsymbol{F} = \boldsymbol{I}$), then the above moduli become identity tensors. Hence, $\boldsymbol{\mathcal{G}}' + i\boldsymbol{\mathcal{G}}'' = G^*(\boldsymbol{\mathcal{I}} + \widetilde{\boldsymbol{\mathcal{I}}})$, where G^* is the complex shear modulus of the material. The identity tensor leads to a symmetry of the wave dynamics, as $(\boldsymbol{\mathcal{I}} + \widetilde{\boldsymbol{\mathcal{I}}}) : \nabla_{\boldsymbol{x}}\boldsymbol{u}_c = \nabla_{\boldsymbol{x}}\boldsymbol{u}_c + \nabla_{\boldsymbol{x}}\boldsymbol{u}_c^T$. However, when large deformations are employed, the wave is scaled in a non-trivial way. Understanding the form of the $\boldsymbol{\mathcal{G}}'$ and $\boldsymbol{\mathcal{G}}''$ moduli is essential in order to separate the loading influence from the intrinsic material properties. Thus, here we are interested in investigating the

form of these moduli for liver tissue, whose behaviour is described by the *vEXP* model

$$\boldsymbol{S} = \delta \mathrm{Dev}[D_t^{\alpha}(\exp(b(II_{\boldsymbol{C}} - 3))\boldsymbol{C})] + \boldsymbol{S}_p. \tag{6.1.3}$$

Following the derivation presented in section 6.A.2, the $\boldsymbol{\mathcal{G}}'$ and $\boldsymbol{\mathcal{G}}''$ moduli which alter the wave dynamics are

$$\begin{aligned}\boldsymbol{\mathcal{G}}' : \nabla_{\boldsymbol{x}} \boldsymbol{u}_c =& \frac{\omega^{\alpha}}{J} \cos\left(\frac{\pi\alpha}{2}\right) \delta \exp(b(II_{\boldsymbol{C}} - 3)) \Bigg\{ 4b(\boldsymbol{B}^2 : \nabla_{\boldsymbol{x}} \boldsymbol{u}_c) \left(\boldsymbol{B}^2 - \frac{II_{\boldsymbol{C}}}{3}\boldsymbol{I}\right) + \\ & \boldsymbol{B}\nabla_{\boldsymbol{x}} \boldsymbol{u}_c \boldsymbol{B} + \boldsymbol{B}\nabla_{\boldsymbol{x}} \boldsymbol{u}_c^T \boldsymbol{B} - \frac{2}{3}(\boldsymbol{B}^2 : \nabla_{\boldsymbol{x}} \boldsymbol{u}_c)\boldsymbol{I} \Bigg\} - JP\nabla_{\boldsymbol{x}} \boldsymbol{u}_c^T \end{aligned} \tag{6.1.4}$$

and

$$\begin{aligned}\boldsymbol{\mathcal{G}}'' : \nabla_{\boldsymbol{x}} \boldsymbol{u}_c =& \frac{\omega^{\alpha}}{J} \sin\left(\frac{\pi\alpha}{2}\right) \delta \exp(b(II_{\boldsymbol{C}} - 3)) \Bigg\{ 4b(\boldsymbol{B}^2 : \nabla_{\boldsymbol{x}} \boldsymbol{u}_c) \left(\boldsymbol{B}^2 - \frac{II_{\boldsymbol{C}}}{3}\boldsymbol{I}\right) + \\ & \boldsymbol{B}\nabla_{\boldsymbol{x}} \boldsymbol{u}_c \boldsymbol{B} + \boldsymbol{B}\nabla_{\boldsymbol{x}} \boldsymbol{u}_c^T \boldsymbol{B} - \frac{2}{3}(\boldsymbol{B}^2 : \nabla_{\boldsymbol{x}} \boldsymbol{u}_c)\boldsymbol{I} \Bigg\}. \end{aligned} \tag{6.1.5}$$

In section 4.2.1.3, the influence of loading on wave behaviour was analysed in the case of a neo-Hookean material undergoing ideal compression and idealised shear wave propagation. That analysis provided a sense of the complexity of interpreting stiffness measurements in deformed materials, even under simplified conditions. Hence, it is expected that interpretation of MRE stiffness measurements in deformed liver tissue is convoluted.

6.1.1.1 Liver sample preparation

In this study, bovine liver tissue is investigated due to its similitude to human liver[121]. Bovine liver was collected from a local abattoir and tested within six hours post mortem. Three livers were acquired, each being used to obtain two large samples ($\approx 10 \times 10 \times 5$ cm), leading to six samples in total.

6.1.1.2 MRE experimental setup

The liver samples were tested two at a time, to reduce scan time and therefore reduce overall post-mortem time. The livers were placed on an acrylic plate. They were fixed against a supporting plate on one lateral side, while on the opposite side they could be compressed by an adjustable plate. A vibrating rod would induce waves at a given frequency, and the sample would be kept in place by the contact plates. The setup is illustrated in Fig. 6.1.1.

Using this setup inside the MR scanner, coronal wave data was recorded using MRE in undeformed and deformed configurations. All liver samples were scanned in the

reference state (uncompressed) and two or three compression states, as follows: two liver samples were compressed by ≈15% and ≈30%; the remaining four liver samples were compressed by ≈10%, 20% and 30%.

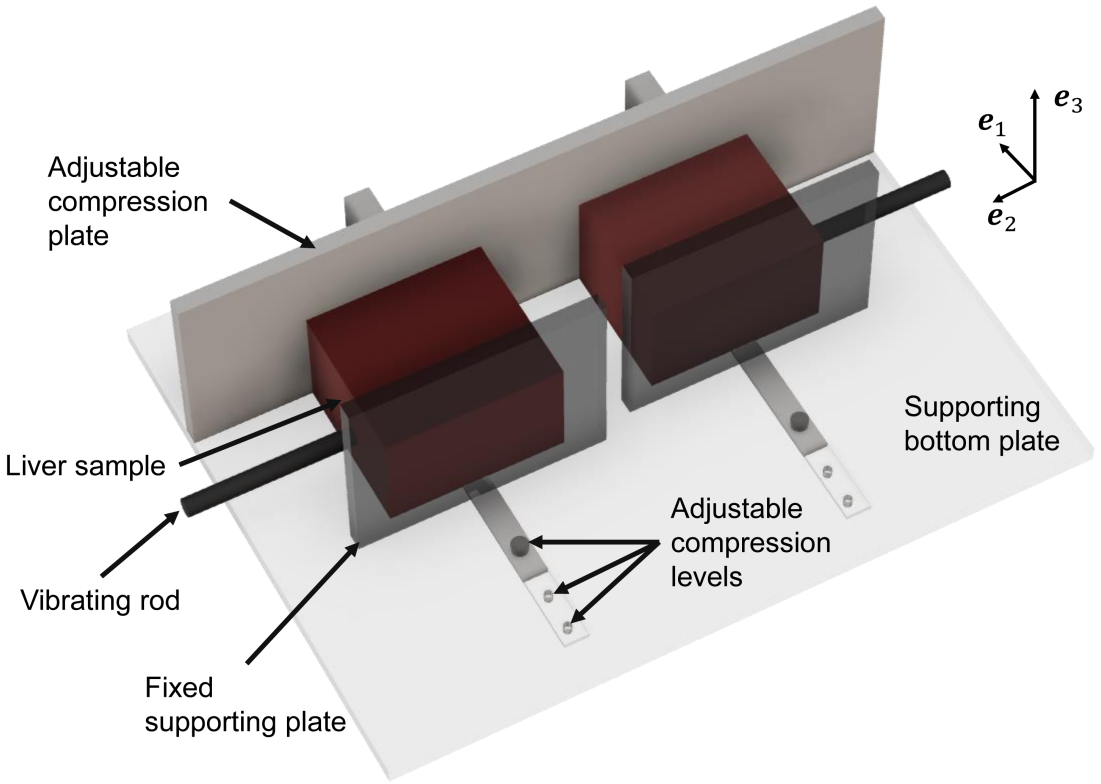

Figure 6.1.1 *Illustration of the liver MRE test setup. Each liver sample, resting on the support plate, was laterally framed by two vertical plates, which prevent the sample from sliding. These would help converting the compressional waves, coming from the vibrating rod, into shear waves. Moreover, one of the vertical plates was fixed, while the other could be moved, thus compressing the liver sample.*

MR acquisition consisted of two primary scans. First, a geometric scan was acquired providing 8 cross-sectional slices with a field of view (FOV) of 256 × 256 mm (resolution of 352×352 pixels and slice thickness of 3 mm). Scan parameters were adjusted to TE/TR= 100.00 / 3000.00 ms.

The second scan was a MRE eXpresso Gradient Echo sequence[71] providing 8 cross–sectional slices with a FOV of 256 × 256 mm (resolution 144 × 144 pixels and slice thickness of 3.0 mm). Driver frequency and motion encoding gradients were set at 60 Hz, and TE/TR at 9.21 / 135.417 ms. The sequence encoded each of the three displacement component directions $\boldsymbol{e}_1$, $\boldsymbol{e}_2$, $\boldsymbol{e}_3$ and a reference non-motion encoded image to remove background phase shifts due to the MRI gradients. Examples of the geometric and wave images can be seen in Fig. 6.1.2, for the undeformed and deformed configurations, in a liver sample compressed by 15% and 30%.

For two liver samples, additional tagged MRI data was acquired during the loading

process, in order to capture the strain that the sample is undergoing. A 2D grid (chequerboard) image was acquired in the $\boldsymbol{e}_1 - \boldsymbol{e}_2$ plane, with a FOV of 256 × 256 mm, resolution 256 × 256 pixels and slice thickness of 10.0 mm. Scan parameters were adjusted to TE/TR= 0.81 / 2.116 ms. Four phases and four dynamics were encoded for each deformation process (0 to 10, 10 to 20, 20 to 30%), with the tag lines being reapplied at the beginning of every phase, due to fading. However, due to the speed of applying the compression, only one or two dynamics were needed to capture the deformation, with the other dynamics showing no changes in the sample geometry.

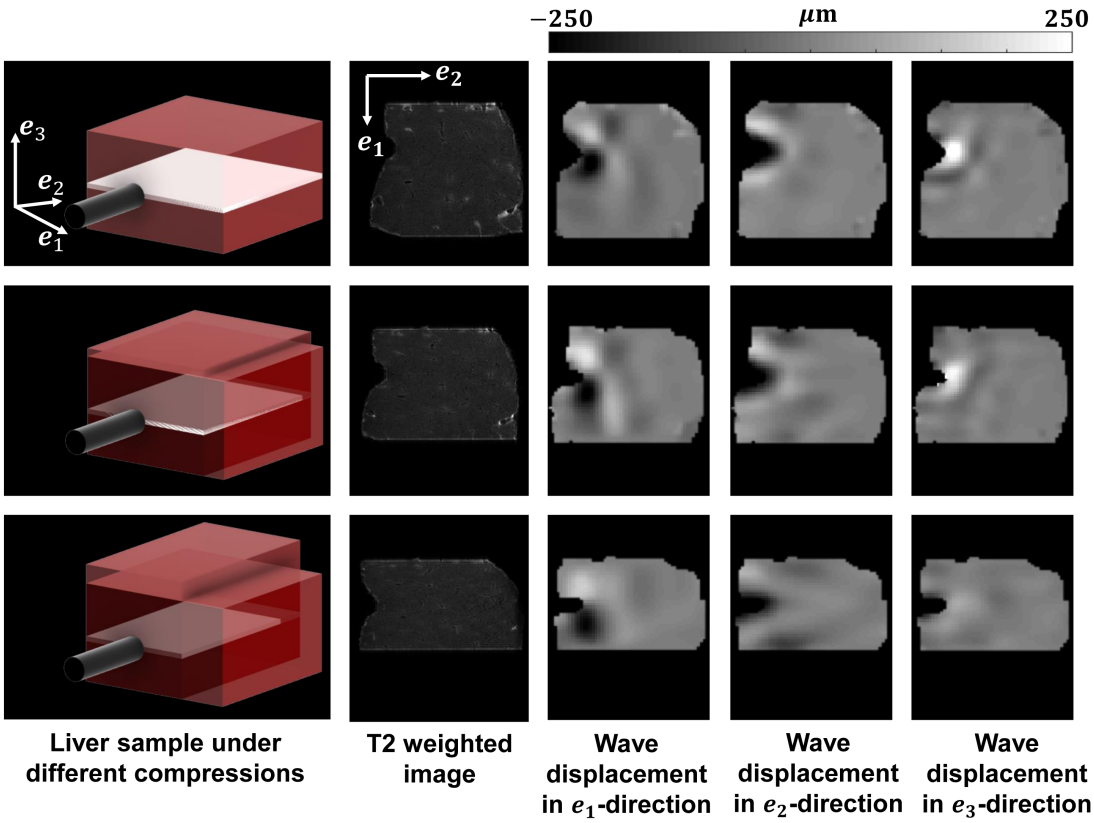

Figure 6.1.2 *Images corresponding to the uncompressed (top row) and compressed (middle and bottom rows) liver samples (here illustrated in liver sample 1). (First column) Liver sample depicted at the different deformation states. The uncompressed state is kept for reference. The piston (grey cylinder) is indenting the liver sample perpendicularly during the MRE scan. Slices are acquired in the coronal plane (depicted in white). (Second column) Cross sectional (coronal) view from the T2 weighted images. The piston indentation can be seen, as well as the compression of the liver in the* $\boldsymbol{e}_1$ *direction and its expansion in the* $\boldsymbol{e}_2$ *direction. Wave displacements from the MRE imaging protocol can be seen in the* $\boldsymbol{e}_1$, $\boldsymbol{e}_2$ *and* $\boldsymbol{e}_3$ *directions (third, fourth, fifth column, respectively).*

6.1.1.3 MRE data analysis

The anatomical images were used to measure the height and width change across the

entire imaged sample. Mean values would then be computed to reflect the average sample height and width in each deformation state. Uniform ideal compression was assumed for most of the analysis, with later analysis relying on metrics from registration methods. Therefore, here a deformation gradient of the form

$$\boldsymbol{F} = \begin{pmatrix} \lambda_1 & 0 & 0 \\ 0 & \lambda_2 & 0 \\ 0 & 0 & \lambda_3 \end{pmatrix} \tag{6.1.6}$$

was employed, where $\lambda_1 = \bar{h}/\bar{H}$, $\lambda_2 = \bar{w}/\bar{W}$. Here, $\bar{H}$ and $\bar{h}$ are the mean sample heights (dimension in the $\boldsymbol{e}_1$ direction) in the undeformed and deformed cases, respectively. Similarly, $\bar{W}$ and $\bar{w}$ are the mean sample widths (dimension in the $\boldsymbol{e}_2$ direction). The change in the $\boldsymbol{e}_3$ direction could not be empirically quantified, due to the imaging protocol only acquiring 8 slices of 3 mm, thus not including the entire liver sample in this direction. Therefore, assuming incompressibility of liver tissue, the deformation in the $\boldsymbol{e}_3$ direction was related to the changes in the other orthogonal directions, as $\lambda_3 = 1/(\lambda_1\lambda_2)$.

Firstly, the data in the uncompressed case was analysed in order to avoid the complications arising from the deformation. Hence, the aim was to retrieve the α and δ material parameters of the *vEXP* model in Eq. (6.1.3). Note that parameter b does not play a role if there is no underlying deformation. In an undeformed case, i.e. $\boldsymbol{F} = \boldsymbol{I}$, $J = 1$ and $P = 0$, the real and imaginary moduli $\boldsymbol{\mathcal{G}'}$ and $\boldsymbol{\mathcal{G}''}$ (Eqs. (6.1.4) and (6.1.5)) are simply

$$\boldsymbol{\mathcal{G}'} : \nabla_{\boldsymbol{x}}\boldsymbol{u}_c = G'\Big(\nabla_{\boldsymbol{x}}\boldsymbol{u}_c + \nabla_{\boldsymbol{x}}\boldsymbol{u}_c^T\Big), \tag{6.1.7a}$$

$$\boldsymbol{\mathcal{G}''} : \nabla_{\boldsymbol{x}}\boldsymbol{u}_c = G''\Big(\nabla_{\boldsymbol{x}}\boldsymbol{u}_c + \nabla_{\boldsymbol{x}}\boldsymbol{u}_c^T\Big), \tag{6.1.7b}$$

where

$$G' = \delta\omega^\alpha \cos\left(\frac{\pi\alpha}{2}\right), \qquad G'' = \delta\omega^\alpha \sin\left(\frac{\pi\alpha}{2}\right) \tag{6.1.8}$$

are the storage and loss moduli, also referred to as stiffness and viscosity, respectively. Thus the nonlinear parameter α can be obtained as

$$\alpha = \frac{2}{\pi}\tan^{-1}\left(\frac{G''}{G'}\right). \tag{6.1.9}$$

where G' and G'' are the average real and imaginary moduli measured across a region of interest. Having identified α, the linear parameter δ was then simply obtained as

$$\delta = \frac{G'}{\omega^\alpha \cos\left(\pi\alpha/2\right)}. \tag{6.1.10}$$

In the uncompressed case, the data was analysed using a divergence free finite element reconstruction developed by Fovargue et al.[61]. This method reconstructs the complex

stiffness modulus G^* by assuming $\boldsymbol{\mathcal{G}}^* = G^*\boldsymbol{\mathcal{I}}$, where $G^* = G' + iG''$. In section 4.2.3.2, this has been referred to as uncorrected reconstruction (UR). The UR does not employ any of the material parameters, and has been subsequently used to analyse the data in all deformation cases.

A modified version of the reconstruction method was also employed. This is the corrected reconstruction (CR) described in section 4.2.3.2. Briefly, this method solves an adapted version of Eq. (6.1.1), recalled below:

$$-\rho\omega^2\boldsymbol{u}_c - \nabla\cdot[M(\boldsymbol{\mathcal{G}}' : \nabla\boldsymbol{u}_c)] - i\nabla\cdot[(N(\boldsymbol{\mathcal{G}}'' : \nabla\boldsymbol{u}_c)] - \nabla\cdot p_c\boldsymbol{I} = \boldsymbol{0}. \tag{6.1.11}$$

Hence, instead of retrieving the stiffness and viscosity moduli G' and G'', the CR employs the material parameters (here α, b, δ) and retrieves the real and imaginary scaling parameters M and N. To better understand the implications of this method, consider the undeformed case, where $\boldsymbol{\mathcal{G}}'$ and $\boldsymbol{\mathcal{G}}''$ are given by Eq. (6.1.7). By using this form in Eq. (6.1.11), for the α and δ parameters obtained using Eqs. (6.1.9) and (6.1.10), M and N would naturally have to be 1, as the UR and CR are equivalent if there is no macro-deformation. Hence, if the material parameters employed in CR correspond to the intrinsic material properties, then M and N should both be 1. Essentially, M and N provide a scaling on the stiffness and viscosity moduli G' and G'', with $M, N > 1$ and $M, N < 1$ signifying that the moduli are underestimated and overestimated, respectively.

After employing the UR on every dataset from each liver sample, the next step was to use the CR in order to perform the analysis. For this, the *vEXP* model was parametrised using the MRE data in undeformed and most compressed case ($\approx 30\%$), as follows:

- The nonlinear parameter α was fixed according to Eq. (6.1.9), using the data in the uncompressed case.
- A sweep over the nonlinear parameter b was employed in the interval [0 1.5], with a step of 0.1. This interval was appropriate given the findings in the rheological case.
- For each b value, the linear parameter δ was sought such that the real linear scaling M was 1, in a least square sense over all pixels. Hence, the error was measured as the pixel-wise difference between the reconstructed values M and unity in undeformed and most compressed case, normalised by the number of pixels, as

$$\text{err} = \sqrt{\frac{\sum_{k=1}^{n} w_c(M_k - 1)^2}{n}}, \tag{6.1.12}$$

  where n is the total number of pixels considered and subscript k iterates over those pixels. A weighting factor w_c, corresponding to the uncompressed and

most compressed case, ensured that the error is equally weighted between the two states.

When employing the CR on the deformed samples, the hydrostatic pressure was computed as $P = -(\boldsymbol{F}\delta\text{Dev}[\exp(b(II_{\boldsymbol{C}} - 3))\boldsymbol{C}]\boldsymbol{F}^T)_{22}$, which was determined by noticing that the traction in the $\boldsymbol{e}_2$ direction is 0. Thus, it was set to counterbalance the elastic restorative force in this direction.

The predictive value of the obtained parameters was assessed by employing the CR on the intermediate compression states ($\approx 15\%$ in two liver samples, and $\approx 10\%$ and $\approx 20\%$ in four liver samples). The average values of maps M and N were investigated, identifying how much they deviate from the ideal value of unity.

For the reconstruction of stiffness maps, masks delimiting the liver samples in the FOV were created. These excluded the vessels, which were identified by applying a threshold on the MRE magnitude image. Because the MRE reconstruction relies on second order derivatives, which use information from two neighbouring pixels in each direction, a new mask (ROI) was created for the statistical analysis. This eroded the original mask by 2 pixels in every direction around the vessels (in 3D), as data in the vessels were presumed to be unreliable for stiffness reconstruction. Additionally, the margins of the mask, corresponding to the margins of the sample, were also eroded in order to avoid peculiar boundary effects.

6.1.2 Finite element model for the loading of liver samples

Efforts were made to cut the liver samples' sides as flat as possible, however this was not entirely achievable. Also, in *ex vivo*, the large liver vessels are not perfused, thus creating empty spaces in the tissue and leading to an additional degree of complexity. Thus, to investigate the effect of the irregular shape and vessels on the deformation, compression simulations were run on a realistic liver sample geometry, using $\mathcal{C}$**heart**. The aim was to attain a better overview on how these factors might influence the deformation gradient.

6.1.2.1 Mesh construction

For the finite element implementation in $\mathcal{C}$**heart**, a mesh was necessary to define the reference domain of the liver sample. Several steps had to be followed in this regard. An example of an anatomical image (corresponding to liver sample 1) was loaded in ITK-SNAP[281], where a manual segmentation of the liver sample tissue and vessels took place. Two masks were created and then loaded in MATLAB R2018b, where they were further smoothed and merged. The tissue volume mask was then imported into SimModeler 6.0, where a linear tetrahedral mesh with further refinement and smoothing around sharp edges was created, encompassing 829491 elements and 152620 linear nodes. Subsequently, in MATLAB, the mesh elements were labelled as tissue or

vessel, according to the merged mask. The tissue volume mask can be seen in the top panel of Fig. 6.1.3, and the labelled mesh can be seen in the bottom panel.

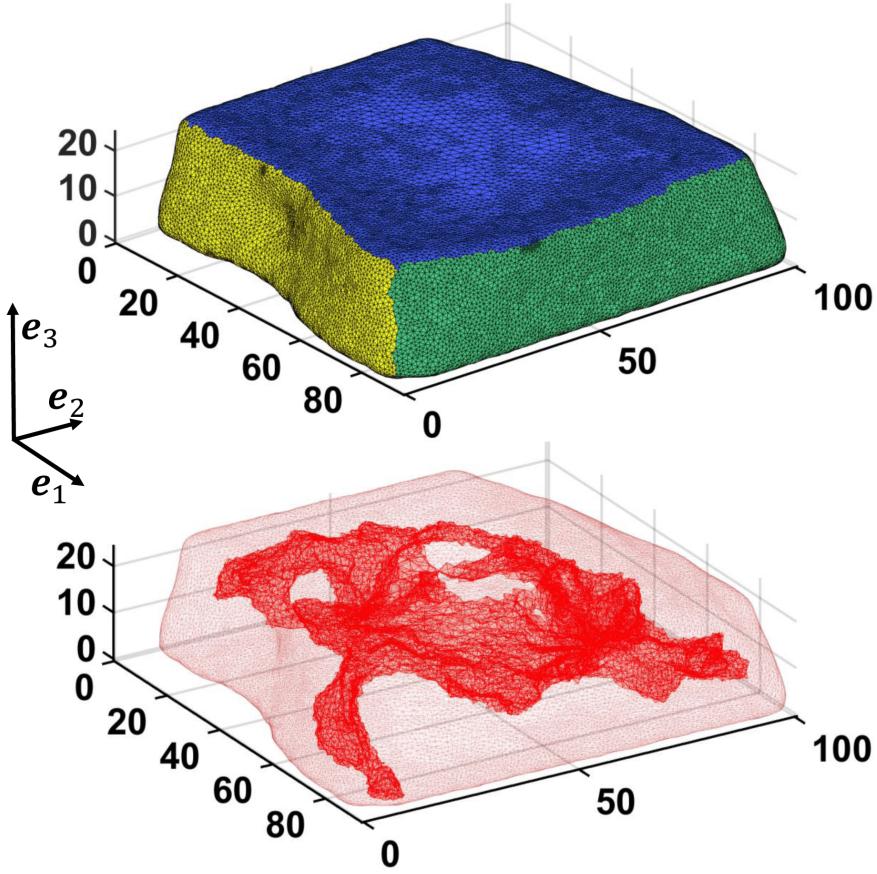

Figure 6.1.3 *Liver sample mesh; The top panel shows the volume mesh of the sample, with delimited sides; The bottom panel shows the mesh capturing the large vessels inside the sample.*

6.1.2.2 Problem specification

The mechanics problem to be solved has to include specifications on the deformation and on the material model. Firstly, in order to simulate a liver sample undergoing ideal compression, the body's boundary is split into six surfaces, corresponding to the intuitive cuboid faces. These are set by the surface element normal direction. The deformation on the compression side (green face in Fig. 6.1.3) was prescribed as

$$\boldsymbol{u}(t) = \begin{pmatrix} X_1\left(\lambda(t) - 1\right) \\ X_2\left(\dfrac{1}{\sqrt{\lambda(t)}} - 1\right) \\ X_3\left(\dfrac{1}{\sqrt{\lambda(t)}} - 1\right) \end{pmatrix}, \tag{6.1.13}$$

where a 15% compression was set to take place over 1 s, e.g. $\lambda(t) = 1 - 0.1\min(t, 1)$.

Restrictions were imposed on the sides in contact with the other support plates. Thus, on the bottom of the sample (face opposite to the blue one), the deformation in the $\boldsymbol{e}_3$ direction was set to 0 (i.e. $u_3 = 0$). Similarly, on the side opposite to the green face, which was in contact with a support plate, no deformation was allowed in the $\boldsymbol{e}_1$ direction (i.e. $u_1 = 0$).

Secondly, the material parameters of the liver tissue and vessels had to be defined. For simplicity, a hyperelastic model was run, as the aim was to gauge the impact of deformation and not to perfectly simulate the experiment. Hence, the elastic exponential model

$$\boldsymbol{S}_e = \delta \exp(b(II_{\boldsymbol{C}} - 3))\boldsymbol{C} \tag{6.1.14}$$

was employed, with $b = 1.5$ and $\delta = 80$ for the liver tissue. While the vessels contained no fluid compartment, they were modelled as a much softer material to avoid complexities associated with contact mechanics. Therefore, power b was set to 0 and δ was set two orders of magnitude softer, at 0.8. The mechanics problem was modelled as compressible, as incompressibility would have led to a very dense problem which requires both linear and quadratic interpolation fields. Thus, instead of relying on the hydrostatic pressure tensor $\boldsymbol{S}_p$, the volumetric changes were modelled as

$$\boldsymbol{S}_{vol} = \left[K_1(J-1)J + K_2 \log(J)\right] \boldsymbol{C}^{-1}, \tag{6.1.15}$$

where K_1 and K_2 are parameters defining the compressibility of a material. A large K_1 leads to S_{vol} becoming dominant over $\boldsymbol{S}_e$ if there is a volume increase, but has less of an impact when the volume diminishes. Conversely, a large K_2 leads to S_{vol} becoming dominant if there is a volume decrease, but has a smaller effect when the volume increases. For the problem considered here, these constants were set as $K_1 = 80000$, $K_2 = 0$ for liver tissue, and $K_1 = 0$, $K_2 = 10$ for vessels. The aim is to ensure that the vessels are highly compressible, thus deforming more than the surrounding tissue.

6.1.3 Registration of deformed liver samples

Registration techniques were also investigated in gauging the deformation between compression states. Thus, a method published by Vishnevskiy et al.[257] was employed. This uses total variation regularisation in order to facilitate the registration of images which were subjected to a non-smooth displacement field. Here, the liver sample compression would be an example of a non-smooth displacement field, as a sudden jump occurs between the undeformed and large compression states.

The registration was employed on both the tagged data and anatomical images of a liver sample. For the tagged data, due to the fading of the tag lines, the image had to be filtered in order to recapture the grid structure. Thus, for each phase and dynamic, the median value of the grid was subtracted from the original image, then an upper

and lower threshold were applied, and subsequently the resulting image was mapped in the [0,1] greyscale interval. Fig. 6.1.4 shows one phase of the original tagged images on the top row, and the corresponding filtered tags on the bottom row. It can be seen that the fading in the original images blurs the grid information, which would impede the registration algorithm to perform well. The filtered images are able to retrieve the grid, albeit showing artefacts near the sample boundaries.

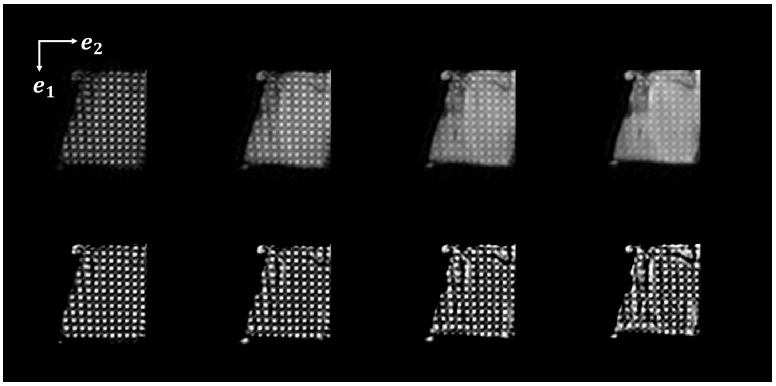

Figure 6.1.4 *Example tagged images of the liver sample. (Top row) Original tags capturing four dynamics during one phase; (Bottom row) Filtered images recovering the grid structure.*

Note that, for the tagged data, a single slice was acquired. This slice was replicated in order to create a volume, which was then used for the registration. For the anatomical images, the entire acquired volume was employed for registration.

6.2 Results and discussion

6.2.1 Harmonic wave motion in undeformed liver samples

The MRE data in undeformed liver samples was analysed using the standard UR. The fractional order α was determined, for each sample, depending on the ratio of the storage and loss moduli, according to Eq. (6.1.9). The values are presented in Table 6.2.1. It can be seen that α is in good agreement with the value predicted from the rheological tests ($\alpha = 0.2$), but also with literature values, ranging between $[0.2, 0.35]$[120,147,232].

The linear parameter δ for each liver sample, computed through Eq. (6.1.10), is also reported in the last column of Table 6.2.1. The parameters are consistent, with a standard deviation of $\approx 20\%$. Noticeably, the first two liver samples employ smaller δ values, meaning that those samples are softer than the other four. Recall that, from each of the three livers, two samples were obtained. Thus, it can indeed be seen that samples 1 and 2, 3 and 4, 5 and 6 are pairwise consistent.

Liver sample	α	b	δ (Pa)	δ (undeformed, Pa)
liver 1 (36.13%)	0.2640	0	328.07	333.91
liver 2 (33.88%)	0.2417	0	263.90	312.11
liver 3 (22.78%)	0.2355	0	482.94	510.50
liver 4 (22.21%)	0.2190	0	446.22	515.31
liver 5 (35.45%)	0.2234	0	433.96	477.38
liver 6 (22.96%)	0.2416	0	437.41	448.08
	nonlinear	nonlinear	linear	linear
mean	0.2375	0	398.75	432.88
std dev	0.0160	0	83.97	88.78

Table 6.2.1 *MRE liver tissue parameters; the error, computed as per Eq.* (6.1.12)*, can be seen in the first column, in brackets.*

It is to be noted that the mean of the δ parameter estimated from the undeformed MRE tests is almost twice the mean of the δ parameter estimated from rheology (231.02 Pa, Fig. 5.3.8). However, recall that in the rheology tests this parameter was decreasing with increasing shear strain, as an effect of shear strain softening. If we focus on the δ parameter obtained in rheology only from the lowest shear strain tests (SS 1%, depicted in the lower right panel of Fig. 5.3.12), then their average is 393.52. This is in better agreement with the MRE data, which suggests that the parametrisation obtained in rheology is suitable for predicting MRE stiffness measurements of liver tissue in undeformed cases. Additionally, since rheology was performed at frequencies of 0.5-2 Hz, while MRE at 60 Hz, it emerges that the fractional model employed is able to capture the frequency dependence exhibited by liver.

6.2.2 Loading bias in harmonic wave motion under compression

In order to test the liver sample behaviour under deformation, harmonic waves were designed to probe the tissue, as shown in Fig. 6.1.2 (columns 3-5). When employing UR to reconstruct the liver sample stiffness in the uncompressed and compressed states, it is observed that the tissue exhibits an apparent stiffness. This is exemplified in liver sample 1, in Fig. 6.2.1. In this particular case, it can be seen that some areas of the liver show an increased stiffness. However, the maps present a high heterogeneity. A summary of the average apparent stiffness of every liver sample in each deformation state can be seen in Fig. 6.2.2. The statistics are based on a ROI which excludes the sample's margins, in order to avoid peculiar boundary effects, but also vessels (as seen in columns 3 and 5 of Fig. 6.2.1). The standard deviations are between $19 - 30\%$, indicating a moderate heterogeneity.

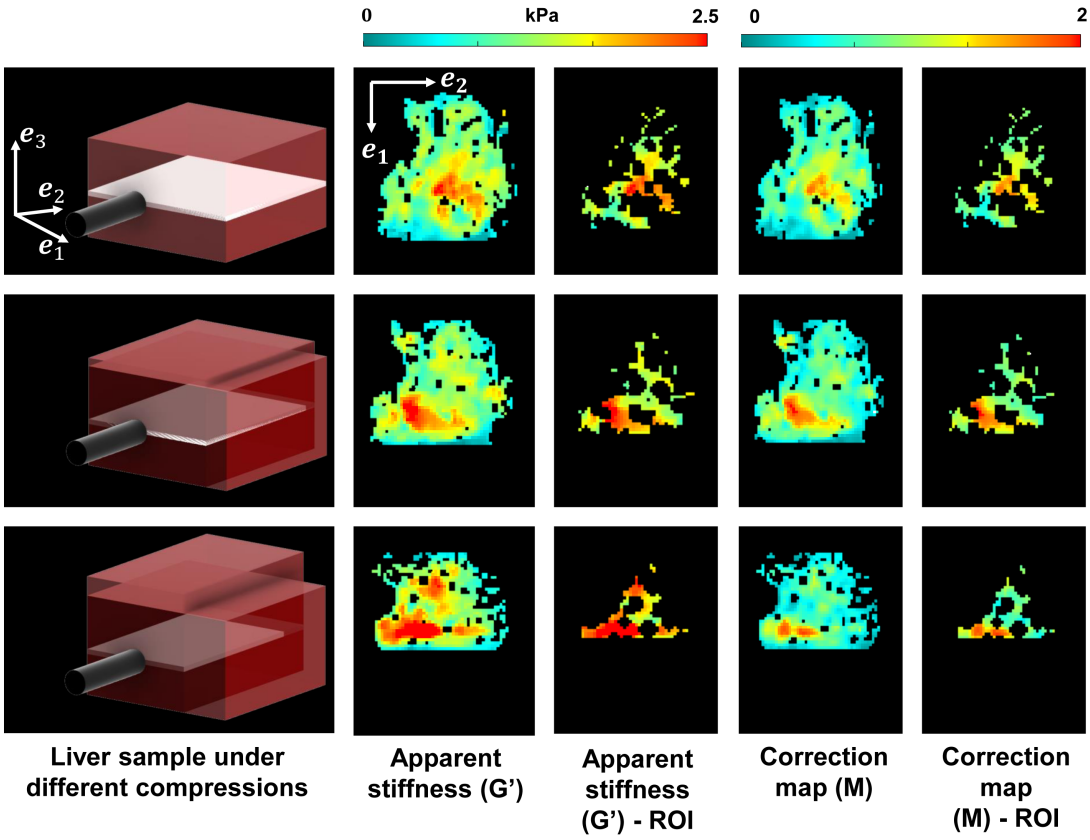

Figure 6.2.1 *Stiffness maps G' and corrected maps M corresponding to the uncompressed (top row) and compressed (middle and bottom rows) liver samples (here illustrated in liver 1). (First column) Liver sample depicted at the different deformation states. The uncompressed state is kept for reference. The piston (grey cylinder) is indenting the phantom perpendicularly during the MRE scan. Slices are acquired in the coronal plane (depicted in white). (Second and third columns) Stiffness estimates using the UR (full mask and ROI). (Fourth and fifth columns) Estimates of map M using the CR (full mask and ROI).*

The loss modulus G'' was also investigated. For each liver sample under compression, the apparent G'' is shown in Fig. 6.2.3. The standard deviations are higher compared to G', mostly between $24-43\%$, and one case 61%. Thus, the loss modulus shows a high heterogeneity. However, it is to be noted that although in the CR the linear parameter δ was estimated using information only from the real stiffness modulus, by optimising the scaling map M, the reconstruction of the imaginary scaling map N is also close to unity. Recall that in the phantom work, this was not achieved due to the little attenuation that the PVA phantoms were posing. Thus, this indicates the suitability of the CR to be used with viscoelastic materials, but also confirms the appropriate identification of parameter α in the context of a fractional derivative model.

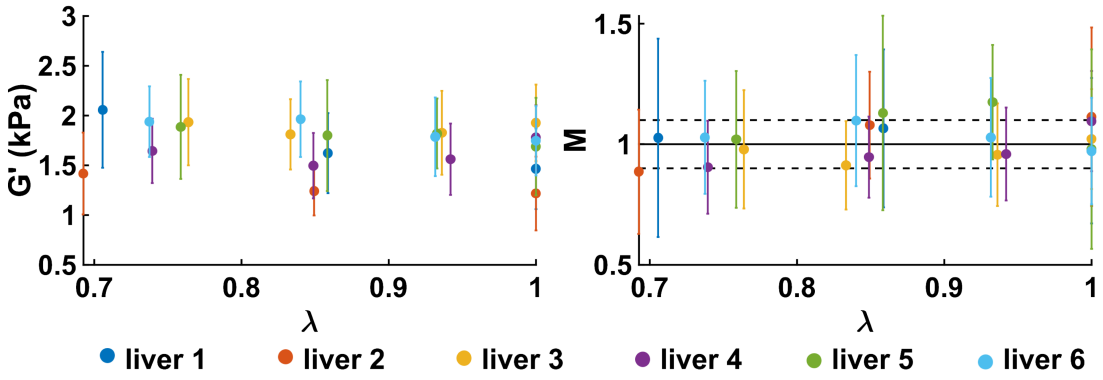

Figure 6.2.2 *Average of stiffness maps G' and corrected maps M over all pixels in a liver sample ROI, in all deformation states.*

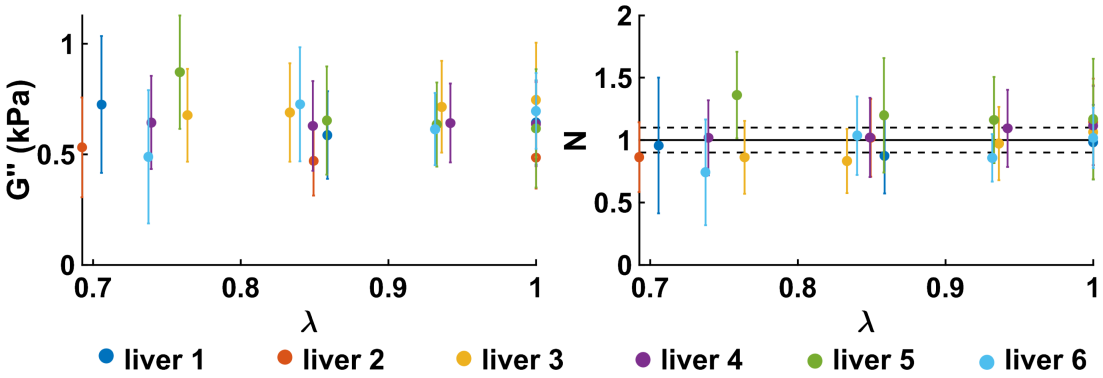

Figure 6.2.3 *Average of stiffness maps G'' and corrected maps N over all pixels in a liver sample ROI, in all deformation states.*

6.2.3 Intrinsic stiffness estimation

It was seen that the liver samples do not exhibit a clear trend with compression. Some samples show an increased stiffness (e.g. livers 1 and 2), while some show a decrease (e.g. liver 4, except in the last compression case). This may be due to the waves' local probing direction. Recall that, in chapter 4, a simplified example showed that deformation leads to apparent anisotropy (section 4.2.1.3). Thus, measured stiffness values may not be intuitive or easily interpretable. Here we employ the CR on the compressed samples, in order to investigate if the intrinsic stiffness parameters can be retrieved.

In order to describe the deformation employed in this experiment, an ideal deformation gradient was used, as described by Eq. (6.1.6). Moreover, tissue is presumed to behave according to the *vEXP* model (Eq. (6.1.3)). Here, in order to characterise the liver samples under deformation, we proceed by investigating the model parameters. Having determined the fractional order α from the uncompressed state, the remaining b and δ parameters were investigated using the data from the uncompressed and most

compressed case. Thus, for b values between $[0, 1.5]$, the best linear parameter δ was identified for each sample. Fig. 6.2.4 shows the error across the investigated b values. The left panel shows the error corresponding to the real modulus G', and the right panel shows the error for the imaginary modulus G''. With one exception in the imaginary case, the minimum error occurs when $b = 0$. This is in contrast to the rheology findings, which indicated the best b parameter to be 1.5. Nonetheless, the linear parameter δ, for the case when $b = 0$, is reported in the fourth column of Table 6.2.1 for each liver sample. A standard deviation of $\approx 21\%$ is observed across samples.

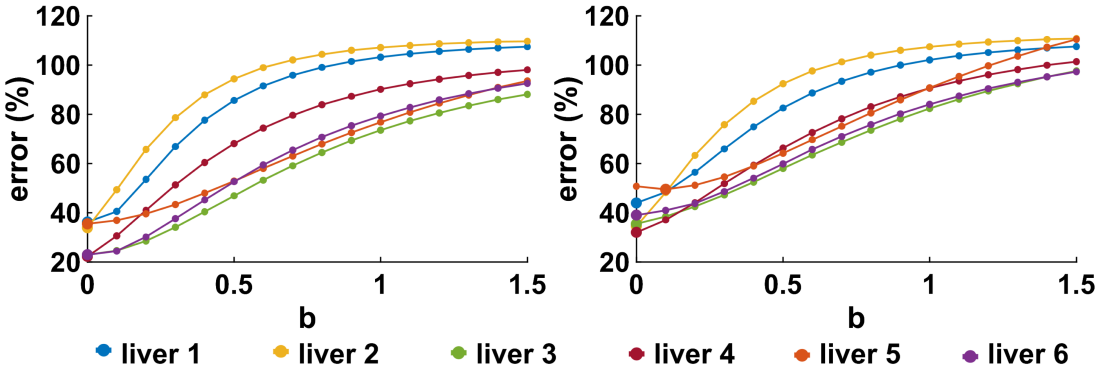

Figure 6.2.4 *The minimum error obtained by fitting the model to the data for each liver sample, sweeping over fixed values of b between 0 and 1.5*

Finally, the CR was used in order to investigate the data in all deformation cases. Using the parameters presented in Table 6.2.1, the corrected maps M and N were reconstructed, according to Eq. (6.1.11). The quantified average and standard deviation of the real and imaginary maps M and N are presented in Figs. 6.2.2 and 6.2.3, respectively. For the real map, it can be seen that most of the cases now lie within 10% of the ideal value of 1. For the imaginary part, the corrected averages lie further, mostly within 20%, with two exceptions. In both cases, the standard deviations are between 18-42%, with one case in the imaginary part reaching 57%. Thus, the heterogeneity is similar or higher compared to the apparent stiffness estimations.

It can be seen that, when applying the pipeline devised in chapter 4 to the ex-vivo bovine liver samples presented in this chapter, there are additional challenges arising. For instance, in the PVA work presented in chapter 4, phantoms of the same shape and size were tested in rheology and MRE. In the case presented here, on *ex vivo* bovine tissue samples, the geometry was different. While some studies indicate that the sample size does not significantly influence the measured parameters[195], this was only probed in small samples (e.g. cylindrical diameter 8 vs 20 mm). However, in the present work, the sample size differed substantially between MRE and rheology. In rheology, small cylindrical samples of radius 10 mm and height 3 mm were investigated. Those were cut such that large vessels were excluded. In MRE, blocks of $\approx 10 \times 10 \times 5$ cm were investigated. This led to the presence of large vessels - some seen in Fig. 6.1.2, but other

slices presented a higher incidence - in all six samples. This leads to two immediate complications: 1) vessels create a discontinuity in the field of the propagating MRE waves and 2) under load, unpressurised vessels compress first, leading to a smaller actual compression on the tissue surrounding them.

Let us first discuss the influence of large vessels on MRE measurements. On the reconstructed stiffness maps, an extended area around the vessels can be excluded, which provides a way of quantifying only the tissue properties. However, the boundaries between tissue and vessels can lead to changes in the direction of the propagating shear waves. Thus, different directions can be probed. This should not have an impact in the case of an undeformed isotropic material. However, under deformation, which leads to apparent anisotropy, a change in the probing direction determines changes in the quantified stiffness, leading to heterogeneous stiffness maps. In this study, although the uncompressed case is meant to be load free, there are two sources of potential deformations. Firstly, the liver sample was fixed between two plates, to ensure no slip during the MRE experiment. This, however, could have led to a preload, especially since the sides of the sample were not perfectly flat. Secondly, the vibrating rod was considerably indenting the sample, as seen in Fig. 6.1.2. These effects have not been accounted for in the analysis performed here. Thus, for a better understanding of the combined effect of large vessels, preload and piston indentation, *in silico* experiments could be carried. This remains a work to be accomplished.

Let us now consider the effect of vessels in the deformation process. In *ex vivo*, perfusion of vessels is lost. Thus, large empty vessels are more prone to being deformed than the surrounding liver tissue. Under compression, this inhomogeneity means that the actual degree of deformation experienced by the liver tissue is different than the one measured by assessing the sample dimension. Since the vessels are distributed in a complex pattern, it is difficult to envision the impact that they have on the deformation.

An *in silico* test was employed in order to gauge the behaviour of liver samples with embedded large vessels under compression. The distribution of vessels can be seen in the bottom panel of Fig. 6.1.3. A compression of 15% was prescribed, in order to simulate the first compression level in liver sample 1. Fig. 6.2.5 shows the diagonal components of the deformation gradient across the liver sample, in a middle slice. The second column shows the deformation pattern in a homogeneous tissue sample, in which vascular structures are not accounted for. It can be seen that the centre of the sample shows a smooth deformation gradient. The values exhibited are close to the ones expected in ideal compression, with the F_{11} component reflecting the approximate compression of 0.85, while the F_{22} and F_{33} components are close to the expected value of 1.08 (obtained as $1/\sqrt{0.85}$). However, the edges exhibit some unevenness. This is due to the shape of the sample, which deviates from a regular cuboid.

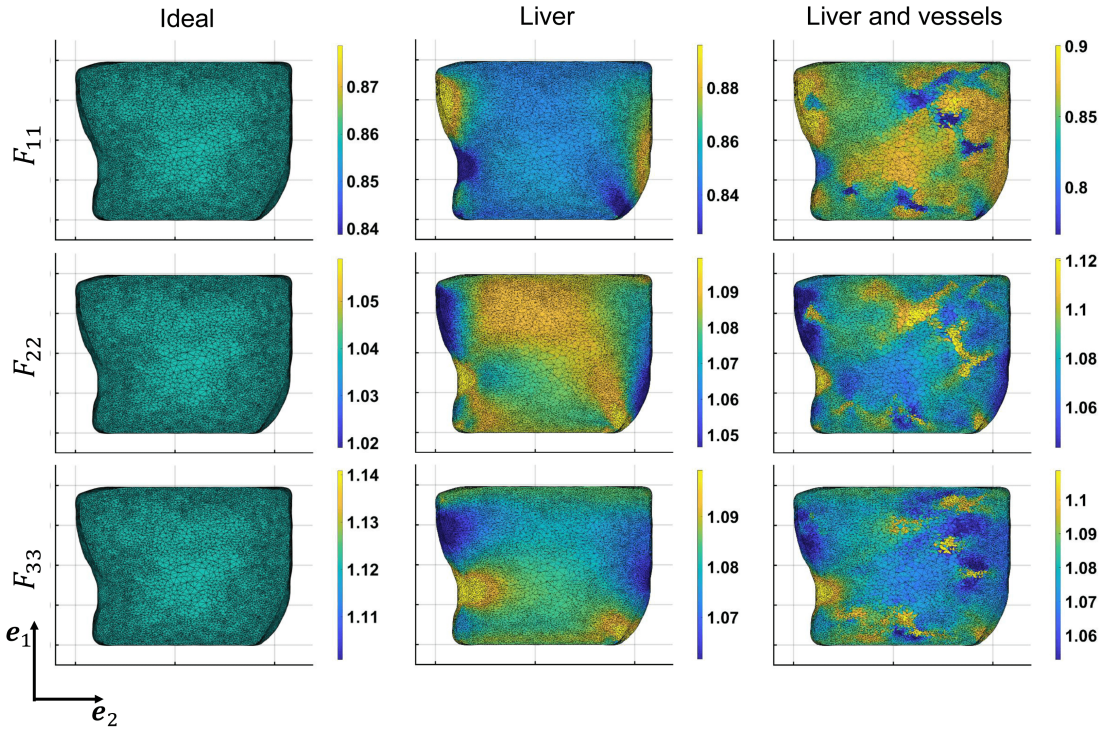

Figure 6.2.5 *Liver sample deformation gradient for* $\approx 15\%$ *compression; (First column) Ideal deformation gradient components, corresponding to Eq.* (6.1.6)*; (Second and third columns) Deformation gradient components obtained from* in silico *investigation in the case of homogeneous liver tissue and liver tissue with embedded vascular structures, respectively.*

When taking into consideration the vessels, the deformation gradient pattern becomes irregular, as seen in the third column. In the F_{11} component, the darker areas are the vessels which are being highly compressed, showing a compression below 0.8. Conversely, the tissue around them exhibits less compression, of ≈ 0.9. This shows that the vessels, which are modelled as being much softer than the liver tissue, absorb the compression. The inhomogeneity in the deformation gradient in this case is obvious, and reflects the intricacy of assessing deformation in large *ex vivo* liver samples. While *in vivo* the vessels are pressurised, their impact on the deformation is likely to be non-trivial as well.

The first column of Fig. 6.2.5 shows the ideal deformation gradient obtained for liver sample 1 at the first compression level, using Eq. (6.1.6). The first diagonal component is ≈ 0.86, which is in good agreement with the simulation considering homogeneous liver tissue. However, the F_{22} component is smaller, ≈ 1.04. As this was obtained from the average sample dimension changes, it indicates that the sample expansion in the $\boldsymbol{e}_2$ direction is smaller than expected, probably due to the piston restricting the sample. Thus, it is inferred that the the sample expands more in the $\boldsymbol{e}_3$ direction ($F_{33} \approx 1.12$). Note that if the measurements were based only on average height deformation, then the F_{22} and F_{33} components would have been in better agreement with the simulation

employing homogeneous liver tissue.

Overall, it can be seen how different the behavior in the deformation gradient is when considering a simplified ideal cuboid compression, actual liver sample geometry, and further on vascular structures embedded in the tissue. Thus, the presence of large vessels has a big impact on the deformation. This must be accounted for when trying to estimate tissue parameters from MRE measurements. In an *in vivo* setting, the compressibility of the vessels would pose a different problem, as they would be pressurised due to blood flow. Nonetheless, the presence of vascularised vessels within liver tissue may still lead to complex deformation patterns. This is a topic that remains to be investigated.

Although MRE measurements of undeformed liver samples match rheology findings, underlying macro-deformation complicates the investigation. Thus, examination of a material must be performed with caution, as tissue characterisation using MRE in loaded samples may not be directly comparable to rheology employing tissue loading.

6.2.4 Deformation estimate from image registration

The tools necessary for undoing the loading bias from MRE measurements require knowledge of the deformation employed and the material model. Thus, image registration was also explored for determining the deformation metrics. Both tagged and anatomical images of the liver samples were investigated.

For the tagged images, the tag lines had to be reapplied during the deformation. The top row of Fig. 6.2.6 shows the sequence of processing these images. Thus, two dynamics were needed to capture the deformation between 0 and 10% compression. The first dynamic shows $\approx 5\%$ compression (denoted by "C"), followed by a tag reapplication (denoted by "R"). The sequence of compression and reapplication of tag lines continues throughout the entire deformation process.

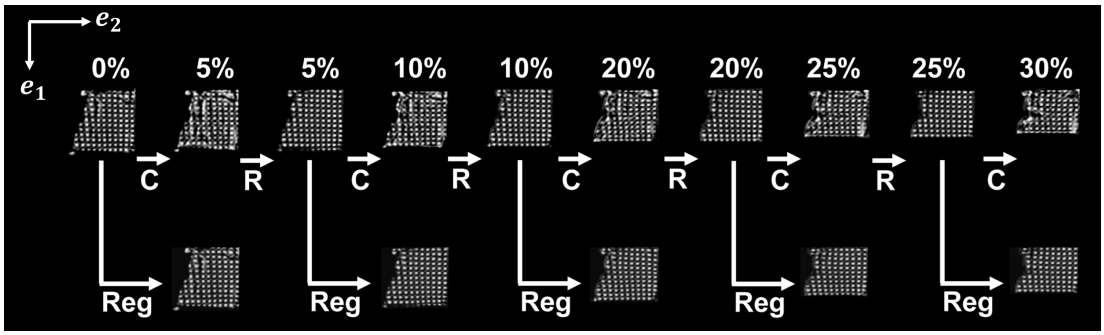

Figure 6.2.6 *Sequence of tagged liver samples; The top row shows the alternating process of compression and reapplication of tag lines; The bottom row shows the registered images for each of the above sequences.*

The registration algorithm was employed within each dynamic, as reapplication of tag lines leads to a fresh grid structure, which does not reflect the changes undergone by the original grid. The results of the registered images between compressions can be seen in the bottom row of Fig. 6.2.6. The displacements obtained between two consecutive loading steps were merged, in order to obtain the total deformation gradient corresponding to 10, 20 and 30% compression.

The registration of anatomical images was explored as well. Fig. 6.2.7 shows the original sample geometry on the top row. The second row shows the uncompressed state registered to 10, 20 and 30% compression states.

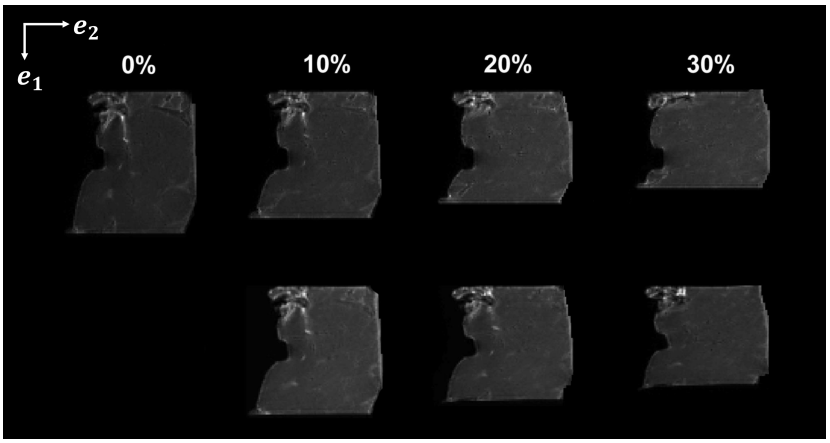

Figure 6.2.7 *Anatomical images of a liver sample; The top row shows the liver sample in undeformed and compressed states; The bottom row shows the uncompressed state registered to the deformed states.*

The deformation gradients obtained from the displacements indicated by the registration were compared to the ideal deformation gradient, obtained from Eq. (6.1.6). Fig. 6.2.8 shows the F_{11} component for these cases. Thus, for the intended 10, 20 and 30% compressions, the ideal case indicates a 0.93, 0.84 and 0.73 change in sample height. The deformations obtained from the tagged images show a more variable pattern. In the centre of the sample, despite the unevenness, the average behaviour resembles the ideal case. At the place of loading, however, the registration indicates a much higher tissue compression - 0.7, 0.5 and 0.2, respectively. The deformation gradient obtained from the anatomical images exhibits a smoother behaviour. Nonetheless, the F_{11} average values appear lower than the ideal case, with deformations indicating $\approx 0.89, 0.75$ and 0.5 compression. In contradiction to the information from tagged data, the deformation gradient from anatomical images indicates a smaller compression at the place of loading, compared to the rest of the sample.

The deformation gradients corresponding to the ideal case, tagged and anatomical data were used with the CR, in order to investigate the intrinsic stiffness estimations. The analysis described in section 6.1.1.3 was employed, with the linear parameter δ being

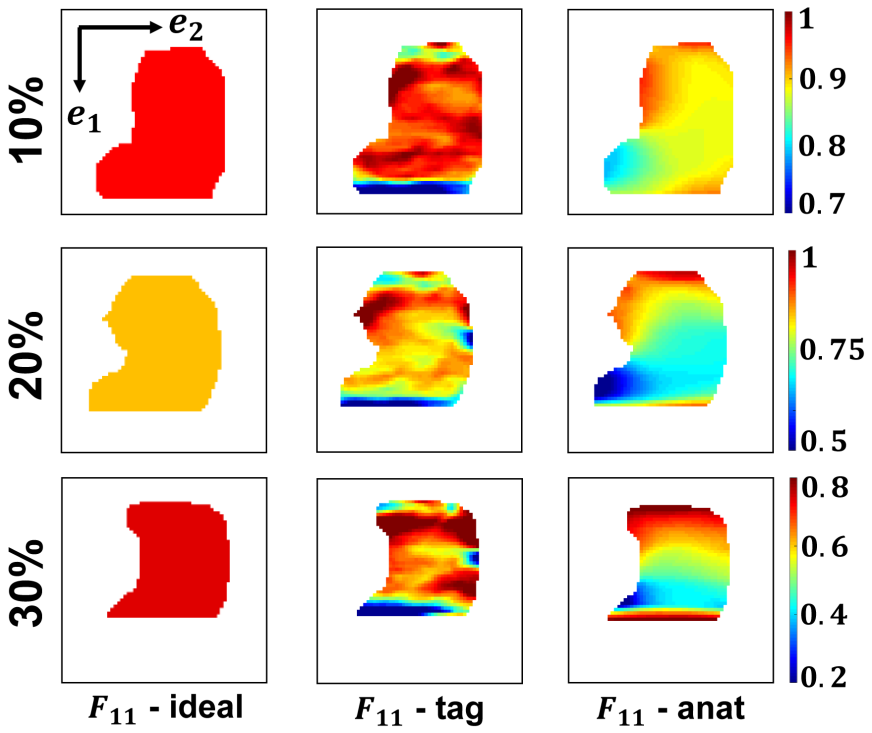

Figure 6.2.8 *First component of the deformation gradient for ≈10, 20 and 30% compression. (Left column) F_{11} corresponding to ideal compression; (Second and third columns) F_{11} obtained from the registration of tagged and anatomical images, respectively.*

estimated from the uncompressed and most compressed cases. Fig. 6.2.9 shows the reconstructed maps M, alongside the results of the UR. The latter were scaled by the apparent mean stiffness G' of the uncompressed and 30% compression case, for a better comparison. This would be equivalent with employing CR with $\boldsymbol{F} = \boldsymbol{I}$ regardless of the compression state.

At first sight, it looks like the stiffness pattern exhibited by the UR in the compression cases does not change drastically in the CR, regardless of the deformation gradient employed. However, at a closer inspection, some differences may be noticed. For instance, the deformation gradient from the anatomical images leads to the identification of some stiffer areas in the first two compression cases, compared to using the other two deformation gradients. In order to quantify the effect of the CR using the different deformation gradients, Fig. 6.2.10 shows the mean and standard deviation of maps M. Those were obtained for δ values of 437.30 (ideal), 409.98 (tag) and 374.36 (anat). It can be observed that using $\boldsymbol{F}$ from the ideal assumption or tagged data leads to similar results. The standard deviations within each compression case are between $\approx 22\%$ and $\approx 25\%$. However, employing $\boldsymbol{F}$ from the anatomical image registration leads to maps M beyond 10% of the ideal value of unity. Additionally, an increased heterogeneity is observed, with standard deviations reaching 33%.

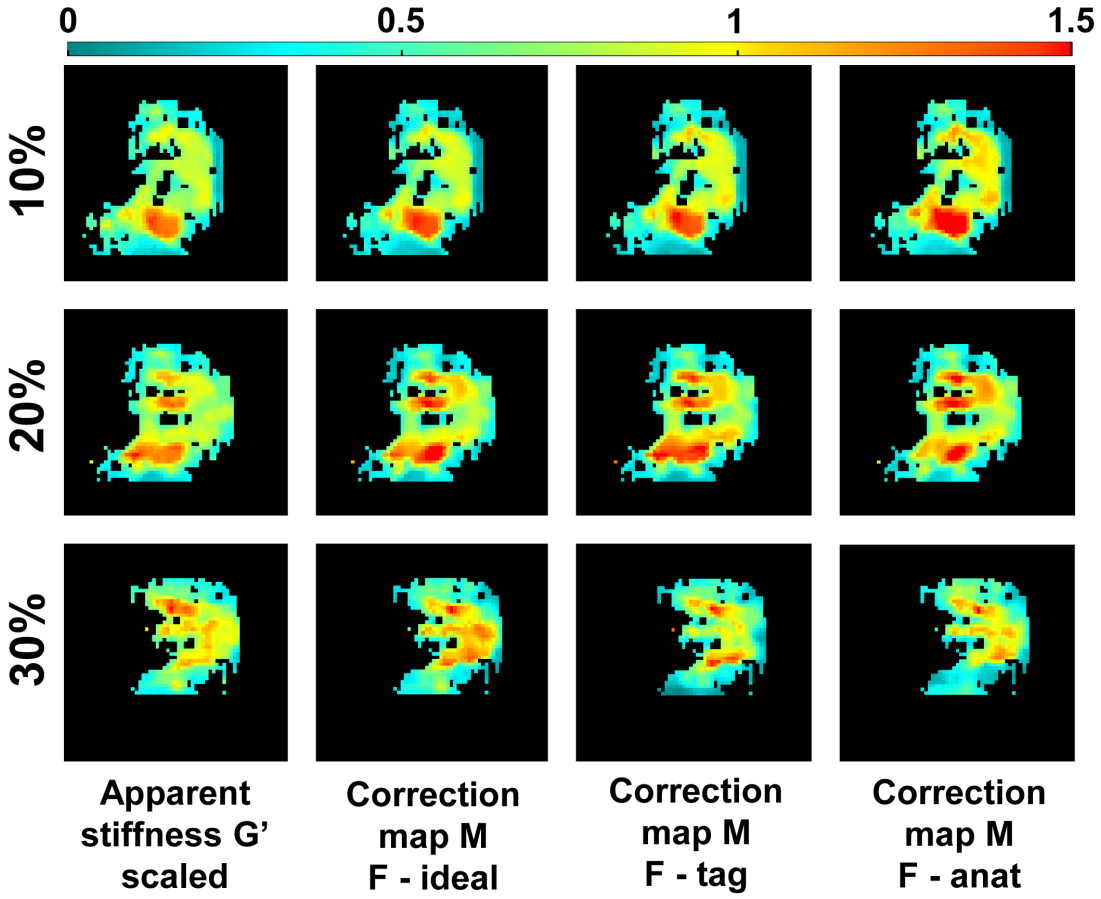

Figure 6.2.9 *Corrected maps M corresponding to ≈10, 20 and 30% compression. (Left column) Apparent stiffness map scaled by the average value; Corrected maps M using deformation metrics from (second column) ideal compression, (third column) registration of tagged images, and (fourth column) registration of anatomical images.*

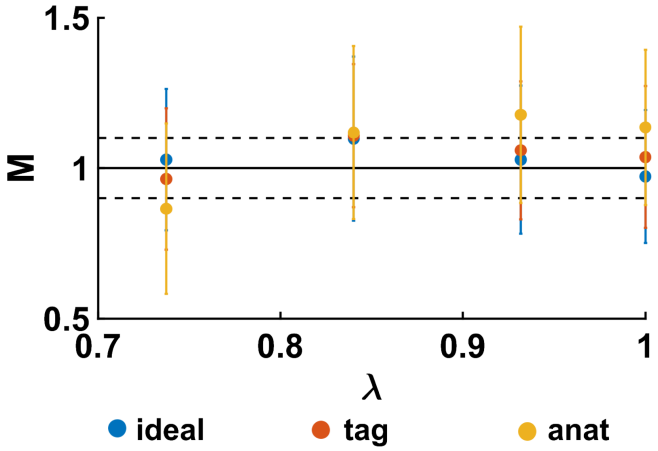

Figure 6.2.10 *Effect of deformation gradient on intrinsic stiffness estimation*

In the case analysed here, the ground truth is unknown. Accordingly, it is possible that none of the deformations gradients employed were actually a close estimate to

the real deformation. One reason behind this could be the presence of a very large vessel in this sample, which can be seen in Fig. 6.2.11, running across four slices. Presumably, this led to a smaller deformation than intended, and consequently to a very small change in stiffness across loading states. This pinpoints the importance that the deformation gradient plays in retrieving the intrinsic stiffness values. As identified before, the deformation gradient coming from the registration of anatomical images led to considerably different results compared to the other two deformation gradients. This was observed both in the scaling map M and in the δ parameter, which was lower.

Although the ideal deformation gradient is not a gold standard to which the strain metrics coming from the registration of tagged and anatomical images should be compared to, it provides an reasonable prediction for the deformation. This was probed in the *in silico* estimation of the deformation gradient, which showed that although the vessels alter the deformation experienced by the surrounding near tissue, the rest of the areas do not deviate extremely from the ideal deformation gradient (Fig. 6.2.5). Thus, by comparing $\boldsymbol{F}$ obtained from the registration of tagged and anatomical images (Fig. 6.2.8), it can be inferred that the registration of anatomical images did not lead to a plausible deformation gradient. This is likely due to the absence of dense internal structures that could have established a one-to-one correspondence between pixels in the undeformed and deformed images. Although the tagged data offered more structure, the fading and frequent reapplication of tag lines led to some information being lost or blurred. Moreover, the tagged data was only 2D, and could not capture the changes happening in the slice direction $\boldsymbol{e}_3$.

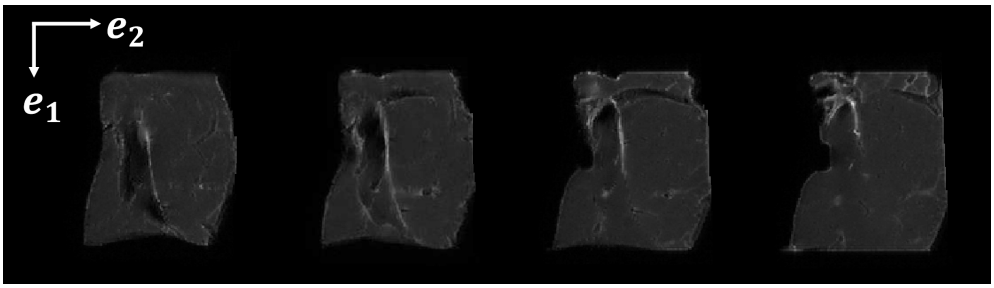

Figure 6.2.11 *Anatomical image of a liver sample. A large vessel can be seen running across four slices.*

The influence of the deformation metrics was also investigated in an *in silico* test, presented in section 6.B. There, two deformation gradients were estimated. The first one was obtained from the registration of structurally detailed images, whereas the second one was obtained from the registration of images with no internal details. Knowing the ground truth, the CR employing the first deformation gradient was able to retrieve the intrinsic stiffness parameter. The second deformation gradient did not lead to satisfactory results. This highlights both the importance of an accurate estimate of $\boldsymbol{F}$, but also the need of a highly detailed structure, which can ensure a pixel-wise correspondence

between deformation states.

An accurate one-to-one correspondence between pixels in the undeformed and deformed images would be essential, as this would allow not only a reliable determination of $\boldsymbol{F}$, but could also lead to a better identification of the scaling map M. Currently, the CR is estimating the tissue model parameters by aiming to map each pixel to unity, as a measure of correct identification. This would stand true for a homogeneous material. However, we saw that the undeformed liver shows some heterogeneity, possibly due to the initial preload. Nonetheless, for a more accurate identification of the model parameters, the corrected stiffness values in the deformed case should match the distribution of the stiffness in the undeformed case, mapped into the deformed image. Here we did not employ this mapping, as the displacements between deformation states were not considered reliable, and a misalignment in the heterogeneous maps would have led to wrong parameter estimates. However, this remains an aim to be pursued, provided that the deformation metrics are accurate.

6.3 Conclusions

In this chapter, the framework developed for retrieving intrinsic stiffness parameters from MRE measurements was tested in loaded liver samples. Firstly, considering the findings from chapter 5, the *vEXP* model was employed in order to derive the analytic form of the stiffness moduli influencing the wave dynamics. The MRE data was analysed in the context of various deformation gradients, obtained from considering simplified ideal compression, or from registration of tagged and anatomical images. In the case of no underlying deformation, the MRE measurements were in good agreement with the rheology findings from chapter 5. This validated the use of the fractional *vEXP* model, which was able to capture the liver behaviour both in the low rheology frequencies, but also in the higher MRE frequencies. However, when deformation was employed, there were complications. Of utmost importance, the impact of unpressurised large vessels on the deformation is considerable. This indicates that locally, strain metrics can be very different compared the ones envisioned through the experimental design. Thus, the presence of large vessels must be taken into account when aiming to characterise liver tissue. In an in vivo setting, this issue would be less acute, due to the presence of vascular pressure, which would prevent the vessels from collapsing under load. However, the exact effect of pressurised vessels on the deformation of liver tissue remains a topic of investigation.

Comprehensive deformation metrics were sought from the registration of tagged images of liver samples, but also from anatomical data. These had their own limitations, with the tagged data being only 2D, and the tag lines fading very quickly, necessitating many processing steps in order to restore the grid structure. Thus, accuracy of the internal features was lost in some areas of the image. The deformation gradient thus obtained

was not able to capture the intricate strains occurring around a large vessel. From the registration of anatomical images, the derived deformation gradient looked unreliable, as the suggested deformations were larger than expected. This is possibly due to the lack of dense anatomical features, which could guide the tracking algorithm, especially in cases of large deformations like the ones employed here.

Taking all into account, the use of the fractional *vEXP* model derived in rheology work proved appropriate for modelling MRE data in undeformed cases. When loading is involved, accurate deformation metrics are crucial for seeking intrinsic stiffness parameters. Thus, improvements remain to be implemented in this area in order to successfully employ the proposed pipeline in *ex vivo* MRE measurements of loaded liver samples. This avenue should be further investigated, as the loading is biasing MRE measurements in an intricate way, which needs to be understood in order to interpret inherent tissue parameters.

Supplementary materials

6.A Nonlinear viscoelasticity in MRE

6.A.1 Simplification to linearised elastic wave equations for viscoelastic materials

In this section the aim is to simplify the perturbed Eq. (2.4.7) of motion following the path presented in section 2.4.1. However, here we consider the context of a viscoelastic model of the form presented in Eq. (5.2.19), where the linear parameter δ is dropped for convenience (i.e. $\delta = 1$). Thus, by employing Perturbation theory, here we expand about the current state $\mathbf{U}$.

Before investigating the components of the stress term $\boldsymbol{F}^{\varepsilon}\boldsymbol{S}^{\varepsilon}$, recall the expansions of the deformation gradient (Eq. (2.4.10)) and hydrostatic stress (Eq. (4.A.8)). Here, the viscoelastic part expansion becomes:

$$\begin{aligned} D_t^{\alpha}(\boldsymbol{S}_e^b)^{\varepsilon} &= D_t^{\alpha}\left(\boldsymbol{S}_e^b + \sum_{n=1}^{\infty}\left([\nabla_{\boldsymbol{F}}]^n \boldsymbol{S}_e^b\right)[:\delta\boldsymbol{F}]^n\right) \\ &\approx D_t^{\alpha}\left(\boldsymbol{S}_e^b + \nabla_{\boldsymbol{F}}\boldsymbol{S}_e^b : \nabla_{\boldsymbol{X}}\boldsymbol{u}^{\varepsilon}\right) + \mathcal{O}(\varepsilon^2) \\ &\approx D_t^{\alpha}\boldsymbol{S}_e^b + D_t^{\alpha}\left(\nabla_{\boldsymbol{F}}\boldsymbol{S}_e^b : \nabla_{\boldsymbol{X}}\boldsymbol{u}^{\varepsilon}\right) + \mathcal{O}(\varepsilon^2), \\ &\approx D_t^{\alpha}\boldsymbol{S}_e^b + \nabla_{\boldsymbol{F}}\boldsymbol{S}_e^b : D_t^{\alpha}\left(\nabla_{\boldsymbol{X}}\boldsymbol{u}^{\varepsilon}\right) + \mathcal{O}(\varepsilon^2), \end{aligned} \tag{6.A.1}$$

where it is assumed that $D_t^{\alpha}\left(\nabla_{\boldsymbol{F}}\boldsymbol{S}_e^b\right) : \nabla_{\boldsymbol{X}}\boldsymbol{u}^{\varepsilon} = 0$, due to the perturbation being applied a long time after the macro deformation. Thus, the wave is independent of the deformation path.

Hence, the components of the stress term $\boldsymbol{F}^{\varepsilon}\boldsymbol{S}^{\varepsilon}$ are given by

$$\begin{aligned} \boldsymbol{F}^{\varepsilon}\boldsymbol{S}^{\varepsilon} = \boldsymbol{F}^{\varepsilon}\left(\mathrm{Dev}\left[D_t^{\alpha}(\boldsymbol{S}_e^b)^{\varepsilon}\right] + \boldsymbol{S}_p^{\varepsilon}\right) \approx \boldsymbol{F}\left(\mathrm{Dev}\left[D_t^{\alpha}\boldsymbol{S}_e^b\right] + \boldsymbol{S}_p\right) + \\ \nabla_{\boldsymbol{X}}\boldsymbol{u}^{\varepsilon}\left(\mathrm{Dev}\left[D_t^{\alpha}\boldsymbol{S}_e^b\right] + \boldsymbol{S}_p\right) \\ \boldsymbol{F}\left\{\mathrm{Dev}\left[\nabla_{\boldsymbol{F}}\boldsymbol{S}_e^b : D_t^{\alpha}\left(\nabla_{\boldsymbol{X}}\boldsymbol{u}^{\varepsilon}\right)\right] + \right. \\ \left.\nabla_{\boldsymbol{F}}\boldsymbol{S}_p : \nabla_{\boldsymbol{X}}\boldsymbol{u}^{\varepsilon} + p^{\varepsilon}J\boldsymbol{C}^{-1}\right\} + \mathcal{O}(\varepsilon^2), \end{aligned} \tag{6.A.2}$$

where the first term of the expansion is equivalent to $\boldsymbol{FS}$, and the operator Dev is defined as in Eq. (5.2.7). Additionally, the term $\nabla_{\boldsymbol{X}}\boldsymbol{u}^{\varepsilon}\mathrm{Dev}\left[D_t^{\alpha}\boldsymbol{S}_e^b\right]$ is considered to be negligible. This has been confirmed by numerical investigation in the case of simple compression, which is the case examined in this chapter. Hence, $\boldsymbol{F}^{\varepsilon}\boldsymbol{S}^{\varepsilon}$ becomes

$$\begin{aligned}\boldsymbol{F}^{\varepsilon}\boldsymbol{S}^{\varepsilon} \approx \boldsymbol{FS} + (\nabla_{\boldsymbol{X}}\boldsymbol{u}^{\varepsilon})\boldsymbol{S}_p + \\ \boldsymbol{F}\left\{\mathrm{Dev}\left[\nabla_{\boldsymbol{F}}\boldsymbol{S}_e^b : D_t^{\alpha}\left(\nabla_{\boldsymbol{X}}\boldsymbol{u}^{\varepsilon}\right)\right] + \nabla_{\boldsymbol{F}}\boldsymbol{S}_p : \nabla_{\boldsymbol{X}}\boldsymbol{u}^{\varepsilon} + p^{\varepsilon}J\boldsymbol{C}^{-1}\right\}.\end{aligned} \tag{6.A.3}$$

For clarity, in index notation,

$$\begin{aligned}(F^{\varepsilon}S^{\varepsilon})_{ij} \approx F_{ik}S_{kj} + \frac{\partial u_i^{\varepsilon}}{\partial X_n}(S_p)_{nj} + \\ F_{ik}\left\{\mathrm{Dev}\left[\frac{\partial (S_e^b)_{kj}}{\partial F_{mn}} D_t^{\alpha}\left(\frac{\partial u_m^{\varepsilon}}{\partial X_n}\right)\right] + \frac{\partial (S_p)_{kj}}{\partial F_{mn}} : \frac{\partial u_m^{\varepsilon}}{\partial X_n} + p^{\varepsilon}JC_{kj}^{-1}\right\}.\end{aligned} \tag{6.A.4}$$

Thus, considering Eqs. (2.4.14) and (6.A.3), the conservation of momentum can be split between macro-deformation and micro-deformation components, *i.e.*

$$\begin{aligned}\left[\rho J\partial_{tt}\boldsymbol{U} - \nabla_{\boldsymbol{X}}\cdot(\boldsymbol{FS})\right] + \rho J\partial_{tt}\boldsymbol{u}^{\varepsilon} - \\ \nabla_{\boldsymbol{X}}\cdot\left((\nabla_{\boldsymbol{X}}\boldsymbol{u}^{\varepsilon})\boldsymbol{S}_p + \boldsymbol{F}\left\{\mathrm{Dev}\left[\nabla_{\boldsymbol{F}}\boldsymbol{S}_e^b : D_t^{\alpha}\left(\nabla_{\boldsymbol{X}}\boldsymbol{u}^{\varepsilon}\right)\right] + \nabla_{\boldsymbol{F}}\boldsymbol{S}_p : \nabla_{\boldsymbol{X}}\boldsymbol{u}^{\varepsilon} + p^{\varepsilon}J\boldsymbol{C}^{-1}\right\}\right) = \boldsymbol{0}.\end{aligned} \tag{6.A.5}$$

With the macro-deformation $\boldsymbol{U}$ satisfying Eq. (2.4.4a), the first square bracketed term on the left-hand side is zero. Hence, a set of linearised elastic wave equations in the reference frame can be formulated:

$$\begin{aligned}\rho J\partial_{tt}\boldsymbol{u}^{\varepsilon} - \nabla_{\boldsymbol{X}}\cdot\Bigg((\nabla_{\boldsymbol{X}}\boldsymbol{u}^{\varepsilon})\boldsymbol{S}_p + \boldsymbol{F}\left\{\mathrm{Dev}\left[\nabla_{\boldsymbol{F}}\boldsymbol{S}_e^b : D_t^{\alpha}\left(\nabla_{\boldsymbol{X}}\boldsymbol{u}^{\varepsilon}\right)\right] + \right. \\ \left.\nabla_{\boldsymbol{F}}\boldsymbol{S}_p : \nabla_{\boldsymbol{X}}\boldsymbol{u}^{\varepsilon} + p^{\varepsilon}J\boldsymbol{C}^{-1}\right\}\Bigg) = \boldsymbol{0},\end{aligned} \tag{6.A.6a}$$

$$\boldsymbol{F}^{-T} : \nabla_{\boldsymbol{X}}\boldsymbol{u}^{\varepsilon} = 0. \tag{6.A.6b}$$

Considering harmonic wave perturbations, let us insert the wave form given by Eq. (2.4.20) into the set of Eq. (6.A.6), noting the Laplace transform $D_t^{\alpha}\left(e^{i\omega t}\right) \approx (i\omega)^{\alpha}e^{i\omega t}, \forall t \gg 0$:

$$-\rho J\omega^2\boldsymbol{u}_c - \tag{6.A.7a}$$

$$\nabla_{\boldsymbol{X}}\cdot\left(\left\{\boldsymbol{F}\left((i\omega)^{\alpha}\mathrm{Dev}\left[\nabla_{\boldsymbol{F}}\boldsymbol{S}_e^b\right] + \nabla_{\boldsymbol{F}}\boldsymbol{S}_p\right) + \boldsymbol{\mathcal{I}}\boldsymbol{S}_p\right\} : \nabla_{\boldsymbol{X}}\boldsymbol{u}_c + p^{\varepsilon}J\boldsymbol{F}^{-T}\right) = \boldsymbol{0},$$

$$\boldsymbol{F}^{-T} : \nabla_{\boldsymbol{X}}\boldsymbol{u}_c = 0. \tag{6.A.7b}$$

When comparing with real data, it is desirable to map the momentum equations into the

physical frame, as exemplified in section 2.4.3. Using Eq. (2.4.3), the gradients with respect to the reference frame can be transformed into the current domain, leading to:

$$\begin{aligned}&\left\{\boldsymbol{F}\left((i\omega)^{\alpha}\mathrm{Dev}\left[\nabla_{\boldsymbol{F}}\boldsymbol{S}_e^b\right]+\nabla_{\boldsymbol{F}}\boldsymbol{S}_p\right)+\boldsymbol{\mathcal{I}}\boldsymbol{S}_p\right\}:\nabla_{\boldsymbol{X}}\boldsymbol{u}_c \\ &=\left\{\boldsymbol{F}\left((i\omega)^{\alpha}\mathrm{Dev}\left[\nabla_{\boldsymbol{F}}\boldsymbol{S}_e^b\right]+\nabla_{\boldsymbol{F}}\boldsymbol{S}_p\right)+\boldsymbol{\mathcal{I}}\boldsymbol{S}_p\right\}:[\nabla_{\boldsymbol{X}}\boldsymbol{u}_c\boldsymbol{F}^{-1}\boldsymbol{F}] \\ &=\left\{\boldsymbol{F}\left((i\omega)^{\alpha}\mathrm{Dev}\left[\nabla_{\boldsymbol{F}}\boldsymbol{S}_e^b\right]+\nabla_{\boldsymbol{F}}\boldsymbol{S}_p\right)\boldsymbol{F}^T+\boldsymbol{\mathcal{I}}\boldsymbol{S}_p\boldsymbol{F}^T\right\}:\nabla_{\boldsymbol{x}}\boldsymbol{u}_c.\end{aligned} \tag{6.A.8}$$

In index notation,

$$\begin{aligned}&\left(\left\{\boldsymbol{F}\left((i\omega)^{\alpha}\mathrm{Dev}\left[\nabla_{\boldsymbol{F}}\boldsymbol{S}_e^b\right]+\nabla_{\boldsymbol{F}}\boldsymbol{S}_p\right)\boldsymbol{F}^T+\boldsymbol{\mathcal{I}}\boldsymbol{S}_p\boldsymbol{F}^T\right\}:\nabla_{\boldsymbol{x}}\boldsymbol{u}_c\right)_{ij} = \\ &F_{ik}\left((i\omega)^{\alpha}\mathrm{Dev}\left[\frac{\partial(S_e)_{kj}}{\partial F_{mn}}\right]+\frac{\partial(S_p)_{kj}}{\partial F_{mn}}\right)\frac{\partial(u_c)_m}{\partial x_l}F_{ln}+\delta_{im}S_{nj}\frac{\partial(u_c)_m}{\partial x_l}F_{ln}.\end{aligned}$$

Subsequently, using Eq. (2.4.2), which links the divergence of a tensor between the physical and reference domains, then the divergence of the stress terms can be re-cast in terms of the physical gradient operator $\nabla_{\boldsymbol{x}}$ as

$$\nabla_{\boldsymbol{X}}\cdot\left(\left\{\boldsymbol{F}\left((i\omega)^{\alpha}\mathrm{Dev}\left[\nabla_{\boldsymbol{F}}\boldsymbol{S}_e^b\right]+\nabla_{\boldsymbol{F}}\boldsymbol{S}_p\right)\boldsymbol{F}^T+\boldsymbol{\mathcal{I}}\boldsymbol{S}_p\boldsymbol{F}^T\right\}:\nabla_{\boldsymbol{x}}\boldsymbol{u}_c\right)=J\nabla_{\boldsymbol{x}}\cdot(\boldsymbol{\mathcal{C}}:\nabla_{\boldsymbol{x}}\boldsymbol{u}_c), \tag{6.A.9}$$

where the 4^{th} order tensor $\boldsymbol{\mathcal{C}}$ encompasses

$$\mathcal{C}_{ijml}=\frac{1}{J}\left(F_{ik}\left((i\omega)^{\alpha}\mathrm{Dev}\left[\frac{\partial(S_e)_{ks}}{\partial F_{mn}}\right]+\frac{\partial(S_p)_{ks}}{\partial F_{mn}}\right)+\frac{\partial F_{ik}}{\partial F_{mn}}(S_p)_{ks}\right)F_{ln}F_{js}. \tag{6.A.10}$$

Combining Eqs. (6.A.8) and (6.A.9) and noting the property linking the divergence of a scalar in the reference domain to the physical frame (Eq. (2.4.1)), then Eq. (6.A.6a) may be written as

$$\rho J\omega^2\boldsymbol{u}_c-J\nabla_{\boldsymbol{x}}\cdot\left(p_c\boldsymbol{I}+\boldsymbol{\mathcal{C}}:\nabla_{\boldsymbol{x}}\boldsymbol{u}_c\right)=\boldsymbol{0}, \tag{6.A.11}$$

and further on as

$$-\rho\omega^2\boldsymbol{u}_c-\nabla_{\boldsymbol{x}}\cdot[(\boldsymbol{\mathcal{G}}'+i\boldsymbol{\mathcal{G}}'')):\nabla_{\boldsymbol{x}}\boldsymbol{u}_c+p_c\boldsymbol{I}]=\boldsymbol{0}. \tag{6.A.12}$$

Here, the real and imaginary scaling moduli $\boldsymbol{\mathcal{G}}'$ and $\boldsymbol{\mathcal{G}}''$ are given by $\boldsymbol{\mathcal{G}}'=\mathrm{Re}(\boldsymbol{\mathcal{C}})$, $\boldsymbol{\mathcal{G}}''=\mathrm{Im}(\boldsymbol{\mathcal{C}})$, *i.e.*

$$\boldsymbol{\mathcal{G}}' = \frac{1}{J}\left(\left\{\boldsymbol{F}\left(\omega^{\alpha}\cos\left(\frac{\pi\alpha}{2}\right)\mathrm{Dev}\left[\nabla_{\boldsymbol{F}}\boldsymbol{S}_e^b\right]+\nabla_{\boldsymbol{F}}\boldsymbol{S}_p\right)+\boldsymbol{\mathcal{I}}\boldsymbol{S}_p\right\}\right)\boldsymbol{F}^T\boldsymbol{F}^T, \tag{6.A.13a}$$

$$\boldsymbol{\mathcal{G}}'' = \frac{\omega^{\alpha}}{J}\sin\left(\frac{\pi\alpha}{2}\right)\boldsymbol{F}\mathrm{Dev}\left[\nabla_{\boldsymbol{F}}\boldsymbol{S}_e^b\right]\boldsymbol{F}^T\boldsymbol{F}^T. \tag{6.A.13b}$$

6.A.2 Viscoelastic moduli estimates for the *vEXP* model

Here we investigate the form of the viscoelastic moduli $\mathcal{G}'$ and $\mathcal{G}''$ for a material described by the *vEXP* model, i.e.

$$\boldsymbol{S} = \delta \mathrm{Dev}[D_t^\alpha \boldsymbol{S}_e^b] + \boldsymbol{S}_p, \qquad \boldsymbol{S}_e^b = \exp(b(II_{\boldsymbol{C}} - 3))\boldsymbol{C}. \tag{6.A.14}$$

Thus, the 4$^{\text{th}}$ order tensor $\boldsymbol{\mathcal{C}}$ can be taken one step further and written as

$$\begin{aligned}\mathcal{C}_{ijml} =& \frac{1}{J}\left(F_{ik}\left((i\omega)^\alpha \delta \mathrm{Dev}\left[\frac{\partial (S_e^b)_{ks}}{\partial F_{mn}}\right] + \frac{\partial (S_p)_{ks}}{\partial F_{mn}}\right) + \frac{\partial F_{ik}}{\partial F_{mn}} S_{ks}\right) F_{ln} F_{js} \\ =& \frac{1}{J}\left((i\omega)^\alpha \delta F_{ik} \mathrm{Dev}\left[\frac{\partial \left(\exp(b(II_{\boldsymbol{C}} - 3))C_{ks}\right)}{\partial F_{mn}}\right] F_{ln} F_{js} + \right. \\ & \left. F_{ik}\frac{\partial (JPC_{ks}^{-1})}{\partial F_{mn}} F_{ln} F_{js} + JP \frac{\partial F_{ik}}{\partial F_{mn}} C_{ks}^{-1} F_{ln} F_{js}\right).\end{aligned} \tag{6.A.15}$$

Let us investigate the differential terms by turn:

$$\begin{aligned}\frac{\partial \left(\exp(b(II_{\boldsymbol{C}} - 3))C_{ks}\right)}{\partial F_{mn}} =& \frac{\partial \left(\exp(b(II_{\boldsymbol{C}} - 3))\right)}{\partial (II_{\boldsymbol{C}} - 3)} \frac{\partial (II_{\boldsymbol{C}} - 3)}{\partial F_{mn}} C_{ks} + \\ & \exp(b(II_{\boldsymbol{C}} - 3)) \frac{\partial C_{ks}}{\partial F_{mn}} \\ =& \exp(b(II_{\boldsymbol{C}} - 3))\big(4b(FC)_{mn} C_{ks} + \delta_{kn} F_{ms} + \delta_{sn} F_{mk}\big).\end{aligned} \tag{6.A.16}$$

The above term is found inside the Dev operator, hence the second part of the operator is applied as follows:

$$\begin{aligned}\frac{1}{3}\frac{\partial \left(\exp(b(II_{\boldsymbol{C}} - 3))C_{pr}\right)}{\partial F_{mn}} C_{pr} C_{ks}^{-1} =& \\ \frac{1}{3}\exp(b(II_{\boldsymbol{C}} - 3))\big(4b(FC)_{mn} C_{pr} + \delta_{pn} F_{mr} + \delta_{rn} F_{mp}\big) C_{pr} C_{ks}^{-1} =& \\ \frac{1}{3}\exp(b(II_{\boldsymbol{C}} - 3))\big(4b(FC)_{mn} II_{\boldsymbol{C}} C_{ks}^{-1} + C_{nr} F_{mr} C_{ks}^{-1} + C_{np} F_{mp} C_{ks}^{-1}\big).&\end{aligned} \tag{6.A.17}$$

The next differential term is

$$\begin{aligned}\frac{\partial (JPC^{-1})_{ks}}{\partial F_{mn}} =& P\left(\frac{\partial J}{\partial F_{mn}} C_{ks}^{-1} + J\frac{\partial C_{ks}^{-1}}{\partial F_{mn}}\right) \\ =& PJ\left(F_{nm}^{-1} C_{ks}^{-1} - F_{km}^{-1} C_{ns}^{-1} - F_{sm}^{-1} C_{nk}^{-1}\right).\end{aligned} \tag{6.A.18}$$

Lastly,

$$\frac{\partial F_{ik}}{\partial F_{mn}} C_{ks}^{-1} = \delta_{im}\delta_{kn} C_{ks}^{-1} = \delta_{im} C_{ns}^{-1}. \tag{6.A.19}$$

On the above terms, if applicable, the left and right multiplication by F_{ik} and $F_{ln}F_{js}$

must be performed. Thus, the term in Eq. (6.A.16) becomes

$$\exp(b(II_{\boldsymbol{C}}-3))F_{ik}\big(4b(FC)_{mn}C_{ks}+\delta_{kn}F_{ms}+\delta_{sn}F_{mk}\big)F_{ln}F_{js}= \exp(b(II_{\boldsymbol{C}}-3))\big(4bB^2_{ij}B^2_{ml}+B_{il}B_{mj}+B_{im}B_{lj}\big) \tag{6.A.20}$$

The term in Eq. (6.A.17) becomes

$$\frac{1}{3}\exp(b(II_{\boldsymbol{C}}-3))F_{ik}\big(4b(FC)_{mn}II_{\boldsymbol{C}}C^{-1}_{ks}+C_{nr}F_{mr}C^{-1}_{ks}+C_{np}F_{mp}C^{-1}_{ks}\big)F_{ln}F_{js}= \frac{1}{3}\exp(b(II_{\boldsymbol{C}}-3))\big(4bII_{\boldsymbol{C}}B^2_{ml}\delta_{ij}+2B^2_{ml}\delta_{ij}\big). \tag{6.A.21}$$

The term in Eq. (6.A.18) becomes

$$PJF_{iq}\left(F^{-1}_{nm}C^{-1}_{ks}-F^{-1}_{km}C^{-1}_{ns}-F^{-1}_{sm}C^{-1}_{nk}\right)F_{ln}F_{js}= PJ\left(\delta_{ij}\delta_{ml}-\delta_{im}\delta_{jl}-\delta_{il}\delta_{jm}\right). \tag{6.A.22}$$

Finally, the term in Eq. (6.A.19) becomes

$$\delta_{im}C^{-1}_{ns}F_{ln}F_{js}=\delta_{im}\delta_{jl}. \tag{6.A.23}$$

Using the terms computed in Eqs. (6.A.20)–(6.A.23) into Eq. (6.A.15), the fourth order tensor $\boldsymbol{\mathcal{C}}$ becomes

$$\begin{aligned}\mathcal{C}_{ijml}=&\frac{1}{J}\Big\{(i\omega)^{\alpha}\delta\Big[\exp(b(II_{\boldsymbol{C}}-3))\left(4bB^2_{ij}B^2_{ml}+B_{il}B_{mj}+B_{im}B_{lj}\right)-\\ &\frac{1}{3}\exp(b(II_{\boldsymbol{C}}-3))\left(4bII_{\boldsymbol{C}}B^2_{ml}\delta_{ij}+2B^2_{ml}\delta_{ij}\right)\Big]\\ &+JP\left(\delta_{ij}\delta_{ml}-\delta_{im}\delta_{jl}-\delta_{il}\delta_{jm}\right)+JP\delta_{im}\delta_{jl}\Big\}\\ =&\frac{(i\omega)^{\alpha}}{J}\delta\exp(b(II_{\boldsymbol{C}}-3))\Big[4b\left(B^2_{ij}B^2_{ml}-\frac{II_{\boldsymbol{C}}}{3}B^2_{ml}\delta_{ij}\right)+\\ &B_{il}B_{mj}+B_{im}B_{lj}-\frac{2}{3}B^2_{ml}\delta_{ij}\Big]+P\left(\delta_{ij}\delta_{ml}-\delta_{il}\delta_{jm}\right).\end{aligned} \tag{6.A.24}$$

Hence, the real and imaginary stiffness moduli $\boldsymbol{\mathcal{G}}'$ and $\boldsymbol{\mathcal{G}}''$ take the form

$$\begin{aligned}\mathcal{G}'_{ijml}=&\frac{\omega^{\alpha}}{J}\cos\left(\frac{\pi\alpha}{2}\right)\delta\exp(b(II_{\boldsymbol{C}}-3))\Big[4b\left(B^2_{ij}B^2_{ml}-\frac{II_{\boldsymbol{C}}}{3}B^2_{ml}\delta_{ij}\right)+\\ &B_{il}B_{mj}+B_{im}B_{lj}-\frac{2}{3}B^2_{ml}\delta_{ij}\Big]+P\left(\delta_{ij}\delta_{ml}-\delta_{il}\delta_{jm}\right),\\ \mathcal{G}''_{ijml}=&\frac{\omega^{\alpha}}{J}\sin\left(\frac{\pi\alpha}{2}\right)\delta\exp(b(II_{\boldsymbol{C}}-3))\Big[4b\left(B^2_{ij}B^2_{ml}-\frac{II_{\boldsymbol{C}}}{3}B^2_{ml}\delta_{ij}\right)+\\ &B_{il}B_{mj}+B_{im}B_{lj}-\frac{2}{3}B^2_{ml}\delta_{ij}\Big].\end{aligned} \tag{6.A.25}$$

The moduli $\boldsymbol{\mathcal{G}}'$ and $\boldsymbol{\mathcal{G}}''$ are influencing the wave dynamics $\nabla_{\boldsymbol{x}}\boldsymbol{u}_c$, leading to an apparent wave dynamic. Let us consider now the analytic formulation of the contraction $(\boldsymbol{\mathcal{G}}' + i\boldsymbol{\mathcal{G}}'')_{ijml} : (\nabla_{\boldsymbol{x}}\boldsymbol{u}_c)_{ml}$, in order to better understand the moduli defining the *vEXP* tissue model:

$$\boldsymbol{\mathcal{G}}' : \nabla_{\boldsymbol{x}}\boldsymbol{u}_c = \frac{\omega^\alpha}{J}\cos\left(\frac{\pi\alpha}{2}\right)\delta\exp(b(II_{\boldsymbol{C}}-3))\Bigg\{4b(\boldsymbol{B}^2 : \nabla_{\boldsymbol{x}}\boldsymbol{u}_c)\left(\boldsymbol{B}^2 - \frac{II_{\boldsymbol{C}}}{3}\boldsymbol{I}\right) + \boldsymbol{B}\nabla_{\boldsymbol{x}}\boldsymbol{u}_c\boldsymbol{B} + \boldsymbol{B}\nabla_{\boldsymbol{x}}\boldsymbol{u}_c^T\boldsymbol{B} - \frac{2}{3}(\boldsymbol{B}^2 : \nabla_{\boldsymbol{x}}\boldsymbol{u}_c)\boldsymbol{I}\Bigg\} - JP\nabla_{\boldsymbol{x}}\boldsymbol{u}_c^T \tag{6.A.26}$$

and

$$\boldsymbol{\mathcal{G}}'' : \nabla_{\boldsymbol{x}}\boldsymbol{u}_c = \frac{\omega^\alpha}{J}\sin\left(\frac{\pi\alpha}{2}\right)\delta\exp(b(II_{\boldsymbol{C}}-3))\Bigg\{4b(\boldsymbol{B}^2 : \nabla_{\boldsymbol{x}}\boldsymbol{u}_c)\left(\boldsymbol{B}^2 - \frac{II_{\boldsymbol{C}}}{3}\boldsymbol{I}\right) + \boldsymbol{B}\nabla_{\boldsymbol{x}}\boldsymbol{u}_c\boldsymbol{B} + \boldsymbol{B}\nabla_{\boldsymbol{x}}\boldsymbol{u}_c^T\boldsymbol{B} - \frac{2}{3}(\boldsymbol{B}^2 : \nabla_{\boldsymbol{x}}\boldsymbol{u}_c)\boldsymbol{I}\Bigg\}. \tag{6.A.27}$$

Note that the term $\nabla_{\boldsymbol{x}}\boldsymbol{u}_c : \boldsymbol{I} = 0$ was reduced, due to the wave considered being a pure shear wave and having only off-diagonal components.

In the particular case when there exists no macro deformation, *i.e.* $\boldsymbol{F} = \boldsymbol{I}$, it follows that the real scaling modulus retains only the terms

$$\boldsymbol{\mathcal{G}}' : \nabla_{\boldsymbol{x}}\boldsymbol{u}_c = \frac{\omega^\alpha}{J}\cos\left(\frac{\pi\alpha}{2}\right)\delta\cdot\left(\nabla_{\boldsymbol{x}}\boldsymbol{u}_c + \nabla_{\boldsymbol{x}}\boldsymbol{u}_c^T\right), \tag{6.A.28}$$

while the imaginary modulus reduces to

$$\boldsymbol{\mathcal{G}}'' : \nabla_{\boldsymbol{x}}\boldsymbol{u}_c = \frac{\omega^\alpha}{J}\sin\left(\frac{\pi\alpha}{2}\right)\delta\cdot\left(\nabla_{\boldsymbol{x}}\boldsymbol{u}_c + \nabla_{\boldsymbol{x}}\boldsymbol{u}_c^T\right), \tag{6.A.29}$$

which is consistent with linear viscoelasticity.

6.B Registration validation

The deformations employed in this study are large, with compressions reaching even 30%. Thus, the registration method employed in this study (section 6.1.3) was tested on images on which a large deformation was imposed. 2D structures resembling a brain shape were used, which were replicated in order to create a volume. The images were either rich in spatial information, in the form of chequerboard, or just simple masks, which captured only the overall shape change under deformation. These can be seen in Fig. 6.B.1, in both reference and deformed state.

The registration algorithm was used on both chequerboard and mask images. The resulting alignment is presented in Fig. 6.B.1. It is observed that the overall shape was well matched, and the inside features of the chequerboard were also well aligned, with

most discrepancies occurring at the edge of the shape.

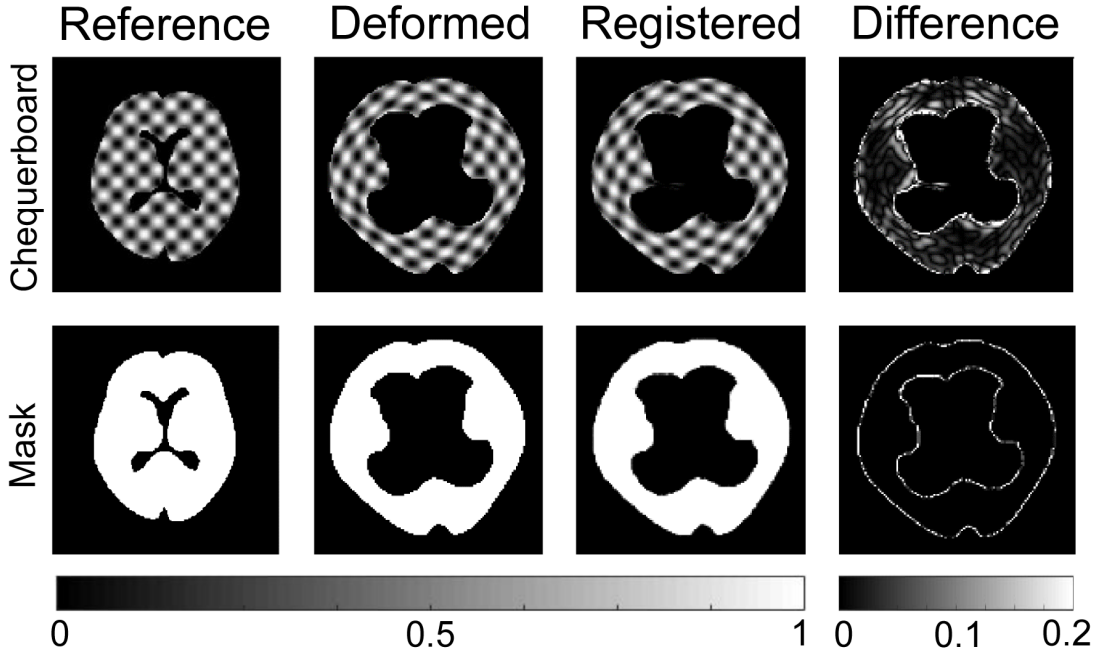

Figure 6.B.1 *Test images for registration; The reference and deformed images are presented in the first two columns. The third column shows the reference image, registered to the deformed state. The last column shows the difference between the deformed state and the registered image.*

The deformed image was originally achieved by applying a field variable deformation on the reference image. This would lead to a deformation gradient as seen in the first column of Fig. 6.B.2. Likewise, the displacements obtained from registering the chequerboard and mask images were used to calculate $\boldsymbol{F}$. Thus, the middle row shows the gradient corresponding to the registration of the chequerboard images, while the third row corresponds to the registration of the mask images. All displacements were mapped onto the space of the deformed image.

It can be seen that the deformation gradient obtained from the chequerboard images is in good agreement with the true deformation gradient, in all components. The diagonal components of $\boldsymbol{F}$ obtained from the mask images are also similar to the ground truth, although some differences are noticeable in F_{22}. Moreover, in the shear directions, F_{12} and F_{21} show larger discrepancies compared to the true deformation gradient. Thus, although the registration handled the image alignment well in both chequerboard and mask image, the highly detailed structure of the chequerboard ensured a more accurate pixel-wise match between the reference and deformed images.

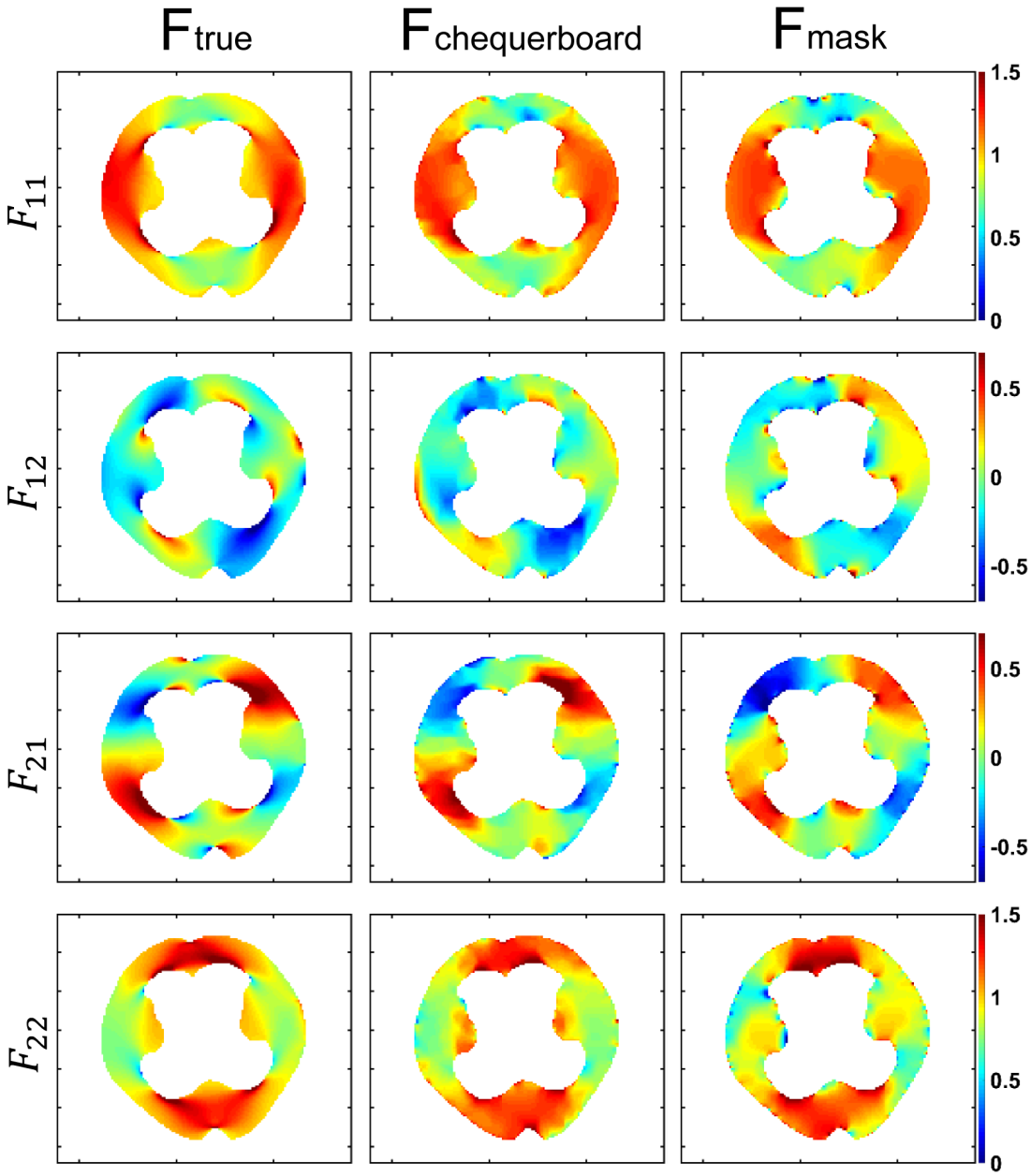

Figure 6.B.2 *Deformation gradient computed from the true applied displacements (first column), displacements obtained from the registration of chequerboard images (second column), or mask images (third column).*

MRE wave propagation was simulated in the deformed structure, by solving a wave problem in $\mathcal{C}$**heart**. A 50 Hz frequency was used. The material was modelled as neo-Hookean, with an intrinsic stiffness of 1.5 kPa. The wave displacements were subsequently employed with the MRE reconstruction methods. Firstly, the UR was used to reconstruct the data. The average stiffness is close to the reference value, being ≈1.44 kPa. However, it can be seen in Fig. 6.B.3 that it shows a heterogeneous pattern, with some areas reaching 2.7 kPa. The quantified standard deviation is 24%. Subsequently, CR was employed with the true deformation gradient. In this case, the

stiffness map became more homogeneous. The quantified average stiffness was 1.44 kPa, but the standard deviation decreased considerably, to only 8%. When using the deformation gradient obtained from the registration of the chequerboard images, the stiffness map was improved compared to the UR. Although the average stiffness was slightly smaller (1.36 kPa), there was less heterogeneity, with a standard deviation of 14.7%. Finally, The deformation metrics obtained from the registration of mask images were also employed with the CR. It can be seen that the stiffness map is very heterogeneous, with a 26% standard deviation, which is even higher than in the case of UR. The average stiffness is 1.34 kPa.

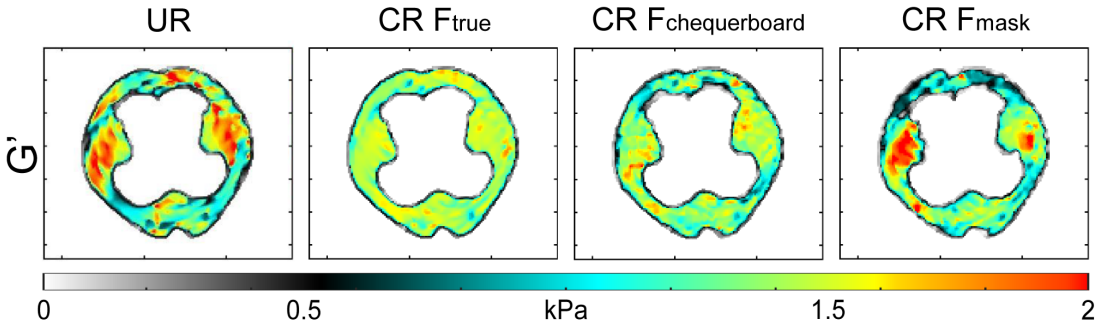

Figure 6.B.3 *Elastography simulated data, reconstructed using UR and CR; for the CR, the deformation gradient was obtained from the true displacements, the chequerboard image registration or the mask image registration. The stiffness map G' is presented in all reconstruction cases. Here, for the CR, the scaling map M was multiplied by the average stiffness parameter of the neo-Hookean model.*

The quantified average stiffness is similar in all reconstruction cases, and within 10% of the intrinsic reference value of 1.5 kPa. However, the heterogeneity of the stiffness map varies greatly. It was seen that employing an accurate deformation gradient leads to an almost uniform stiffness map, whereas a good estimate of $\boldsymbol{F}$, from the chequerboard image registration, significantly improves the homogeneity of the stiffness map. However, an inaccurate deformation gradient leads to a poor estimate of the intrinsic stiffness across the entire map, with a high heterogeneity. Thus it is clear that the quality of the deformation gradient has a great influence on the retrieval of intrinsic stiffness parameters.

7 In vivo MRE liver characterisation

Liver inflammation and fibrosis are progressive pathologies and are staged according to severity. Inflammation is the mechanism through which the liver is responding to an insulting signal, e.g. hepatitis viruses, alcohol consumption, etc., and is defined by cell accumulation at the place of injury. This process is meant to restore the normal function of the liver, which auto-regulates itself once the injurious signal disappears. However, under chronic conditions, progressive fibrosis occurs, resulting in an increased deposition of extracellular collagen matrix (ECM). However, earlier detection and classification of the stage of inflammation and fibrosis can lead to better disease management. This necessitates an accurate diagnosis method. Numerous studies have illustrated a positive correlation between fibrosis severity and MRE stiffness measurements. Nonetheless, inflammation also affects stiffness quantification, possibly leading to an overestimation of the stage of fibrosis.

In this chapter, we present preliminary comparisons between patients with inflammation and fibrosis, and healthy volunteers, using MRE measurements acquired in end-expiration and end-inspiration. The scanning procedure is presented in section 7.1, followed by the description of the data analysis process (section 7.2). The latter revolves around linear viscoelasticity, as accurate deformation metrics between respiratory states could not be obtained. However, section 7.3 discusses the implications of respiratory deformation on MRE measurements, in both healthy volunteers and patients. Final remarks are drawn in section 7.4

7.1 Scanning protocol

Eleven patients (both males and females, aged 37-75 years) agreed to participate in this prospective study. The patients underwent a liver biopsy procedure within 6.5 months of the date of the MRE scan, which provided the METAVIR score of inflammation and fibrosis. The patients had mixed underlying causes of liver disease, related to viral, autoimmune and alcoholic hepatitis, and a non-alcoholic fatty liver. Additionally, 15 healthy volunteers (both males and females, aged 25-32 years) with no known liver disease were recruited to participate in this study. All subjects gave informed consent for participation in this study, which was conducted in agreement with the Declaration

of Helsinki.

The scanning protocol included an anatomical T2-weighted image, consisting of 12 cross-sectional sagittal slices with in-plane pixel dimensions of 0.977×0.977 mm, and a slice thickness of 4 mm. Subsequently, MRE images were acquired using a gradient echo sequence[202] on both a 3T Achieva (TE / TR=4.60 / 67.708 ms) and a Siemens 3T PET-MRI scanner (TE / TR=7.38 / 80.00 ms). Eight slices were acquired, with voxel size being $4 \times 4 \times 4$ mm isotropic. For generating waves in the liver, a vibrating transducer, driven by the rotation of an eccentric mass[216], was placed on the right side of the thorax, above the last rib. The mechanical vibration frequency was set to 48 or 50 Hz, respectively. The MRE scan consisted of four breath-hold acquisitions, for encoding the wave displacements in $\boldsymbol{e}_1$, $\boldsymbol{e}_2$ and $\boldsymbol{e}_3$ directions, and a reference scan. The protocol was repeated for end-expiration and end-inspiration states.

The sagittal plane was chosen because, during respiratory motion, the liver undergoes the least through-slice movement in the left-right direction[111], compared to foot-head (transversal) or anterior-posterior (coronal). Thus, by imaging in the sagittal plane, we ensure that the same liver area is imaged in both expiration and inspiration.

7.2 MRE data analysis

The anatomical T2 weighted images were used to provide detailed quantitative information of the configuration of the liver in expiration and inspiration. The MRE data were reconstructed using the method proposed by Fovargue et al.[61], in both respiratory states. An example of the anatomical image, stiffness map, and wave propagation in the $\boldsymbol{e}_1$, $\boldsymbol{e}_2$ and $\boldsymbol{e}_3$ directions is shown in Fig. 7.2.1 for a healthy volunteer at expiration and inspiration.

Masks were created to delimit the liver in the imaged FOV. Vessels were excluded by applying a threshold on the MRE magnitude image. For the statistical analysis, a ROI was created by eroding the mask by two pixels in each direction. This was done in order to avoid pixels reconstructed from unreliable areas, e.g. vessels or liver margins, where second order derivatives of the displacement field may be inaccurate.

From the acquired data, three out of the eleven patients were excluded due to vessel artefacts affecting the quality of the MRE scan. The details of the remaining eight participants are presented in Table 7.2.1. Out of the 15 healthy volunteers, three were excluded due to misalignment of respiratory states between the four acquisitions employed during an MRE scan.

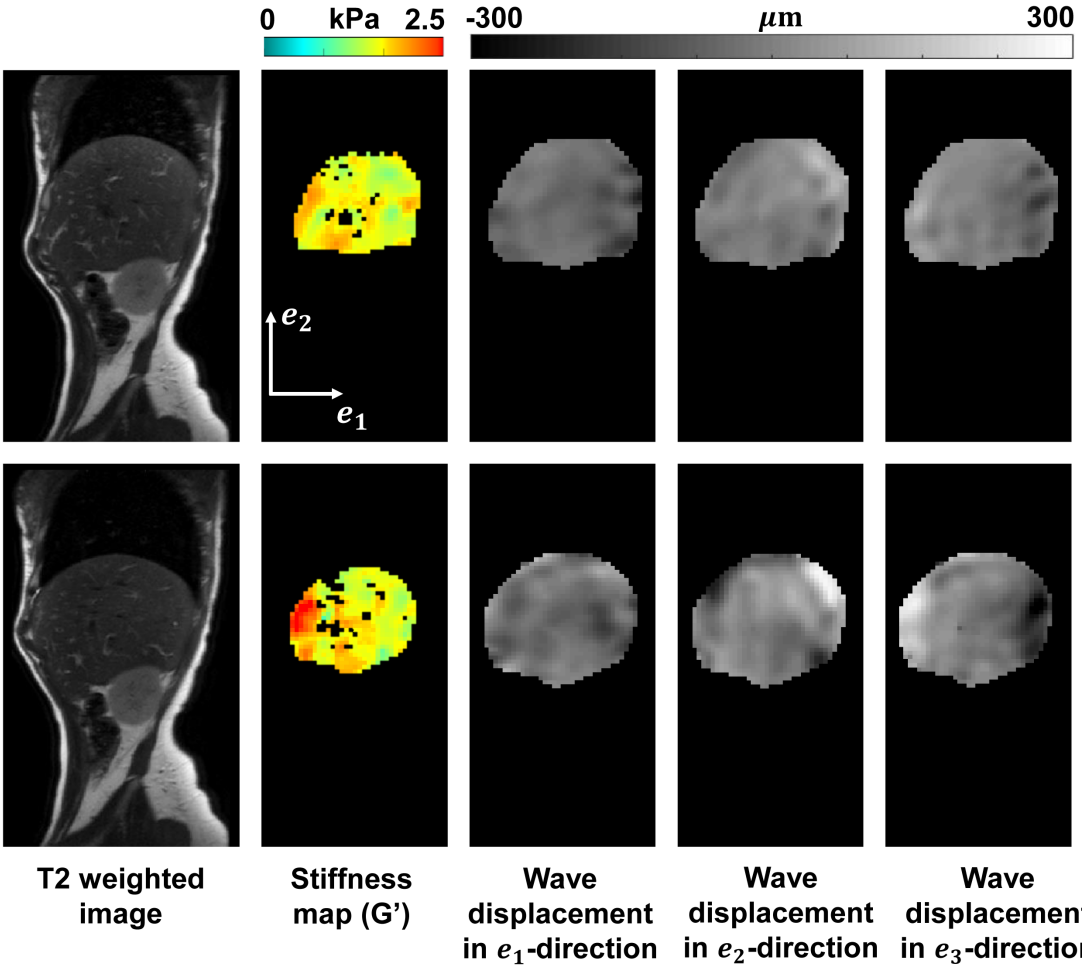

Figure 7.2.1 In vivo *liver images. (First column) The anatomical images show the liver in expiration (top row) and inspiration (bottom row); (Second column) Stiffness maps in expiration and inspiration; Wave displacements are imaged in the* $\boldsymbol{e}_1$ *direction (third column),* $\boldsymbol{e}_2$ *direction (fourth column) and* $\boldsymbol{e}_3$ *direction (fifth column).*

Case	Age	Gender	Interval	Cause	Fibrosis	Inflammation
P1	62	F	5.5	NAFLD	F3	A1
P2	54	M	5.0	AH	F3	NA
P3	54	M	1.0	HBV	F1	A0
P4	73	M	6.4	NASH	F4	A0
P5	49	F	1.0	HBV	F0	A2
P6	50	M	1.5	NASH	F2/3	A3
P7	75	F	3.0	AIH	F0	A0
P8	61	F	3.5	NASH	F4	A1

Table 7.2.1 *Patient age and gender, interval between the date of biopsy and MRE scan, underlying cause of pathology, fibrosis and inflammation scores are reported.*

Relating the *in vivo* liver data to the *vEXP* model (Eq. (5.2.19)), the fractional order

term α was determined based on the ratio of the imaginary and real moduli G'' and G', as in Eq. (6.1.9). This was done considering the end-expiration state to be the undeformed liver state. However, this assumption may not necessarily be accurate. Since deformation could not be accurately quantified, linear viscoelasticity was employed. Results are presented for the stiffness and viscosity maps G' and G''. The δ parameter of the *vEXP* could be related to those by employing Eq. (6.1.10). However, in the absence of deformation quantification, it would not bring additional value to the investigation.

7.3 Results and discussion

Healthy volunteers and patients were scanned using MRE, with measurements being acquired at end-expiration and end-inspiration. In both groups, changes in mean stiffness values of up to 27% are observed. Fig. 7.3.1 shows the average G' and G'' values for patients (P) and healthy volunteers (HV), and no particular trend is identified between expiration and inspiration, as values can either increase or decrease. This emphasises the complex effect of deformation on wave propagation, as two patients who are well separated in expiration state (different stiffness quantification) might look similar in inspiration, or vice-versa.

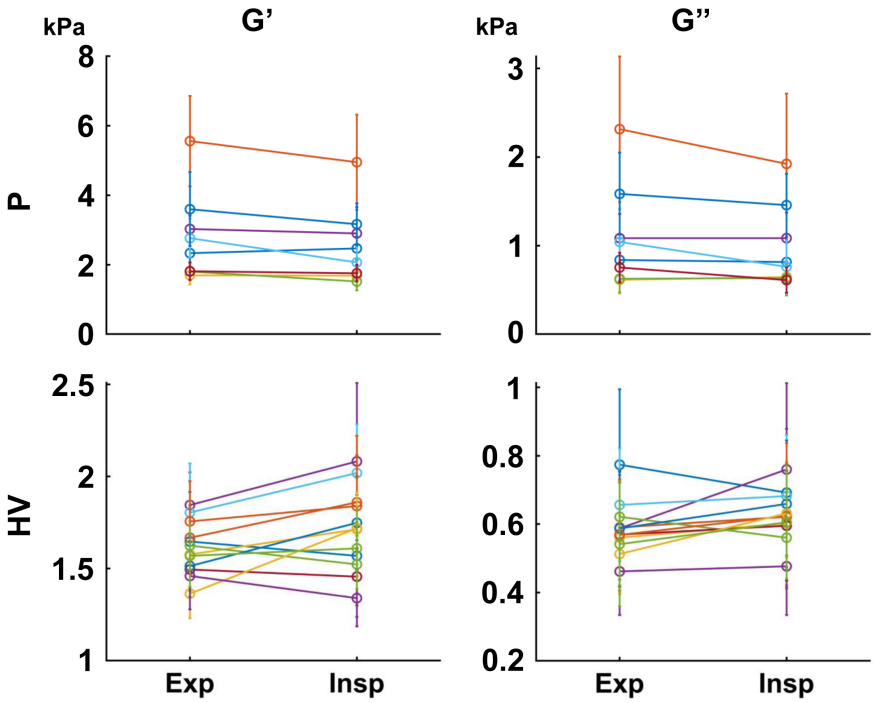

Figure 7.3.1 *Average stiffness and viscosity estimates for patients (top row) and healthy volunteers (bottom row), compared between expiration and inspiration. Error bars represent one standard deviation.*

In order to investigate differences among patients and volunteers, stiffness and viscosity

measures are compared. The patient data are separated in two fibrosis groups, i.e. F0-1 and F2-4, due to insufficient representation within each of the five fibrosis stages. Likewise, inflammation scores are grouped as A0-1 and A2-3. Thus, in expiration, it can be seen in Fig. 7.3.2 that both stiffness and viscosity are considerably lower in patients with incipient fibrosis compared to advanced fibrosis. Average values characterising the healthy volunteers are lower than in patients with F0-1, but there is an overlap between these two groups. At end-inspiration, the differences between the two patient groups remain noticeable. However, there is little distinction between liver stiffness in the healthy versus F0-1 group.

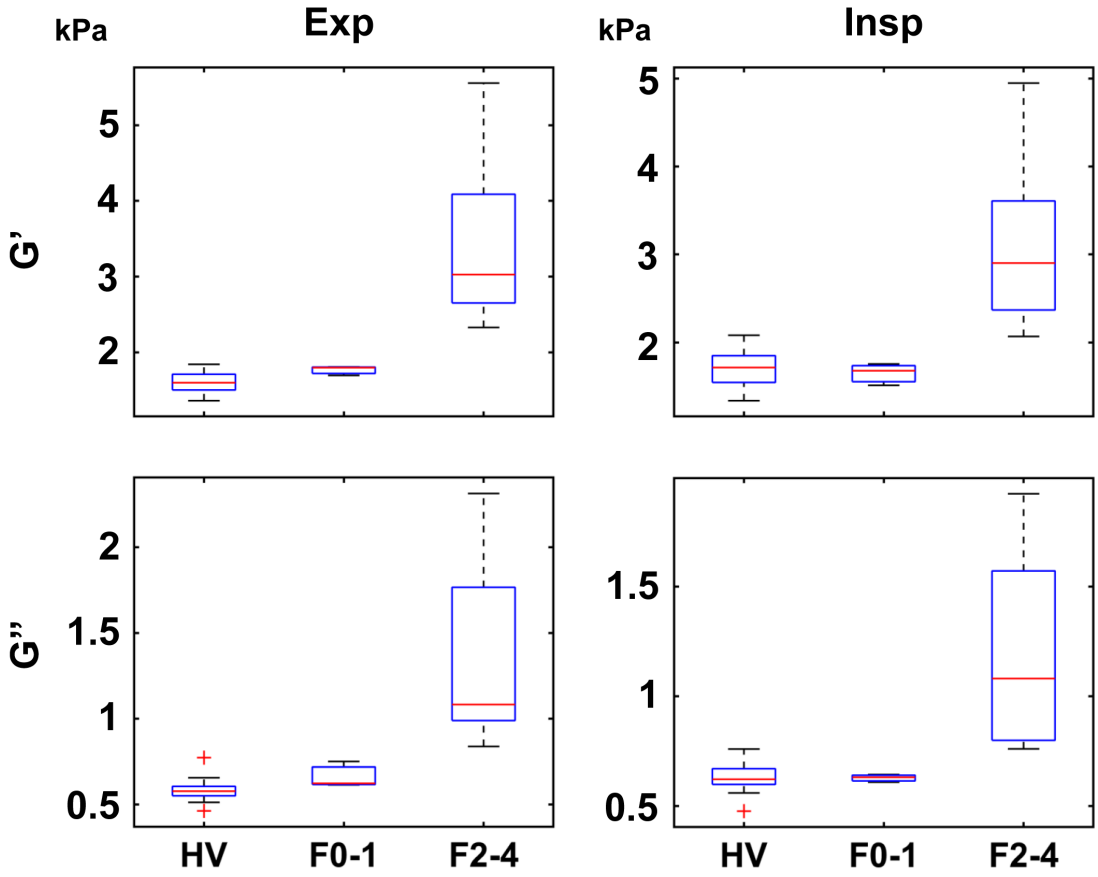

Figure 7.3.2 *Comparison of average liver stiffness (top row) and viscosity (bottom row), at both end-expiration (left column) and end-inspiration (right column), between healthy volunteers, patients with early degrees of fibrosis (F0-1) and patients with advanced fibrosis (F2-4). Red lines show the median, the boxes' edges correspond to the* 25^{th} *and* 75^{th} *percentiles, the black bars show extreme data points and the red crosses indicate outliers.*

When stratifying patients based on their inflammation score, stiffness and viscosity show no clear differences between the two patient groups. Fig. 7.3.3 shows that the difference in stiffness between healthy volunteers and patients is greater than at end-inspiration. These observations are quantified in Table 7.3.1, where average values and standard deviations are presented for healthy volunteers and patients grouped by

fibrosis stage or inflammation grade.

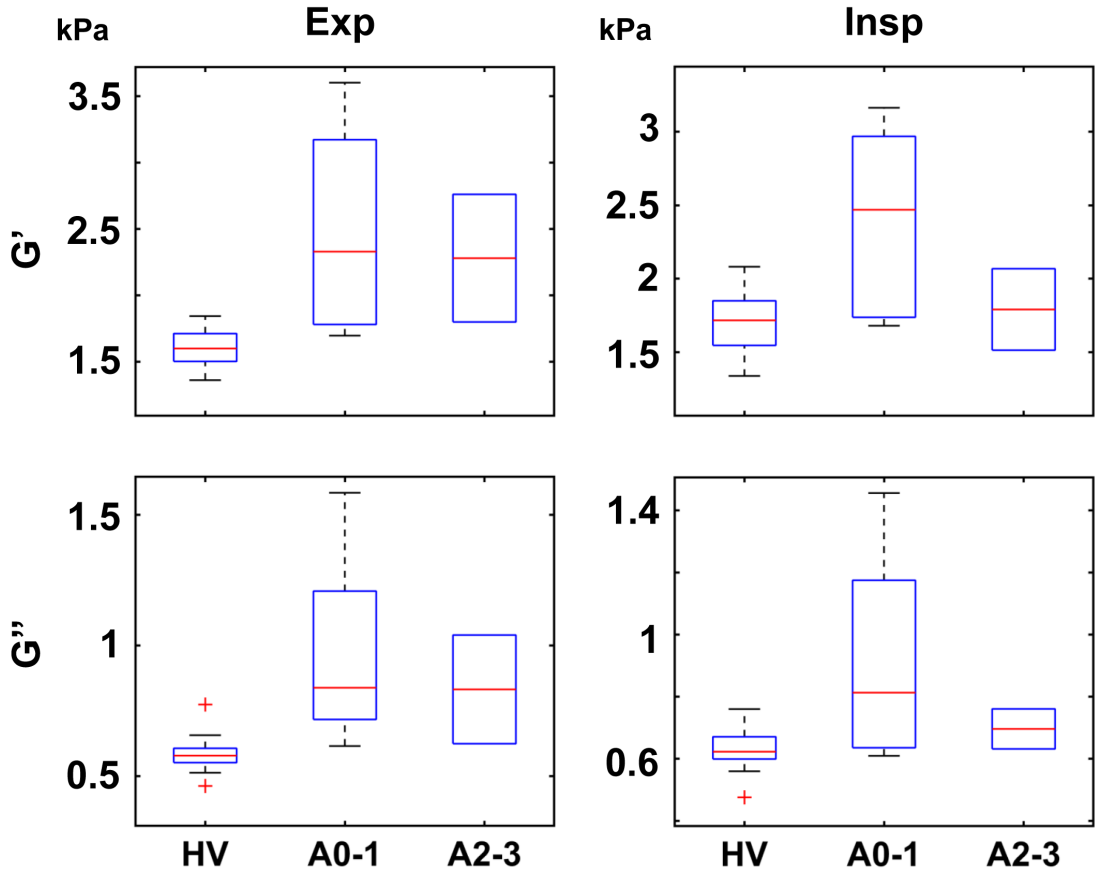

Figure 7.3.3 *Comparison of average liver stiffness (top row) and viscosity (bottom row), at both end-expiration (left column) and end-inspiration (right column), between healthy volunteers, patients with early grades of inflammation (A0-1) and patients with moderate to severe inflammation (A2-3). Red lines show the median, the boxes' edges correspond to the* 25^{th} *and* 75^{th} *percentiles, the black bars show extreme data points and the red crosses indicate outliers.*

Group	G' exp (kPa)	G'' exp (kPa)	G' insp (kPa)	G'' insp (kPa)
HV	1.61 ± 0.14	0.59 ± 0.08	1.71 ± 0.22	0.63 ± 0.07
F0-1	1.77 ± 0.06	0.66 ± 0.08	1.65 ± 0.12	0.63 ± 0.02
F2-4	3.45 ± 1.26	1.37 ± 0.6	3.11 ± 1.11	1.21 ± 0.49
A0-1	2.49 ± 0.81	0.97 ± 0.38	2.39 ± 0.66	0.92 ± 0.35
A2-4	2.28 ± 0.68	0.83 ± 0.29	1.79 ± 0.39	0.70 ± 0.09

Table 7.3.1 *Average stiffness and viscosity values for healthy volunteers and patients; Patient data is grouped according to fibrosis stage (F0-1 and F2-4) and inflammation grade (A0-1 and A2-4). The data is presented for both end-expiration and end-inspiration.*

In order to analyse the effect of inflammation within each fibrosis stage, Fig. 7.3.4 shows a graph of the stiffness versus fibrosis stage, where each point is labelled with the corresponding inflammation grade. In the early fibrosis stages, the effect of inflammation cannot be distinguished. However, in the later stages, inflammation leads to a higher estimated stiffness. Thus, the stiffness measured in a patient with F2 stage and A3 grade is higher than in a patient with F3 stage and A1 grade. Likewise, between two patients with F4 stage, the stiffness is higher in the patient with a higher inflammation grade. The same observations apply for the viscosity measurements. When carrying out the same investigation at end-inspiration, it can be seen that the influence of inflammation grade on fibrosis stiffness measurements diminishes, leading to a more discernible pattern between fibrosis stage and stiffness, but also viscosity measures. However, a larger patient cohort is needed in order to draw a definite conclusion in this sense.

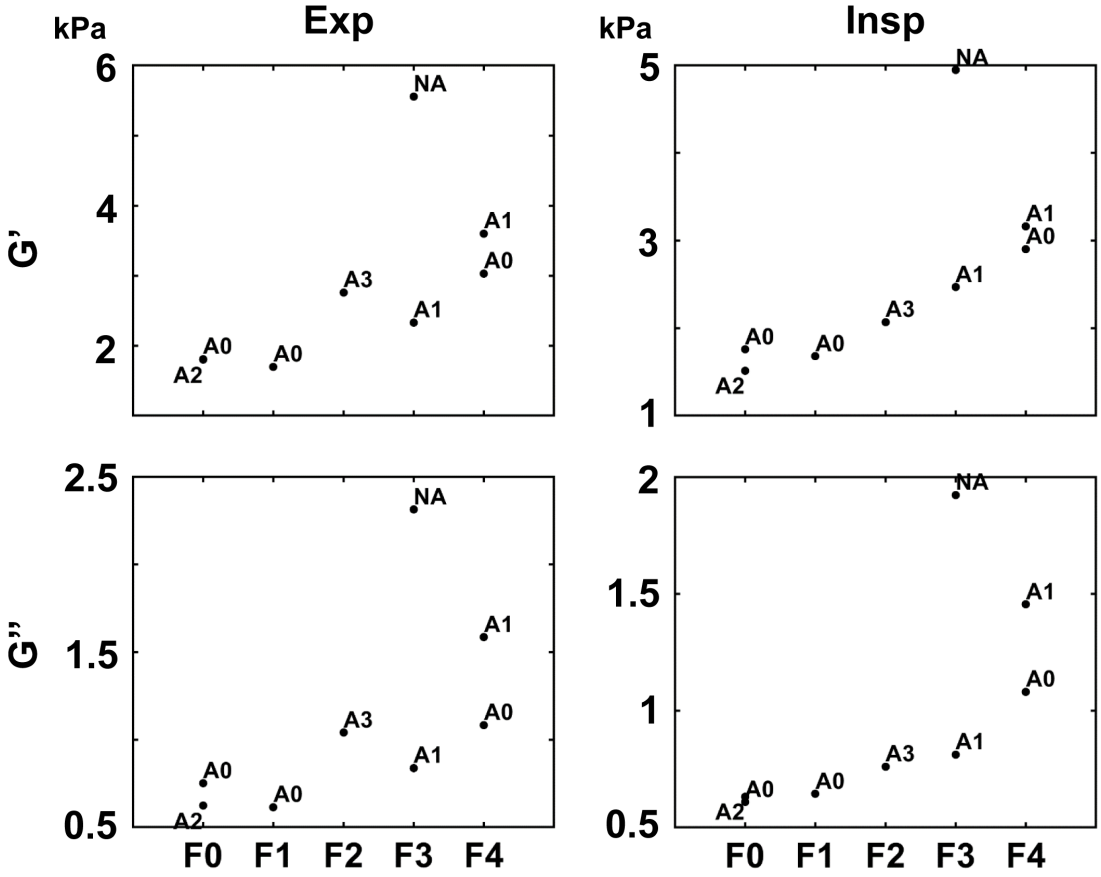

Figure 7.3.4 *Effect of inflammation within each fibrosis stage, shown in stiffness (top row) and viscosity (bottom row), at end-expiration (left column) and end-inspiration (right column).*

The effect of fibrosis within each inflammation grade was also investigated. Thus, Fig. 7.3.5 shows the stiffness versus inflammation grade graph, where each point is labelled with the corresponding fibrosis stage. Generally, a higher fibrosis score led to

a higher quantified stiffness within each inflammation grade, with one exception where the values are close (A0 and F0 or F1, respectively). The same is noticed for viscosity as well. In inspiration, the observations remains valid, with the additional mention that for viscosity, the exception noted above does not apply. This means that fibrosis remains the dominant determinant of MRE stiffness and viscosity measurements, with inflammation additionally altering the quantified values. This is not in accordance with a study by Sinkus et al.[232], who found that viscosity increases with inflammation. Nonetheless, the underlying reasons remain to be investigated. The study mentioned above had insufficient patients with low inflammation grades. Thus, a direct comparison may not be appropriate, as most of the patients in this cohort had low inflammation grades.

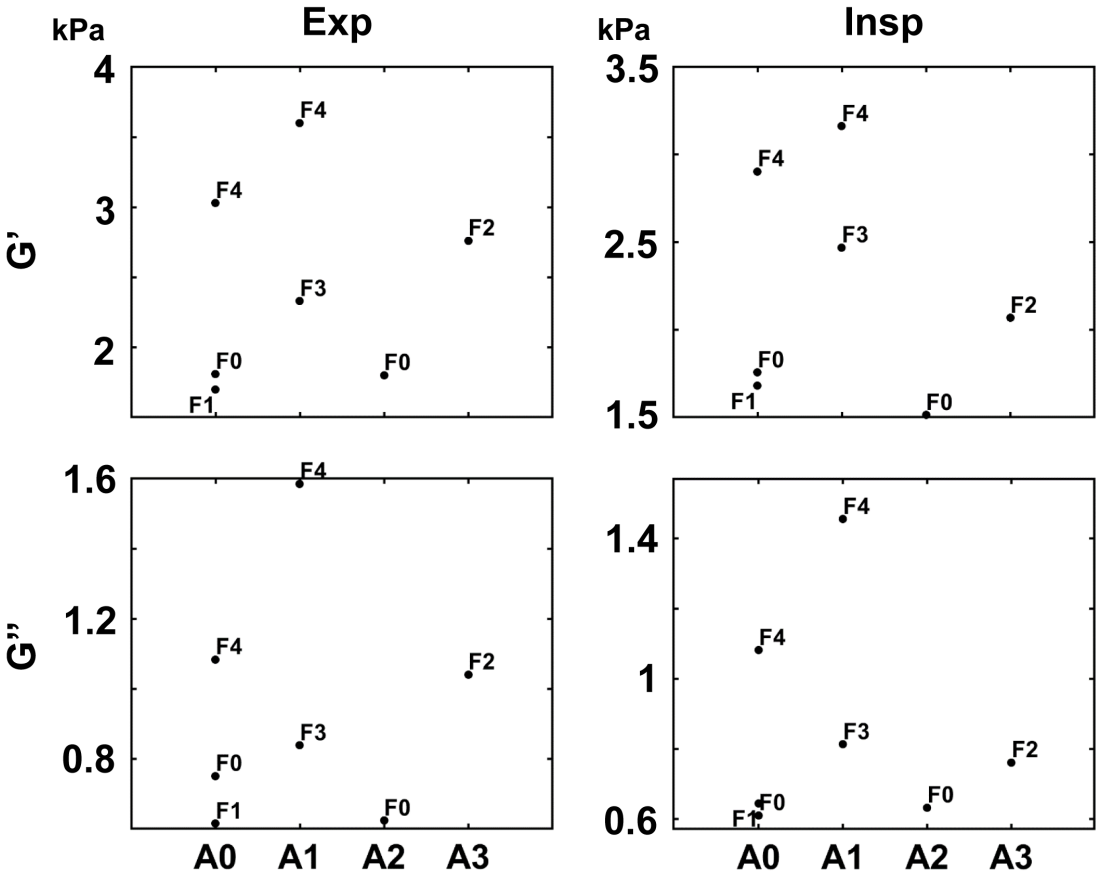

Figure 7.3.5 *Effect of fibrosis within each inflammation grade, shown in stiffness (top row) and viscosity (bottom row), at end-expiration (left column) and end-inspiration (right column).*

Lastly, considering that the *in vivo* liver behaviour is described by the *vEXP* model devised in chapter 5, the fractional order α was investigated for each patient. When grouping the patients by either fibrosis stage or inflammation grade, no definite correlation is noticed. The fractional order parameter α may appear slightly increased in patients with higher degrees of fibrosis, yet more data is needed, as the differences are

very small. Larger cohort studies, like the one performed by Sinkus et al.[232], also did not find a correlation between α and fibrosis or inflammation.

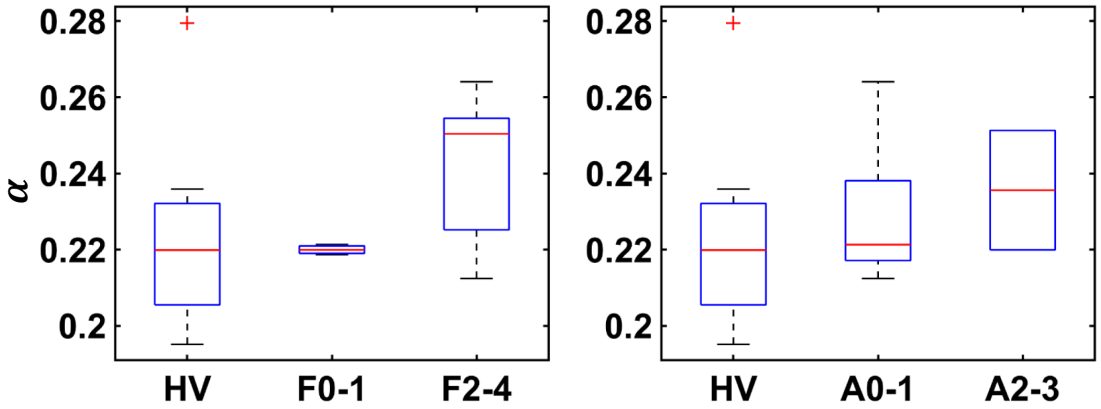

Figure 7.3.6 *Comparison of fractional order α parameter between healthy volunteers and patients grouped by either fibrosis (left) or inflammation (right), at end-expiration. Red lines show the median, the boxes' edges correspond to the 25^{th} and 75^{th} percentiles, the black bars show extreme data points and the red crosses indicate outliers.*

Overall, in this study statistical significance can not be drawn due to the small sample size. Thus, in expiration, F0-1 only differs from F2-4 with a significance value p=0.066 in a two-sample t-test. Statistical significance is not reached in inspiration either (p=0.07). A larger patient cohort is needed to validate the differences observed between fibrosis groups. Nevertheless, it is to be noted that the MRE measurements of healthy volunteers are in accordance with findings from the MRE *ex vivo* liver investigation, as average stiffness and viscosity values were between 1.5-2 kPa and 0.5-0.8 kPa, respectively, in both studies. Additionally, estimated values of α were found to be comparable to those identified in literature and in the *ex vivo* work (chapter 5), with an average of 0.22.

In this study, one limitation to be addressed is the identification of blood vessels. With the current threshold method, areas varying in intensity due to MR body coil positioning might be incorrectly identified as vessel, or conversely, some vessels may remain unidentified. Here, the results presented above employ a ROI where two pixels around each vessel were excluded in each direction. By carrying out the same analysis using a ROI where just the vessels are excluded, but not the area around them, the observed behaviour remains the same. However, in this case statistical significance is reached in differentiating F0-1 from F2-4 in both expiration and inspiration, with p=0.040 and p=0.045, respectively.

Another area to be improved is the quality of the biopsy reports. Here, one case was missing information on the inflammatory activity. Additional consistency between different patients reports, but also a second evaluation of biopsies would have been desirable, for inter-user agreement on the fibrosis and inflammation scores.

The discussion above revolves around particular observations. Richer data is needed in order to draw compelling statistical significance and verify the trends observed. Regardless, the data presented in both healthy volunteers and patients is sufficient to infer that deformation due to respiratory motion affects MRE measurements. This needs to be further investigated, as it is unknown which is the undeformed state of the liver. Although end-expiration is often employed, it may not be the reference state, especially since patients may exhale deeply or shallowly. Likewise, inspiration may be deep, employing the diaphragm, or shallow, only in the chest. Thus, with so much variability in the breathing process, a reference state cannot be identified. However, exploring measurements in different respiratory states might lead to a better characterisation of the liver, which could be further explored to better differentiate inflammation and fibrosis stages. One potential avenue is by employing the framework devised in chapter 4. For this, accurate deformation metrics are needed, as identified in chapter 6. Provided these are available, MRE measurements in two respiratory states (e.g. end-inspiration and end-expiration) may be examined by acknowledging the deformation effects. A liver constitutive model (e.g. *vEXP* presented in chapter 5) could then be parametrised based on two deformation states, potentially leading to a correlation between model parameters and disease.

7.4 Conclusions

The investigation presented in this chapter regarding differences observed in MRE liver measurements between healthy volunteers and distinct patient groups are in agreement with literature findings. Despite the small cohort size, a positive trend is observed between fibrosis stage and stiffness, with inflammation further leading to an increase in stiffness within each fibrosis group. Evidently, a larger patient cohort would have led to more definitive conclusions. However, the impact of deformation due to the respiratory motion was probed in both healthy volunteers and patients, with the latter comprising a larger cohort. Thus, a better understanding of MRE measurements is necessary, especially when trying to differentiate fibrosis stages by establishing cut-off stiffness values. Finally, an idea advanced here is that the bias introduced by large deformations on wave propagation behaviour could actually be utilised effectively. As there is uncertainty regarding the reference, undeformed state of the liver *in vivo*, MRE measurements in two (or more) distinct respiratory states could be employed in determining intrinsic tissue parameters.

8 Conclusions and future directions

The incidence of liver disease has increased over the last 50 years, affecting people of all ages, since underlying causes like hepatitis may even originate in childhood. In the UK, liver disease has been confirmed as the main cause of death in adults aged 35-49 years old. For a better management of patients with liver disease, accurate diagnostic methods are sought. Biopsy is the gold standard in assessing disease severity, but non-invasive alternatives are being investigated. MRE is a promising alternative since numerous studies have shown direct correlations between MRE-derived stiffness estimates and progression of liver disease. However, MRE assumes that the liver is undeformed.

The objective of this thesis was to investigate MRE as an assessment method for liver inflammation and fibrosis in the context of underlying large deformations due to the respiratory motion. As classical MRE relies on linear viscoelasticity, the aim was to introduce nonlinear viscoelasticity in order to account for and suitably interpret these large deformations.

As a first step towards this goal, the theoretical framework for interpreting MRE wave propagation in deformed bodies was established. This was achieved by studying small amplitude wave propagation in such bodies using perturbation theory and Cauchy's equations of motion. The finding was an explicit form of the stiffness moduli (section 2.4), which indicated a dependence on the material model and deformation metrics. Since liver tissue shows strain-rate dependence behaviour and hysteresis, viscoelasticity was examined.

Viscoelasticity poses many complications in constitutive modelling problems, since the response of viscoelastic materials at any point in time depends on their deformation history. Simple viscoelastic models based on spring and dash-pot rheological constituents cannot capture the behaviour of highly nonlinear materials. Moreover, increasing the complexity of models in order to adjust them to capture nonlinear behaviour leads to a large number of material parameters that cannot be determined independently. An alternative is to use models comprising a spring-pot rheological constituent. This is described by fractional order derivatives that can be tuned to exhibit both elasticity and viscosity. To accommodate the use of such models, chapter 3 introduced a Prony series

approximation to the Caputo fractional derivative, which allows for a computationally efficient integration of past deformation history. This simplification opened to door for using fractional viscoelastic models in the description of rheological data over long time scales. Furthermore, it facilitated the integration of constitutive models devised from rheology into MRE.

Building on the theoretical and computational framework for investigating MRE wave propagation in nonlinear viscoelastic materials under deformation, an experiment was designed to support the theory in chapter 4. PVA phantoms were vibrated under a range of compressions, proving that standard MRE analysis is sensitive to underlying deformations. The PVA constitutive behaviour was represented by a fractional viscoelastic polynomial model, which was further integrated into the MRE analysis. As the deformation was known, it was proven that combined knowledge of the material model and deformation can be used to estimate the intrinsic stiffness of the material, thus undoing the deformation bias affecting MRE measurements. One drawback of this study was the impossibility of determining the intrinsic viscosity of the material, due to the PVA exhibiting almost an exclusively elastic behaviour. Nonetheless, this was subsequently addressed in liver tissue, where it was shown that integration of material model and deformation into MRE analysis led to qualitatively comparable results in stiffness and viscosity. This observation points towards the suitability of the pipeline devised in chapter 4 to be employed with MRE measurements of deformed viscoelastic bodies in order to retrieve intrinsic material parameters.

After experimental validation in simple PVA phantoms, the first step in bringing the proposed theoretical framework closer to intrinsic liver characterisation was to determine a liver constitutive model. In chapter 5, a simple viscoelastic model, based on fractional order derivatives, was employed to model behaviour of liver tissue. Rheology data, acquired at a range of combined deformations and frequencies, was examined, leading to a comprehensive testing of liver samples. The modelling approach was based on fractional viscoelastic models utilising polynomial, Ogden and exponential forms. The most significant challenge was posed by the shear strain softening effect, hypothesised to be a consequence of the testing protocol. This was addressed by allowing the linear parameters of the model to be inter-test independent, while ensuring that the nonlinear model parameters could describe the datasets altogether. Hence, this allowed for a good representation of the data using the above mentioned models. The fractional viscoelastic exponential *vEXP* model was preferred due to better accuracy than the polynomial vMR^* model and the use of strain metrics that are cheaper to compute than for the *vOG* model. Despite the fact that a single linear model parameter could not be identified for the entire dataset, the average of the parameters determined for the low shear strain cases matched the linear parameters determined from *ex vivo* MRE testing, indicating the suitability of the model to be used across methodologies (rheology and MRE).

The pipeline developed in chapter 4 was tested on *ex vivo* liver samples in MRE experiments. The theoretical stiffness moduli affecting the wave propagation were determined using the *vEXP* model. Thus, in chapter 6, it was shown that consistency between rheology and MRE could be achieved in undeformed cases. However, deformation led to challenges that could not be resolved in the present work, but were thoroughly investigated. Firstly, unpressurised blood vessels led to a deformation gradient pattern that was too complex to be approximated by metrics derived under the assumption of ideal compression. Thus, registration methods were employed, but their use was hindered either by the quality of the tagged liver data acquired, or by the lack of dense distinctive markers in the anatomical images of the liver samples. Thus, the deformation employed with the devised pipeline yielded suboptimal results in identifying intrinsic stiffness parameters. Indeed, the importance of measuring deformation accurately within the pipeline was demonstrated in an *in silico* test in section 6.B. It was shown that pixel-wise deformation accuracy is needed in order to undo the deformation bias, whereas inexact approximations yield no benefit. Thus, methods that could accurately measure deformation need further investigation. This can benefit the process of retrieving intrinsic stiffness parameters from MRE measurements in a deformed body.

The work in this thesis was performed with the ultimate purpose of investigating, and potentially improving, MRE measurements in patients with inflammation and fibrosis. Thus, chapter 7 presented the clinical picture and drew a preliminary comparison between healthy volunteers and various patient groups. Importantly, it was shown that the deformation of the liver due to the respiratory motion leads to different quantified stiffness and viscosity measures. This is a problem that needs to be addressed in order to obtain repeatable and reliable MRE stiffness estimates. Alternatively, measurements in two deformation states (e.g. the ones employed here, end-expiration and end-inspiration) could be used for a better determination of intrinsic tissue parameters. In both cases, it is necessary to understand and account for the effect of deformation on MRE wave propagation. This could improve the accuracy of the diagnosis from MRE stiffness measurements in patients with liver inflammation and fibrosis.

8.1 Future directions

The work presented in this thesis is interdisciplinary as it integrates aspects of nonlinear mechanics, experimental design and testing, MRE imaging as well as liver constitutive modelling. These areas can be further explored in different directions, some of which are discussed below.

8.1.1 Deformation metrics

The most essential piece needed in order to apply the proposed pipeline into MRE *ex*

vivo and *in vivo* tissue investigation is the optimisation of methods to measure deformation. Medical image registration is a vast field under continuous improvement. Novel registration methods should be thoroughly investigated in order to determine the most suitable algorithms and settings that can be used in order to achieve satisfactory pixel-wise accuracy between deformation states. Alternatively, methods of image acquisition could be devised in order to facilitate image registration, e.g. improving quality of anatomical images.

In this thesis, the *ex vivo* MRE experiment ensured that there is a perfect correspondence between the anatomical and MRE images, in order to simplify the mapping of the deformation metrics from anatomical images onto the MRE domain. If the anatomical data acquired *in vivo* were to be used for quantifying the deformation gradient between respiratory states, then an additional challenge would be to map this onto the MRE images. This is needed because these datasets were acquired separately, and participants cannot always achieve consistency between breath holds. Further variability of breath holds affects MRE analysis as well, since four separate acquisitions are needed in order to reconstruct the data.

8.1.2 Liver constitutive modelling beyond MRE

In this study, fractional viscoelastic liver constitutive models were devised by analysing rheology data at a range of large deformations and frequencies. Among these, the *vEXP* model is preferred for accuracy and computational cost. This could be further investigated in contexts unrelated to MRE. For instance, the transportation industry is concerned with the liver's behaviour at large deformations. A model that can yield good predictions for sudden high impacts can be used for devising safer cars, car seats, seatbelts and airbags.

In the medical research field, other areas that employ liver constitutive modelling are surgery simulation and medical device design. For those, an accurate response of the liver to mechanical stimuli involving cutting, puncturing and pressing is needed. By employing a nonlinear viscoelastic liver model, realistic tissue response to the above stimuli could be gauged.

8.1.3 MRE beyond liver tissue investigation

In this thesis, the impact of deformation on wave propagation was investigated for purposes related to liver deformation due to respiration. However, much of this work is applicable in other tissues. For example, the framework developed here could also be applied in breast MRE. During the MRE scan, the breast is fixed between two plates, which can lead to tissue compression. This induces a deformation bias that is variable between patients, thus complicating inter-subject comparisons. With a good understanding of the effect of deformation on wave propagation, not only could the bias

be undone, but the deformation could be used to lead to a more apparent distinction of healthy and diseased tissue. As the breast is more accessible than the liver, the deformations employed can be better controlled and thus even designed to aid MRE assessment of the breast.

Another direction in which the work presented in this thesis could be further developed is cardiac MRE. This is a particularly challenging area, as the heart is anisotropic, has dynamic stiffness and is subjected to large cyclic deformations[77,132]. The framework presented in this study could be adapted for anisotropic materials and further employed in undoing the deformation bias in the heart arising from the cardiac cycle. This would constitute just one step in advancing MRE characterisation of the heart, as other challenges (e.g. accurate data reconstruction in thin walls) remain to be addressed.

Overall, this thesis comprises elements with a broad applicability within and beyond MRE. Proposing an alternative MRE analysis method and a novel liver constitutive model, it has the potential to improve performance of MRE as a diagnosis tool for liver inflammation and fibrosis.

Bibliography

[1] Sherif R Z Abdel-misih and Mark Bloomston. "Liver Anatomy". In: *Surg. Clin. NA* 90.4 (2010), pp. 643–653.

[2] Laurence Annet, Frank Peeters, Jorge Abarca-Quinones, Isabelle Leclercq, Pierre Moulin, and Bernard E. Van Beers. "Assessment of diffusion-weighted MR imaging in liver fibrosis". In: *J. Magn. Reson. Imaging* 25.1 (2007), pp. 122–128.

[3] Kristi S. Anseth, Christopher N. Bowman, and Lisa Brannon-Peppas. "Mechanical properties of hydrogels and their experimental determination". In: *Biomaterials* 17.17 (1996), pp. 1647–1657.

[4] Kristy B Arbogast, Kirk L Thibault, B Scott Pinheiro, Karen I Wineyt, and Susan S Margulies. "A high-frequency shear device for testing soft biological tissues". In: *J. Bmnechanics* 30.7 (1997), pp. 159–757.

[5] Michael J P Arthur. "Reversibility of liver fibrosis and cirrhosis following treatment for hepatitis C". In: *Gastroenterology* 122.5 (2002), pp. 1525–1528.

[6] Patrick Asbach, Dieter Klatt, Uwe Hamhaber, Jürgen Braun, Rajan Somasundaram, Bernd Hamm, and Ingolf Sack. "Assessment of liver viscoelasticity using multifrequency MR elastography". In: *Magn. Reson. Med.* 60.2 (2008), pp. 373–379.

[7] L. Asner, M. Hadjicharalambous, R. Chabiniok, D. Peressutti, E. Sammut, J. Wong, G. Carr-White, R. Razavi, A. P. King, N. Smith, J. Lee, and D. Nordsletten. "Patient-specific modeling for left ventricular mechanics using data-driven boundary energies". In: *Comput. Methods Appl. Mech. Eng.* 314 (2017), pp. 269–295.

[8] Andrea Baiocchini, Claudia Montaldo, Alice Conigliaro, Alessio Grimaldi, Virginia Correani, Francesco Mura, Fabiola Ciccosanti, Nicolina Rotiroti, Alessia Brenna, Marzia Montalbano, Gianpiero D'Offizi, Maria Rosaria Capobianchi, Riccardo Alessandro, Mauro Piacentini, Maria Eugenia Schininà, Bruno Maras, Franca Del Nonno, Marco Tripodi, and Carmine Mancone. "Extracellular matrix molecular remodeling in human liver fibrosis evolution". In: *PLoS One* 11.3 (2016), e0151736.

[9] Rajarshi Banerjee, Michael Pavlides, Elizabeth M. Tunnicliffe, Stefan K. Piechnik, Nikita Sarania, Rachel Philips, Jane D. Collier, Jonathan C. Booth, Jurgen E. Schneider, Lai Mun Wang, David W. Delaney, Ken A. Fleming, Matthew D. Robson, Eleanor Barnes, and Stefan Neubauer. "Multiparametric magnetic resonance for the non-invasive diagnosis of liver disease". In: *J. Hepatol.* 60.1 (2014), pp. 69–77.

[10] Harvey Thomas Banks, Shuhua Hu, and Zackary R. Kenz. "A brief review of elasticity and viscoelasticity for solids". In: *Adv. Appl. Math. Mech.* 3.1 (2011), pp. 1–51.

[11] P Bedossa and T Poynard. "An algorithm for the grading of activity in chronic hepatitis C. The METAVIR Cooperative Study Group." In: *Hepatology* 24.2 (1996), pp. 289–93.

[12] P. Bedossa. "Intraobserver and Interobserver Variations in Liver Biopsy Interpretation in Patients with Chronic Hepatitis C". In: *Hepatology* 20.1 (1994), pp. 15–20.

[13] B. Bernstein, E. A. Kearsley, and L. J. Zapas. "A Study of Stress Relaxation with Finite Strain". In: *Trans. Soc. Rheol.* 7.1 (1963), pp. 391–410.

[14] Annalisa Berzigotti and Laurent Castera. "Update on ultrasound imaging of liver fibrosis". In: *J. Hepatol.* 59.1 (2013), pp. 180–182.

[15] L E Bilston, Z Liu, and N Phan-Thien. "Large strain behaviour of brain tissue in shear: some experimental data and differential constitutive model." In: *Biorheology* 38.4 (2001), pp. 335–45.

[16] Carolin Birk and Chongmin Song. "An improved non-classical method for the solution of fractional differential equations". In: *Computational Mechanics* 46.5 (2010), pp. 721–734.

[17] Anna M Birzle and Wolfgang A Wall. "A viscoelastic nonlinear compressible material model of lung parenchyma–Experiments and numerical identification". In: *Journal of the mechanical behavior of biomedical materials* 94 (2019), pp. 164–175.

[18] Susanne Bonekamp, Ihab Kamel, Steven Solga, and Jeanne Clark. "Can imaging modalities diagnose and stage hepatic fibrosis and cirrhosis accurately?" In: *J. Hepatol.* 50.1 (2009), pp. 17–35.

[19] Javier Bonet and Richard D Wood. *Nonlinear Continuum Mechanics for Finite Element Analysis*. 2008.

[20] Adriaan van den Bos. "Appendix C: Positive Semidefinite and Positive Definite Matrices". In: *Param. Estim. Sci. Eng.* Hoboken, NJ, USA: John Wiley & Sons, Inc., 2007, pp. 259–263.

[21] Yvan Boulanger, Mourad Amara, Luigi Lepanto, Gilles Beaudoin, Bich N Nguyen, Guy Allaire, Marc Poliquin, and Viviane Nicolet. "Diffusion-weighted MR imaging of the liver of hepatitis C patients". In: *NMR Biomed.* 16.3 (2003), pp. 132–136.

[22] Norman F. Boyd, Qing Li, Olga Melnichouk, Ella Huszti, Lisa J. Martin, Anoma Gunasekara, Gord Mawdsley, Martin J. Yaffe, and Salomon Minkin. "Evidence that breast tissue stiffness is associated with risk of breast cancer". In: *PLoS One* 9.7 (2014). Ed. by Judy R. Rees, e100937.

[23] Franco Brezzi and Richard S Falk. "Stability of higher-order Hood–Taylor methods". In: *SIAM Journal on Numerical Analysis* 28.3 (1991), pp. 581–590.

[24] British Liver Trust. URL: `http://www.britishlivertrust.org.uk/about-us/media-centre/facts-about-liver-disease/` (visited on 01/09/2019).

[25] British Liver Trust. URL: `http://www.britishlivertrust.org.uk/liver-information/` (visited on 01/09/2019).

[26] Elizabeth M. Brunt, Vincent W.-S. Wong, Valerio Nobili, Christopher P. Day, Silvia Sookoian, Jacquelyn J. Maher, Elisabetta Bugianesi, Claude B. Sirlin, Brent A. Neuschwander-Tetri, and Mary E. Rinella. "Nonalcoholic fatty liver disease". In: *Nat. Rev. Dis. Prim.* 1.1 (2015), p. 15080.

[27] S Budday, Gerhard Sommer, J Haybaeck, P Steinmann, GA Holzapfel, and Ellen Kuhl. "Rheological characterization of human brain tissue". In: *Acta biomaterialia* 60 (2017), pp. 315–329.

[28] S Budday, Gerhard Sommer, GA Holzapfel, Paul Steinmann, and Ellen Kuhl. "Viscoelastic parameter identification of human brain tissue". In: *Journal of the mechanical behavior of biomedical materials* 74 (2017), pp. 463–476.

[29] Adela Capilnasiu, Lynne Bilston, Ralph Sinkus, and David Nordsletten. "Nonlinear viscoelastic constitutive model for bovine liver tissue". In: *Submitted to Biomech. Model. Mechanobiol.* (2019).

[30] Adela Capilnasiu, Myrianthi Hadjicharalambous, Daniel Fovargue, Dharmesh Patel, Ondrej Holub, Lynne Bilston, Hazel Screen, Ralph Sinkus, and David Nordsletten. "Magnetic resonance elastography in nonlinear viscoelastic materials under load". In: *Biomech. Model. Mechanobiol.* 18.1 (2019), pp. 111–135.

[31] M. Caputo. "Linear Models of Dissipation whose Q is almost Frequency Independent–II". In: *Geophys. J. Int.* 13.5 (1967), pp. 529–539.

[32] Emily Carey and William D Carey. "Noninvasive tests for liver disease, fibrosis, and cirrhosis: Is liver biopsy obsolete?" In: *Cleve. Clin. J. Med.* 77 (2010), pp. 519–527.

[33] Christophe Cassinotto, Matthieu Feldis, Julien Vergniol, Amaury Mouries, Hubert Cochet, Bruno Lapuyade, Arnaud Hocquelet, Etienne Juanola, Juliette Foucher, François Laurent, and Victor De Ledinghen. "MR relaxometry in chronic liver diseases: Comparison of T1 mapping, T2 mapping, and diffusion-weighted imaging for assessing cirrhosis diagnosis and severity". In: *Eur. J. Radiol.* 84.8 (2015), pp. 1459–1465.

[34] G Casula, JM Carcione, et al. "Generalized mechanical model analogies of linear viscoelastic behaviour". In: *Bollettino di geofisica teorica ed applicata* (1992).

[35] Radomir Chabiniok, Vicky Y. Wang, Myrianthi Hadjicharalambous, Liya Asner, Jack Lee, Maxime Sermesant, Ellen Kuhl, Alistair A. Young, Philippe Moireau, Martyn P. Nash, Dominique Chapelle, and David A. Nordsletten. "Multiphysics and multiscale modelling, data–model fusion and integration of organ physiology in the clinic: ventricular cardiac mechanics". In: *Interface Focus* 6.2 (Feb. 2016), p. 20150083. DOI: `10.1098/rsfs.2015.0083`.

[36] Simon Chatelin, Jennifer Oudry, Nicolas Périchon, Laurent Sandrin, Pierre Allemann, Luc Soler, and Rémy Willinger. "In vivo liver tissue mechanical properties by transient elastography: Comparison with dynamic mechanical analysis". In: *Biorheology* 48.2 (2011), pp. 75–88.

[37] Kyu Jin Choi, Jong Keon Jang, Seung Soo Lee, Yu Sub Sung, Woo Hyun Shim, Ho Sung Kim, Jessica Yun, Jin Young Choi, Yedaun Lee, Bo Kyeong Kang, Jin Hee Kim, So Yeon Kim, and Eun Sil Yu. "Development and validation of a deep learning system for staging liver fibrosis by using contrast agent–enhanced CT images in the liver". In: *Radiology* 289.3 (2018), pp. 688–697.

[38] RM Christensen. "A nonlinear theory of viscoelasticity for application to elastomers". In: *Journal of Applied Mechanics* 47.4 (1980), pp. 762–768.

[39] Cheekong Chui, E. Kobayashi, X. Chen, T. Hisada, and I. Sakuma. "Combined compression and elongation experiments and non-linear modelling of liver tissue for surgical simulation". In: *Med. Biol. Eng. Comput.* 42.6 (2004), pp. 787–798.

[40] E C Clarke, S Cheng, M Green, R Sinkus, and L E Bilston. "Using static preload with magnetic resonance elastography to estimate large strain viscoelastic properties of bovine liver". In: *J. Biomech.* 44.13 (2011), pp. 2461–2465.

[41] Julien Clin, Carl Eric Aubin, Stefan Parent, Archana Sangole, and Hubert Labelle. "Comparison of the biomechanical 3D efficiency of different brace designs for the treatment of scoliosis using a finite element model". In: *Eur. Spine J.* 19.7 (2010), pp. 1169–1178.

[42] Bernard D Coleman and Walter Noll. "Foundations of linear viscoelasticity". In: *Reviews of modern physics* 33.2 (1961), p. 239.

[43] Luciana Costa-Silva, Silvia Marinho Ferolla, Agnaldo Soares Lima, Paula Vieira Teixeira Vidigal, and Teresa Cristina de Abreu Ferrari. "MR elastography is effective for the non-invasive evaluation of fibrosis and necroinflammatory activity in patients with nonalcoholic fatty liver disease". In: *Eur. J. Radiol.* 98 (2018), pp. 82–89.

[44] Mathieu Couade, Mathieu Pernot, Emmanuel Messas, Alain Bel, Maguette Ba, Albert Hagege, Mathias Fink, and Mickael Tanter. "In Vivo quantitative mapping of myocardial stiffening and transmural anisotropy during the cardiac cycle". In: *IEEE Trans. Med. Imaging* 30.2 (2011), pp. 295–305.

[45] C Couinaud. "Liver lobes and segments: notes on the anatomical architecture and surgery of the liver." In: *Presse Med.* 62.33 (1954), pp. 709–12.

[46] Mehdi Dalir and Majid Bashour. "Applications of fractional calculus". In: *Applied Mathematical Sciences* 4.21 (2010), pp. 1021–1032.

[47] Lakshmi Prasad Dasi, Jane Grande-Allen, Karyn Kunzelman, and Ellen Kuhl. "The pursuit of engineering the ideal heart valve replacement or repair: a special issue of the annals of biomedical engineering". In: *Annals of biomedical engineering* 45.2 (2017), pp. 307–309.

[48] Maya De Buhan and Pascal Frey. "A generalized model of non-linear viscoelasticity: numerical issues and applications". In: *International Journal for Numerical Methods in Engineering* 86.13 (2011), pp. 1544–1557.

[49] Deepti Dhall, Stacey A. Kim, Christopher Mc Phaul, Evan P. Kransdorf, Jon A. Kobashigawa, Vinay Sundaram, James Mirocha, and Maha Guindi. "Heterogeneity of Fibrosis in Liver Biopsies of Patients With Heart Failure Undergoing Heart Transplant Evaluation". In: *Am. J. Surg. Pathol.* 42.12 (2018), pp. 1617–1624.

[50] K Diethelm. "Generalized compound quadrature formulae for finite-part integrals". In: *IMA Journal of Numerical Analysis* 17.3 (July 1997), pp. 479–493. DOI: 10.1093/imanum/17.3.479.

[51] K. Diethelm, N.J. Ford, A.D. Freed, and Yu. Luchko. "Algorithms for the fractional calculus: A selection of numerical methods". In: *Computer Methods in Applied Mechanics and Engineering* 194.6-8 (Feb. 2005), pp. 743–773. DOI: 10.1016/j.cma.2004.06.006.

[52] Kai Diethelm. "An Improvement of a Nonclassical Numerical Method for the Computation of Fractional Derivatives". In: *Journal of Vibration and Acoustics* 131.1 (2009), p. 014502. DOI: 10.1115/1.2981167.

[53] Kai Diethelm. "An investigation of some nonclassical methods for the numerical approximation of Caputo-type fractional derivatives". In: *Numerical Algorithms* 47.4 (Mar. 2008), pp. 361–390. DOI: 10.1007/s11075-008-9193-8.

[54] Yangkun Du, Chaofeng Lü, Weiqiu Chen, and Michel Destrade. "Modified multiplicative decomposition model for tissue growth: Beyond the initial stress-free state". In: *J. Mech. Phys. Solids* 118 (2018), pp. 133–151.

[55] Michael G. Dunn and Frederick H. Silver. "Viscoelastic Behavior of Human Connective Tissues: Relative Contribution of Viscous and Elastic Components". In: *Connective Tissue Research* 12.1 (Jan. 1983), pp. 59–70. DOI: 10.3109/03008208309005612.

[56] T. Elgeti, J. Rump, U. Hamhaber, S. Papazoglou, B. Hamm, J. Braun, and I. Sack. "Cardiac magnetic resonance elastography. Initial results". In: *Invest Radiol* 43.11 (2008), pp. 762–772.

[57] Thomas Elgeti and Ingolf Sack. *Magnetic Resonance Elastography of the Heart*. 2014.

[58] Giovanna Ferraioli, Carmine Tinelli, Barbara Dal Bello, Mabel Zicchetti, Gaetano Filice, and Carlo Filice. "Accuracy of real-time shear wave elastography for assessing liver fibrosis in chronic hepatitis C: A pilot study". In: *Hepatology* 56.6 (2012), pp. 2125–2133.

[59] L Ferrero-Miliani, O H Nielsen, P S Andersen, and S E Girardin. *Chronic inflammation: Importance of NOD2 and NALP3 in interleukin-1β generation*. 2007.

[60] Carmen Fierbinteanu-Braticevici, Dan Andronescu, Radu Usvat, Dragos Cretoiu, Cristian Baicus, and Gabriela Marinoschi. "Acoustic radiation force imaging sonoelastography for noninvasive staging of liver fibrosis." In: *World J. Gastroenterol.* 15.44 (2009), pp. 5525–32.

[61] Daniel Fovargue, Sebastian Kozerke, Ralph Sinkus, and David Nordsletten. "Robust MR elastography stiffness quantification using a localized divergence free finite element reconstruction". In: *Med. Image Anal.* 44 (2018), pp. 126–142.

[62] Daniel Fovargue, David Nordsletten, and Ralph Sinkus. "Stiffness reconstruction methods for MR elastography". In: *NMR Biomed.* (2018).

[63] A. D. Freed and K. Diethelm. "Fractional Calculus in Biomechanics: A 3D Viscoelastic Model Using Regularized Fractional Derivative Kernels with Application to the Human Calcaneal Fat Pad". In: *Biomechanics and Modeling in Mechanobiology* 5.4 (Mar. 2006), pp. 203–215. DOI: 10.1007/s10237-005-0011-0.

[64] S L Friedman, F J Roll, J Boyles, and D M Bissell. "Hepatic lipocytes: the principal collagen-producing cells of normal rat liver." In: *Proc. Natl. Acad. Sci. U. S. A.* 82.24 (1985), pp. 8681–5.

[65] Scott L Friedman. "Liver fibrosis – from bench to bedside". In: *J.Hepatol.* 38 Suppl 1 (2003), S38–S53.

[66] Y C Fung. "Elasticity of soft tissues in simple elongation." In: *Am. J. Physiol.* 213.6 (1967), pp. 1532–1544.

[67] Yuan-Cheng Fung. *Biomechanics*. Springer New York, 1993. DOI: 10.1007/978-1-4757-2257-4.

[68] Thiranja P Babarenda Gamage, Vijayaraghavan Rajagopal, Matthias Ehrgott, Martyn P. Nash, and Poul M F Nielsen. "Identification of mechanical properties of heterogeneous soft bodies using gravity loading". In: *Int. J. Numer. Method. Biomed. Eng.* 27.3 (2011), pp. 391–407.

[69] Guang-hua Gao, Zhi-zhong Sun, and Ya-nan Zhang. "A finite difference scheme for fractional sub-diffusion equations on an unbounded domain using artificial boundary conditions". In: *Journal of Computational Physics* 231.7 (Apr. 2012), pp. 2865–2879. DOI: 10.1016/j.jcp.2011.12.028.

[70] Zhan Gao, Kevin Lister, and Jaydev P. Desai. "Constitutive modeling of liver tissue: Experiment and theory". In: *Ann. Biomed. Eng.* 38.2 (2010), pp. 505–516.

[71] Philippe Garteiser, Ramin S. Sahebjavaher, Leon C. Ter Beek, Septimiu Salcudean, Valérie Vilgrain, Bernard E. Van Beers, and Ralph Sinkus. "Rapid acquisition of multifrequency, multislice and multidirectional MR elastography data with a fractionally encoded gradient echo sequence". In: *NMR Biomed.* 26.10 (2013), pp. 1326–1335.

[72] T Christian Gasser, Martin Auer, F Labruto, J Swedenborg, and J Roy. "Biomechanical rupture risk assessment of abdominal aortic aneurysms: model complexity versus predictability of finite element simulations". In: *European Journal of Vascular and Endovascular Surgery* 40.2 (2010), pp. 176–185.

[73] T Christian Gasser, A Nchimi, J Swedenborg, J Roy, N Sakalihasan, D Böckler, and Alexander Hyhlik-Dürr. "A novel strategy to translate the biomechanical rupture risk of abdominal aortic aneurysms to their equivalent diameter risk: method and retrospective validation". In: *European Journal of Vascular and Endovascular Surgery* 47.3 (2014), pp. 288–295.

[74] T Christian Gasser, Ray W Ogden, and Gerhard A Holzapfel. "Hyperelastic modelling of arterial layers with distributed collagen fibre orientations". In: *J. R. Soc. Interface* 3.6 (2006), pp. 15–35.

[75] J.-L. Gennisson, M. Rénier, S. Catheline, C. Barrière, J. Bercoff, M. Tanter, and M. Fink. "Acoustoelasticity in soft solids: Assessment of the nonlinear shear modulus with the acoustic radiation force". In: *J. Acoust. Soc. Am.* 122.6 (2007), pp. 3211–3219.

[76] Edoardo Giannini, Domenico Risso, Federica Botta, Bruno Chiarbonello, Alberto Fasoli, Federica Malfatti, Paola Romagnoli, Emanuela Testa, Paola Ceppa, and Roberto Testa. "Validity and clinical utility of the aspartate aminotransferase-alanine aminotransferase ratio in assessing disease severity and prognosis in patients with hepatitis C virus-related chronic liver disease". In: *Arch. Intern. Med.* 163.2 (2003), pp. 218–224.

[77] Kevin J. Glaser, Armando Manduca, and Richard L. Ehman. "Review of MR elastography applications and recent developments". In: *J. Magn. Reson. Imaging* 36.4 (2012), pp. 757–774.

[78] Sevan Goenezen, Jean-Francois Dord, Zac Sink, Paul E Barbone, Jingfeng Jiang, Timothy J Hall, and Assad A Oberai. "Linear and Nonlinear Elastic Modulus Imaging: An Application to Breast Cancer Diagnosis". In: *IEEE Trans. Med. Imaging* 31.8 (2012), pp. 1628–1637.

[79] Ruediger S. Goertz, Joerg Sturm, Lukas Pfeifer, Dane Wildner, David L. Wachter, Markus F. Neurath, and Deike Strobel. "ARFI cut-off values and significance of standard deviation for liver fibrosis staging in patients with chronic liver disease". In: *Ann. Hepatol.* 12.6 (2013), pp. 935–941.

[80] Gene H. (Gene Howard) Golub and Charles F. Van Loan. *Matrix computations*. Johns Hopkins University Press, 1996, p. 694.

[81] Sabrina A. Gonzalez-Blohm, James J. Doulgeris, William E. Lee, Thomas M. Shea, Kamran Aghayev, and Frank D. Vrionis. "The Current Testing Protocols for Biomechanical Evaluation of Lumbar Spinal Implants in Laboratory Setting: A Review of the Literature". In: *Biomed Res. Int.* 2015 (2015), pp. 1–15.

[82] Zachary D. Goodman. *Grading and staging systems for inflammation and fibrosis in chronic liver diseases*. 2007.

[83] Karl F. Graff. *Wave motion in elastic solids*. Dover Publications, 1991, p. 649.

[84] AE Green and RS Rivlin. "The mechanics of non-linear materials with memory". In: *Archive for rational mechanics and analysis* 4.1 (1959), pp. 387–404.

[85] Albert Edward Green and Ronald S Rivlin. "The mechanics of non-linear materials with memory". In: *Archive for Rational Mechanics and Analysis* 1.1 (1957), pp. 1–21.

[86] M. A. Green, G. Geng, E. Qin, R. Sinkus, S. C. Gandevia, and L. E. Bilston. "Measuring anisotropic muscle stiffness properties using elastography". In: *NMR Biomed.* 26.11 (2013), pp. 1387–1394.

[87] M. A. Green, R. Sinkus, S. C. Gandevia, R. D. Herbert, and L. E. Bilston. "Measuring changes in muscle stiffness after eccentric exercise using elastography". In: *NMR Biomed.* 25.6 (2012), pp. 852–858.

[88] Michael A. Green, Lynne E. Bilston, and Ralph Sinkus. " *I*n vivo brain viscoelastic properties measured by magnetic resonance elastography". In: *NMR Biomed.* 21.7 (2008), pp. 755–764.

[89] MS Green and AV Tobolsky. "A new approach to the theory of relaxing polymeric media". In: *The Journal of Chemical Physics* 14.2 (1946), pp. 80–92.

[90] A M Gressner. "Transdifferentiation of hepatic stellate cells (Ito cells) to myofibroblasts: a key event in hepatic fibrogenesis." In: *Kidney Int. Suppl.* 54 (1996), S39–45.

[91] Mircea Grigorescu. "Noninvasive biochemical markers of liver fibrosis." In: *J. Gastrointestin. Liver Dis.* 15.2 (2006), pp. 149–59.

[92] David Groshar, Gleb Slobodin, and Eli Zuckerman. "Quantitation of Liver and Spleen Uptake of 99mTc-Phytate Colloid Using SPECT: Detection of Liver Cirrhosis". In: *J. Nucl. Med.* 43.3 (2002), pp. 312–317.

[93] Alexander R Guimaraes, Luiz Siqueira, Ritika Uppal, Jamu Alford, Bryan C Fuchs, Suguru Yamada, Kenneth Tanabe, Raymond T Chung, Gregory Lauwers, Michael L Chew, Giles W Boland, Duhyant V Sahani, Mark Vangel, Peter F Hahn, and Peter Caravan. "T2 relaxation time is related to liver fibrosis severity". In: *Quant. Imaging Med. Surg.* 6.2 (2016), pp. 103–114.

[94] Osman Gültekin, Gerhard Sommer, and Gerhard A. Holzapfel. "An orthotropic viscoelastic model for the passive myocardium: continuum basis and numerical treatment". In: *Computer Methods in Biomechanics and Biomedical Engineering* 19.15 (May 2016), pp. 1647–1664. DOI: 10.1080/10255842.2016.1176155.

[95] Boling Guo, Xueke Pu, and Fenghui Huang. "Numerical Methods for the Fractional Ordinary Differential Equations". In: *Fractional Partial Differential Equations and Their Numerical Solutions*. World Scientific, Mar. 2015, pp. 286–298. DOI: 10.1142/9543.

[96] Morton E. Gurtin, Eliot. Fried, and Lallit. Anand. *The mechanics and thermodynamics of continua*. Cambridge University Press, 2010, p. 694.

[97] Myrianthi Hadjicharalambous, Jack Lee, Nicolas P. Smith, and David A. Nordsletten. "A displacement-based finite element formulation for incompressible and nearly-incompressible cardiac mechanics". In: *Comput. Methods Appl. Mech. Eng.* 274 (2014), pp. 213–236.

[98] Taiyo L Harada, Kazuhiro Saito, Yoichi Araki, Jun Matsubayashi, Toshitaka Nagao, Katsutoshi Sugimoto, and Koichi Tokuuye. "Prediction of high-stage liver fibrosis using ADC value on diffusion-weighted imaging and quantitative enhancement ratio at the hepatobiliary phase of Gd-EOB-DTPA–enhanced MRI at 1.5 T". In: *Acta radiol.* 59.5 (2018), pp. 509–516.

[99] I. Hariton, G. DeBotton, T. C. Gasser, and G. A. Holzapfel. "Stress-driven collagen fiber remodeling in arterial walls". In: *Biomech. Model. Mechanobiol.* 6.3 (2007), pp. 163–175.

[100] R. Hilfer. "Fractional Diffusion Based on Riemann-Liouville Fractional Derivatives†". In: *The Journal of Physical Chemistry B* 104.16 (Apr. 2000), pp. 3914–3917. DOI: 10.1021/jp9936289.

[101] M Hirata, S M Akbar, N Horiike, and M Onji. "Noninvasive diagnosis of the degree of hepatic fibrosis using ultrasonography in patients with chronic liver disease due to hepatitis C virus." In: *Eur. J. Clin. Invest.* 31.6 (2001), pp. 528–535.

[102] S. Holm and R. Sinkus. "A unifying fractional wave equation for compressional and shear waves". In: *J. Acoust. Soc. Am.* 127.3 (2010), pp. 1828–1828.

[103] Sverre Holm. *Waves with Power-Law Attenuation*. Springer, 2019.

[104] G Holzapfel. *Nonlinear solid mechanics: A continuum approach for engineering*. Vol. First Edit. Wiley, 2000, p. 455.

[105] G.A. Holzapfel, T.C. Gasser, and M. Stadler. "A structural model for the viscoelastic behavior of arterial walls: Continuum formulation and finite element analysis". In: *European Journal of Mechanics - A/Solids* 21.3 (Jan. 2002), pp. 441–463. DOI: 10.1016/s0997-7538(01)01206-2.

[106] Gerhard A Holzapfel. "Nonlinear solid mechanics: a continuum approach for engineering science". In: *Meccanica* 37.4 (2002), pp. 489–490.

[107] Gerhard A Holzapfel and Thomas C Gasser. "A viscoelastic model for fiber-reinforced composites at finite strains: Continuum basis, computational aspects and applications". In: *Computer methods in applied mechanics and engineering* 190.34 (2001), pp. 4379–4403.

[108] Gerhard A Holzapfel and Ray W Ogden. "Constitutive modelling of passive myocardium: a structurally based framework for material characterization". In: *Philos. Trans. R. Soc. A Math. Phys. Eng. Sci.* 367.1902 (2009), pp. 3445–3475.

[109] Gerhard A Holzapfel and Ray W Ogden. *Mechanics of biological tissue*. Springer Science & Business Media, 2006.

[110] Gerhard A Holzapfel and Juan C Simo. "A new viscoelastic constitutive model for continuous media at finite thermomechanical changes". In: *International Journal of Solids and Structures* 33.20 (1996), pp. 3019–3034.

[111] Yong Hu, Yong-Kang Zhou, Yi-Xing Chen, and Zhao-Chong Zeng. "Magnitude and influencing factors of respiration-induced liver motion during abdominal compression in patients with intrahepatic tumors." In: *Radiat. Oncol.* 12.1 (2017), p. 9.

[112] A Huber, L Ebner, M Montani, N Semmo, Choudhury Roy, J Heverhagen, and A Christe. "Computed tomography findings in liver fibrosis and cirrhosis". In: *Swiss Med. Wkly.* 144.0708 (2014).

[113] Thomas JR Hughes. *The finite element method: linear static and dynamic finite element analysis*. Courier Corporation, 2012.

[114] Laurent Huwart, Frank Peeters, Ralph Sinkus, Laurence Annet, Najat Salameh, Leon C ter Beek, Yves Horsmans, and Bernard E Van Beers. "Liver fibrosis: Non-invasive assessment with MR elastography". In: *NMR Biomed.* 19.2 (2006), pp. 173–179.

[115] Laurent Huwart, Christine Sempoux, Najat Salameh, Jacques Jamart, Laurence Annet, Ralph Sinkus, Frank Peeters, Leon C ter Beek, Yves Horsmans, and Bernard E Van Beers. "Liver Fibrosis: Noninvasive Assessment with MR Elastography versus Aspartate Aminotransferase-to-Platelet Ratio Index". en. In: *Radiology* 245.2 (2007), pp. 458–466.

[116] Laurent Huwart, Christine Sempoux, Eric Vicaut, Najat Salameh, Laurence Annet, Etienne Danse, Frank Peeters, Leon C ter Beek, Jacques Rahier, Ralph Sinkus, Yves Horsmans, and Bernard E Van Beers. "Magnetic Resonance Elastography for the Noninvasive Staging of Liver Fibrosis". In: *Gastroenterology* 135.1 (2008), pp. 32–40.

[117] Kamal Ishak, Amelia Baptista, Leonardo Bianchi, Francesco Callea, Jan De Groote, Fred Gudat, Helmut Denk, Valeer Desmet, Gerhard Korb, Roderick N.M. MacSween, M. James Phillips, Bernard G. Portmann, Hemming Poulsen, Peter J. Scheuer, Martin Schmid, and Heribert Thaler. "Histological grading and staging of chronic hepatitis". In: *J. Hepatol.* 22.6 (1995), pp. 696–699.

[118] H Iwamoto, H Sakai, S Tada, M Nakamuta, and H Nawata. "Induction of apoptosis in rat hepatic stellate cells by disruption of integrin-mediated cell adhesion." In: *J. Lab. Clin. Med.* 134.1 (1999), pp. 83–89.

[119] Shidong Jiang, Jiwei Zhang, Qian Zhang, and Zhimin Zhang. "Fast Evaluation of the Caputo Fractional Derivative and its Applications to Fractional Diffusion Equations". In: *Communications in Computational Physics* 21.3 (Feb. 2017), pp. 650–678. DOI: 10.4208/cicp.oa-2016-0136.

[120] Petr Jordan, Amy E Kerdok, Robert D Howe, and Simona Socrate. "Identifying a minimal rheological configuration: a tool for effective and efficient constitutive modeling of soft tissues." In: *J. Biomech. Eng.* 133.4 (2011), p. 41006.

[121] Madhan Ke and S Raju. "Comparative Histology of Human and Cow , Goat and Sheep Liver". In: *J. Surg. Acad.* (2014), pp. 10–13.

[122] Andrew R Kemper, Anthony C Santago, Joel D Stitzel, Jessica L Sparks, and Stefan M Duma. "Biomechanical response of human liver in tensile loading." In: *Ann. Adv. Automot. Med.* 54 (2010), pp. 15–26.

[123] Amy E Kerdok, Mark P Ottensmeyer, and Robert D Howe. "Effects of perfusion on the viscoelastic characteristics of liver". In: *J. Biomech.* 39.12 (2006), pp. 2221–2231.

[124] Amy Elizabeth Kerdok. "Characterizing the Nonlinear Mechanical Response of Liver to Surgical Manipulation". In: (2006).

[125] Tae Hoon Kim, Ji Eon Kim, Jong Hyun Ryu, and Chang Won Jeong. "Development of liver surface nodularity quantification program and its clinical application in nonalcoholic fatty liver disease". In: *Sci. Rep.* 9.1 (2019), p. 9994.

[126] Deirdre M. King, Carmel M. Moran†, John D. McNamara, Andrew J. Fagan§, and Jacinta E. Browne. "Development of a Vessel Mimicking Material for Use". In: *Ultrasound Med. Biol.* 37.5 (2011), pp. 813–826.

[127] Miklos Z. Kiss, Tomy Varghese, and Timothy J. Hall. "Viscoelastic characterization of in vitro canine tissue". In: *Phys. Med. Biol.* 49.18 (2004), pp. 4207–4218.

[128] Dieter Klatt, Uwe Hamhaber, Patrick Asbach, Jürgen Braun, and Ingolf Sack. "Noninvasive assessment of the rheological behavior of human organs using multifrequency MR elastography: a study of brain and liver viscoelasticity". In: *Phys. Med. Biol.* 52.24 (2007), pp. 7281–7294.

[129] Miwa Koinuma, Isamu Ohashi, Kaoru Hanafusa, and Hitoshi Shibuya. "Apparent diffusion coefficient measurements with diffusion-weighted magnetic resonance imaging for evaluation of hepatic fibrosis." In: *J. Magn. Reson. Imaging* 22 (2005), pp. 80–85.

[130] A. Kolipaka, K. P. McGee, P. A. Araoz, K. J. Glaser, A. Manduca, A. J. Romano, and R. L. Ehman. "MR elastography as a method for the assessment of myocardial stiffness: Comparison with an established pressure-volume model in a left ventricular model of the heart". In: *Magn. Reson. Med.* 62.1 (2009), pp. 135–140.

[131] Arunark Kolipaka, Shivani R. Aggarwal, Kiaran P. McGee, Nandan Anavekar, Armando Manduca, Richard L. Ehman, and Philip A. Araoz. "Magnetic resonance elastography as a method to estimate myocardial contractility". In: *J. Magn. Reson. Imaging* 36.1 (2012), pp. 120–127.

[132] Arunark Kolipaka, Philip A. Araoz, Kiaran P. McGee, Armando Manduca, and Richard L. Ehman. "Magnetic resonance elastography as a method for the assessment of effective myocardial stiffness throughout the cardiac cycle". In: *Magn. Reson. Med.* 64.3 (2010), pp. 862–870.

[133] W. Michael Lai, Erhard Krempl, and David H. Rubin. *Introduction to Continuum Mechanics*. Elsevier Science & Technology, Aug. 20, 2009. 536 pp. ISBN: 0750685603.

[134] Roderic S. Lakes. *Viscoelastic Solids (1998)*. CRC Press, Nov. 1999. DOI: 10.1201/9781315121369.

[135] L D Landau and E M Lifshitz. *Course of Theoretical Physics: Volume 7, Theory of Elasticity*. 1975.

[136] Y. Lanir. "Constitutive equations for fibrous connective tissues". In: *Journal of Biomechanics* 16.1 (Jan. 1983), pp. 1–12. DOI: 10.1016/0021-9290(83)90041-6.

[137] Patrick Le Tallec, Christophe Rahier, and Ahmed Kaiss. "Three-dimensional incompressible viscoelasticity in large strains: formulation and numerical approximation". In: *Computer methods in applied mechanics and engineering* 109.3-4 (1993), pp. 233–258.

[138] J. Lee, A. Cookson, I. Roy, E. Kerfoot, L. Asner, G. Vigueras, T. Sochi, S. Deparis, C. Michler, N. P. Smith, and D. A. Nordsletten. "Multiphysics Computational Modeling in **CHeart**". In: *SIAM Journal on Scientific Computing* 38.3 (Jan. 2016), pp. C150–C178. DOI: 10.1137/15m1014097.

[139] A Levin and J Wyman. "The viscous elastic properties of muscle". In: *Proceedings of the Royal Society of London. Series B, Containing Papers of a Biological Character* 101.709 (1927), pp. 218–243.

[140] Maïté Lewin, Armelle Poujol-Robert, Pierre Yves Boëlle, Dominique Wendum, Elisabeth Lasnier, Magalie Viallon, Jérôme Guéchot, Christine Hoeffel, Lionel Arrivé, Jean Michel Tubiana, and Raoul Poupon. "Diffusion-weighted magnetic resonance imaging for the assessment of fibrosis in chronic hepatitis C". In: *Hepatology* 46.3 (2007), pp. 658–665.

[141] Su-Mei Li, Guang-Xia Li, Dong-Mei Fu, Yu Wang, and Li-Qun Dang. "Liver fibrosis evaluation by ARFI and APRI in chronic hepatitis C." In: *World J. Gastroenterol.* 20.28 (2014), pp. 9528–33.

[142] Shujing Li, Xicui Sun, Minjie Chen, Zhekang Ying, Yamin Wan, Liya Pi, Bin Ren, and Qi Cao. "Liver Fibrosis Conventional and Molecular Imaging Diagnosis Update." In: *J. Liver* 8.1 (2019).

[143] Yan Li, Jianxin Deng, Jun Zhou, and Xueen Li. "Elastic and viscoelastic mechanical properties of brain tissues on the implanting trajectory of sub-thalamic nucleus stimulation". In: *Journal of Materials Science: Materials in Medicine* 27.11 (Sept. 2016). DOI: 10.1007/s10856-016-5775-5.

[144] Xi Zhang Lin, Ming Hwui Horng, Yung Nien Sun, Shu Chu Shiesh, Nan Haw Chow, and Xiou Zhen Guo. "Computer morphometry for quantitative measurement of liver fibrosis: Comparison with Knodell's score, colorimetry and conventional description reports". In: *J. Gastroenterol. Hepatol.* 13.1 (1998), pp. 75–80.

[145] F. Liu, P. Zhuang, V. Anh, I. Turner, and K. Burrage. "Stability and convergence of the difference methods for the space–time fractional advection–diffusion equation". In: *Applied Mathematics and Computation* 191.1 (Aug. 2007), pp. 12–20. DOI: 10.1016/j.amc.2006.08.162.

[146] Yi Liu, Ge Wang, and L. Z. Sun. "Anisotropic Elastography for Local Passive Properties and Active Contractility of Myocardium from Dynamic Heart Imaging Sequence". In: *Int. J. Biomed. Imaging* 2006 (2006), pp. 1–15.

[147] Z Liu and L Bilston. "On the viscoelastic character of liver tissue: experiments and modelling of the linear behaviour." In: *Biorheology* 37.3 (2000), pp. 191–201.

[148] Rohit Loomba, Jeffrey Cui, Tanya Wolfson, William Haufe, Jonathan Hooker, Nikolaus Szeverenyi, Brandon Ang, Archana Bhatt, Kang Wang, Hamed Aryafar, Cindy Behling, Mark A Valasek, Grace Y Lin, Anthony Gamst, David A Brenner, Meng Yin, Kevin J Glaser, Richard L Ehman, and Claude B Sirlin. "Novel 3D Magnetic Resonance Elastography for the Noninvasive Diagnosis of Advanced Fibrosis in NAFLD: A Prospective Study". In: *Am. J. Gastroenterol.* 111.7 (2016), pp. 986–994.

[149] J Lubliner. "A model of rubber viscoelasticity". In: *Mechanics Research Communications* 12.2 (1985), pp. 93–99.

[150] JN Lyness and D Jespersen. "Moderate degree symmetric quadrature rules for the triangle". In: *IMA Journal of Applied Mathematics* 15.1 (1975), pp. 19–32.

[151] Luca Macarini and Luca P. Stoppino. "Radiologic Assessment of Liver Fibrosis – Present and Future". In: *Pract. Manag. Chronic Viral Hepat.* 2013.

[152] J. Tenreiro Machado, Virginia Kiryakova, and Francesco Mainardi. "Recent history of fractional calculus". In: *Communications in Nonlinear Science and Numerical Simulation* 16.3 (Mar. 2011), pp. 1140–1153. DOI: 10.1016/j.cnsns.2010.05.027.

[153] E L Madsen, G R Frank, M A Hobson, S Lin-Gibson, T J Hall, J Jiang, and T A Stiles. "Instrument for determining the complex shear modulus of soft-tissue-like materials from 10 to 300 Hz." In: *Phys. Med. Biol.* 53.19 (2008), pp. 5313–5342.

[154] Richard L Magin. *Fractional calculus in bioengineering*. Begell House Redding, 2006.

[155] Richard L. Magin. "Fractional Calculus in Bioengineering, Part 1". In: *Critical Reviews in Biomedical Engineering* 32.1 (2004), pp. 1–104. DOI: 10.1615/critrevbiomedeng.v32.i1.10.

[156] Lawrence E. Malvern. *Introduction to the mechanics of a continuous medium*. Prentice-Hall, 1969, p. 713.

[157] A. Manduca, T. E. Oliphant, M. A. Dresner, J. L. Mahowald, S. A. Kruse, E. Amromin, J. P. Felmlee, J. F. Greenleaf, and R. L. Ehman. "Magnetic resonance elastography: Non-invasive mapping of tissue elasticity". In: *Med. Image Anal.* 5.4 (2001), pp. 237–254.

[158] Jacques Marescaux, Jean Marie Clément, Vincent Tassetti, Christophe Koehl, Stéphane Cotin, Yves Russier, Didier Mutter, Hervé Delingette, and Nicholas Ayache. "Virtual reality applied to hepatic surgery simulation: The next revolution". In: *Ann. Surg.* 228.5 (1998), pp. 627–634.

[159] Y. K. Mariappan, K. J. Glaser, and Richard L. E. "Magnetic Resonance Elastography: a Review". In: *Clin. Anat.* 23.5 (2010), pp. 497–511.

[160] Fabio Marra. "Hepatic stellate cells and the regulation of liver inflammation". In: *J. Hepatol.* 31.6 (1999), pp. 1106–1119.

[161] Antonio Martinez-Hernandez and Peter S. Amenta. *The hepatic extracellular matrix - I. Components and distribution in normal liver*. 1993.

[162] B. Mathieu, P. Melchior, A. Oustaloup, and Ch. Ceyral. "Fractional differentiation for edge detection". In: *Signal Processing* 83.11 (Nov. 2003), pp. 2421–2432. DOI: 10.1016/s0165-1684(03)00194-4.

[163] MATLAB. *version 9.4.0.813654 (R2018a)*. Natick, Massachusetts: The MathWorks Inc., 2018.

[164] James Clerk Maxwell. "Iv. on the dynamical theory of gases". In: *Philosophical transactions of the Royal Society of London* 157 (1867), pp. 49–88.

[165] M McCormick, D Nordsletten, D Kay, and N Smith. "Modelling left ventricular function under assist device support". In: *International Journal for Numerical Methods in Biomedical Engineering* 27.7 (2011), pp. 1073–1095.

[166] M. McCormick, D.A. Nordsletten, D. Kay, and N.P. Smith. "Simulating left ventricular fluid–solid mechanics through the cardiac cycle under LVAD support". In: *J. Comput. Phys.* 244 (2013), pp. 80–96.

[167] Matthew McCormick, David Nordsletten, Pablo Lamata, and Nicolas P. Smith. "Computational analysis of the importance of flow synchrony for cardiac ventricular assist devices". In: *Comput. Biol. Med.* 49 (2014), pp. 83–94.

[168] M. D.J. McGarry, C L Johnson, B P Sutton, J G Georgiadis, E. E.W. Van Houten, A J Pattison, J B Weaver, and K D Paulsen. "Suitability of poroelastic and viscoelastic mechanical models for high and low frequency MR elastography". In: *Med. Phys.* 42.2 (2015), pp. 947–957.

[169] John G McHutchison, Larry M Blatt, Maria De Medina, John R Craig, Andrew Conrad, Eugene R Schiff, and Myron J Tong. "Measurement of serum hyaluronic acid in patients with chronic hepatitis C and its relationship to liver histology". In: *J. Gastroenterol. Hepatol.* 15.8 (2000), pp. 945–951.

[170] Marc Andre Meyers and Krishan Kumar Chawla. *Mechanical Behavior of Materials*. Cambridge University Press, Jan. 16, 2014. 882 pp. ISBN: 0521866758.

[171] K. Miller, A. Wittek, and G. Joldes. "Biomechanical Modeling of the Brain for Computer-Assisted Neurosurgery". In: *Biomechanics of the Brain*. Springer New York, 2011, pp. 111–136. DOI: 10.1007/978-1-4419-9997-9_6.

[172] Karol Miller. "Constitutive modelling of abdominal organs". In: *J. Biomech.* 33.3 (2000), pp. 367–373.

[173] Sarthak Misra, K T Ramesh, and Allison M Okamura. "Modelling of non-linear elastic tissues for surgical simulation." In: *Comput. Methods Biomech. Biomed. Engin.* 13.6 (2010), pp. 811–818.

[174] Evan Mitsoulis. "50 Years of the K-BKZ Constitutive Relation for Polymers". In: *ISRN Polym. Sci.* 2013 (2013), pp. 1–22.

[175] M Mooney. "A Theory of Large Elastic Deformation". In: *J. Appl. Phys.* 11.9 (1940), p. 582.

[176] James E. Moore, Lucas H. Timmins, and John F. LaDisa. "Coronary artery bifurcation biomechanics and implications for interventional strategies". In: *Catheterization and Cardiovascular Interventions* 76.6 (Nov. 2010), pp. 836–843. DOI: 10.1002/ccd.22596.

[177] Sebastian Mueller, Gunda Millonig, Lucie Sarovska, Stefanie Friedrich, Frank M Reimann, Maria Pritsch, Silke Eisele, Felix Stickel, Thomas Longerich, Peter Schirmacher, and Helmut Karl Seitz. "Increased liver stiffness in alcoholic liver disease: differentiating fibrosis from steatohepatitis." In: *World J. Gastroenterol.* 16.8 (2010), pp. 966–972.

[178] Diego A. Murio. "Implicit finite difference approximation for time fractional diffusion equations". In: *Computers & Mathematics with Applications* 56.4 (Aug. 2008), pp. 1138–1145. DOI: 10.1016/j.camwa.2008.02.015.

[179] Nahyup Kang, Min Woo Lee, and Taehyun Rhee. "Simulating Liver Deformation during Respiration Using Sparse Local Features". In: *IEEE Comput. Graph. Appl.* 32.5 (2012), pp. 29–38.

[180] M. P. Nash and P. J. Hunter. "Computational Mechanics of the Heart". In: *J. Elast.* 61.1/3 (2000), pp. 113–141.

[181] Man M Nguyen, Shiwei Zhou, Jean-Luc Robert, Vijay Shamdasani, and Hua Xie. "Development of oil-in-gelatin phantoms for viscoelasticity measurement in ultrasound shear wave elastography." In: *Ultrasound Med. Biol.* 40.1 (2014), pp. 168–176.

[182] S Nicolle, P Vezin, J-F Palierne, K Nagayama, T Matsumoto, and A King. "A strain-hardening bi-power law for the nonlinear behaviour of biological soft tissues." In: *J. Biomech.* 43.5 (2010), pp. 927–932.

[183] Kathy Nightingale. "Acoustic Radiation Force Impulse (ARFI) Imaging: a Review." In: *Curr. Med. Imaging Rev.* 7.4 (2011), pp. 328–339.

[184] D. Nordsletten, M. McCormick, P. J. Kilner, P. Hunter, D. Kay, and N. P. Smith. "Fluid-solid coupling for the investigation of diastolic and systolic human left ventricular function". In: *Int. J. Numer. Method. Biomed. Eng.* 27.7 (2011), pp. 1017–1039.

[185] D.A. Nordsletten, S.A. Niederer, M.P. Nash, P.J. Hunter, and N.P. Smith. "Coupling multi-physics models to cardiac mechanics". In: *Prog. Biophys. Mol. Biol.* 104.1-3 (2011), pp. 77–88.

[186] Bengt Norén, Mikael Fredrik Forsgren, Olof Dahlqvist Leinhard, Nils Dahlström, Johan Kihlberg, Thobias Romu, Stergios Kechagias, Sven Almer, Örjan Smedby, and Peter Lundberg. "Separation of advanced from mild hepatic fibrosis by quantification of the hepatobiliary uptake of Gd-EOB-DTPA". In: *Eur. Radiol.* 23.1 (2013), pp. 174–181.

[187] Robert V. O'Toole, Branislav Jaramaz, Anthony M. DiGioia, Christopher D. Visnic, and Robert H. Reid. "Biomechanics for preoperative planning and surgical simulations in orthopaedics". In: *Comput. Biol. Med.* 25.2 (1995), pp. 183–191.

[188] R W Ogden. "Large Deformation Isotropic Elasticity - On the Correlation of Theory and Experiment for Incompressible Rubberlike Solids". In: *Proc. R. Soc. A Math. Phys. Eng. Sci.* 326.1567 (1972), pp. 565–584.

[189] R. W. Ogden. *Non-linear elastic deformations*. Dover Publications, 1997, p. 532.

[190] R Parker and C A McCune. "Diagnosis and treatment of alcoholic hepatitis". In: *Frontline Gastroenterol.* 5.2 (2014), pp. 123–129.

[191] Anna K Paulsson, Sue S Yom, Mekhail Anwar, Dilini Pinnaduwage, Atchar Sudhyadhom, Alexander R Gottschalk, Albert J Chang, and Martina Descovich. "Respiration-Induced Intraorgan Deformation of the Liver." In: *Technol. Cancer Res. Treat.* 16.6 (2017), p. 1533034616687193.

[192] Michael Pavlides, Rajarshi Banerjee, Joanne Sellwood, Catherine J. Kelly, Matthew D. Robson, Jonathan C. Booth, Jane Collier, Stefan Neubauer, and Eleanor Barnes. "Multiparametric magnetic resonance imaging predicts clinical outcomes in patients with chronic liver disease". In: *J. Hepatol.* 64.2 (2016), pp. 308–315.

[193] V Pazos, R Mongrain, and J C Tardif. "Polyvinyl alcohol cryogel: Optimizing the parameters of cryogenic treatment using hyperelastic models". In: *J. Mech. Behav. Biomed. Mater.* 2.5 (2009), pp. 542–549.

[194] Antonella Pellicoro, Prakash Ramachandran, John P Iredale, and Jonathan a Fallowfield. "Liver fibrosis and repair: immune regulation of wound healing in a solid organ." In: *Nat. Rev. Immunol.* 14.3 (2014), pp. 181–194.

[195] Maryna Perepelyuk et al. "Normal and Fibrotic Rat Livers Demonstrate Shear Strain Softening and Compression Stiffening: A Model for Soft Tissue Mechanics". In: *PLoS One* 11.1 (2016). Ed. by Sanjay Kumar, e0146588.

[196] Thomas Peter and Gerlind Plonka. "A generalized Prony method for reconstruction of sparse sums of eigenfunctions of linear operators". In: *Inverse Problems* 29.2 (Jan. 2013), p. 025001. DOI: 10.1088/0266-5611/29/2/025001.

[197] Perry J. Pickhardt, Kyle Malecki, Oliver F. Hunt, Claire Beaumont, John Kloke, Timothy J. Ziemlewicz, and Meghan G. Lubner. "Hepatosplenic volumetric assessment at MDCT for staging liver fibrosis". In: *Eur. Radiol.* 27.7 (2017), pp. 3060–3068.

[198] Perry J. Pickhardt, Kyle Malecki, John Kloke, and Meghan G. Lubner. "Accuracy of liver surface nodularity quantifcation on MDCT as a noninvasive biomarker for staging hepatic fibrosis". In: *Am. J. Roentgenol.* 207.6 (2016), pp. 1194–1199.

[199] Igor Podlubny. *Fractional differential equations: an introduction to fractional derivatives, fractional differential equations, to methods of their solution and some of their applications*. Vol. 198. Academic press, 1998.

[200] Daniel Potts and Manfred Tasche. "Parameter estimation for exponential sums by approximate Prony method". In: *Signal Processing* 90.5 (May 2010), pp. 1631–1642. DOI: 10.1016/j.sigpro.2009.11.012.

[201] Thierry Poynard, Mona Munteanu, Olivier Deckmyn, Yen Ngo, Fabienne Drane, Jean Marie Castille, Chantal Housset, Vlad Ratziu, and Franoise Imbert-Bismut. "Validation of liver fibrosis biomarker (FibroTest) for assessing liver fibrosis progression: Proof of concept and first application in a large population". In: *J. Hepatol.* 57.3 (2012), pp. 541–548.

[202] D Prezzi, R Neji, J Stirling, S Jeljeli, H Verma, T O'Brien, B Challacombe, A Chandra, V Goh, and R Sinkus. "Characterization of Renal Tumors: Initial Experience Integrating Biomechanical and Morphological Assessment Using 3 Tesla Magnetic Resonance Imaging and Elastography (MRE)". In: *Proc. ISMRM 24th Annu. Meet. Exhib. Singapore*. Singapore.

[203] Eric C. Qin, Ralph Sinkus, Guangqiang Geng, Shaokoon Cheng, Michael Green, Caroline D. Rae, and Lynne E. Bilston. "Combining MR elastography and diffusion tensor imaging for the assessment of anisotropic mechanical properties: A phantom study". In: *J. Magn. Reson. Imaging* 37.1 (2013), pp. 217–226.

[204] Alfio Quarteroni and Alberto Valli. *Numerical approximation of partial differential equations*. Vol. 23. Springer Science & Business Media, 2008.

[205] Vijay Rajagopal, Poul M.F. Nielsen, and Martyn P. Nash. "Modeling breast biomechanics for multimodal image analysis-successes and challenges". In: *Wiley Interdiscip. Rev. Syst. Biol. Med.* 2.3 (2010), pp. 293–304.

[206] Manuel K Rausch, Frederick A Tibayan, Neil B Ingels, D Craig Miller, and Ellen Kuhl. "Mechanics of the mitral annulus in chronic ischemic cardiomyopathy". In: *Annals of biomedical engineering* 41.10 (2013), pp. 2171–2180.

[207] Hayley M. Reynolds, Jaykumar Puthran, Anthony Doyle, Wayne Jones, Poul M. F. Nielsen, Martyn P. Nash, and Vijay Rajagopal. "Mapping Breast Cancer Between Clinical X-Ray and MR Images". In: *Comput. Biomech. Med.* New York, NY: Springer New York, 2011, pp. 81–90.

[208] R S Rivlin and D W Saunders. "Large Elastic Deformations of Isotropic Materials. VII. Experiments on the Deformation of Rubber". In: *Philos. Trans. R. Soc. A Math. Phys. Eng. Sci.* 243.865 (1951), pp. 251–288.

[209] B. Robert, R. Sinkus, JL. Gennisson, and M. Fink. "Application of Dense-MR-elastography to the human heart". In: *Magn. Reson. Med.* 62.5 (2009), pp. 1155–1163.

[210] Don C Rockey, Stephen H Caldwell, Zachary D Goodman, Rendon C Nelson, and Alastair D Smith. "Liver biopsy." In: *Hepatology* 49.3 (2009), pp. 1017–1044.

[211] Don C. Rockey. "Fibrosis reversal after hepatitis C virus elimination". In: *Curr. Opin. Gastroenterol.* 35.3 (2019), pp. 137–144.

[212] Jacob Rosen, Jeffrey D Brown, Smita De, Mika Sinanan, and Blake Hannaford. "Biomechanical properties of abdominal organs in vivo and postmortem under compression loads." In: *J. Biomech. Eng.* 130.2 (2008), p. 021020.

[213] Bertram Ross. "The development of fractional calculus 1695–1900". In: *Historia Mathematica* 4.1 (Feb. 1977), pp. 75–89. DOI: 10.1016/0315-0860(77)90039-8.

[214] Olivier Rouvière, Meng Yin, M Alex Dresner, Phillip J Rossman, Lawrence J Burgart, Jeff L Fidler, and Richard L Ehman. "MR elastography of the liver: preliminary results." In: *Radiology* 240.2 (2006), pp. 440–448.

[215] Liangyou Rui. "Energy metabolism in the liver". In: *Compr. Physiol.* 4.1 (2014), pp. 177–197.

[216] Jurgen Henk Runge, Stefan Heinz Hoelzl, Jelizaveta Sudakova, Ayse Sila Dokumaci, Jules Laurent Nelissen, Christian Guenthner, Jack Lee, Marian Troelstra, Daniel Fovargue, Jaap Stoker, Aart Johannes Nederveen, David Nordsletten, and Ralph Sinkus. "A novel magnetic resonance elastography transducer concept based on a rotational eccentric mass: Preliminary experiences with the gravitational transducer". In: *Phys. Med. Biol.* 64.4 (2019), p. 045007.

[217] J.-F. Palierne S. Nicolle. "Comportement viscoélastique non linéaire des organe s pleins de l ' abdomen". In: *Congrès Français de Mécanique* (2015).

[218] Behnam Saberi, Alia S Dadabhai, Julie Nanavati, Lin Wang, Russell T Shinohara, and Gerard E Mullin. "Vitamin D levels do not predict the stage of hepatic fibrosis in patients with non-alcoholic fatty liver disease: A PRISMA compliant systematic review and meta-analysis of pooled data." In: *World J. Hepatol.* 10.1 (2018), pp. 142–154.

[219] Ingolf Sack, Bernd Beierbach, Jens Wuerfel, Dieter Klatt, Uwe Hamhaber, Sebastian Papazoglou, Peter Martus, and Jürgen Braun. "The impact of aging and gender on brain viscoelasticity". In: *NeuroImage* 46.3 (July 2009), pp. 652–657. DOI: 10.1016/j.neuroimage.2009.02.040.

[220] Anthony E. Samir, Manish Dhyani, Abhinav Vij, Atul K. Bhan, Elkan F. Halpern, Jorge Méndez-Navarro, Kathleen E. Corey, and Raymond T. Chung. "Shear-Wave Elastography for the Estimation of Liver Fibrosis in Chronic Liver Disease: Determining Accuracy and Ideal Site for Measurement". In: *Radiology* 274.3 (2015), pp. 888–896.

[221] Richard Allan Schapery. *A theory of non-linear thermoviscoelasticity based on irreversible thermodynamics*. American Society of Mechanical Engineers, 1966.

[222] Rudolf Scherer, Shyam L. Kalla, Yifa Tang, and Jianfei Huang. "The Grünwald–Letnikov method for fractional differential equations". In: *Comput. Math. with Appl.* 62.3 (2011), pp. 902–917.

[223] K. Schregel, E. Wuerfel nee Tysiak, P. Garteiser, I. Gemeinhardt, T. Prozorovski, O. Aktas, H. Merz, D. Petersen, J. Wuerfel, and R. Sinkus. "Demyelination reduces brain parenchymal stiffness quantified in vivo by magnetic resonance elastography". In: *Proc. Natl. Acad. Sci.* 109.17 (2012), pp. 6650–6655.

[224] Scott L Friedman. *Pathogenesis of hepatic fibrosis - UpToDate*.

[225] Scott L. Friedman and Michael J.P. Arthur, Scott L. Friedman, and Michael J P Arthur. "Reversing Hepatic Fibrosis". In: *Sci. Med. (Phila).* (2002), pp. 194–205.

[226] VE Shamanskii. "A modification of Newton's method". In: *Ukrainian Mathematical Journal* 19.1 (1967), pp. 118–122.

[227] Juan Carlos Simo. "On a fully three-dimensional finite-strain viscoelastic damage model: formulation and computational aspects". In: *Computer methods in applied mechanics and engineering* 60.2 (1987), pp. 153–173.

[228] Siddharth Singh, Sudhakar K. Venkatesh, Zhen Wang, Frank H. Miller, Utaroh Motosugi, Russell N. Low, Tarek Hassanein, Patrick Asbach, Edmund M. Godfrey, Meng Yin, Jun Chen, Andrew P. Keaveny, Mellena Bridges, Anneloes Bohte, Mohammad Hassan Murad, David J. Lomas, Jayant A. Talwalkar, and Richard L. Ehman. "Diagnostic performance of magnetic resonance elastography in staging liver fibrosis: A systematic review and meta-analysis of individual participant data". In: *Clin. Gastroenterol. Hepatol.* 13.3 (2015), 440–451.e6.

[229] R Sinkus, J Lorenzen, D Schrader, M Lorenzen, M Dargatz, and D Holz. "High-resolution tensor MR elastography for breast tumour detection." In: *Phys. Med. Biol.* 45.6 (2000), pp. 1649–1664.

[230] R. Sinkus, M. Tanter, S. Catheline, J. Lorenzen, C. Kuhl, E. Sondermann, and M. Fink. "Imaging anisotropic and viscous properties of breast tissue by magnetic resonance-elastography". In: *Magn. Reson. Med.* 53.2 (2005), pp. 372–387.

[231] R. Sinkus, M. Tanter, T. Xydeas, S. Catheline, J. Bercoff, and M. Fink. "Viscoelastic shear properties of in vivo breast lesions measured by MR elastography." In: *Magn. Reson. Imaging* 23.2 (2005), pp. 159–165.

[232] Ralph Sinkus, Simon Lambert, Khaled Z. Abd-Elmoniem, Caryn Morse, Theo Heller, Christian Guenthner, Ahmed M. Ghanem, Sverre Holm, and Ahmed M. Gharib. "Rheological determinants for simultaneous staging of hepatic fibrosis and inflammation in patients with chronic liver disease". In: *NMR Biomed.* 31.10 (2018), e3956.

[233] Ralph Sinkus, Katja Siegmann, Tanja Xydeas, Mickael Tanter, Claus Claussen, and Mathias Fink. "MR elastography of breast lesions: understanding the solid/liquid duality can improve the specificity of contrast-enhanced MR mammography." In: *Magn. Reson. Med.* 58.6 (2007), pp. 1135–1144.

[234] Andrew Dennis Smith, Kristin K. Porter, Asser Abou Elkassem, Rupan Sanyal, and Mark E. Lockhart. "Current imaging techniques for noninvasive staging of hepatic fibrosis". In: *Am. J. Roentgenol.* 213.1 (2019), pp. 77–89.

[235] Gerhard Sommer, Daniel Ch. Haspinger, Michaela Andrä, Michael Sacherer, Christian Viertler, Peter Regitnig, and Gerhard A. Holzapfel. "Quantification of Shear Deformations and Corresponding Stresses in the Biaxially Tested Human Myocardium". In: *Annals of Biomedical Engineering* 43.10 (Feb. 2015), pp. 2334–2348. DOI: 10.1007/s10439-015-1281-z.

[236] Gerhard Sommer, Andreas J. Schriefl, Michaela Andrä, Michael Sacherer, Christian Viertler, Heimo Wolinski, and Gerhard A. Holzapfel. "Biomechanical properties and microstructure of human ventricular myocardium". In: *Acta Biomaterialia* 24 (Sept. 2015), pp. 172–192. DOI: 10.1016/j.actbio.2015.06.031.

[237] F. Staub, C. Tournoux-Facon, J. Roumy, C. Chaigneau, M. Morichaut-Beauchant, P. Levillain, C. Prevost, C. Aubé, J. Lebigot, F. Oberti, J. B. Galtier, H. Laumonier, H. Trillaud, P. H. Bernard, J. F. Blanc, S. Sironneau, F. Machet, J. Drouillard, V. de Ledinghen, P. Couzigou, P. Foucher, L. Castéra, F. Tranquard, Y. Bacq, L. D'Altéroche, P. Ingrand, and J. P. Tasu. "Liver fibrosis staging with contrast-enhanced ultrasonography: Prospective multicenter study compared with METAVIR scoring". In: *Eur. Radiol.* 19.8 (2009), pp. 1991–1997.

[238] Kaspar-Josche Streitberger, Edzard Wiener, Jan Hoffmann, Florian Baptist Freimann, Dieter Klatt, Jürgen Braun, Kui Lin, Joyce McLaughlin, Christian Sprung, Randolf Klingebiel, and Ingolf Sack. "In vivo viscoelastic properties of the brain in normal pressure hydrocephalus". In: *NMR in Biomedicine* (2010), n/a–n/a. DOI: 10.1002/nbm.1602.

[239] J. I. Suárez, B. M. Vinagre, A. J. Calderón, C. A. Monje, and Y. Q. Chen. "Using Fractional Calculus for Lateral and Longitudinal Control of Autonomous Vehicles". In: *Computer Aided Systems Theory - EUROCAST 2003*. Springer Berlin Heidelberg, 2003, pp. 337–348. DOI: 10.1007/978-3-540-45210-2_31.

[240] K J M Surry, H J B Austin, A Fenster, and T M Peters. "Poly(vinyl alcohol) cryogel phantoms for use in ultrasound and MR imaging". In: *Phys. Med. Biol.* 49.24 (2004), pp. 5529–5546.

[241] Francis Sutherland and Julie Harris. "Claude Couinaud". In: *Arch. Surg.* 137.11 (2002), pp. 1305–1310.

[242] Orjan G. Martinsen Sverre Grimnes. *Bioimpedance and Bioelectricity Basics*. ACADEMIC PR INC, Sept. 1, 2014. 584 pp. ISBN: 0124114709.

[243] M. M. Swindle, A. Makin, A. J. Herron, F. J. Clubb, and K. S. Frazier. "Swine as Models in Biomedical Research and Toxicology Testing". In: *Vet. Pathol.* 49.2 (2012), pp. 344–356.

[244] Larry A Taber. *Nonlinear Theory of Elasticity*. World Scientific, 2004.

[245] K Takamizawa and K Hayashi. "Strain energy density function and uniform strain hypothesis for arterial mechanics." In: *J. Biomech.* 20.1 (1987), pp. 7–17.

[246] Kristy Tan, Shaokoon Cheng, Lauriane Jugé, and Lynne E. Bilston. "Characterising soft tissues under large amplitude oscillatory shear and combined loading". In: *J. Biomech.* 46.6 (2013), pp. 1060–1066.

[247] An Tang, Guy Cloutier, Nikolaus M Szeverenyi, and Claude B Sirlin. "Ultrasound elastography and MR elastography for assessing liver fibrosis: Part 1, principles and techniques". In: *Am. J. Roentgenol.* 205.1 (2015), pp. 22–32.

[248] R. N. Thurston and K. Brugger. "Third-Order Elastic Constants and the Velocity of Small Amplitude Elastic Waves in Homogeneously Stressed Media". In: *Phys. Rev.* 133.6A (1964), A1604–A1610.

[249] C Truesdell. "The simplest rate theory of pure elasticity". In: *Communications on pure and applied mathematics* 8.1 (1955), pp. 123–132.

[250] Chien-Cheng Tseng, Soo-Chang Pei, and Shih-Chang Hsia. "Computation of fractional derivatives using Fourier transform and digital FIR differentiator". In: *Signal Processing* 80.1 (Jan. 2000), pp. 151–159. DOI: 10.1016/s0165-1684(99)00118-8.

[251] Elijah E. W. Van Houten, J B Weaver, M I Miga, F E Kennedy, and K D Paulsen. "Elasticity reconstruction from experimental MR displacement data: initial experience with an overlapping subzone finite element inversion process." In: *Med. Phys.* 27.1 (2000), pp. 101–7.

[252] Elijah E.W. Van Houten, Marvin M. Doyley, Francis E. Kennedy, John B. Weaver, and Keith D. Paulsen. "Initial in vivo experience with steady-state subzone-based MR elastography of the human breast". In: *J. Magn. Reson. Imaging* 17.1 (2003), pp. 72–85.

[253] Niklas Verloh, Ingo Einspieler, Kirsten Utpatel, Karin Menhart, Stefan Brunner, Frank Hofheinz, Jörg van den Hoff, Philipp Wiggermann, Matthias Evert, Christian Stroszczynski, Dirk Hellwig, and Jirka Grosse. "In vivo confirmation of altered hepatic glucose metabolism in patients with liver fibrosis/cirrhosis by 18F-FDG PET/CT". In: *EJNMMI Res.* 8.1 (2018), p. 98.

[254] D R Veronda and R A Westmann. "Mechanical characterization of skin-finite deformations." In: *J. Biomech.* 3.1 (1970), pp. 111–124.

[255] David C. Viano, Albert I. King, John W. Melvin, and Kathleen Weber. "Injury biomechanics research: An essential element in the prevention of trauma". In: *J. Biomech.* 22.5 (1989), pp. 403–417.

[256] Carmen Vinaixa, Angel Rubín, Victoria Aguilera, and Marina Berenguer. "Recurrence of hepatitis C after liver transplantation." In: *Ann. Gastroenterol. Q. Publ. Hell. Soc. Gastroenterol.* 26.4 (2013), pp. 304–313.

[257] Valery Vishnevskiy, Tobias Gass, Gabor Szekely, Christine Tanner, and Orcun Goksel. "Isotropic Total Variation Regularization of Displacements in Parametric Image Registration". In: *IEEE Trans. Med. Imaging* 36.2 (2017), pp. 385–395. DOI: 10.1109/TMI.2016.2610583.

[258] Eugenia Vispo, Pablo Barreiro, José del Valle, Ivana Maida, Victor de Ledinghen, Carmen Quereda, Alberto Moreno, Juan Macías, Laurent Castera, Juan Antonio Pineda, and Vincent Soriano. "Overestimation of liver fibrosis staging using transient elastography in patients with chronic hepatitis C and significant liver inflammation". In: *Antivir. Ther.* 14 (2009), pp. 187–193.

[259] B C Wang, G R Wang, D H Yan, and Y P Liu. "An experimental study on biomechanical properties of hepatic tissue using a new measuring method." In: *Biomed. Mater. Eng.* 2.3 (1992), pp. 133–138.

[260] Chao-cheng Wang and C. (Clifford) Truesdell. *Introduction to rational elasticity*. Noordhoff International Pub. Co, 1973, p. 556.

[261] Vicky Y. Wang, H.I. Lam, Daniel B. Ennis, Brett R. Cowan, Alistair A. Young, and Martyn P. Nash. "Modelling passive diastolic mechanics with quantitative MRI of cardiac structure and function". In: *Med. Image Anal.* 13.5 (2009), pp. 773–784.

[262] Zhijie Wang, Mark J. Golob, and Naomi C. Chesler. "Viscoelastic Properties of Cardiovascular Tissues". In: *Viscoelastic and Viscoplastic Materials*. InTech, Sept. 2016, pp. 141–163. DOI: 10.5772/64169.

[263] Ian R. Wanless and John S. Lentz. "Fatty liver hepatitis (steatohepatitis) and obesity: An autopsy study with analysis of risk factors". In: *Hepatology* 12.5 (1990), pp. 1106–1110.

[264] Marc Weilbeer. *Efficient numerical methods for fractional differential equations and their analytical background*. Papierflieger, 2005.

[265] Noel S. Weiss. "Breast Cancer Mortality in Relation to Clinical Breast Examination and Breast Self-Examination". In: *Breast J.* 9.s2 (2003), S86–S89.

[266] E. Wiechert. "Gesetze der Elastischen Nachwirkung für Constante Temperatur". In: *Annalen der Physik* 286.10 (1893), pp. 335–348. DOI: 10.1002/andp.18932861011.

[267] Flugge Wilhelm. *Viscoelasticity*. London: Springer-Verlag, t975, 1975.

[268] Christopher D. Williams, Joel Stengel, Michael I. Asike, Dawn M. Torres, Janet Shaw, Maricela Contreras, Cristy L. Landt, and Stephen A. Harrison. "Prevalence of nonalcoholic fatty liver disease and nonalcoholic steatohepatitis among a largely middle-aged population utilizing ultrasound and liver biopsy: A prospective study". In: *Gastroenterology* 140.1 (2011), pp. 124–131.

[269] World Health Organization. *Global hepatitis report, 2017. Global Hepatitis Programme*. Tech. rep. 2017, p. 68.

[270] Ziheng Wu, Timothy C. Ovaert, and Glen L. Niebur. "Viscoelastic properties of human cortical bone tissue depend on gender and elastic modulus". In: *Journal of Orthopaedic Research* 30.5 (Nov. 2011), pp. 693–699. DOI: 10.1002/jor.22001.

[271] Wenfeng Xia, Daniele Piras, Michelle Heijblom, Wiendelt Steenbergen, Ton G van Leeuwen, and Srirang Manohar. "Poly(vinyl alcohol) gels as photoacoustic breast phantoms revisited." In: *J. Biomed. Opt.* 16 (2011), p. 75002.

[272] Jingping Xu, Sakya Tripathy, Jonathan M Rubin, Ryan W Stidham, Laura a. Johnson, Peter D R Higgins, and Kang Kim. "A New Nonlinear Parameter in the Developed Strain-to-Applied Strain of the Soft Tissues and Its Application in Ultrasound Elasticity Imaging". In: *Ultrasound Med. Biol.* 38.3 (2012), pp. 511–523.

[273] Jun Xu, Xiao Liu, Yukinori Koyama, Ping Wang, Tian Lan, In-Gyu Kim, In H Kim, Hsiao-Yen Ma, and Tatiana Kisseleva. "The types of hepatic myofibroblasts contributing to liver fibrosis of different etiologies." In: *Front. Pharmacol.* 5 (2014), p. 167.

[274] Kuan Xu and Shidong Jiang. "A Bootstrap Method for Sum-of-Poles Approximations". In: *Journal of Scientific Computing* 55.1 (June 2012), pp. 16–39. DOI: 10.1007/s10915-012-9620-9.

[275] Yale Medical Cell Biology. URL: http://medcell.med.yale.edu/systems%7B%5C_%7Dcell%7B%5C_%7Dbiology%7B%5C_%7Dold/liver%7B%5C_%7Dand%7B%5C_%7Dpancreas%20/images/liver%7B%5C_%7Dcartoon.jpg (visited on 01/01/2015).

[276] Q. Yang, F. Liu, and I. Turner. "Numerical methods for fractional partial differential equations with Riesz space fractional derivatives". In: *Applied Mathematical Modelling* 34.1 (Jan. 2010), pp. 200–218. DOI: 10.1016/j.apm.2009.04.006.

[277] Wen Chun Yeh, Pai Chi Li, Yung Ming Jeng, Hey Chi Hsu, Po Ling Kuo, Meng Lin Li, Pei Ming Yang, and Huang Lee Po. "Elastic modulus measurements of human liver and correlation with pathology". In: *Ultrasound Med. Biol.* 28.4 (2002), pp. 467–474.

[278] M. Yin, J. Chen, K. J. Glaser, J. A. Talwalkar, and R. L. Ehman. "Abdominal magnetic resonance elastography." In: *Top. Magn. Reson. Imaging* 20.2 (2009), pp. 79–87.

[279] N Yoganandan, F A Pintar, T A Gennarelli, and M R Maltese. "Patterns of abdominal injuries in frontal and side impacts." In: *Annu. proceedings. Assoc. Adv. Automot. Med.* 44 (2000), pp. 17–36.

[280] Lixia Yuan and Om P. Agrawal. "A Numerical Scheme for Dynamic Systems Containing Fractional Derivatives". In: *Journal of Vibration and Acoustics* 124.2 (2002), p. 321. DOI: 10.1115/1.1448322.

[281] Paul A. Yushkevich, Joseph Piven, Heather Cody Hazlett, Rachel Gimpel Smith, Sean Ho, James C. Gee, and Guido Gerig. "User-guided 3D active contour segmentation of anatomical structures: Significantly improved efficiency and reliability". In: *Neuroimage* 31.3 (2006), pp. 1116–1128. DOI: 10.1016/j.neuroimage.2006.01.015.

[282] Samaneh Soradi Zeid. "Approximation methods for solving fractional equations". In: *Chaos, Solitons & Fractals* 125 (Aug. 2019), pp. 171–193. DOI: 10.1016/j.chaos.2019.05.008.

[283] Deliang Zhang, Zhide Guo, Pu Zhang, Yesen Li, Xinhui Su, Linyi You, Mengna Gao, Chang Liu, Hua Wu, and Xianzhong Zhang. "Simplified quantification method for in vivo SPECT/CT imaging of asialoglycoprotein receptor with 99m Tc-p(VLA-co-VNI) to assess and stage hepatic fibrosis in mice". In: *Sci. Rep.* 6.1 (2016), p. 25377.

[284] Olgierd Cecil Zienkiewicz, Robert Leroy Taylor, Robert Leroy Taylor, and Robert Lee Taylor. *The finite element method: solid mechanics*. Vol. 2. Butterworth-heinemann, 2000.

[285] Marianne Ziol, Adriana Handra-Luca, Adrien Kettaneh, Christos Christidis, Frédéric Mal, Farhad Kazemi, Victor De Lédinghen, Patrick Marcellin, Daniel Dhumeaux, Jean Claude Trinchet, and Michel Beaugrand. "Noninvasive assessment of liver fibrosis by measurement of stiffness in patients with chronic hepatitis C". In: *Hepatology* 41.1 (2005), pp. 48–54.

[286] Mark E Zobitz, Zong-Ping Luo, and Kai-Nan An. "Determination of the Compressive Material Properties of the Supraspinatus Tendon". In: *J. Biomech. Eng.* 123.1 (2001), p. 47.

[287] C. Zopf, S.E. Hoque, and M. Kaliske. "Comparison of approaches to model viscoelasticity based on fractional time derivatives". In: *Computational Materials Science* 98 (Feb. 2015), pp. 287–296. DOI: 10.1016/j.commatsci.2014.11.012.

[288] Miguel Eugenio Zoubek, Christian Trautwein, and Pavel Strnad. *Reversal of liver fibrosis: From fiction to reality*. 2017.